FINAL REPORT

Contract Number NAS5—31363

OCEAN OBSERVATIONS WITH EOS/MODIS:
Algorithm Development and Post Launch Studies

(December 14, 1991 — May 14, 2004)

Submitted by

Kenneth J. Voss, PI and Howard R. Gordon
Department of Physics
University of Miami
Coral Gables, FL 33124

and

William M. Balch
Bigelow Laboratory for Ocean Sciences
McKown Point
W. Boothbay Harbor, ME 04575

May 2004

Preface

The importance of ocean color measurements to study the global distribution and variability of phytoplankton is well-understood, and will not be repeated here. Suffice it to say that global phytoplankton pigment fields are required every two days. It has been known since about 1980 that the strong light scattering by detached coccoliths from coccolithophores can be easily observed in satellite imagery of the oceans. The fact that coccoliths play a role in the global carbon cycle through sedimentation, and that dimethylsulfide (DMS) produced by coccolithophores may be a major source of cloud condensation nuclei, are strong motivations for developing a global understanding of the distribution and variance of these organisms in space and time. Development and validation of algorithms for the production of data sets of phytoplankton pigments and coccolith concentration is the focus of our participation on MODIS Experiment Team.

The principal focus of this research was the development, maintenance, and validation of algorithms for the retrieval of the nadir-viewing water-leaving radiance from MODIS data. The nadir-viewing water-leaving radiances are required for all of the proposed oceanic data products from MODIS. These algorithms are usually collectively referred to as "atmospheric correction;" however, along with a basic algorithm to remove the effects of scattering in the atmosphere between the sea surface and the sensor, they also deal with corrections for the radiance added by whitecaps, for the radiance added by direct sun light reflection from the sea surface (sun glitter) in situations where it is sufficiently weak that it is not a dominant source of radiance at the sensor, and for the scan and sun angle effects on the water-leaving radiance.

A secondary focus was development, maintenance, and validation of algorithms for a study of the global distribution of the concentration of detached coccoliths from a ubiquitous species of coccolithophores (*Emiliania huxleyi*).

This Final Report is divided into two parts. The first (Part 1) deals exclusively with the atmospheric correction focus. The second (Part 2) deals exclusively with the coccolithophore algorithm. There are two appendices. Appendix I provides an annotated bibliography of the all of the contract-supported papers that were published in peer-reviewed journals. The annotations describe how the research described in the particular publication contributed to the total research effort. Appendix II provides the final revision (Revision 5) of the water-leaving radiance Algorithm Theoretical Basis Document (ATBD). It provides the state of the Terra/MODIS algorithms at the conclusion of the contract.

FINAL REPORT

Contract Number NAS5—31363

OCEAN OBSERVATIONS WITH EOS/MODIS:
Algorithm Development and Post Launch Studies

(December 14, 1991 — May 14, 2004)

Part 1: ATMOSPHERIC CORRECTION

Submitted by

Kenneth J. Voss, PI and Howard R. Gordon
Department of Physics
University of Miami
Coral Gables, FL 33124

May 2004

ATMOSPHERIC CORRECTION

Introduction

Following the work of *Clarke, Ewing and Lorenzen* [1970] showing that the chlorophyll concentration in the surface waters of the ocean could be deduced from aircraft measurements of the spectrum of upwelling light from the sea — the "ocean color" — NASA launched the Coastal Zone Color Scanner (CZCS) on Nimbus-7 in late 1978 [*Gordon et al.*, 1980; *Hovis et al.*, 1980]. The CZCS was a proof-of-concept mission with the goal of measuring ocean color from space. This goal was achieved, and the potential yield of ocean color studies to the understanding of biological processes in the oceans has led to the launching, by various countries, of a total of 16 instruments capable of observing ocean color. The most sophisticated of these instruments being MODIS, the focus of this report.

The realization of the promise of ocean color rests squarely on two observations: (1) that there exists a more or less universal relationship between the color of the ocean and the chlorophyll concentration for most open ocean waters; and (2) that it is possible to develop algorithms to remove the interfering effects of the atmosphere from the imagery (atmospheric correction). Although the post CZCS instruments all have more or less the same spectral bands as CZCS in the visible, they were all designed to facilitate atmospheric correction via the addition of spectral bands in the near infrared (NIR), where the ocean for the most part can be considered to be a non-emitting black body.

This portion of the report focuses on our work relating to the extension of the atmospheric correction algorithm for CZCS [*Gordon*, 1978; *Gordon et al.*, 1983] to MODIS (initially to SeaWiFS for testing and validation). The algorithm is described in detail in the MODIS Normalized Water-leaving Radiance Algorithm Theoretical Basis Document, Version 5 Attached as Appendix 1 [See also *Gordon* [1997]].

Background

The reflectance of the ocean-atmosphere system as measured at the top of the atmosphere, ρ_t, can be decomposed into a part due to backscattering within that atmosphere and reflection off the sea surface, and a part due to photons that penetrate the sea surface and are backscattered *out* of the water – the normalized water-leaving reflectance, $[\rho_w]_N$, i.e.,

$$\rho_t(\lambda) = \rho_r(\lambda) + \rho_a(\lambda) + \rho_{ra}(\lambda) + t_v\rho_{wc}(\lambda) + T\rho_g(\lambda) + t_vt_s[\rho_w(\lambda)]_N$$

where $\rho_r(\lambda)$ and $\rho_a(\lambda)$ are, respectively, the reflectances due to scattering by the air (Rayleigh) and scattering by the aerosol, *each in the absence of the other*, $\rho_{ra}(\lambda)$ is a correction resulting from the fact that air and aerosols are simultaneously present in the atmosphere, $\rho_{wc}(\lambda)$ is the component of reflectance due to whitecaps on the sea surface, and $\rho_g(\lambda)$ the reflectance due to the specular reflection of direct sunlight off the sea surface (sun glitter). The quantities t_v and t_s are the diffuse transmittances of the atmosphere from the sun to the surface (t_s) and from the surface to the sensor (t_v), and T is the direct transmittance from the surface to the sensor.

Gordon and Wang [1994] developed the basic MODIS atmospheric correction algorithm. Its performance was then validated through simulations and, starting in 1997, through direct application to SeaWiFS imagery, as the launch of MODIS was (at that time) two years away. The basic idea of atmospheric correction is to (1) use TOMS data to account of Ozone absorption in the atmosphere, (2) use the wind speed (derived from NCEP analysis) to discard pixels for which $\rho_g(\lambda)$ is significant and to estimate ρ_{wc}, (3) use the wind speed and atmospheric pressure to estimate $\rho_r(\lambda)$, and (4) use the fact that $[\rho_w(\lambda)]_N$ is negligible in the NIR (765 and 865 nm for SeaWiFS, 749, and 869 nm for MODIS) to estimate the combination $\rho_r(\lambda) + \rho_{ra}(\lambda)$ at these wavelengths. The latter estimate is then used to extrapolate$\rho_r(\lambda) + \rho_{ra}(\lambda)$ from the NIR to the visible. Finally, expressions for the t's, also based in the NIR imagery, are used to estimate $[\rho_w(\lambda)]_N$ in the visible. All of the bio-physical products derived from ocean color use these $[\rho_w(\lambda)]_N$ estimates as input data.

It was recognized early in the development of the algorithm [*Gordon and Wang*, 1994] that multiple scattering had a significant effect on $\rho_r(\lambda) + \rho_{ra}(\lambda)$, that the effect grew as the aerosol concentration increased, and that the significance of multiple scattering was itself dependent on the properties of the aerosol, e.g., the multiple scattering effect computed for an aerosol with given chemical-physical properties could not be applied to those of an aerosol with different properties, even if their optical thicknesses were comparable. Thus, aerosol models were required to assess $\rho_r(\lambda) + \rho_{ra}(\lambda)$ in the visible from $\rho_r(\lambda) + \rho_{ra}(\lambda)$ in the NIR, and to estimate the diffuse transmittances.

In addition to this basic algorithm as described above, there were several algorithmic issues that have been resolved during our involvement with MODIS. These included

- assessing the possible effect of approximating the atmosphere as a plane-parallel medium as opposed to a spherical shell medium [*Ding and Gordon*, 1994],
- analyzing the effects of, and developing an approximate method to correct for, the polarization sensitivity of ocean color instruments [*Gordon, Du and Zhang*, 1997b] (a particularly serious problem with MODIS),
- developing an approach for computing the exact diffuse transmittance and its dependence on the bi-directional reflectance distribution (BRDF) of the water [*Yang and Gordon*, 1997],
- analyzing the effects of, and developing an approximate method to correct for, the polarization sensitivity of ocean color instruments [*Gordon, Du and Zhang*, 1997b] (a particularly serious problem with MODIS),
- developing a method for dealing with sensors with spectral bands that have significant out-of-band characteristics [*Gordon*, 1995],
- examining the effects of stratospheric aerosols and thin cirrus clouds on ocean color imagery and proposing an algorithm to remove the latter using the MODIS 1.38 μm band [*Gordon et al.*, 1996] 1997], and
- measuring the spectral reflectance $\rho_{wc}(\lambda)$ of whitecaps as a function of wind speed and verifying the *Frouin, Schwindling and Deschamps* [1996] spectral variation *Moore, Voss and Gordon* [1997].

When merited, modifications based on these studies have been included in the SeaWiFS/MODIS atmospheric correction algorithm. The validity of the MODIS algorithm was demonstrated with the success of SeaWiFS and later confirmed with MODIS.

As a result of the computational studies during development of the MODIS algorithm, it became apparent that additional data sets were needed to help resolve outstanding issues, but instrumentation to measure these parameters was not generally available. Thus, several new instruments were developed during the course of our effort. In an effort to understand the spectral reflectance of whitecaps mentioned above, we started with various commercial imaging devices. However, these were not suitable for acquiring the necessary data set, and as a result, we had to build a custom radiometer to study whitecaps [*Moore, Voss and Gordon*, 1998]. As part of our effort to understand the light scattering from aerosols, we needed measurements of the downwelling skylight radiance distribution, including polarization. These measurements were required to be performed on a ship, necessitating development of unique instrumentation [*Liu and Voss*, 1997; *Voss and Liu*, 1997] This system is based on the same fisheye technology used in our in-water radiance distribution camera systems, but sequential images with linear polarizers allowed the state of the linear polarization of the skylight to be determined. As aerosols scatter light predominately through small angles, we also needed measurements of the sky radiance distribution very close to the sun (the solar aureole). We then developed an instrument that could make these measurements from the solar disk out to 10° [*Ritter and Voss*, 2000] on a moving platform. With these instruments and commercially available sun photometers we are able to make a complete set of sky radiance distribution data to study aerosol scattering and its polarization.

As the numerical simulations developed, we found that the vertical distribution of aerosols became important in the case of strongly-absorbing aerosols [*Gordon, Du and Zhang*, 1997a]. However there was very little data on the vertical distribution of aerosols over the ocean. The natural instrument for this problem is a lidar system; however most lidar systems have been large and awkward to use at sea. This was remedied in the mid-90's when Science and Engineering Services, Inc. began producing the Micro-Pulse Lidar (MPL) [*Spinhirne, Ball and Scott*, 1995]. We were able to acquire this system and operate it in various field campaigns. The MPL was used in several cruises near Lanai in Hawaii where we found that almost all of the aerosols were in the marine boundary layer, which was capped at approximately 1-2 km [*Welton*, 1998]. Investigations of Saharan Dust, and biomass burning were carried out during the ACE-II experiment in Tenerife, Canary Islands [*Welton et al.*, 2000] and on a cruise from Norfolk, Va. to Cape Town, SA [*Voss et al.*, 2001]. Pollution and marine aerosols over the Indian Ocean were measured during INDOEX [*Welton et al.*, 2002], while pollution aerosols, Asian dust and Pacific marine aerosols were studied during ACE-ASIA [*Bates*, 2003]. Although we are still in the process of working with the ACE-ASIA data set, the results from the vertical structure of the aerosols measured during these field campaigns have influenced our atmospheric correction algorithm development, particularly in the case of strongly-absorbing aerosols.

Unresolved Issues: Descriptions

In spite of the SeaWiFS/MODIS success, there are still unresolved or partially resolved atmospheric correction issues for the MODIS algorithms. These are

- the inability of the basic algorithm to deal with strongly-absorbing aerosols, e.g., windblown dust,
- the inability of the basic algorithm to deal with Case 2 coastal waters for which $[\rho_w]_N$ is not negligible in the NIR, and which often occur in the presence of strongly-absorbing aerosols (urban pollution),
- the lack of a provision for dealing with bi-directional reflectance distribution function (BRDF) effects that are known to cause systematic differences between $[\rho_w]_N$, typically measured at nadir in calibration and validation exercises, and that measured by the sensor in the particular viewing direction for the given pixel,
- the absence of water BRDF effects in estimation of the diffuse transmittance factor t_v,
- and uncertainty in the MODIS polarization characterization.

In addition, although neglect of the polarization properties of light scattered from aerosols has been shown to be relatively unimportant in atmospheric correction [*Gordon*, 1997], the MODIS instruments have significant polarization sensitivity, and it is important to know the polarization state of the radiance measured by MODIS [*Gordon, Du and Zhang*, 1997b] Neglect of aerosol (and water) polarization in atmospheric correction can lead to systematic variations of derived products that are difficult to understand.

- Better characterization of the aerosol's influence on the polarization of the radiance at the top of the atmosphere is required in the atmospheric correction algorithm to properly account for the polarization sensitivity of the MODIS instruments.

We are presently carrying out research directed toward solving these problems with the goal of placing remedies in the MODIS processing algorithms.

Unresolved Issues: Current Status

The MODIS atmospheric correction algorithm is at present capable of producing adequate water-leaving radiances only in the absence of strongly absorbing aerosols, e.g., carbonaceous aerosols involved in urban pollution and desert dust carried over the oceans by the winds. In their presence, the algorithm overestimates the aerosol contribution to the radiance at the sensor [*Gordon*, 1997], and thus underestimates L_w in the blue leading to too-high pigment concentrations. In addition, in its present form, it is capable of operating properly only in Case 1 waters, i.e., waters for which the optical properties are determined by the water itself and by phytoplankton and their immediate detrital material [*Gordon and Morel*, 1983]. A fundamental assumption of the atmospheric correction algorithm is that in such waters there is negligible or low water-leaving radiance in the near infrared (NIR). The complication of non-negligible, but still low, water-leaving radiance in the NIR in Case 1 waters can be handled in a relatively simple manner [*Siegel et al.*, 2000]. However, in Case 2 waters, the optical properties can depend on a number of other constituents, and when there is a high concentration of suspended material in addition to phytoplankton, e.g., from resuspended benthic sediments in coastal areas, there is significant water-leaving radiance in the NIR.

The principal difficulty with either strongly absorbing aerosols or Case 2 waters is that the top-of-atmosphere reflectance in the NIR does not provide sufficient information to characterize the aerosol's absorption [*Gordon*, 1997], or (in Case 2 waters) the spectral variation of the aerosol's reflectance. This means that the sensor's spectral bands in the visible must be used to characterize the aerosol as well as to retrieve the water's bio-optical properties. An algorithm that addresses such situations must utilize a model of oceanic reflectance in addition to aerosol models. We have developed two algorithms for dealing with absorbing aerosols: (1) the spectral matching algorithm (SMA) [*Gordon, Du and Zhang*, 1997a] , and (2) the spectral optimization algorithm SOA [*Chomko and Gordon*, 1998]. Two models of the reflectance as a function of bio-optical state have been employed with these algorithms: (1) the *Gordon et al.* [1988] model that provides water-leaving reflectance as a function of phytoplankton pigments (the sum of the concentrations of chlorophyll *a* and phaeophytin *a*) and a scattering parameter; and (2) the *Garver and Siegel* [1997] as modified by *Maritorena, Siegel and Peterson* [2002], which provides the water's reflectance as a function of the absorption coefficient of colored detrital matter — particulate and dissolved — [a_{cdm}] at 443 nm, the absorption coefficient of phytoplankton at 443 nm [a_{ph}], and the backscattering coefficient of particulate matter [b_{bp}] at 443 nm.

Improved atmospheric correction in dust

The MODIS atmospheric correction algorithm is at present capable of producing adequate water-leaving radiances only in the absence of strongly absorbing aerosols. In their presence, the algorithm overestimates the aerosol contribution to the radiance at the sensor [*Gordon*, 1997], and thus underestimates L_w the blue leading to too-high pigment concentrations.

In the Atlantic and Indian Oceans, a predominant absorbing aerosol in the marine atmosphere is the mineral dust coming from Africa [*Herman et al.*, 1997]. This dust is strongly absorbing in the blue because it contains ferrous minerals [*Patterson*, 1981]. In addition, the impact of this absorption is very dependent on the vertical distribution of the aerosol [*Gordon*, 1997]. This is of primary importance for Saharan dust [*Moulin et al.*, 2001b]. Because of these difficulties, the present MODIS and SeaWiFS algorithms do not process pixels if high L_t is detected in the NIR. The quasi-permanent presence of dust degrades satellite ocean color products in the Tropical Atlantic and Arabian Sea where large areas are not sampled, sometimes for as long as an entire month. An example from the Arabian Sea is provided in Figure 1. It shows that almost the entire Arabian Sea is unsampled during the Southwest Monsoon because of dust from Africa. This failure of the atmospheric correction also prevents observation of the potential fertilization effect due to the supply of nutrients contained in dust to the surface water [*Young et al.*, 1991].

[*Moulin et al.*, 2001b] have reported a technique for atmospheric correction through African dust based in the spectral matching algorithm (SMA) of *Gordon, Du and Zhang* [1997a], that allows retrieval of $[\rho_w]_N$ and the chlorophyll concentration at dust optical depths as high as 0.8. *Banzon et al.* [2004] have used this algorithm to process the SeaWiFS imagery from the Arabian Sea during 2000 shown in Figure 2 in a novel manner. SMA was used to select the "best" aerosol model from a set of 18 we developed for use in this region [*Moulin et al.*, 2001a]. The selected model was then used to subtract the aerosol component from the imagery yielding the normalized water-leaving reflectance. These values of $[\rho_w]_N$ were used as input to the now-standard SeaWiFS OC4v4

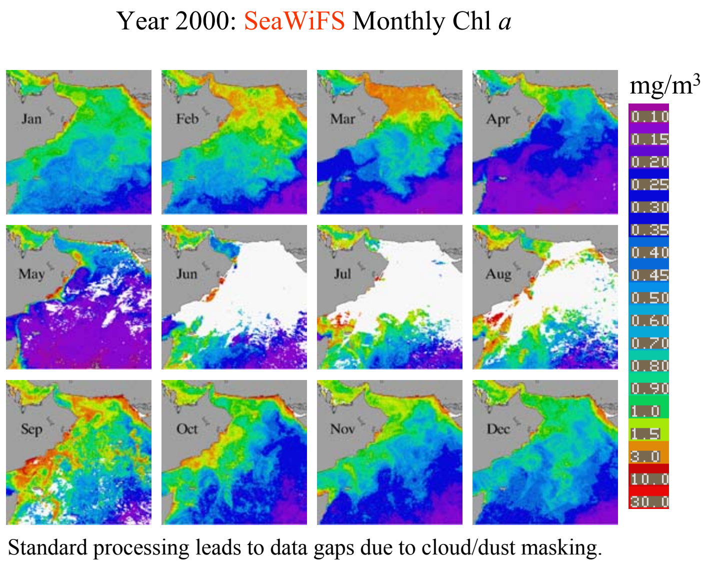

Figure 1. Monthly concentration of chlorophyll *a* derived from SeaWiFS imagery using the standard atmospheric correction algorithm [*Gordon and Wang*, 1994].

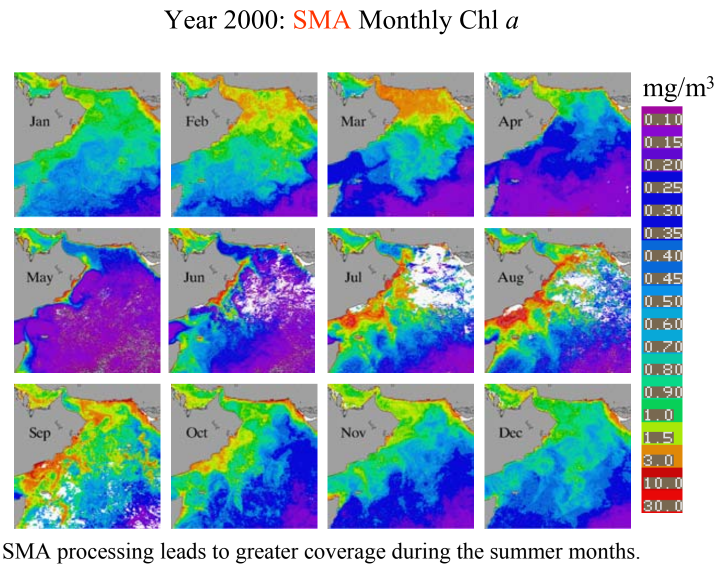

Figure 2. Monthly concentration of chlorophyll *a* derived from SeaWiFS imagery using the spectral matching algorithm [*Moulin et al.*, 2001b].

bio-optical algorithm to estimate the concentration of chlorophyll a (Chl). The comparison with the standard SeaWiFS algorithm is striking – there is a dramatic increase in coverage during the monsoon period that clearly reveals the enhanced productivity unseen in the standard processing.

There are several issues that must be resolved to operate this algorithm in a seamless manner with the present atmospheric correction, that is adequate in areas with non-absorbing aerosols. The first is simply porting our SMA code to the MODIS processing environment and ensuring that it performs properly. The second is finding a method for distinguishing areas with dust from areas of non-absorbing aerosols at higher-than-normal concentrations. The third is to devise a method to ensure continuity between areas that use the standard processing and those using the SMA processing.

Extension of Spectral Optimization to Case 2 Waters

A spectral optimization algorithm was developed by [*Chomko and Gordon*, 1998]. Its purpose was to provide atmospheric correction in atmospheres that were contaminated by strongly absorbing aerosol of the carbonaceous type, i.e., refractive index nearly independent of wavelength. Such aerosols are expected off the U.S. East Coast in summer and in many coastal areas in the world. This algorithm was originally tested with SeaWiFS imagery [*Chomko and Gordon*, 2001] using the *Gordon et al.* [1988] bio-optical model, and later validated with the *Garver and Siegel* [1997] bio-optical model using SeaWiFS chlorophyll a and aircraft estimates of a_{cdm} [*Chomko et al.*, 2003]. The algorithm in the form validated by *Chomko et al.* [2003] assumes the absence of water-leaving radiance in the NIR; however, extension to the cases where this is no longer true is immediate: operate the algorithm in an iterative manner, where at each stage in the iteration, water-leaving radiance in the NIR is computed from the derived bio-optical parameters from the previous iteration. We have tested this idea in the sediment-dominated Case 2 waters of Pamlico Sound, NC. Figure 3 shows the two retrieved parameters of the aerosol model ω_0, the aerosol single scattering albedo, and ν, the free parameter in the power-law size distribution. Neither of these atmospheric parameters would be expected to be very different over the Sound and over the near-by ocean, i.e., we would expect continuity in both going from the Sound into the open ocean. Figure 3 shows that when the algorithm is operated in the Case 1 mode ω_0 is lower and ν is higher over the Sound than the off-shore waters. In contrast, almost complete continuity is observed when the

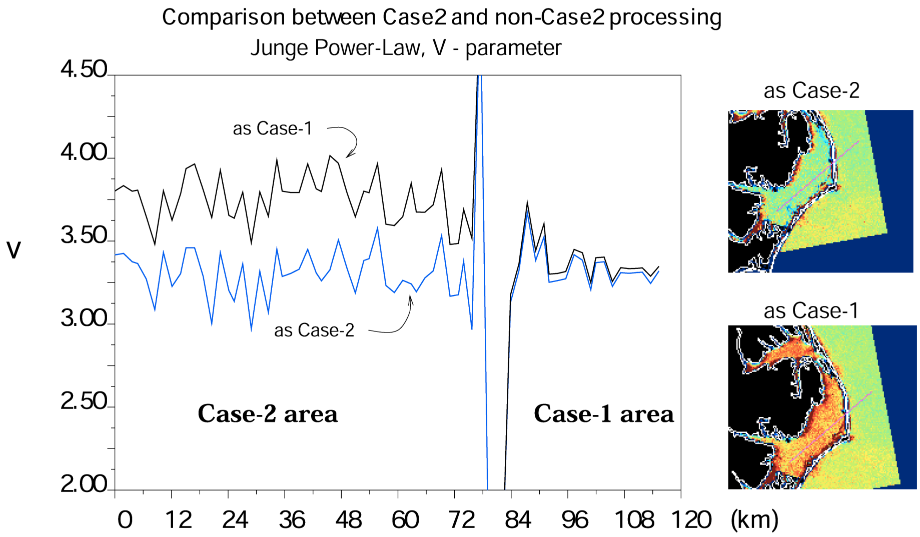

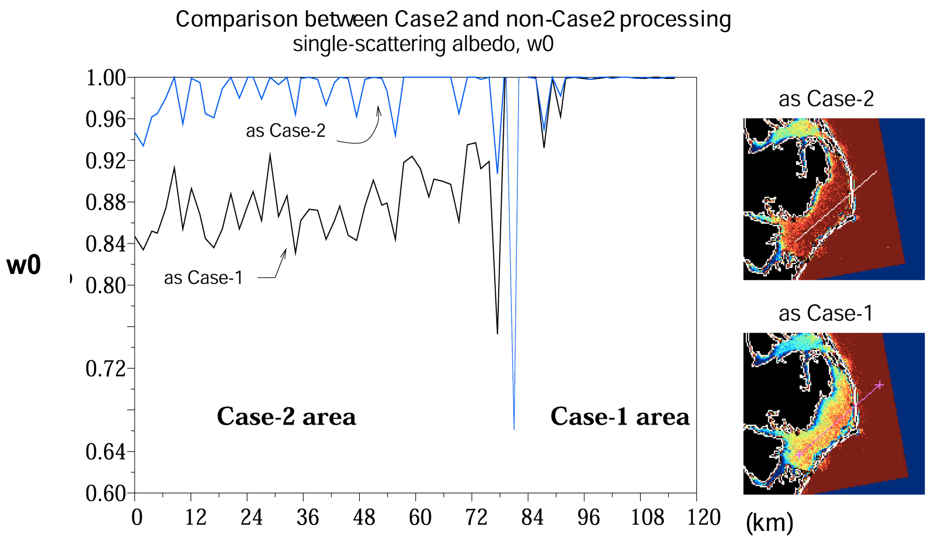

Figure 3. Comparison of the retrieved values of ν and ω_0 between Case 1 and Case 2 processing with the SOA. Note that the atmospheric parameters are virtually unchanged in going from the open ocean to the coastal waters with the Case 2 processing.

algorithm is operated in the Case 2 mode. This suggests that atmospheric correction was achieved in these turbid Case 2 waters. In this case, the quality of the retrieved bio-optical properties will be completely determined by the quality of the bio-optical model. We believe that it should be possible to tune the *Garver and Siegel* [1997] model parameters to the particular waters under examination to retrieve bio-optical parameters; however, such tuning will have to be site specific and season specific. We are in the process of validation of this algorithm for the Case 2 waters of the Chesapeake Bay, and have begun implementation in the MODIS processing environment.

Water reflectance BRDF

The standard definition of normalized water leaving radiance, $[\rho_w]_N$ defined above, or $[L_w]_N$ where L is radiance, is referenced to the nadir viewing direction. In general, measurements of upwelling radiance for use in algorithm development/validation and vicarious calibration are performed using in-water radiometers which measure the upwelling *nadir* radiance, or are performed above water using the remote sensing reflectance, R_{rs}, technique. The measurements obtained either way are usually assumed to be equivalent to the satellite measurement by assuming that the ocean is acting as a lambertian reflector, in other words, the radiance exiting the surface is independent of view angle. If the satellite measurement precision is low, this is a reasonable assumption. However, measurements [*Voss*, 2001] and modeling [*Morel and Gentili*, 1996] have shown that this is not a valid assumption in general. In the case of MODIS, with its high precision radiometry, the variation of the bi-directional reflectance function (BRDF) from the lambertian ideal *is* important. In particular it is important to identify and isolate variations due to the BRDF (a true geophysical parameter) as opposed to cross scan variations and instrument artifacts that should be calibrated out of the data set.

Another aspect of MODIS that makes characterizing the BRDF so important is the scan geometry of MODIS on both the Aqua and Terra platforms. Since the satellite equator crossing is significantly before (Terra) and after (Aqua) noon, relative view-illumination geometry varies significantly along the scan line.

Figure 4 shows an example of Terra/MODIS scan lines for several northern latitudes, for day 243 of 2000. For higher latitudes (45°N or larger) the scan geometry becomes more symmetric from left to right (nearly perpendicular to the sun-nadir plane, and similar to SeaWiFS), but at lower latitudes the scan line ranges from the solar to anti-solar direction (close to the principle plane) over a region where the upwelling radiance distribution can change significantly. Thus, characterization of the BRDF is particularly important for the MODIS normalized water-leaving radiance.

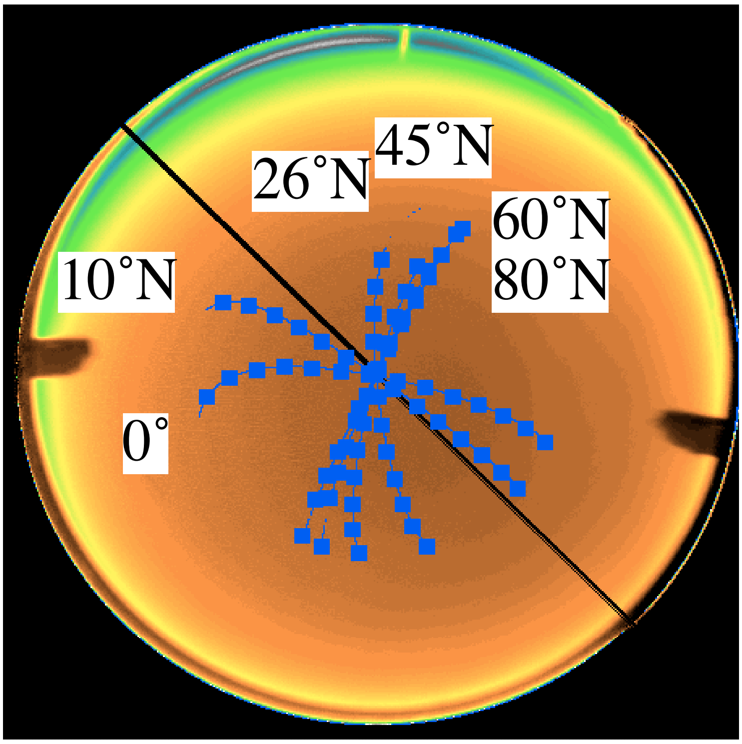

Figure 4. Variation of MODIS-Terra scan line geometry relative to the upwelling radiance distribution. The solid line is the principal plane, containing the nadir direction (center) and the solar azimuth (towards the upper left). The lines correspond to a scan line in a MODIS image ranging from the equator (0°) north. The scan line for 10°N is almost directly along the principal plane, thus would have the largest BRDF variation along the scan line.

The ocean BRDF is a result of both the downwelling light field geometry and the optical characteristics of the water and constituents in the water (backscattering, absorption, etc.). Thus, the BRDF changes with solar zenith angle, wavelength, and water constituents, making it difficult to predict. The backscattering portion of the light scattering phase function for marine particulates is particularly difficult to model because it is dependent on particle shape [*Mischenko, Travis and Macke*, 2000], and measurements may be very dependent on sample volume and particle density [*Zaneveld et al.*, 2002]. The implication of the latter point is that instruments that measure the shape of the volume scattering function (VSF), and necessarily have small volumes (on the order of cm^2), may not make a measurement relevant to the large volume average VSF on which the BRDF depends. Thus measurements of the in-situ BRDF are critical for this problem.

There are two different applications for the BRDF data that require different measurement strategies. The ultimate goal for the operational MODIS $[\rho_w]_N$ retrieval is a model that can predict the BRDF for each situation. However, because of the difficulties in modeling the particulates, this model will have to be carefully validated experimentally in varied water types. For general use it is necessary to take more extensive measurements through a long period of time so that the BRDF variation with solar zenith angle can be determined. In this case measurements taken continuously throughout the day in one location will provide a range of solar zenith angles, for a specific water type. Unfortunately due to ship costs, it is seldom feasible to sit at one location and make these measurements over an extended period of time so different days and cruises must be averaged together. In the end, these measurements can be compared with an existing model, e.g., [*Morel, Antoine and Gentili*, 2002], and also can be used to tune the model parameters to better fit the real world.

For vicarious calibration efforts [*Gordon*, 1987; *Gordon*, 1998] a fundamental requirement is to accurately determine the water leaving radiance viewed by the satellite. In this case a model will probably never be sufficiently accurate to totally remove the BRDF effect due to environmental variability. For calibration purposes it is necessary to make measurements of the BRDF in correlation with the other nadir upwelling radiance measurements during the period of the satellite overpass. However, the instantaneous upwelling radiance distribution measured at a point is strongly dependent on the specific air-sea surface at that moment while the satellite effectively views an extended average of this by looking at 1 km^2 pixels. For this application, it is necessary to average many BRDF images taken in rapid succession to get an equivalent view.

A BRDF measurement difficulty is that instrument self shadowing [*Gordon and Ding*, 1992] can interfere. In this measurement it is particularly important, as the preferred measurement geometry for ocean color is toward the anti-solar point, precisely where the instrument shadow will be located. For most of our current work we have been using the RADS-II instrument [*Voss and Chapin*, 1992]. This instrument was built with ONR support to look at both the upwelling and downwelling radiance distributions and, because of this application, is fairly large (0.50 m long, 0.40 m in diameter). Instrument self shadowing effects can be seen in simulations [*Doyle and Voss*, 2000] and in the data.

In 2002, we developed the NuRADS instrument specifically to look at only the upwelling radiance distribution. A picture of the NuRADS instrument, side by side with the RADS-II instrument is shown in **Figure 4**. Besides casting a smaller shadow by virtue of its size (0.3 m long, 0.24 m

Figure 5. The RADS-II instrument on the left, the NuRADS instrument on the right.

in diameter), the floatation for the instrument consists of 10 cm of foam attached to the end, with the same diameter as the instrument. This contrasts with the 0.7 m diameter round float used for RADS-II. In addition the electronics and software of the NuRADS has been updated, resulting in lower noise and much faster data acquisition. In the current experimental configuration this instrument is tethered to the ship by a neutrally buoyant cable, and allowed to float approximately 30 – 50 meters from the ship. This enables the instrument to avoid ship shadow problems. The instrument takes a data set every 2 minutes (6 wavelengths and associated dark images), and can be set to make these measurements continuously.

Since the *Morel, Antoine and Gentili* [2002] model of the BRDF (or $Q = L_u/E_u$, where E_u is the upwelling irradiance just beneath the surface) is the currently published standard for this effect, we made and are still making an extensive effort to compare this model with our set of measurements. In 1999, during the MODIS Ocean Characterization Experiment (MOCE)-5 cruise, we made upwelling BRDF measurements during the periods of the SeaWiFS overpass (it was pre-MODIS Terra launch) in varying water types. We are currently working with André Morel on testing his newest model [*Morel, Antoine and Gentili*, 2002] with this data. A sample of the comparisons is shown in **Figure 5** in two ways. This is one of the better agreements between model and data from this cruise. Figure 6 shows the measured Q, normalized to Nadir on the

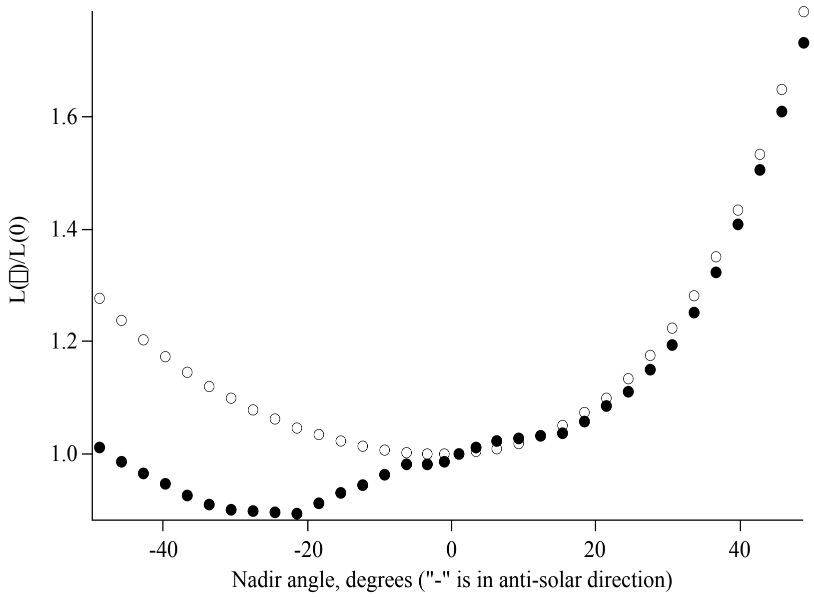

Figure 6. Comparison of the L_u model of *Morel, Antoine and Gentili* [2002] (open symbols) with experimental measurements (filled symbols) in the principal plane (plane containing the sun and the zenith). Measurement conditions: 440 nm, $\theta_0 = 38°$, $C = 10.1$ mg/m^3.

left, while the model's prediction for this Chlorophyll and solar zenith angle is shown on the right [effectively $L_u(\theta, \phi)/L_u(\text{Nadir})$, where θ and ϕ are, respectively, the polar and azimuth angles of the viewing direction]. The angles shown (up to 48° from nadir), are the subsurface angle, and is the range of angles that will be able to exit a flat air-sea interface. One can see both that the qualitative agreement between data and model is very good, and the range of this normalized Q is between 0.9 and 1.7, indicating a maximum of 70% error if this effect is not taken into account at large viewing angles. **Figure 5b** shows the quantitative difference between the model and data. In the forward direction (small azimuth angle) the agreement is excellent. However, in the backward direction the agreement is degraded. Since this data was acquired with the RADS-II instrument, one explanation is that this is the area of possible instrument self shading. However, an additional complication is that this portion of the radiance distribution is determined by the difficult-to-model (or measure) backward part of the volume scattering function, so disagreement with the model is not unexpected. Thus, it is important to redo these measurements with the NuRADS instrument (and its smaller instrument shadow) to determine the validity of the model in this important region.

We have been participated with Dennis Clark, NOAA, on all of the MOCE cruises and on many of the cruises dedicated to MOBY swap out. These have provided radiance distribution data for the vicarious calibration efforts. In addition we participated on a cruise with a small boat that allowed continuous measurements of the upwelling radiance distribution throughout the day in single locations near Honolulu. With these measurements we are starting to develop an empirical model for the BRDF correction of MOBY data to account for the difference between the MOBY nadir view and the actual satellite viewing geometry for the full range of solar zenith angles experienced at MOBY. Unfortunately because of the instantaneous light field noise experienced in these images it will take more than the one cruise to definitively settle this issue. Unfortunately

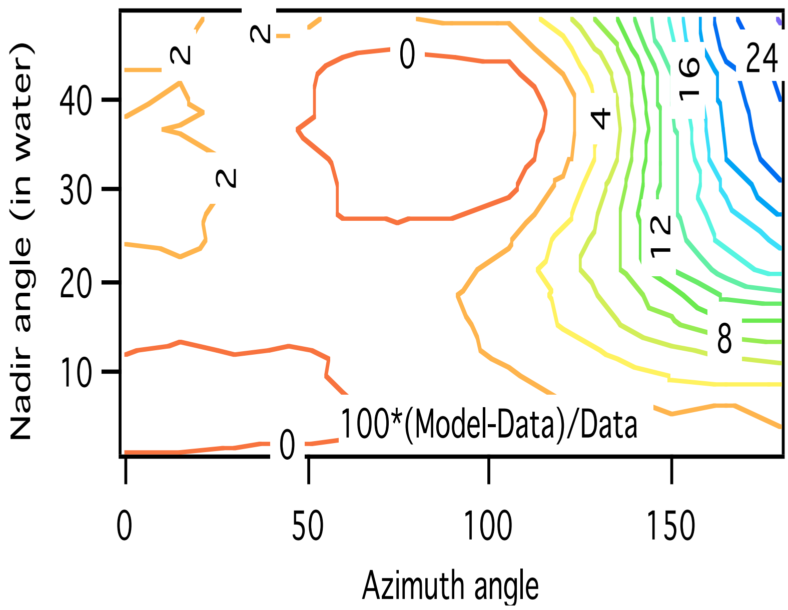

Figure 7. % difference between model prediction and data for example shown in Figure 6. Measurement conditions: 440 nm, $\theta_0 = 38°$, $C = 10.1$ mg/m^3.

because of the instantaneous light field noise experienced in these images it will take more than the one cruise to definitively settle this issue.

BRDF Effects in the Diffuse Transmittance.

An exact relationship for the diffuse transmittance for a light propagating in the direction –

$\hat{\xi}_0$ has been given by *Yang and Gordon* [1997]:

$$t(-\hat{\xi}_0) = \frac{1}{F_0|\hat{\xi}_0 \bullet \hat{n}_0|T_f(\hat{\xi}_0)} \int_{\Omega_d} |\hat{\xi} \bullet \hat{n}| L_R(\hat{\xi}) \frac{L_u(-\hat{\xi})}{L_u(-\hat{\xi}'_0)} \, d\Omega(\hat{\xi}), \tag{1}$$

where $L_u(-\hat{\xi})$ is the upward radiance distribution incident just beneath the sea surface for which we want t, $\hat{\xi}'_0$ and $\hat{\xi}_0$ are related by Snell's law, and Ω_d indicates the integral is to be evaluated over all downward $\hat{\xi}$.

These equations are both exact. The quantity T_f is the Fresnel reflectance of the interface, and $\hat{n}$ is the unit normal to the surface. In the present algorithm, L_u in the integral are taken to be a constant (i.e., totally diffuse), so the integral is just the downwelling irradiance from the sun and sky just beneath the sea surface. This approximation can cause an error of $\sim \pm 4\%$. This error coupled with the BRDF error for L_u itself means that the error in the retrieved $[\rho_w]_N$ could be as much as 15-20% or even higher, viewing in the principle plane.

Uncertainty in the MODIS Polarization Characterization

We have not been confident in the polarization sensitivity characterization of Terra MODIS largely due to the presence of a 4-cycle pattern in the response as the polarized source is rotated through 360°(the pattern should have two cycles). Thus we have been trying to understand the polarization characteristics of MODIS from fundamentals. For the last several months we have been working with Dr. Eugene Waluschka, and others at Goddard and MCST, modeling the polarization sensitivity of the MODIS sensor. During this time we have been assembling an optical model of the MODIS sensor using ZEMAX. In this work, Dr. Waluschka supplied the basic optical layout model and Samuel Pellicori generated thin film prescriptions for the coatings used on the various surfaces. To date we have applied the coatings on each of the surfaces, developed macros which allow averaging over the filter pass band and entrance aperture, and replicated the initial polarization sensitivity experiments that were performed before launch. Right now we have the thin film data for Terra and we are concentrating on this instrument. An example of the output of the polarization sensitivity and phase, for band 9, is shown in Figure 8. At this point the polarization sensitivity of the modeled system seems to be a factor of 2 below the pre-launch values. We will be investigating the model components through the summer to see which components are important to the polarization sensitivity of the instrument, and how sensitive the eventual polarization response is to the details of these components. We hope to replicate the pre-launch experiments, then

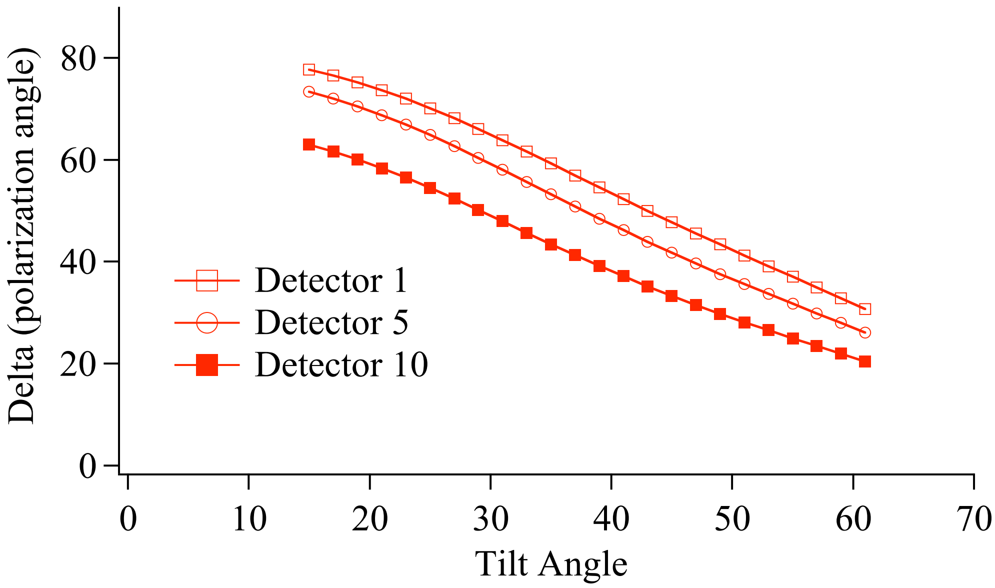

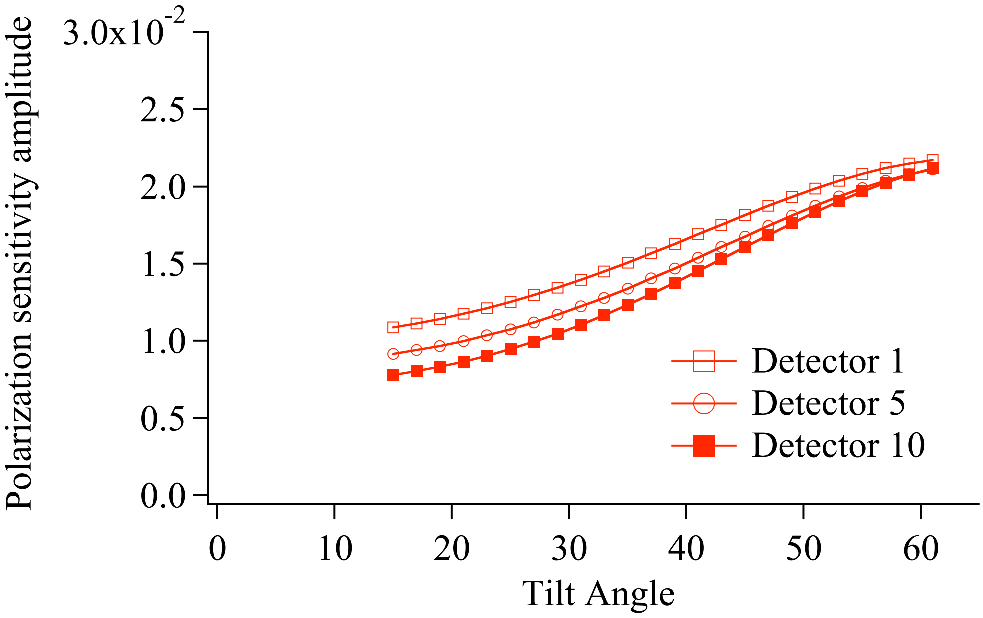

Figure 8. Polarization angle (upper) and sensitivity (lower) modeled for Terra/MODIS using ZEMAX.

look into the effect of in-space film degradation on the polarization sensitivity. Since there is no mechanism for doing a post launch polarization calibration we are hoping to put bounds on the expected polarization changes that might have occurred in flight, given the changes in the overall unpolarized instrument response.

Aerosol and Water Polarization Effects on Calibration and Atmospheric Correction.

The radiation reaching the top of the atmosphere is polarized by Rayleigh scattering, aerosol scattering, and surface reflection. The radiance backscattered out of the water is also polarized. *Gordon, Brown and Evans* [1988] showed that it was important, even in the case of CZCS to include polarization in the Rayleigh scattering component in the atmosphere; however, *Gordon* [1997] showed that ignoring polarization in the other atmospheric components was of little importance.

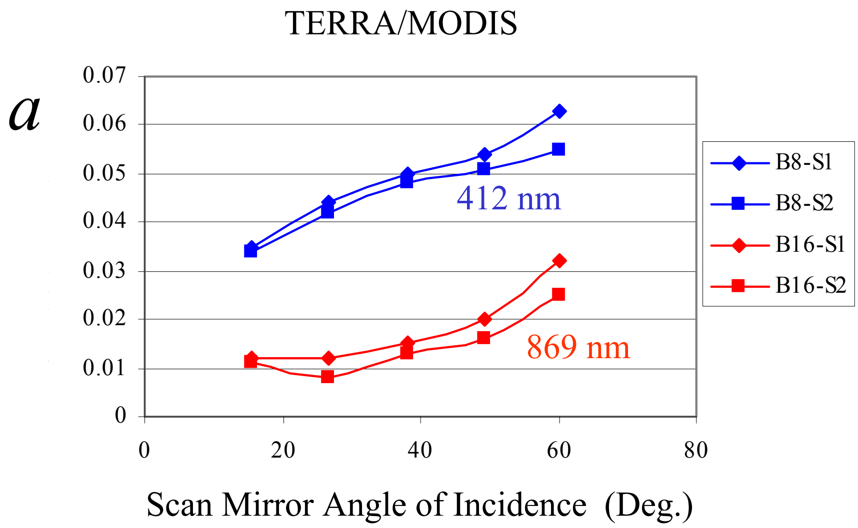

Figure 9. Polarization-sensitivity amplitude a for the Terra version of MODIS for Bands 8 (412 nm) and 16 (869 nm). S1 and S2 refer to the two sides of the MODIS scan mirror.

Although the polarization of the radiance backscattered out of the water has not been studied in any detail in the ocean using modern instrumentation, degrees of polarization as high a 40% have been observed in the past [*Ivanoff*, 1974].

The polarization of the top of the atmosphere light field is a significant problem only because the MODIS instrument displays a significant sensitivity to the polarization of the radiance being measured. Figure 9 shows this sensitivity for the 412 and 869 nm bands of TERRA/MODIS. The degree of polarization of ρ_t at 412 nm can be greater than 50% in some portions of the scan, thus the error in ρ_t — the product of the sensitivity and the degree of polarization, could be as high as ±2.5-3% at this wavelength. An error in the total radiance in the blue of this magnitude is totally unacceptable. Based on the analysis of polarization sensitivity by *Gordon, Du and Zhang* [1997b], a correction has been applied to MODIS imagery assuming that the polarization of the top-of-atmosphere radiance is that of molecular scattering. Figure 10 shows the efficacy of this revised correction method using simulated data. Later this was modified to assuming that the

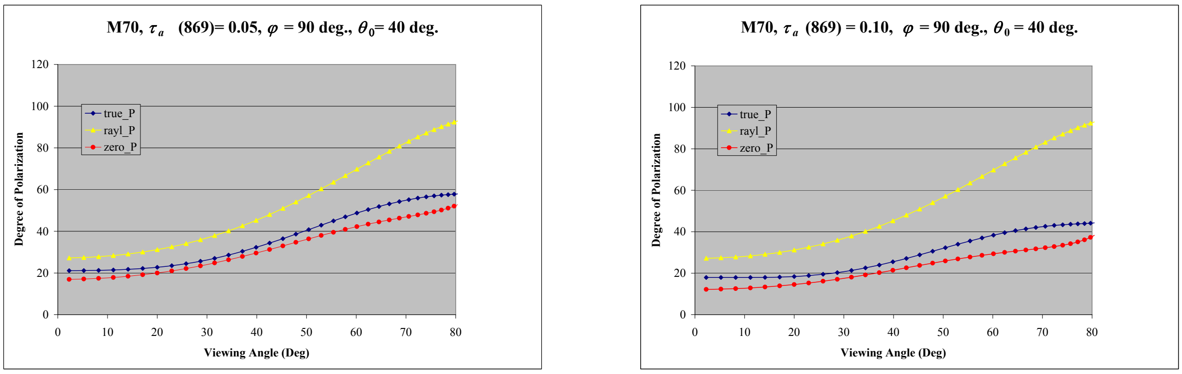

Figure 10. Efficacy of the revised polarization-sensitivity correction method. The true degree of polarization is compared to that in a pure Rayleigh scattering atmosphere and that in which all other contributors to the radiance are unpolarized. The computations are for a wavelength of 869 nm and the geometry is the perpendicular plane (similar to the MODIS scan at moderate sun angles) for a solar zenith angle of 40°. The aerosol model M70, characteristic of the MOBY calibration site, is used in the simulation. Left panel is for $\tau_a(869) = 0.05$ (a clear maritime atmosphere) and the right panel is for $\tau_a(869) = 0.10$ (a more typical maritime atmosphere).

non-molecular part was totally depolarized. The latter appeared to produce more consistent $[\rho_w]_N$ retrievals.

It is important to mention here that any error in the estimate of the polarization of the top-of-atmosphere radiance at the MOBY calibration site will result in an error that will propagate through the algorithms and result in a degraded MODIS product. It is believed that many of the artifacts observed in MODIS products result from error in the assumptions regarding the polarization of the top-of-atmosphere radiance at the calibration site and in operational use, and thus, in order to improve both,

- determination of the aerosol and water contributions to the polarization state of the top-of-atmosphere radiance at the MOBY calibration site, and
- improved estimates of the polarization state of the top-of-atmosphere radiance in general operation of the algorithm,

are required.

Lessons Learned

The algorithm development effort we have reported here has led to a reliable atmospheric correction procedure for MODIS as evidenced by the excellent SeaWIFS data processed using the same basic algorithm. However, there have been significant difficulties involved producing consistent ocean color data with the Terra MODIS, even to the extent that the processing of the data has been halted at the direction of NASA Headquarters. These difficulties are partially due to unstable instrument performance in the sense of random and sudden calibration shifts. In addition, there are time variations in the response versus scan angle (RVS) of the instrument and uncertainty in the MODIS polarization sensitivity characterization. Separating the variability in the products that these difficulties produce from real geophysical variability and eliminating these effects from the data has proven to be a formidable task that is yet to be completed.

The main lessons from our experience with MODIS are probably more relevant to instrument teams struggling with the design of new ocean color instruments, e.g., VIRS, etc., than to MODIS per se. In addition, as it seems apparent that future ocean color instruments will be of the "shared use" variety, i.e., general purpose instruments like MODIS to be shared by the ocean, atmosphere, and land communities, our observations are made with this in mind.

- A calibration facility like MOBY is absolutely essential to consistent ocean color products.

One could not even begin to address the difficulties with MODIS without the MOBY facility. Other than examination of the consistency between derived products on the edges of overlapping orbits, MOBY provided the only data upon which to build a picture of the RVS for the two mirror sides.

In addition, it provided a means to establish quasi- continuity across the various calibration epochs. For SeaWiFS it provided a continuous validation of the vicarious calibration.

- Polarization sensitivity of ocean color instruments must be kept to a minimum (zero if possible). More adequate polarization characterization procedures are needed.

The polarization specification for MODIS ($< 2\%$ for bands 9-16 and, although apparently omitted from the specification, 2.3% for band 8) was based on what simulations showed could be corrected in the data given adequate characterization. However, it is not clear even now that adequate characterization of polarization was achieved. The measurements have artifacts which are not well understood, and for which there are disagreements concerning procedures for removing them from the data. In our opinion, the best solution to this problem is to keep the polarization sensitivity much lower that 2% in future sensors. Alternatively, better characterization procedures should be developed. Sensors should not fly with polarization sensitivities exceeding 2%.

- New instruments must avoid RVS problems by having a fixed angle of incidence on all elements in the optical train during both earth view and on-board calibration.

This has been accomplished with previous sensors and should be revived.

- An accurate ZEMAX (commercial optical ray tracing program) model of the instrument should be developed at the same time an instrument is being constructed. Instrument characterization experiments should be simulated while the instrument is being characterized and compared with the simulations. This model should be turned over to NASA to help in analyzing and checking the characterization data. This model would also be useful if unexpected artifacts occur in the data stream.

We are currently trying to develop an instrument model for MODIS Terra, as part of our polarization work. The time this should have been done is at the initial instrument construction. When the polarization characterization was performed on Terra there was a large artifact that crept into the experiment. Having a model simulation to compare with the experimental result would have allowed this artifact to be recognized more quickly and the experiment repeated correctly. A model, validated through the instrument characterization period, would also be useful for simulating instrument changes through the flight period.

References

Banzon, V. F., R. E. Evans, H. R. Gordon and R. M. Chomko, SeaWiFS observations of the Arabian Sea Southwest Monsoon bloom for the year 2000, 2004, *Deep Sea Research II* (Submitted).

Bates, D., Lidar measurements of marine aerosols with improved analysis techniques, 2003, Ph.D. Diseration, Univ. of Miami, Coral Gables, Fl.

Chomko, R. and H. R. Gordon, Atmospheric correction of ocean color imagery: Use of the Junge power-law aerosol size distribution with variable refractive index to handle aerosol absorption, *Applied Optics*, *37*, 5560–5572, 1998.

Chomko, R. M. and H. R. Gordon, Atmospheric correction of ocean color imagery: Test of the spectral optimization algorithm with SeaWiFS, *Applied Optics*, *40*, 2973–2984, 2001.

Chomko, R. M., H. R. Gordon, S. Maritorena and D. A. Siegel, Simultaneous determination of oceanic and atmospheric parametters for ocean color imagery by spectral optimization: A validation, *Rem. Sens. Environ.*, *84*, 208–220, 2003.

Clarke, G. L., G. C. Ewing and C. J. Lorenzen, Spectra of Backscattered Light from the Sea Obtained From Aircraft as a Measurement of Chlorophyll Concentration, *Science*, *167*, 1119–1121, 1970.

Ding, K. and H. R. Gordon, Atmospheric correction of ocean color sensors: Effects of earth curvature, *Applied Optics*, *33*, 7096–7016, 1994.

Doyle, J. P. and K. J. Voss, 3D instrument self shading effects on in-water multi-directional radiance measurements, 2000, *Ocean Optics XV*, Monaco, November 2000.

Frouin, R., M. Schwindling and P. Y. Deschamps, Spectral reflectance of sea foam in the visible and near-infrared: In-situ measurements and implications for remote sensing of ocean color and aerosols, *Jour. Geophys. Res.*, *101C*, 14,361–14,371, 1996.

Garver, S. A. and D. A. Siegel, Inherent optical property inversion of ocean color spectra and its biogeochemical interpretation: 1 time series from the Sargasso Sea, *Jour. Geophys. Res.*, *102C*, 18607–18625, 1997.

Gordon, H. R., Removal of Atmospheric Effects from Satellite Imagery of the Oceans, *Applied Optics*, *17*, 1631–1636, 1978.

Gordon, H. R., Calibration Requirements and Methodology for Remote Sensors Viewing the Oceans in the Visible, *Remote Sensing of Environment*, *22*, 103–126, 1987.

Gordon, H. R., Remote sensing of ocean color: a methodology for dealing with broad spectral bands and significant out-of-band response , *Applied Optics*, *34*, 8363–8374, 1995.

Gordon, H. R., Atmospheric Correction of Ocean Color Imagery in the Earth Observing System Era, *Jour. Geophys. Res.*, *102D*, 17081–17106, 1997.

Gordon, H. R., In-orbit calibration strategy for ocean color sensors, *Remote Sensing of Environment*, *63*, 265–278, 1998.

Gordon, H. R., J. W. Brown and R. H. Evans, Exact Rayleigh Scattering Calculations for use with the Nimbus-7 Coastal Zone Color Scanner, *Applied Optics*, *27*, 862–871, 1988.

Gordon, H. R., O. B. Brown, R. H. Evans, J. W. Brown, R. C. Smith, K. S. Baker and D. K. Clark, A Semi-Analytic Radiance Model of Ocean Color, *Jour. Geophys. Res.*, *93D*, 10909–10924, 1988.

Gordon, H. R., D. K. Clark, J. W. Brown, O. B. Brown, R. H. Evans and W. W. Broenkow, Phytoplankton pigment concentrations in the Middle Atlantic Bight: comparison between ship determinations and Coastal Zone Color Scanner estimates, *Applied Optics*, *22*, 20–36, 1983.

Gordon, H. R., D. K. Clark, J. L. Mueller and W. A. Hovis, Phytoplankton pigments derived from the Nimbus–7 CZCS: initial comparisons with surface measurements, *Science*, *210*, 63–66, 1980.

Gordon, H. R. and K. Ding, Self-Shading of In-Water Optical Instruments, *Limnology and Oceanography*, *37*, 491–500, 1992.

Gordon, H. R., T. Du and T. Zhang, Remote sensing of ocean color and aerosol properties: resolving the issue of aerosol absorption, *Applied Optics*, *36*, 8670–8684, 1997a.

Gordon, H. R., T. Du and T. Zhang, Atmospheric correction of ocean color sensors: analysis of the effects of residual instrument polarization sensitivity, *Applied Optics*, *36*, 6938–6948, 1997b.

Gordon, H. R. and A. Y. Morel, *Remote Assessment of Ocean Color for Interpretation of Satellite Visible Imagery: A Review*, Springer-Verlag, New York, 1983, 114 pp.

Gordon, H. R. and M. Wang, Retrieval of water-leaving radiance and aerosol optical thickness over the oceans with SeaWiFS: A preliminary algorithm, *Applied Optics*, *33*, 443–452, 1994.

Gordon, H. R., T. Zhang, F. He and K. Ding, Effects of stratospheric aerosols and thin cirrus clouds on atmospheric correction of ocean color imagery: Simulations, *Applied Optics*, *36*, 682–697, 1997.

Herman, J. R., P. K. Bhartia, O. Torres, C. Hsu, C. Seftor and E. Celarier, Global Distribution of Absorbing Aerosols from Nimbus-7/TOMS Data, *Jour. Geophys. Res.*, *102D*, 16911–16922, 1997.

Hovis, W. A., D. K. Clark, F. Anderson, R. W. Austin, W. H. Wilson, E. T. Baker, D. Ball, H. R. Gordon, J. L. Mueller, S. Y. E. Sayed, B. Strum, R. C. Wrigley and C. S. Yentsch, Nimbus 7 coastal zone color scanner: system description and initial imagery, *Science*, *210*, 60–63, 1980.

Ivanoff, A., Polarization Measurements in the Sea, in *Optical Aspects of Oceanography*, edited by N. G. Jerlov and E. S. Nielsen, pp. 151–175, Academic Press, London, 1974.

Liu, Y. and K. J. Voss, Polarized radiance distribution measurements of skylight. II. Experiment and data, *Applied Optics*, *36*, 8753–8764, 1997.

Maritorena, S., D. A. Siegel and A. R. Peterson, Optimization of semi-analytical ocean color model for global scale applications, *Applied Optics*, *41*, 2705–2714, 2002.

Mischenko, M., L. D. Travis and A. Macke, T-Matrix Method and its applications, in *Light Scattering by Non-spherical Particles*, edited by M. Mischenko, L. D. Travis and J. Hovenier, pp. 147–172, Academic Press, San Diego, 2000.

Moore, K. D., K. J. Voss and H. R. Gordon, Spectral reflectance of whitecaps: Their contribution to water-leaving radiance, *Jour. Geophys. Res.*, *105C*, 6493–6499, 2000.

Moore, K. D., K. J. Voss and H. R. Gordon, Spectral reflectance of whitecaps: Instrumentation, calibration, and performance in coastal waters, *Jour. Atmos. Ocean. Tech.*, *15*, 496–509, 1998.

Morel, A., D. Antoine and B. Gentili, Bidirectional reflectance of oceanic waters: accounting for Raman emission and varying particle scattering phase function, *Applied Optics*, *41*, 6289 – 6306, 2002.

Morel, A. and B. Gentili, Diffuse reflectance of oceanic waters. III. Implication of bidirectionality for the remote sensing problem, *Applied Optics*, *35*, 4850–4862, 1996.

Moulin, C., H. R. Gordon, V. F. Banzon and R. H. Evans, Assessment of Saharan dust absorption in the visible from SeaWiFS imagery, *Jour. Geophys. Res.*, *106D*, 18,239–18,250, 2001a.

Moulin, C., H. R. Gordon, R. M. Chomko, V. F. Banzon and R. H. Evans, Atmospheric correction of ocean color imagery through thick layers of Saharan dust, *Geophys. Res. Lett.*, *28*, 5–8, 2001b.

Patterson, E. M., Optical properties of crustal aerosol: relation to chemical and physical characteristics, *Jour. Geophys. Res.*, *86C*, 3236–3246, 1981.

Ritter, J. M. and K. J. Voss, A New Instrument for Measurement of the Solar Aureole Radiance Distribution from Unstable Platforms, *Jour. Atmosph. Ocean. Techn.*, *17*, 1040–1047, 2000.

Siegel, D. A., M. Wang, S. Maritorena and W. Robinson, Atmospheric correction of satellite ocean color imagery: the black pixel assumption, *Applied Optics*, *39*, 3582–3591, 2000.

Spinhirne, J. D., J. Ball and V. S. Scott, Compact eye-safe LIDAR systems, *Rev. Laser Eng*, *23*, 26–23, 1995.

Voss, K. J., In-water spectral radiance distribution measurements, 2001, *Physics of Quantum Electronics*, January 2001, Snowbird, Utah.

Voss, K. J. and A. C. Chapin, Next generation in-water radiance distribution camera system, *Society of Photo-Optical Instrumentation Engineers, Ocean Optics XI*, *1750*, 384–387, 1992.

Voss, K. J. and Y. Liu, Polarized radiance distribution measurements of skylight. I. System description and characterization, *Applied Optics*, *36*, 6083–6094, 1997.

Voss, K. J., E. J. Welton, J. Johnson, A. Thompson, P. K. Quinn and H. R. Gordon, Lidar Measurements During Aerosols99, *Jour. Geophys. Res.*, *106D*, 20821–20832, 2001.

Welton, E. J., Measurements of Aerosol Optical Properties over the Ocean Using Sunphotometers and Lidar, 1998, Ph. D. Disertation, Univ. of Miami, Coral Gables, Fl.

Welton, E. J., K. J. Voss, H. R. Gordon, H. Maring, A. Smirnov, B. Holben, B. Schmid, J. M. Livingston, P. B. Russell,, P. A. Durkee, P. Formenti and M. O. Andreae, Ground-based lidar measurements of aerosols during ACE-2: Instrument description, results, and comparisons with other ground-based and airborne measurements, *Tellus*, *52B*, 568–593, 2000.

Welton, E. J., K. J. Voss, P. K. Quinn, P. J. Flatau, K. Markowicz, J. R. Campbell, J. D. Spinhirne, H. R. Gordon and J. Johnson, Measurements of aerosol vertical profiles and optical properties during INDOEX 1999 using micro-pulse lidars, *Jour. Geophys. Res.*, *107D*, 18–1–18-20, 2002, doi:10.1029/2000JD000038.

Yang, H. and H. R. Gordon, Remote sensing of ocean color: Assessment of the water-leaving radiance bidirectional effects on the atmospheric diffuse transmittance, *Applied Optics*, *36*, 7887–7897, 1997.

Young, R. W., K. L. Carder, P. R. Betzer, D. K. Costello, R. A. Duce, G. R. Ditullio, N. W. Tindale, E. A. Laws, M. Uematsu, J. T. Merrill and R. A. Feeley, Atmospheric Iron Inputs and Primary Productivity: Phytoplankton Responses in the North Pacific, *Global Biogeochemical Cycles*, *5*, 119–134, 1991.

.

FINAL REPORT

Contract Number NAS5—31363

OCEAN OBSERVATIONS WITH EOS/MODIS:

Algorithm Development and Post Launch Studies

(December 14, 1991 — May 14, 2004)

Part 2: RETRIEVAL OF DETACHED COCCOLITH/CALCITE CONCENTRATION

Submitted by

William M. Balch
Bigelow Laboratory for Ocean Sciences
POB 475
McKown Point
W. Boothbay Harbor, ME 04575

May 2004

The work accomplished on this project fell into several areas: 1) laboratory experiments to determine the optical scattering properties of cultured and naturally-occurring coccolithophores, 2) use of these data to derive a two-band calcite algorithm, 3) use of these data to derive a three-band calcite algorithm, 4) algorithm revisions to make the derived calcite concentrations more accurate, 5) validation of the two-band algorithm using data collected from field campaigns all over the world, 6) attendance at weekly meetings on the MODIS products, 7) publication of manuscripts in the peer-reviewed literature.

Algorithm Evaluation/Improvement

Work in this area focused on preliminary estimates of volume scattering of suspended coccoliths, using cultures and field suspensions from blooms, or flow-cytometer-sorted suspensions. It was critical in this work to include as many naturally-occurring coccolithophores in order to derive an accurate average backscattering cross-section to use in the MODIS algorithm (<u>with definable error limits</u>). The work also involved culturing the various species under a wide range of growth conditions in order to understand the species-specific and growth-dependent variability in coccolith size, shape and scattering properties. A number of peer-reviewed publications resulted from this phase of the contract (summarized in the Annotated Bibliography (Appendix I)).

Validation of MODIS Algorithms and Products

As coccoliths and suspended PIC (particulate inorganic carbon or calcium carbonate) are new products, and as Terra was finally launched in December 1999 and Aqua launched in May '02, there were relatively few data sets available for validation, particularly for the coccolith and suspended calcite products. This was because coccolith concentration (PIC) is not frequently measured at sea by oceanographers, while chlorophyll concentration is. In conjunction with our NASA SEAWiFS activities, much of our validation estimates come from the Gulf of Maine (over 70 cruises), the site of frequent blooms of coccolithophores, and a region readily accessible from our laboratory. We nonetheless also provided sea truth data from: the Florida Straits (2 cruises), Arabian Sea (2 cruises), Equatorial Pacific (1 cruise), North Atlantic (south of Iceland; 1 cruise), and NW Atlantic Continental Slope (3 cruises).

Validation of regional PIC

During the period of this contract, we acquired thousands of PIC samples. These were processed using inductively-coupled plasma atomic absorption. Coccolith counts were performed on parallel samples and the tedious microscope counts were all completed. Parallel PIC samples and coccolith counts were analyzed to check the coccolith-to-carbon conversion, also important in the MODIS two band algorithm. We demonstrated using previous data that satellite-derived normalized water-leaving radiances are statistically correlated to the absolute PIC concentration, accounting for as much as 40% of the variance. Moreover, we demonstrated that the $[L_w]_N$'s are even better correlated to the coccolith concentration; coccolith concentration impressively accounts for just over 50% of the variance in $[L_w]_N$'s in the blue and green wavelengths. Note, this is apart from any correlation with chlorophyll. Such high correlations are the reason that the 2-band MODIS algorithm works as well as it does.

Chalk-Ex

Another aspect of algorithm validation were our Chalk-Ex experiments. For this experiment, we used Cretaceous coccolith chalk from the U.K. (with a median particle size identical to *Emiliania huxleyi* coccoliths) to make five patches, approximately 2 km x 1 km in size, which could be viewed by MODIS Terra or Aqua. The patches had sufficient calcite to provide concentrations equal to a typical bloom (but over negligible area as compared to typical coccolithophore blooms). In order to integrate the chalk concentrations, we focused on data processing, specifically on the Kriging techniques used to contour the calcite concentration (for the accuracy of the contouring programs is inherently important for defining the accuracy of the MODIS PIC algorithm). We optimized the contouring routine, and re-processed 3-D calcite information from the last four patches, for comparison to the MODIS results. Presentations on various aspects of this work were given at numerous MODIS meetings. Data from this work has been included in the most recent publication (Balch, W. M., Howard Gordon, B. C. Bowler, D. T. Drapeau, E. S. Booth. 2004 Calcium Carbonate Budgets in the Surface Global Ocean based on MODIS Data. To be submitted to the Journal of Geophysical Research.). The reader is referred to the complete list of 19 publications (Appendix I) that have resulted wholly, or in part, from this contract.

New validation data

Gulf of Maine cruises aboard the M/S *Scotia Prince* ferry resumed in early May of 2004 and have been funded for another three years through NASA IDS. Given the success of our MODIS recompete proposal, we will continue this work for another 3 years as well as performing 3 AMT cruises between the U.K. and Falkland Islands in which we sample suspended PIC as well as suspended biogenic silica and relate this to above-water radiance measurements.

<u>Validation of global PIC and coccolithophore pigment data</u>

Cautions when using coccolith/PIC data products

The coccolithophore data products are "provisionally validated", given that we have defined the RMS error based on ship validation measurements, under a wide range of PIC concentrations, using the collection 4 re-processed data. We nonetheless caution using these data from shallow ocean regions, particularly near carbonate banks (e.g. Grand Bahamas), where bottom reflectance will appear as a high-reflectance coccolithophore bloom (presumably such pixels would be flagged due to their shallowness). Moreover, near river mouths and in shallow waters, resuspended sediments (of non-calcite origin) may appear as high suspended calcite concentrations. Only use these data if the waters are sufficiently deep to not have such bottom resuspension or direct river impact. Beware that MODIS-derived coccolith concentrations assume that the coccoliths are from the Prymnesiophyte, *E. huxleyi*. If this is not true, then inaccuracies will increase although the errors are not expected to be large. Even when using the data in units of mg m^{-3}, they nevertheless assume a constant backscattering cross-section for *E. huxleyi*, which is known to vary with the size of the calcite particle.

Web Links to Relevant Information

The algorithm theoretical basis document for the coccolithophore products can be found at: http://modis.gsfc.nasa.gov/MODIS/ATBD/atbd_mod23.pdf

More information about the algorithm and inputs can be found in:

Esaias, W., et al., 1998, Overview of MODIS Capabilities for Ocean Science Observations, *IEEE Transactions on Geoscience and Remote Sensing*, **36**, 1250—1265.

Anticipated future efforts:

This is the last report under this subcontract. Given that our MODIS re-compete proposal was funded, our future MODIS efforts will continue from our work described here. Future efforts will involve:

a) Further work-up of the results from the Gulf of Maine during 2003.

b) Continued sampling for PIC validation in the Gulf of Maine in ’04 (12 more trips will be scheduled for clear-sky days)

c) Submission of the manuscript on the PIC algorithm and recent validation work

d) Any required revisions for our submitted paper on the Gulf of Maine results.

e) Processing of data from our June ’03 Chalk-Ex experiment, specifically comparing the MODIS-derived results with the shipboard estimates of PIC concentration.

Referencing Data in Journal Articles

Results derived from this algorithm should cite the paper of Gordon et al.(Gordon et al. 1988) for the original discussion, and (Balch et al. 1996; Balch et al. 1999) for field data on the backscattering cross-section of calcite.

Citations

Balch, W. M., K. Kilpatrick, P. M. Holligan, D. Harbour, and E. Fernandez. 1996. The 1991 coccolithophore bloom in the central north Atlantic. II. Relating optics to coccolith concentration. Limnol. Oceanogr. **41:** 1684-1696.

Balch, W. M., D. T. Drapeau, T. L. Cucci, R. D. Vaillancourt, K. A. Kilpatrick, and J. J. Fritz. 1999. Optical backscattering by calcifying algae--Separating the contribution by particulate inorganic and organic carbon fractions. J. Geophys. Res. **104:** 1541-1558.

Gordon, H. R., O. B. Brown, R. H. Evans, J. W. Brown, R. C. Smith, K. S. Baker, and D. K. Clark. 1988. A semianalytic radiance model of ocean color. J. Geophys. Res. **93:** 10909-10924.

APPENDIX I

Refereed Journal Articles from MODIS Contract:

An Annotated Description

Refereed Journal Articles from MODIS Contract: An Annotated Description

Atmospheric Correction: Computational/Theoretical

1) M. Wang and H. R. Gordon, Retrieval of the Columnar Aerosol Phase Function and Single Scattering Albedo from Sky Radiance over the Ocean: Simulations, *Applied Optics*, **32**, 4598-4609 (1993).

   In this paper, a method was developed for retrieving the aerosol scattering phase function and single scattering albedo from measurements of sky radiance and aerosol optical depth over the oceans. An important feature of the method is the fact that no assumptions are made regarding the shape of the aerosol particles. The method was employed by Cattrall, Carder, and Gordon [2003] to estimate the single scattering albedo of airborne dust transported across the Tropical Atlantic from Africa to Florida. The resulting single scattering albedo estimates agreed well with models of Moulin et al. [2001] constructed to reproduce SeaWiFS radiances in observed over intense dust storms.

2) H. R. Gordon and M. Wang, Retrieval of water-leaving radiance and aerosol optical thickness over the oceans with SeaWiFS: A preliminary algorithm, *Applied Optics*, **33**, 443-452 (1994).

   This paper describes the basis of the atmospheric correction algorithm that was developed for MODIS under the present contract. It is shown that the concept is capable of retrieving the water-leaving radiance (at 443 nm) in low-chlorophyll waters with an uncertainty of ± 5%, the stated goal for MODIS. The algorithm was applied to SeaWiFS as a test bed for MODIS.

3) K. Ding and H. R. Gordon, Atmospheric correction of ocean color sensors: Effects of earth curvature, *Applied Optics*, **33**, 7096-7016 (1994).

   All of the radiative transfer simulations carried out in developing the basic SeaWiFS/MODIS atmospheric correction algorithm were carried out using radiative transfer theory in plane-parallel geometry, i.e., assumes that the earth and its atmosphere are both flat. However, it is known that radiative transfer computations in plane-parallel and spherical shell geometries do not yield identical results. Because of the significantly improved radiometric sensitivity of MODIS over CZCS and SeaWiFS, it was suspected that the plane parallel approximation would lead to excessive error in the algorithm.

This was investigated and the results reported in the above paper. The most significant findings were that the error is negligible for the solar zenith angles less than 70 degrees, and that as long as the Rayleigh scattering contribution to the radiance was computed using spherical shell geometry, there was virtually no difference in the correction algorithm's performance.

4) H. R. Gordon and M. Wang, Influence of Oceanic Whitecaps on Atmospheric Correction of SeaWiFS, *Applied Optics*, **33**, 7754-7763 (1994).

In this paper the influence of whitecaps on the correction algorithm was studied through simulations. The results suggested that extant models of whitecap reflectance were sufficiently accurate for atmospheric correction. These models assumed that whitecaps were actually "white." When measurements in the surf zone indicated that the reflectance of breaking waves had higher reflectance in the blue than in the near-infrared, our conclusion was modified [Gordon 1997]. We then set out to measure the spectral reflectance of oceanic whitecaps in order to provide an effective whitecap correction (See Moore, Voss, and Gordon [1998, 2000]).

5) M. Wang and H. R. Gordon, A Simple, Moderately Accurate, Atmospheric Correction Algorithm for SeaWiFS, *Remote Sensing of Environment*, **50**, 231-239 (1994)

When the MODIS algorithm was initially structured for SeaWiFS, the computational speed was very poor. Thus, we studied the efficacy of an algorithm that was identical to the MODIS approach, but used single scattering for the aerosol contribution. The results are reported in this paper. The accuracy was significantly degraded, but was sufficient for some applications, e.g., at-sea processing to guide ships to important sampling areas. The method is of little interest now, as computer technology has significantly increased processing speeds

6) K. Ding and H. R. Gordon, Analysis of the influence of O_2 "A" band absorption on atmospheric correction of ocean color imagery, *Applied Optics*, **34**, 2068-2080 (1995).

In order to test the MODIS algorithm with SeaWiFS data, atmospheric absorption by the O_2 "A" band had to be considered because it directly influences the shorter near-infrared band of SeaWiFS (MODIS avoids this absorption by using a narrower band). This paper describes our analysis of the O_2 "A" band's influence, and describes a method for atmospheric correction in the presence of the absorption. This method is presently used in SeaWiFS processing.

7) H. R. Gordon and T. Zhang, Columnar Aerosol Properties Over Oceans by Combining Surface and Aircraft Measurements: Simulations. *Applied Optics*, **34**, 5552-5555 (1995).

This paper explores the possibility of combining surface and aircraft measurements of downwelling and upwelling radiance to determine aerosol properties for the purpose of vicarious calibration. A complete sensitivity analysis is provided in a later paper.

8) H. R. Gordon, Remote sensing of ocean color: a methodology for dealing with broad spectral bands and significant out-of-band response, *Applied Optics*, **34**, 8363-8374 (1995).

The SeaWiFS sensor showed very large out-of-band response in the near infrared. In order to test the MODIS algorithm with SeaWiFS data, this out-of-band response had to be addressed. This paper describes atmospheric correction of sensors showing large out-of-band response. The methodology is applicable to any sensor and is presently used in both SeaWiFS and MODIS processing.

9) H. Yang, H. R. Gordon and T. Zhang, Island perturbation to the sky radiance over the ocean: Simulations, *Applied Optics*, **34**, 8354-8362 (1995).

Part of our effort was to provide a vicarious calibration strategy for MODIS. It was envisaged that measurements of sky radiance and aerosol optical depth from small islands could be used to retrieve the aerosol optical properties (scattering phase function and single scattering albedo) using the method of Gordon and Wang [1993]. It was important to understand any influence that the island might have on the sky radiance. This paper describes an assessment of the perturbation to the sky radiance and provides an iterative method to correct for the perturbation.

10) H. R. Gordon and T. Zhang, How well can radiance reflected from the ocean-atmosphere system be predicted from measurements at the sea surface?, *Applied Optics*, **35**, 6527-6543 (1996).

This paper provides the basis for vicarious calibration through inversion of sky radiance to predict the top-of-atmosphere radiance. It is shown that the uncertainty in the predicted top-of-atmosphere radiance is approximately equal to the uncertainty in the measurement of the sky radiance.

11) H. R. Gordon, T. Zhang, F. He, and K. Ding, Effects of stratospheric aerosols and thin cirrus clouds on atmospheric correction of ocean color imagery: Simulations, *Applied Optics*, **36**, 682-697 (1997).

In the Gordon and Wang [1994] atmospheric correction algorithm it is assumed that the aerosol is in a thin layer near the surface. However, it is well known that thin cirrus and aerosols from volcanic sources are extant in the stratosphere. Here, we studied the affect of such aerosols on the atmospheric correction algorithm. Specifically, we determined the magnitude of the influence, and examined several approaches to reducing the magnitude through utilizing the 1380 nm band on MODIS.

12) T. Zhang and H. R. Gordon, Columnar aerosol properties over oceans by combining surface and aircraft measurements: sensitivity analysis, *Applied Optics*, **36**, 2650-2662 (1997).

This paper provides an alternate method of vicarious calibration, where sky radiance measurements are combined with aircraft measurements to better determine the aerosol scattering phase function and single scattering albedo for vicarious calibration.

13) H. R. Gordon, Atmospheric Correction of Ocean Color Imagery in the Earth Observing System Era, *Jour. Geophys. Res.*, **102D**, 17081-17106 (1997).

This paper describes the state of the MODIS atmospheric correction algorithm at launch. It is a shortened version of the MODIS normalized water-leaving radiance ATBD (Version 3).

14) D. K. Clark, H. R. Gordon, K. J. Voss, Y. Ge, W. Broenkow, and C. Trees, Validation of Atmospheric Correction over the Oceans, *Jour. Geophys. Res.*, **102D**, 17209-17217 (1997).

This paper describes the strategy for validation of atmospheric correction.

15) H. R. Gordon, T. Du, and T. Zhang, Atmospheric Correction of Ocean Color Sensors: Analysis of the Effects of Residual Instrument Polarization Sensitivity, *Applied Optics*, **36**, 6938-6948 (1997).

The MODIS instrument displays a significant sensitivity to the polarization of the top-of-atmosphere radiance (as much as 6% at 412 and 3% at 869 on the eastern side of the scan). This paper assesses the affect on MODIS products of such sensitivity to polarization, and provides a preliminary method for effecting a correction.

16) H. Yang and H. R. Gordon, Remote sensing of ocean color: Assessment of the water-leaving radiance bidirectional effects on the atmospheric diffuse transmittance, *Applied Optics*, **36**, 7887-7897 (1997).

It is well known that there is significant bidirectionality to the water-leaving radiance. It is less well known that this bidirectionality influences the diffuse transmittance of the atmosphere. This paper describes the connection in detail and provides an exact computation of the diffuse transmittance if the bidirectionality is ignored. This computation is used in the MODIS processing.

17) T. Zhang and H. R. Gordon, Retrieval of elements of the columnar aerosol scattering phase matrix from sky radiance over the ocean: simulations, *Applied Optics*, **36**, 7948-7959 (1997).

In an attempt to derive polarization properties of the aerosol scattering, the Wang and Gordon [1993] sky radiance inversion algorithm was extended to include polarization. It was discovered that two elements of the aerosol scattering phase matrix could be retrieved from measurement of the full Stokes vector of the sky radiance.

18) H. R. Gordon, T. Du, and T. Zhang, Remote sensing ocean color and aerosol properties: resolving the issue of aerosol absorption, *Applied Optics*, **36**, 8670-8684 (1997).

The Gordon and Wang [1994] MODIS atmospheric correction algorithm does not perform properly in atmospheres with strongly absorbing aerosols. The difficulty is that the absorption affects are manifest only in the visible, not in the near infrared atmospheric correction bands. This paper describes one solution to this problem. In this method, the top-of-atmosphere radiance spectrum (violet through near infrared) is compared to that produced by models of the water-leaving radiance and models of the aerosol. The retrieved parameters (chlorophyll, aerosol model, etc.) are those that give the best fit of the modeled to the measured radiance. It is called the spectral matching algorithm, and has been successfully used by Moulin et al. [2001] to perform atmospheric corrections in atmospheres contaminated by Saharan dust.

19) H. Yang and H. R. Gordon, Retrieval of the Columnar Aerosol Phase Function and Single Scattering Albedo from Sky Radiance over Land: Simulations, *Applied Optics*, **37**, 978-997 (1998).

This extends the Wang and Gordon [1993] sky radiance retrieval algorithm to operation over land.

20) H. R. Gordon, In-orbit calibration strategy for ocean color sensors, *Remote Sensing of Environment*, **63**, 265-278 (1998).

This paper outlines the strategy of vicarious calibration of ocean color sensors, including estimates of the error expected after calibration.

21) W. E. Esaias, M. R. Abbott, O. B. Brown, J. W. Campbel, K. L. Carder, D. K. Clark, R. L. Evans, F. E. Hoge, H. R. Gordon, W. M. Balch, R. Letelier, and

P. Minnett, An overview of MODIS capabilities for ocean science observations, *IEEE Transactions on Geoscience and Remote Sensing*, **36**, 1250-1265 (1998).

This is an overview of MODIS and the processing algorithms.

22) R. Chomko and H. R. Gordon, Atmospheric correction of ocean color imagery: Use of the Junge power-law aerosol size distribution with variable refractive index to handle aerosol absorption, *Applied Optics* **37**, 5560-5572 (1998).

This paper describes a second method of dealing with absorbing aerosols: the spectral optimization algorithm. In this case no effort is made developing models of absorbing aerosols. Here, Junge power-law size distributions of particles with wavelength independent refractive indices are assumed. The optical properties are computed using Mie theory, and a model of the dependence of the water-leaving radiance on the concentration of chlorophyll, etc. is assumed. The free parameters are then estimated by fitting the top-of-atmosphere radiance to that produced by the models. Standard optimization techniques are used to provide a "best" fit.

23) C. Moulin, H. R. Gordon, R. M. Chomko, V. F. Banzon, and R. H. Evans, Atmospheric correction of ocean color imagery through thick layers of Saharan dust, *Geophys. Res. Lett.*, **28**, 5—8, 2001.

This paper reports using the spectral matching algorithm [Gordon, Du, Zhang 1997] to perform atmospheric correction in the presence of Saharan dust at optical thicknesses as high as 0.8.

24) C. Moulin, H. R. Gordon, V. F. Banzon, and R. H. Evans, Assessment of Saharan dust absorption in the visible from SeaWiFS imagery, *J. Geophys. Res.*, **106D**, 18,239—18,249, 2001.

This paper describes the development and validation of models used in atmospheric correction in regions contaminated by Saharan dust.

25) H. R. Gordon, G. C. Boynton, W. M. Balch, S. B. Groom, D. S. Harbour, and T. J. Smyth, Retrieval of Coccolithophore Calcite Concentration from SeaWiFS Imagery, *Geophys. Res. Lett.* **28**: 1587—1590, 2001.

We had already developed an algorithm for retrieving the coccolithophore calcite concentration from the water-leaving radiance using the 443 and 551 nm bands; however, that algorithm was also sensitive to the chlorophyll concentration. This paper provides an alternative that uses only the red and near-infrared bands, and is relatively insensitive to the chlorophyll concentration. The algorithm simultaneously performs atmospheric correction and calcite retrieval, and can be used to estimate the fluorescence line height as well.

26) R. M. Chomko and H. R. Gordon, Atmospheric correction of ocean color imagery: Test of the spectral optimization algorithm with SeaWiFS, *Applied Optics*, **40**, 2973—2984, 2001.

This paper applies the Chomko and Gordon [1998] spectral optimization algorithm to ocean color data, showing that it performs as well as standard algorithms.

27) M. Wang and H. R. Gordon, Calibration of ocean color scanners: How much error is acceptable in the near infrared?, *Remote Sensing of Environment* **82,** 497—504, 2002.

This paper discusses the need for accurate absolute calibration of the longer-wave near infrared band on present and planned ocean color sensors. The main conclusion is that, with present algorithms, significant calibration error is acceptable as long as the visible bands are vicariously calibrated with respect to the near-infrared bands.

28) R. M. Chomko, H. R. Gordon, S. Maritorena, D. A. Siegel, Simultaneous retrieval of oceanic and atmospheric parameters for ocean color imagery by spectral optimization: A validation, *Remote Sensing of Environment* **84,** 208—220, 2003.

Here we apply a more sophisticated water model to the spectral optimization algorithm. The resulting absorption of CDOM is validated validated using airborne oceanic lidar, and the retrieved chlorophyll concentration is validated using SeaWiFS eight-day means. This paper showed that in Case 1 waters it is possible to separate CDOM absorption and chlorophyll absorption. It also provides an approach for processing imagery from Case 2 waters.

29) H. R. Gordon, Comment on "Pitfalls in atmospheric correction of ocean color imagery: how should aerosol optical properties be computed?" *Applied Optics*, **42**, 542—544 (2003).

This comment refutes the claim that SeaWiFS processing requires aerosol models that are more realistic that those presently employed.

30) V. F. Banzon, R. E. Evans, H. R. Gordon and R. M. Chomko, SeaWiFS observations of the Arabian Sea Southwest Monsoon bloom for the year 2000, *Deep Sea Research II*, (Submitted).

This describes application of the Moulin et al., [2001] algorithm for atmospheric correction in dust to the Arabian Sea in summer. A novel approach is taken in which spectral matching is used to derive the appropriate aerosol model and water-leaving radiances. The water-leaving radiances are then used in the SeaWiFS OC4v4 bio-optical algorithm is used to derive the chlorophyll *a* concentration. The results show a dramatic improvement in coverage during the important Southwest Monsoon regime.

31) D. Antoine, A. Morel, H. R. Gordon, V. F. Banzon, and R. E. Evans, Retrospective processing of the CZCS archive (1979-86) as a basis for analyzing satellite ocean color observations in search of long-term trends. I: Revised algorithms, sensitivity analyses and calibration considerations, *Global Biogeochemical Cycles* (In revision).

32) D. Antoine, A. Morel, H. R. Gordon, V. F. Banzon, and R. E. Evans, Retrospective processing of the CZCS archive (1979-86) as a basis for analyzing satellite ocean color observations in search of long-term trends. II: Global distributions of the chlorophyll biomass, the aerosol optical thickness, and the Angstrom exponent, *Global Biogeochemical Cycles* (In revision).

These papers describe the reprocessing of the CZCS data set in an effort to build a multi year time series in search of long term trends. The philosophy that we adopt is that, since the CZCS is the weakest link in the sensor chain, ocean color data from all subsequent sensors should be processed with improved CZCS algorithms to provide a consistent time series. The first paper deals with the methodology and the second with the results.

Atmospheric Correction: Experimental/Validation

33) A. Morel, K. J. Voss, and B. Gentilli, " Bi-directional reflectance of oceanic waters: A comparison of model and experimental results", *J. Geophys. Res*., **100**: 13,143-13,150, 1995.

This paper was an early comparison of an early version of the Morel-Gentilli oceanic BRDF model with experimental data taken off of the coast of California with the RADS-1 instrument. The data set was in one location, hence the range of chlorophyll was limited. However there was a wide spread in solar zenith angles. The comparison showed that for this chlorophyll value (around 0.3 mg/m3) the model worked fairly well at predicting the shape of the radiance distribution.

34) K. J. Voss and Y. Liu, "Polarized radiance distribution measurements of skylight: I. system description and characterization", *Applied Optics*, **36** :6083-6094, 1997.

This paper described a method to obtain the polarized sky radiance distribution, from sequential images of the sky using the fisheye sky radiance distribution camera system. By taking 3 images in quick succession, each with a polarizer in a different orientation, the Stokes vector of the skylight can be determined. The instrument is described in this paper along with the steps required for instrument calibration and characterization.

35) Y. Liu and K. J. Voss, "Polarized radiance distribution measurements of skylight: II. experiment and data", *Applied Optics*, **36**: 8753 - 8764, 1997.

This paper described the use of the polarized spectral sky radiance distribution camera system, in particular in use for two measurement locations in Miami. This system was then used on several MODIS Optical Characterization Experiments. The aim was to obtain polarized sky radiance distribution measurements over the ocean to learn about the polarization properties of atmospheric aerosols over the ocean.

36) K.D. Moore, K.J. Voss, and H.R. Gordon, Spectral reflectance of whitecaps: Instrumentation, calibration, and performance in coastal waters, *Jour. Atmos. Ocean. Tech*., **15**, 496-509, 1998.

Understanding the whitecap reflectance is required to effect a correction for their presence. This paper describes a radiometer specifically designed to measure the whitecap reflectance in spectral bands of interest in ocean color analysis.

37) A. Smirnov, B. Holben, I. Slutsker, E. J. Welton, and P. Formenti, "Optical properties of Saharan dust during ACE-2, *Jour. Geophys. Res*., 103D, 28079 - 28092, 1998.

An important aerosol type over the Atlantic ocean is Saharan dust. This aerosol is particularly difficult as it is an absorbing aerosol. Hence, the aerosol vertical distribution affects the atmospheric correction algorithm. Significant effort was made in investigating this aerosol type, as it was considered one of the more likely failure points for the atmospheric correction. One experiment we participated in was the ACE-2 experiment, which took place around the Canary Islands and was focused on Saharan Dust and European pollution outbreaks. By participating in the larger aerosol chemistry experiments we were able to get chemical information on the aerosols along with the optical data we were collecting. This is a theme that will be shown through much of our experimental papers described below.

38) J. M. Ritter and K. J. Voss, A new instrument to measure the solar aureole from an unstable platform, *J. Atm. And Ocean. Techn*., **17**: 1040 –1047, 2000.

The sky radiance camera does not capture the area within 15-20 degrees of the sun. The solar aureole camerea system was developed to obtain the sky radiance very close to the sun (the solar aureole). This region was required to constrain the estimate of the single scattering albedo for the aerosols, since so much of the scattered light from the aerosols is in this small angle region.

39) K.D. Moore, K.J. Voss, and H.R. Gordon, Spectral reflectance of whitecaps: Their contribution to water-leaving radiance, *Jour. Geophys. Res.*, **105C**, 6493—6499, 2000.

Measurements of the reflectance of oceanic whitecaps made using the radiometer described in above paper are reported and an analysis of the reflectance as a function of wavelength and wind speed is presented. The important results are that the oceanic whitecaps show approximately half of the spectral variation of surf-zone breaking waves, and that literature estimates of the reflectance as a function of wind speed are 3-4 times too high.

40) B. Schmid, J.M. Livingston, P.B. Russell, P.A. Durkee, H.H. Jonsson, D.R. Collins, R.C. Flagan, J.H. Seinfeld, S. Grasso, D.A. Hegg, E. Ostrom, K.J. Noone, E.J. Welton, K.J. Voss, H.R. Gordon, P. Formenti, and M.O. Andreae, Clear-sky closure studies of lower tropospheric aerosol and water vapor during ACE-2 using airborne sunphotometer, airborne in-situ, space-borne, and ground-based measurements, *Tellus*, **52B**, 636—651, 2000.

The important point of this paper for this project was the comparison of the aerosol profiles obtained with an airborne sunphotometer and the surface based lidar system. This was a validation of our lidar inversion techniques. There was also aerosol information obtained from aerosol sampling systems on the aircraft and the ground which helped in testing the inversions.

41) B. N. Holben, D.Tanre, A.Smirnov, T. F. Eck, I. Slutsker, N. Abuhassan, W. W. Newcomb, J. Schafer, B. Chatenet, F. Lavenue, Y. J. Kaufman, J. Vande Castle, A. Setzer, B. Markham, D. Clark, R. Frouin, R. Halthore, A. Karnieli, N. T. O'Neill, C. Pietras, R. T. Pinker, K. Voss, G. Zibordi, An emerging ground-based aerosol climatology: Aerosol Optical Depth from AERONET, *J. Geophys. Res*., **106**, 12067 - 12097, 2001.

As part of this project, we set up a CIMEL automated sun-sky photometer at the Dry Tortugas, off of Key West Florida. Our interest in this site was to provide aerosol information at a site surrounded by clear water which could be used for validation of the atmospheric correction algorithm. This site is particularly useful as it is impacted by clean maritime aerosols, Saharan Dust transport, and continental aerosols at various times of the year. This paper describes the overall data set, which our CIMEL is part of.

42) E. J. Welton, K. J. Voss, H. R. Gordon, H. Maring, A. Smirnov, B. Holben, B. Schmid, J.M. Livingston, P.B. Russell, P.A. Durkee, P. Formenti, and M.O. Andreae, Ground-based lidar measurements of aerosols during ACE-2:

Instrument description, results, and comparisons with other ground-based and airborne measurements, *Tellus*, , **52B**, 568—593, 2000.

This was the primary paper which discussed the results of our lidar systems use during ACE-2. In it we show vertical and horizontal distributions of aerosols around the experiment site, including some during a strong Saharan Dust outbreak.

43) A. S. Ackerman, O. B. Toon, D. E. Stevens, A. J. Heymsfie1d, V. Ramanathan, and E. J. Welton, Reduction of tropical cloudiness by soot, *Science,* **288,** 1042-1047,2000.

This paper used the lidar data in combination with other data sets to look at the indirect effect of aerosols on clouds and radiative transfer.

44) P. K. Quinn, D. J. Coffman, T. S. Bates, T. L. Miller, J. E. Johnson, K. Voss, E. J. Welton, C. Neusüss, Dominant Aerosol Chemical Components and Their Contribution to Extinction During the Aerosols99 Cruise Across the Atlantic, *J. Geophys. Res.,* **106**, 20783 – 20810, 2001.

Another experiment we took part in was the Aerosols99 cruise from Norfolk, Va. to Cape Town, South Africa. This was the lead in to the larger INDOEX experiment. This cruise turned out to be very useful as we had lidar data through much of the Atlantic Ocean, and exprieenced clean Maritime atmospheres, Saharan Dust, and a biomass burning aerosol mass. Working with the chemists allowed us to separate these different events.

45) K. J. Voss, E. J. Welton, P. K. Quinn, R. Frouin, M. Miller, and R. M. Reynolds, Aerosol Optical Depth measurements during the Aerosols99 experiment, *J. Geophys. Res.,* **106**, 20811 – 20820, 2001.

During the cruise Aerosol Optical depth was measured by several different methods including lidar and several types of sunphotometers. This paper described the difference between the data sets, and some of the advantages/disadvantages if each method. It also described the entire sunphotomter data set for this cruise.

46) K. J. Voss, E.J. Welton, J. Johnson, A. Thompson, P. K. Quinn, and H. R. Gordon, Lidar Measurements During Aerosols99, *J. Geophys. Res*., **106D**, 20821—20832, 2001.

This paper described the lidar results combined with the chemical analysis, obtained during this cruise. We found that the maritime aerosol was mostly constrained near the surface (first 1km), but the biomass burning and Saharan Dust aerosol could be throughout the air column. In fact at times the surface chemistry was indicating that the overlaying aerosol should be clean maritime, but the lidar profiles indicated a strong upper layer aerosol was actually the dominant aerosol at that position. It shows the importance of having vertical distributions of aerosols in these experiments.

47) E. J. Welton, K. J. Voss, P. K. Quinn, P. J. Flatau, K. Markowicz, J. R. Campbell, J. D. Spinhirne, H. R. Gordon, J. Johnson, Measurements of aerosol vertical profiles and optical properties during INDOEX 1999 using micro-pulse lidars. *J. Geophys. Res.*, **107D**, 18-1—18-20, 2002. (10.1029/2000JD000038).

The Aerosols99 cruise led into the multinational aerosol experiment in the Indian Ocean, INDOEX. The Indian Ocean is influenced by dust from the Arabian Peninsula, clean maritime air and a significant amount of the time by pollution aerosols from the Indian sub contenent. The lidar was used to look at vertical distributions of these aerosols through the cruise. The pollution aerosols extended very high in the atmosphere (up to 5km) versus the maritime aerososl were constrained to very near (1 km) the surface.

48) P. K. Quinn, D. J. Coffman, T. S. Bates, T. L. Miller, J. E. Johnson, E. J. Welton, C. Neustiss, M. Miller, and P. J. Sheridan, Aerosol Optical Properties during INDOEX 1999: Means, Variability, and Controlling *Factors,Journal of Geophysical Research,* 107D(19) 19-1-19-25, 2002. (10.1002912000JD000037).

This paper described the ehemistry measured at the ship on the surface during the INDOEX experiment. This chemistry was associated with the lidar measurements described in the previous paper.

49) C. Cattrall, K.L. Carder, K.T. Thome, H. R. Gordon, Solar-reflectance-based calibration of spectral radiometers, *Geophys. Res. Lett.*, **29**, 2-1—2-4, 2002. (doi:10.1029/2002GL015130)

This describes a novel solar-based calibration of a spectral radiometer used for measuring sky radiance. The application was estimation of the single scattering albedo of Saharan dust (See next paper).

50) C. Cattrall, K. L. Carder, and H. R. Gordon, Columnar aerosol single-scattering albedo and phase function retrieved from sky radiance over the oceans: Measurements of African dust, *Jour. Geophys. Res.,* **108(D9)**, 4287, 2003. (doi:10.1029/2002JD002497)

This paper describes the application of the Wang and Gordon [1993] sky radiance inversion algorithm to estimate the single scattering albedo of Saharan dust. Measurements were made at the Dry Tortugas in the Gulf of Mexico during a dust outbreak. The retrieved single scattering albedo agreed well with the models proposed by Moulin et al. [2001] to explain the spectral variation of top-of-atmoaphere radiance over intense dust outbreaks.

51) T. X. P. Zhao, I Laszlo, B. N. Holben, C. Pietras, and K. J. Voss, "Validation of two-channel VIRS retrievals of aerosol optical thickness over ocean and quantitative evalution of the impact from potential subpixel cloud contamination and surface wind effect, *J Geophys. Res*. 108(D3), 4106, doi:10.1029/2002JD002346, 2003.

This paper used the data from our CIMEL station in the Dry Tortugas, along with other CIMEL stations to look at a two channel algorithm to obtain aerosol optical thickness. It shows the utility of the ground-based CIMEL stations on islands for algorithm development and validation.

52) H. Du and K. J. Voss, Effects of point spread function on calibration and radiometric accuracy of CCD camera, *Applied Optics*, **43**: 665 - 670, 2004.

This paper describes the effect of the point spread function on the aureole camera system. One of the major problems is during the calibration of the device, the size of the calilbration source must be accounted for in the data reduction process. If not, this can be a significant source of calibration error (5% or more).

53) T. X. P. Zhao, O. Dubovik, A. Smirnov, B. N. Holben, J. Sapper, C. Pietras, K. J. Voss, and R. Frouin, Regional Evaluation of an advanced very high resolution radiometer (AVHRR) two channel aersol retrieveal algorithm, J. *Geophys. Res.*, **109**:doi:10.1029/2003JD003817, 2004.

This is another paper using the CIMEL station in the Dry Tortugas to look at satellite validation and algorithm development.

Coccolithophore-derived Calcite Algorithm

52) W. M. Balch, J. J. Fritz, and E. Fernandez, Decoupling of calcification and photosynthesis in the coccolithophore *Emiliania huxleyi* under steady-state light limited growth. Marine Ecology Progress Series, 14287-97 (1996).

This paper summarized experiments on the rate of calcite production as a function of their growth. This work was important for understanding the variability in the calcite-dependent light scatter per coccolith, essential for the MODIS calcite algorithm.

53) W. M. Balch and K. A. Kilpatrick, Calcification rates in the equatorial Pacific along 140 W, Deep Sea Research, 43971 - 993 (1996).

Summary of estimates of calcite per coccolith for natural populations of coccolithophores. Data from these natural populations were used in the derivation of the MODIS calcite algorithm.

54) W. M. Balch and B. Bowler, Sea surface temperature gradients, baroclinicity, and vegetation gradients in the sea, J. Plank. Res., 19, 1829- 1858 (1998).

Method for remote estimation of vegetation gradients in the sea based on changes in satellite-derived SST. This provides a means to approximate expected algal concentrations under clouds based on thermal observations on either side of the cloud.

55) W. M. Balch, D. T. Drapeau, T. L. Cucci, R. D. Vaillancourt, K. A. Kilpatrick, and J. J. Fritz, Optical backscattering by calcifying Algae - separating the contribution by particulate inorganic and organic carbon fraction, J. Geophys. Res., 104C, 1541 - 1558 (1999).

This paper is the most comprehensive summary of the calcite composition of various species of coccolithophores and their light scattering properties. These data were used in the MODIS 2 band calcite algorithm.

56) K. J. Voss, W. M. Balch, and K. A. Kilpatrick, Scattering and attenuation properties of Emiliania huxleyi cells and their detached coccoliths, Limnol. Oceanogr., 43, 870 - 876 (1998).

This paper describes a laboratory experiment with *Emiliania huxleyi*. In this experiment the volume scattering function and the beam attenuation was measured spectrally of E. huxleyi in two states: whole cells with coccoliths attached and cells with detached coccoliths. From these measurements we could deduce the scattering due to plated cells, naked cells, and the coccoliths themselves.

57) Milliman, J., PJ. Troy, W. Balch, A.K. Adams, Y-H. Li, and F.T. MacKenzie. 1999. Biologically-mediated dissolution of calcium carbonate above the chemica11ysoc1ine? *Deep-Sea Res. I,* 46,1653-1669.

This paper summarizes the observations of previously-unexplained calcite disappearance in the sea. This is one of the first accounts of supra-lysocline dissolution of calcite, presumably caused by grazing and bacterial metabolism.

58) W. M. Balch, K. A. Kilpatrick, P. M. Holligan, and C. Trees, The 1991 Coccolithophore Bloom in the Central North Atlantic I. Optical Properties and Factors affecting their distribution. Limnology and Oceanography. 41: 1669-1683.

This paper describes the optical properties of the largest mesoscale coccolithophore bloom ever observed. Satellite images showed that it spanned the entire North Atlantic. Explanations on the vertical distributions were also presented, and physical factors discussed which explain the distributions.

59) W. M. Balch, K. A. Kilpatrick, P. Holligan, D. Harbour, and E. Fernandez, The 1991 Coccolithophore Bloom in the Central North Atlantic II. Relating Optics to Coccolith Concentration. Limnology and Oceanography. 41: 1684-1696.

This is the companion paper to the previous paper, and provides field data relating the backscattering of coccoliths to their PIC concentration. These data were also used in the MODIS PIC algorithm.

60) E. Fernandez, J. J. Fritz, and W. M. Balch, Growth dependent chemical composition of the coccolithophorid Emiliania huxleyi in light-limitedd chemostats. J. Exp. Mar. Biol. Ecol. 207: 149-160.

This paper discusses the other organic constituents of coccolithophores as a function of growth rate. In particular, this paper documented, for the first time, the large lipid content of coccolithophores (perhaps for floatation).

61) J. J. Fritz and W. M. Balch, A coccolith detachment rate determined from chemostat cultures of the coccolithophore Emiliania huxleyi. J. Exp. Mar. Biol. Ecol. 207: 127-147.

This paper describes the rate of detachment of coccoliths from E. huxleyi as a function of growth. It demonstrates the fast appearance of coccolithophore blooms as seen in remotely-sensed images.

62) Balch, W.M., D. Drapeau, B. Bowler and J. Fritz, Continuous measurements of calcite dependent light scattering in the Arabian Sea, *Deep Sea Research I,* 48, 2423-2452 (2001).

This paper provides estimates of calcite scattering in the Arabian Sea, and provides, through continuous analysis, estimates of typical fraction of total backscattering due to coccolithophore calcite.

63) Vaillancourt, R. D. and W. M. Balch, Size distribution of coastal sub-micron particles determined by flow, field flow fractionation, *Limnology and Oceanography,* 45, 485492,2000.

This paper discusses a method for determination of sub-micron aggregates using Flow Field Fractionation. It also describes the importance of sub-micron aggregates in coastal seawater, their size and concentration.

64) Graziano, L., W. Balch, D. Drapeau, B.Bow1er, and S. Dunford, Organic and inorganic carbon production in the Gulf of Maine, *Continental Shelf Research,* 20,685-705,2000.

This paper provides estimates of calcite concentration and calcification in non-bloom waters of the Gulf of Maine, as measured during three surveys.

65) Balch, W.M., D. Drapeau, and J. Fritz, Monsoonal forcing of calcification in the Arabian Sea, *Deep Sea Research II,* 47, 1301-1333,2000.

This work provides the first comprehensive survey of calcite concentration and production measurements in the Arabian Sea.

66) Balch, W.M., J. Vaughn, J. Novotny, D.T. Drapeau, R.D. Vaillancourt, J. Lapierre, and A. Ashe, Light scattering by viral suspensions, *Limnology and Oceanography,* 45, 492498, 2000.

This paper provides the first estimates of the importance of viruses to total optical backscattering. The justification for this work was in trying to account for the "missing backscattering" observed in the ocean. We concluded that viruses on their own are not the source of "missing backscattering".

67) Balch, W.M., Vaughn, J.M., Novotny, J.F., Drapeau, D.T., Goes, J.I., Lapierre, J.M., Scally, E, Vining, C.L., Ashe, A., and Vaughn, J.M. Jr. 2002. Fundamental changes in light scattering associated with infection of marine bacteria by bacteriophage. Limnology and Oceanography. 47(5): 1554-1561.

This paper describes the observation that the principal optical effect of viruses in the sea is on their hosts. We address the possibility that the decreases in scattering of an infected host population are large enough to be seen from space.

68) Campbell, J.W., D. Antoine, R. Armstrong, K. Arrigo, W. Balch, and others. 2002. Comparison of algorithms for estimating ocean primary productivity from surface chlorophyll, temperature, and irradiance. Global Biogeochemical.Cycles, 16(3), (10.1029/2001GB001444).

This paper is an attempt to provide better primary production estimates based on space-based measurements. These results were important for choosing the MODIS primary productivity algorithm.

69) Balch WM and Drapeau DT (2004) Backscattering by Coccolithophorids and Coccoliths: Sample Preparation, Measurement and Analysis Protocols. In: Mueller JL, Fargion GS, McClain CR (eds) Ocean Optics Protocols For Satellite Ocean Color Sensor Validation, Revision 5: Biogeochemical and

Bio-Optical Measurements and Data Analysis Protocols. National Aeronautical and Space administration, Goddard Space Flight Space Center, Greenbelt, Maryland, pp 2737.

This paper outlines the methodology used for determining the scattering properties of coccolithophore coccoliths.

70) Broerse, AT.C., Tyrrell, T., Young, 1. R., Poulton, A J., Merico, A and W. M. Balch. 2003. The cause of bright waters in the Bering Sea in winter. Continental and Shelf Research. 23: 1579-1596.

This paper demonstrates that late winter bright "blooms" of water in the Bering Sea were not related to coccolithophore blooms, as previously contended, but were instead due to resuspension of opal sediments from the shelf sediments during intense mixing. We also demonstrated that the derived silica concentrations were sufficient to provide enough backscattering to look like a coccolithophore bloom.

71) Balch, W. M., Howard Gordon, B. C. Bowler, D. T. Drapeau, E. S. Booth. 2004. Calcium Carbonate Budgets in the Surface Global Ocean based on MODIS Data. To be submitted to the Journal of Geophysical Research.

This paper provides a formal algorithm description of the improved 2-band algorithm, as well as application of the algorithm using MODIS data to produced global maps of suspended calcium carbonate.

Presentations and Abstracts

(Personnel supported by MODIS on this contract in **Bold**):

1994:

"Oceans and atmospheres: an experimentalist view from Miami", **K. J. Voss**, Ispra, Italy, June.

"Aerosol optical depth over the North Atlantic", Bigelow Laboratory for Ocean Sciences, Boothbay Harbor, Me., **K. J. Voss**, July.

1995:

“Theoretical Basis of the SeaWiFS/MODIS Normalized Water Leaving Radiance Algorithm (Atmospheric Correction) and its relationship to Vicarious Calibration”, **H. R. Gordon,** CEOS/IVOS Calibration and Validation Workshop.

“Calcification and Photosynthetic Rates of Coccolithophores Under Steady Growth”, **W. M. Balch and J. J. Fritz**, Emiliania Huxleyi and Oceanic Carbon Cycle, London, April,

“A coccolith detachment rate determined from chemostat cultures of the coccolithophore Emiliania huxleyi”, **W. M. Balch and J. J. Fritz**, Emiliana Huxleyi and Oceanic Carbon Cycle, London, April,

“Polarization measurement of the spectral radiance distribution using a CCD camera system (RADS-II)”, **Y. Liu and K. J. Voss**, OSA Annual Meeting

“Measurement of the Spectral Reflectance of Whitecaps in the Open Ocean”, **K. D. Moore, K. J. Voss, and H. G. Gordon,** AGU Ocean Sciences.

1996:

“Whitecaps: Spectral reflectance in the open ocean and their contribution to water-leaving radiance”, **K. D. Moore, K. J. Voss, and H. R. Gordon**, Ocean Optics XIII, Halifax Nova Scotia, October.

1997:

“Polarized radiance distribution measurements of skylight for passive remote sensing of aerosol optical properties”, **K. J. Voss and Y. Liu**, OSA Remote Sensing Technical Meeting, OSA Sante Fe. N. M., February.

“Preliminary Lidar results from the aerosol characterization experiment 2 (ACE-2)”, **E. J. Welton, K. J. Voss**, H. Maring, AGU Fall Meeting.

““Solar Aureole measurements of volcanic aerosol in the Killauea Plume ”, **J. Ritter, K. J. Voss, H. R. Gordon**, D. Clark, L. Koval, AGU Fall Meeting.

“Condensation Nuclei in the marine boundary layer in the tropical Atlantic ocean: relation to air mass characteristics”, X. Li, H. Maring, K. Rhoads, E. Welton, **K. Voss**, B. Doddredge, J. Merrill, J. M. Prospero, , AGU Fall Meeting.

“Retrieval of aerosol properties over land”, **H. Yang and H. R. Gordon**, AGU Spring Meeting.

“Radiative Characteristics of Specific Aerosols in a Maritime Environment”, E. **J. Welton, K. J. Voss**, and J. M. Prospero”, AGU Spring Meeting.

“A new instrument for shipborne radiometric measurements of the solar aureole”, **J. M. Ritter, K. J. Voss, and H. R. Gordon**, AGU Spring Meeting.

“Solar Aureole measurements of volcanic aerosol in the Kilauea plume”, **J. Ritter, K. Voss, H. Gordon**, D. Clark, and L. Koval, , AGU Fall meeting.

“Preliminary Lidar Results from the aerosol Characterization experiment 2 (ACE-2)”, **E. J. Welton and K. J. Voss**, AGU Fall meeting.

1998:

“SeaWiFS Calibration Initialization: Preliminary Results”, **H. R. Gordon, K. J. Voss**, J. W. Brown, P. **V. F. Banzon**, R. E. Evans, D. K. Clark, L. Kovar, M. Yuen, M. Feinhoz, and M. Yarbrough, Ocean Optics XIV, Kona, Hawaii, November.

“The Numbus 7 coastal zone color scanner: a retrospective”, **H. R. Gordon**, AGU Fall meeting, San Francisco, December.

“Upwelling in-water radiance distribution measurements near the MOBY site in Hawaii”, **K. J. Voss**, D. K. Clark, and C. Trees, AGU/Ocean sciences meeting, San Diego, February.

“Three Dimensional Investigation of Lower Tropospheric Aerosol and Water Vapor during ACE-2 by Means of Airborne Sunphotometry”, B. Schmid, J. Livingston, P. Russell, P. Durkee, **E. Welton, K. Voss**, P. Formenti, M. Andreae, S. Gasso., CAGP, Seattle, August.

1999:

“Satellite remote sensing of mineral dust in the visible from Meteosat to Sea WiFS, Workshop on Mineral Dust”, C. Moulin, **H.R Gordon, V.F. Banzon**, RH. Evans, F. Dulac, C.E. Lambert, D. Tame, Boulder, CCO, June.

"Measurements of the vertical distribution of aerosols and clouds during INDOEX 1999 Using Micro-pulse Lidars", **E. Welton**, P. Flatau, **K. Voss**, **H. Gordon**, K. Markowicz, J. Campell, J. Spinhirne, Poster Paper (A32B-07), AGU Fall Meeting. San Francisco, CA, December.

"Clear-sky Closure Studies of Tropospheric Aerosol and Water Vapor During ACE-2 Using Airborne Sunphotometer, Airborne in-situ, Space-borne and Ground-based Measurement", B. Schmid, D. R Collins, S. Gasso, E. Ostrom, **E. Welton**, P. A. Durkee, J. M. Livingston, P. B. Russell, R C. Flagan, J. H. Seinfe1d, D. A. Hegg, K. J. Noone, **K. J. Voss**, **H. R Gordon**, J. Reagan, and J. Spinhirne, Abstract (A32E-08), AGU Fall Meeting, San Francisco, December.

"Mineral dust observations with SeaWiFS: Dust models derived from spectral measurements", C. Moulin, **H.R Gordon, R. M. Chomko, V.F. Banzon**, and RH. Evans, Abstract (A41F-12), AGU Fall Meeting, San Francisco, December.

"Ocean Color and Aerosols", P.J. Flatau, G. Mitchell, A. Subramaniam, J. Wieland, **E.J. Welton**, K. Markowicz, J. Nelson, **K. Voss, H. Gordon**, R.M. Reynolds, M. Miller, T. Nakajima, K. Rutlidge, M. Kahru, Abstract (A31E-09) AGU Fall Meeting, San Francisco, December.

"Combined use of visible and infrared channels to identify and correct African dust aerosols", R Evans, C. Moulin, P. Minnett, H. Gordon, V. Banzon, and C. Moulin, Paper Number 3868--71, EUROPTO, Rome, Italy.

"Backscattering probability and calcite-dependent backscattering in the Gulf of Maine", **W. M. Balch, D. T. Drapeau, B. Bowler**, A. Ashe, A., Vaillancourt, R, Dunford, S., and Graziano, L., Proceedings of the ASLO Meeting, Santa Fe, NM. *ASLO Santa Fe,* February.

"Clear column closure studies of urban-marine and mineral-dust aerosols using aircraft, ship, satellite and ground-based measurements in ACE-2", B. Schmid, P.B. Russell, J.M. Livingston, S. Gasso, D. Hegg, D. Collins and J. Seinfeld, E. Ostrom , K. Noone, P.A. Durkee, **E.J. Welton, K. Voss**, V.N. Kapustin, T.S. Bates and P.K. Quinn. International Conference and Workshops on Aerosols, Radiation budget - Land surfaces - Ocean color: the contribution of POLDER and new generation spaceborne sensors to global change studies, Meribel (France), January.

2000:

"MODIS Atmospheric Correction Performance: Initial Evaluation", **H.R. Gordon**, , MODIS Science Team Meeting, Greenbelt, MD, June.

“Chalk-Ex”, **W. M. Balch**, MODIS Science Team Meeting, Greenbelt, MD, June.

“Performance of advanced atmospheric correction algorithms for ocean color sensors: SeaWiFS and MODIS”, **R. M. Chomko** and **H.R Gordon,** , *IGARSS 2000,* Hilton Hawaiian Village, Honolulu, Hawaii, July.

“Decadal evolution of the global oceanic biomass as inferred from a 20-year record of ocean color (from CZCS to SeaWiFS)”, D. Antoine, A. Morel, **H.R Gordon,** RH. Evans, and **V.F. Banzon**, *Oceans from Space "Venice 2000",* Scuola Grande Confraternita di San Teodoro, Venice, Italy, October.

“Advances in atmospheric correction of ocean color sensors (Case 1 waters)”, **H.R. Gordon,** *Oceans from Space "Venice 2000",* Scuola Grande Confraternita di San Teodoro, Venice, Italy, October.

“New estimate of the marine productivity in the dust contaminated Tropical Atlantic using the spectral matching algorithm for atmospheric correction of SeaWiFS and POLDER ocean color imagery”, **C. Moulin, H.R Gordon, V.F. Banzon,** RH. Evans, S. Giraud, J.-M. Nicolas, G. Bonnafoux and P.-Y. Deschamps, , *Oceans from Space "Venice 2000",* Scuola Grande Confraternita di San Teodoro, Venice, Italy, October.

“Performance of the spectral-optimization algorithm for atmospheric correction of SeaWiFS and MODIS ocean color imagery”, **RM. Chomko** and **H.R Gordon,***Oceans from Space "Venice 2000",* Scuola Grande Confraternita di San Teodoro, Venice, Italy, October.

“An algorithm for retrieval of coccolithophore calcite concentration from Sea WiFS imagery”, **H.R Gordon, G.C. Boynton, W.M. Balch,** S.B. Groom, D.S. Harbour, and TJ. Smyth, *Oceans from Space "Venice 2000",* Scuola Grande Confraternita di San Teodoro, Venice, Italy, October.

"Upwelling Radiance distribution measurements and the ocean "BRDF"", **K. J. Voss,** Oceans from Space 2000, Venice, Italy, October.

“Advanced Atmospheric correction algorithms”, **H.R Gordon, RM. Chomko,** and **C. Moulin,** *Ocean Optics XV,* Musee Oceanographique, Monaco, October.

“New estimate of the marine productivity in the dust contaminated Tropical Atlantic using the spectral matching algorithm for atmospheric correction of Sea WiFS and POLDER ocean color imagery”, C. **Moulin, H.R. Gordon, V.F. Banzon,** RH. Evans, S. Giraud, J.-M. Nicolas, G. Bonnafoux and P.-Y. Deschamps, , *Ocean Optics XV,* Musee Oceanographique, Monaco, October.

"3D Instrument Self-Shading effects on in-water multi-directional radiance measurements", J. P. Doyle and **K. J. Voss**, Ocean Optics XV, Monaco, October.

2001:

"Validation of the MODIS suspended calcite product", **W. M. Balch, D. Drapeau, B. Bowler**, A. Ashe, J. Goes, E. Scally, **H. Gordon**, K. Kilpatrick, and R. Evans.

"MOD 18 Normalized Water-leaving Radiance", **H.R. Gordon**, R. Evans, E. Kearns, K. Kilpatrick, **K. Voss**, and the RSMAS Remote Sensing Laboratory staff.

"In-water spectral radiance distribution measurements", **K. J. Voss**, Physics of Quantum Electronics, Snowbird, Utah, January.

2002:

"New observations of coccoliths from satellites, ferries, towed vehicles and balloons", **Balch,** W. M., Keynote talk. Coccolithophores from molecular processes to global impact, Conference at Centro Stefano Franscini, Monte Verita, Ascona, Switzerland, February.

"Quantitative, space-based measurements of oceanic suspended ocean calcium carbonate with MODIS and SeaWiFS", **Balch, W.M., Bowler, B., Drapeau**, D., **Gordon,** H., Scally, E., Ashe, A., AGU/ASLO Ocean Sciences Meeting, Honolulu, Hawaii. February.

"MODIS coccolith algorithm: Results" **Balch, W. M., B. Bowler, D. Drapeau**, J. Goes and E. Booth, MODIS Team Meeting, Greenbelt, MD, July.

"A multi-year record of bio-optical properties in the Gulf of Maine", **Drapeau, D. T., W.M. Balch,** B**.C. Bowler**, E. Scally, J. Goes, A. Ashe, AGU/ASLO Ocean Sciences Meeting, Honolulu, Hawaii, February 2002.

"An Algorithm for Coastal Water and the Status of its Implementation into the MODIS Processing Stream", **H.R Gordon, RM. Chomko**, R.E. Evans, J.W. Brown, S. Walsh and W. Baringer, MODIS Team Meeting, Greenbelt, MD, July.

"Radiance distribution measurements in clear water", **K. J. Voss** and D. K. Clark, Poster, MODIS Team Meeting. Greenbelt, MD, July.

"Radiance distribution measurements in clear water", **K. J. Voss** and D. K. Clark, Poster, IWG Meeting. Baltimore, MD, July.

"Atmospheric correction of ocean color imagery: alpha to psi", **H.R Gordon** presented a short course (6 hrs) at *Ocean Optics* XVI, Santa Fe, NM (on Nov. 16,2002).

"Application of the Spectral Matching Algorithm to Recover Chlorophyll Time Series During the Arabian Sea Southwest Monsoon", **P.F. Banzon**, R.H. Evans, **H.R. Gordon,** and **R.M. Chomko**, Eos. Trans. AGU, 83(4), Ocean Sciences Meet. Suppl. Abstract OS 12I-04.

"Suspended Chalk and Ocean Optics", **W.M. Balch**, **H.R. Gordon, B.C. Bowler**, **D.T. Drapeau**, J. Goes, and E. Booth, *Ocean Optics XVI,* Santa Fe, NM, November.

"Use of a Neural Network Approach to Improve atmospheric Correction of Ocean Color Imagery", J. Cedric, S. Thiria, B. Galios, M. Crapon, C. Moulin, and **H.R. Gordon,** *Ocean Optics XVI,* Santa Fe, NM, November.

"Application of the Spectral Matching Algorithm to Arabian Sea Sea WiFS Imagery", **P.F. Banzon,** R.H. Evans, **H.R. Gordon,** and **R.M. Chomko**, *Ocean Optics XVI,* Santa Fe, NM, November.

"Optical properties of submicron particles in seawater using flow field flow fractionation", Goes, J. **I., W. M. Balch,** J. Vaughn, Ocean Optics XVI. November.

"Chalk-Ex: An Ocean Optics Manipulation Experiment on the Fate of Calcite Particles", **Balch, W. M.,** Plueddemann, A. Pilskaln, C., Dam, H., McManus, G., AGU Fall Meeting, San Francisco, December.

"Optical Results From the November '01 "Chalk-Ex" Ocean Optics Manipulation Experiment", **Bowler, B., W. M. Balch, D. Drapeau**, J. Goes, and E. Booth, AGU Fall Meeting, San Francisco, December.

"Evolution of stratification and shear during ChalkEx-2001", A. Plueddemann, **W.M. Balch,** C.H. Pilskaln, AGU Fall Meeting, San Francisco, December.

"Evidence of DOM removal by Cretaceous CaC03 particles during Chalk-Ex 2001", Goes, J. **I., W.M. Balch, B. Bowler, D. Drapeau**, E. Booth, AGU Fall Meeting, San Francisco, December.

2003:

"Remote sensing calcium carbonate from space- use of a five-year coastal time series to understand coccolithophore ecology", **Balch, W. M., Drapeau, D. T., Bowler**, B. C., Booth, E. S., Goes, 1. I., Gordon, H. R., ASLO Aquatic Sciences Meeting, Salt Lake City, Utah, February.

“CalVal in coastal waters”, **K. J. Voss**, Ocean Color Team Meeting, Miami, Fl., April.

“Chalk-Ex: Transport of optically active particles from the surface mixed layer”, **Balch, W. M.,** Albert Plueddemann, Cindy Pilskaln- Bigelow Lab, Hans Dam, George McManus, J. Goes, University of Rhode Island, November.

“BRDF of clear water”, **K. J. Voss**, MOBY calibration/reprocessing meeting,, Honolulu, Hi., November.

Students Supported by MODIS Contract

Kuiyuan Ding, Ph. D. Physics, 1993, "Radiative transfer in spherical shell atmospheres for correction of ocean color remote sensing".

Tianming Zhang, Ph. D. Physics, 1995, "Remote Sensing of aerosol properties over the ocean by combining surface and aircraft measurements".

Haoyu Yang, Ph. D. Physics, 1996, "Retrieval of Aerosol Optical Properties over Land".

Tao Du, Ph. D. Physics, 1996, "Effects of polarization and absorbing aerosols on atmospheric correction in ocean color remote sensing".

Yi Liu, Ph. D. Physics, 1996, "Measurement of the polarized radiance distribution".

Joseph Ritter, Ph. D. Physics, 1998, "Remote measurement of aerosol scattering properties and the development of a novel imaging solar aureole radiometer".

Ellsworth Welton, Ph. D. Physics, 1998, "Measurements of aerosol optical properties over the ocean using sunphotometry and lidar".

Roman Chomko, Ph. D. Physics, 1999, "Atmospheric correction of ocean color imagery: use of Junge power-law size distribution".

David Bates, Ph. D. Physics, 2003, "Lidar measurements of marine aerosols with improved analysis techniques".

Hong Du, Ph. D. Physics, 2004, " Comparison of lab based and solar reflectance based calibrations of Aureole camera".

Jennifer Fritz, Ph.D. Biological Oceanography, 1997. "Growth dependence of coccolith detachment, carbon fixation and other associated processes by the coccolithophore, *Emiliania huxleyi*"

APPENDIX II

MODIS Normalized Water-Leaving Radiance
Algorithm Theoretical Basis Document
(Revision 5)

MODIS Normalized Water-leaving Radiance
Algorithm Theoretical Basis Document
(MOD 18)

Version 5

Submitted by

Howard R. Gordon and Kenneth J. Voss
Department of Physics
University of Miami
Coral Gables, FL 33124

Under Contract Number NAS5-31363

May 2004

TABLE OF CONTENTS

Preface

This algorithm theoretical basis document (ATBD) describes the algorithm for retrieving the normalized water-leaving radiance (reflectance) from MODIS imagery. It replaces Version 0 which was submitted on July 30, 1993, Version 1 submitted February 28, 1994, Version 2 submitted November 1, 1994, Version 3 submitted August 15, 1996, and Version 4 submitted April 30, 1999. Version 1 was peer reviewed in the spring of 1994 and reviewer suggestions were incorporated into Version 2. Version 3 covered additional developments between 1994 and 1996 and was peer reviewed in November of 1996. Version 4 incorporates the progress of studies relevant to the algorithm since Version 3. Version 5 describes the state of the algorithms at the close of the contract. Possible algorithm enhancements, as well as outstanding issues that require further research, are identified in this document.

The basic algorithm described here has been used to process SeaWiFS imagery (since its launch in 1997), with some SeaWiFS-specific modifications. Experience gained with SeaWiFS imagery has been invaluable for assessing the performance of the algorithm. The algorithm has been used in MODIS ocean processing for both Terra and Aqua; however, it does not reflect any changes made by the Ocean Color Discipline Processing Group at GSFC for processing Aqua data.

Chapters 1–4 describe the algorithm in its present form, and also detail outstanding issues that require further work. Chapter 5 describes possible enhancements to the code to deal with these issues.

The authors acknowledges the aid of M. Wang in the preparation of Version 0 of this ATBD, K. Ding preparation of Version 1, K. Ding and F. He in the preparation of Version 2, and T. Zhang, K. Moore, H. Yang, and Tao Du in the preparation of Version 3, and G.C. Boynton, R. Chomko and C. Moulin in the preparation of Version 4.

1.0 Introduction

Following the work of *Clarke, Ewing and Lorenzen* [1970] showing that the chlorophyll concentration in the surface waters of the ocean could be deduced from aircraft measurements of the spectrum of upwelling light from the sea — the "ocean color" — NASA launched the Coastal Zone Color Scanner (CZCS) on Nimbus-7 in late 1978 [*Gordon et al.*, 1980; *Hovis et al.*, 1980]. The CZCS was a proof-of-concept mission with the goal of measuring ocean color from space. It was a scanning radiometer that had four bands in the visible at 443, 520, 550, and 670 nm with bandwidths of 20 nm, one band in the near infrared (NIR) at 750 nm with a bandwidth of 100 nm, and a thermal infrared band (10.5 to 12.5 μm) to measure sea surface temperature. The four visible bands possessed high radiometric sensitivity (well over an order of magnitude higher than other sensors designed for earth resources at that time, e.g., the MSS on the Landsat series) and were specifically designed for ocean color. The CZCS experience demonstrated the feasibility of the measurement of phytoplankton pigments, and possibly even productivity [*Morel and André*, 1991; *Platt and Sathyendranath*, 1988], on a *global* scale. This feasibility rests squarely on two observations: (1) there exists a more or less universal relationship between the color of the ocean and the phytoplankton pigment concentration for most open ocean waters; and (2) it is possible to develop algorithms to remove the interfering effects of the atmosphere from the imagery. In this document we will describe the basis of the algorithm for removing the atmospheric effects from MODIS imagery over the ocean to derive the normalized water-leaving radiance in the visible. The process of deriving the normalized water-leaving radiance from imagery of the oceans is usually termed *atmospheric correction.*

1.1 The Normalized water-leaving radiance

The normalized water-leaving radiance, $[L_w]_N$, was defined by *Gordon and Clark* [1981] through

$$L_w(\lambda) = a_\oplus^{-2}\,[L_w(\lambda)]_N \cos\theta_0 \exp\left[-\left(\frac{\tau_r(\lambda)}{2} + \tau_{Oz}(\lambda)\right)\left(\frac{1}{\cos\theta_0}\right)\right], \qquad (1)$$

where $L_w(\lambda)$ is the radiance backscattered *out* of the water at a wavelength λ, $\tau_r(\lambda)$, $\tau_{Oz}(\lambda)$ are the optical thicknesses of the atmosphere associated with molecular (Rayleigh) scattering and Ozone absorption, respectively, and $a_\oplus$ is the earth-sun distance in AU. θ_0 is the solar zenith angle. The normalized water-leaving radiance is approximately the radiance that would exit the ocean in the absence of the atmosphere, with the sun at the zenith, at the mean earth-sun distance (1 AU). This definition was motivated by the desire to remove, as much as possible, the effects of the atmosphere and the solar zenith angle from $L_w(\lambda)$; however, *Morel and Gentili* [1993] have shown that a residual dependence on θ_0 remains in $[L_w(\lambda)]_N$ (See Section 3.1.1.13.4). The normalized water-leaving radiance is used in other algorithms to derive nearly all of the MODIS ocean products, e.g, the chlorophyll concentration. As such, it plays a central role in the application of MODIS imagery to the oceans.

In the remainder of this document, for the most part, we will abandon the use of radiance in the description of the algorithm in favor of reflectance. The reflectance ρ associated with a radiance L is defined to be $\pi L/F_0 \cos\theta_0$, where F_0 is the extraterrestrial solar irradiance, and θ_0 is the solar zenith angle, i.e., the angle between the line from the pixel under examination to the sun and the local vertical. Reflectance is favored because it may be possible to more accurately calibrate MODIS in reflectance rather than radiance. The desired normalized water-leaving radiance can easily be converted to normalized water-leaving reflectance $[\rho_w]_N$ through

$$[\rho_w]_N = \frac{\pi}{\overline{F}_0}[L_w]_N, \tag{2}$$

where $\overline{F}_0$ is the mean extraterrestrial solar irradiance at the mean earth sun distance, i.e., $\overline{F}_0 = a_\oplus^2 F_0$. Then Eq. (1) becomes

$$\rho_w(\lambda) = [\rho_w(\lambda)]_N \exp\left[-\left(\frac{\tau_r(\lambda)}{2} + \tau_{Oz}(\lambda)\right)\left(\frac{1}{\cos\theta_0}\right)\right] = [\rho_w(\lambda)]_N t(\theta_0, \lambda), \tag{3}$$

where $t(\theta_0, \lambda)$ is the CZCS *approximation* to the diffuse transmittance of the atmosphere (See Section 3.1.1.5). Thus, retrieving $[\rho_w]_N$ is equivalent to retrieving $[L_w]_N$. The factor $\pi/\overline{F}_0$ in Eq. (2) is ≈ 0.017 at 443 and 555 nm. It should be noted that some algorithms use "remote sensing reflectance" ($R_{rs} = L_w/E_d$, where E_d is the downward irradiance just above the sea surface) rather than $[\rho_w]_N$ [*Lee et al.*, 1994; *Lee et al.*, 1996]; however, to a good approximation $[\rho_w]_N = \pi R_{rs}$.

1.2 Outline of the Document

This document is structured in the following manner. First we provide background on the algorithm's role in MODIS products, explain why atmospheric correction is necessary and difficult, and discuss the characteristics of MODIS and SeaWiFS that make atmosphere correction possible. In the main body of the document we develop the proposed algorithm in detail, test it with simulated data, and then discuss the remaining research problems and issues. Next, we provide our present implementation of the algorithm. Finally, we describe possibilities for enhancement of the algorithm.

2.0 Overview and Background Information

The purpose of retrieving the normalized water-leaving reflectances $[\rho_w(\lambda)]_N$ is that they are required inputs into algorithms for recovering most of the MODIS ocean products. In this sense they are fundamental to nearly all of the MODIS ocean applications. The accuracy of these products rests squarely on the accuracy of the retrieval of $[\rho_w(\lambda)]_N$.

2.1 Experimental Objectives

The ultimate objective of the application of MODIS imagery over the ocean is to study the primary production, and its spatial and temporal variation, of the oceans on a global scale to better understand the ocean's role in the global carbon cycle. A required component in the estimation of primary productivity is the concentration of chlorophyll a. Estimation of the concentration of chlorophyll a from MODIS imagery requires the normalized water-leaving reflectance. An example of how this is accomplished is provided by the CZCS. Figure 1 provides $[\rho_w(\lambda)]_N$ at $\lambda = 443$ and 550 nm as a function of the pigment concentration (the sum of the concentrations of chlorophyll

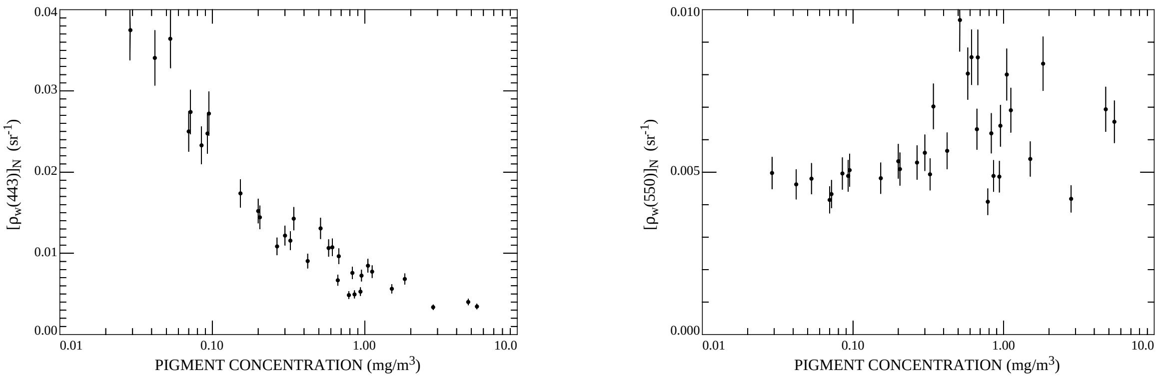

Figure 1. Normalized water-leaving reflectance as a function of pigment concentration. Redrawn from *Gordon et al.* [1988]. Left panel: 443 nm. Right panel: 550 nm.

a and its degradation product phaeophytin a) in the water. Figure 2 gives the algorithm used to estimate the pigment concentration from $[\rho_w(443)]_N/[\rho_w(550)]_N$. It can be well represented by

$$\log_{10} 3.33C = -1.2 \log_{10} R + 0.5(\log_{10} R)^2 - 2.8(\log_{10} R)^3, \quad (4)$$

with $R = 0.5[\rho_w(443)]_N/[\rho_w(550)]_N$. Thus, the pigment concentration C is directly related to the radiance ratios. Analysis [*Gordon*, 1990] suggests that the pigment concentration can be derived from the radiance ratio with an error of $\sim \pm 20\%$. Because of relationships such as these that relate bio-optical parameters to $[\rho_w(\lambda)]_N$, the normalized water-leaving reflectance plays a central role in the application of ocean color imagery to the oceans, and atmospheric correction becomes a critical

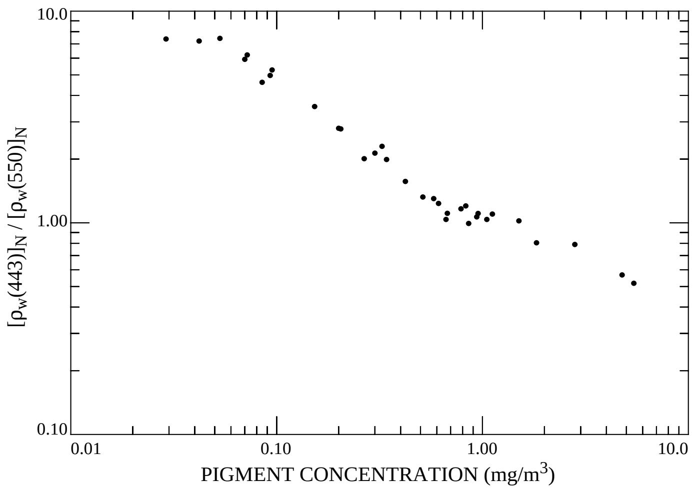

Figure 2. Normalized water-leaving reflectance ratio as a function of pigment concentration. Redrawn from *Gordon et al.* [1988].

factor in determining the fidelity with which bio-optical parameters can be retrieved. When ratios of $[\rho_w]_N$'s are used in computations, as in Eq. (4), small errors of the same sign in the two $[\rho_w]_N$'s will tend to cancel. In most cases the errors in the retrieval of the two $[\rho_w]_N$'s in such ratios *will* have the same sign.

2.2 Historical Perspective

The algorithm for the retrieval of the $[\rho_w]_N$'s from MODIS imagery follows from experience gained with the CZCS. Its purpose is to identify and remove the component of the radiance measured at the sensor that arises from molecular and aerosol scattering in the atmosphere, as well as reflection from the air-sea interface. Since the aerosol concentration and properties are variable in space and time, their effects are unknown *a priori*. The radiometric sensitivity of the CZCS was sufficiently low that it was not necessary to deal with the full complexities of multiple scattering. However, with the increased sensitivity of SeaWiFS and MODIS, multiple scattering in the atmosphere becomes a central issue in the retrieval algorithms for $[\rho_w]_N$. Examples of important secondary issues not addressed in the CZCS algorithm are the presence of whitecaps on the sea surface and the influence of earth curvature on the algorithm.

2.3 Instrument Characteristics

The MODIS and SeaWiFS instruments have similar characteristics (Table 1). The main differences are that MODIS has spectral bands that are half to one-forth as wide as SeaWiFS, MODIS is 12-bit digitized as opposed to 10-bit for SeaWiFS, and MODIS has approximately twice the SNR. The positions of the spectral bands are similar.

Of critical importance for the retrieval of $[\rho_w]_N$ are spectral bands 7 and 8 (745–785 nm and 845–885 nm, respectively) on SeaWiFS and bands 15 and 16 (745–755 nm and 857–872 nm, respectively) on MODIS. Because of the strong absorption by liquid water, virtually no light will exit the ocean in these bands, except in the most turbid coastal waters, so all of the radiance measured by the sensor originates from the scattering of solar irradiance by the atmosphere and the sea surface. These bands can therefore be used to assess the atmospheric effects. Band 6 on SeaWiFS (660–680 nm) and band 13 on MODIS (662–672 nm) can also be utilized in waters with pigment concentration $\lesssim 0.5 - 1.0$ mg/m^3, but probably not in coastal waters. Band 7 on SeaWiFS overlaps the O_2 "A" absorption band centered at ~ 762 nm. The influence of this absorption band on SeaWiFS atmospheric correction has been studied by *Ding and Gordon* [1995]; however, as MODIS band 15 does not overlap the O_2 absorption, we shall not discuss this issue further in this document.

The application of these bands to atmospheric correction is straightforward in principle: one assesses the contribution of the atmosphere in the NIR and extrapolates it into the visible.

3.0 Algorithm Description

This section provides a description of the entire algorithm. Before beginning, a few preliminaries are useful. Table 1 provides the MODIS radiometric specifications in terms of reflectance for a solar zenith angle of 60°and viewing near the scan edge. For convenience we also provide the "noise equivalent reflectance" (NE$\Delta\rho$) for the SeaWiFS and CZCS bands closest to the given

Table 1: Comparison of the radiometric performance of MODIS, SeaWiFS, and CZCS for $\theta_0 = 60°$ near the scan edge. MODIS and SeaWiFS NE$\Delta\rho$'s are from the radiometric specifications. CZCS is from in-orbit measurements.

Band	λ (nm)	ρ_{max} (sr^{-1})	ρ_t (sr^{-1})	$[\rho_w]_N$ (sr^{-1})	NE$\Delta\rho$ (sr^{-1})		
					MODIS	SeaWiFS	CZCS
8	412	0.50	0.34	0.040	0.00018	0.00068	–
9	443	0.46	0.29	0.038	0.00016	0.00043	0.0011
10	488	0.36	0.23	0.024	0.00014	0.00034	–
11	531	0.30	0.19	0.0090	0.00013	–	0.00058
12	551	0.25	0.154	0.0040	0.00010	0.00027	0.00064
13	670	0.17	0.105	0.0004	0.00004	0.00023	0.00051
14	681	0.17	0.105	0.0003	0.00004	–	–
15	748	0.15	0.081	–	0.000085	0.00018	–
16	869	0.13	0.069	–	0.000076	0.00015	–

MODIS band. Note that MODIS is typically 2-3 times more sensitive than SeaWiFS, which in turn is approximately twice as sensitive as CZCS. Exceptions are the MODIS bands 13 and 14 which are to be used to measure the chlorophyll *a* fluorescence near 683 nm [*Neville and Gower*, 1977]. These bands are ~ 6 times more sensitive than SeaWiFS and ~ 12 times more sensitive than CZCS. The table also provides the typical top-of-the-atmosphere reflectance ρ_t and the normalized water-leaving reflectance $[\rho_w]_N$ for a very low pigment concentration (Sargasso Sea in summer) [*Gordon and Clark*, 1981]. Note that $[\rho_w]_N$ is only a small fraction of ρ_t. To recover $[\rho_w]_N$ in the blue (443 nm) for these waters with an error < 5% requires an atmospheric correction of $\sim \pm 0.001$ to ± 0.002 in reflectance, i.e., about five to ten times the NE$\Delta\rho$. This is our goal for MODIS band 9. It is shown later that when this goal is met, the error in $[\rho_w]_N$ at 550 nm will be ~ 3–4 times smaller than that at 443 nm. In this case, Figure 1 shows that the error in the ratio R in Eq. (4)

usually will be dominated by error in $[\rho_w]_N$ at 443 nm, the exception being very low values of C.

3.1 Theoretical Description

In this section we provide the theoretical basis of the algorithm. We begin by discussing the basic physics of the algorithm, starting with single scattering and progressing into the multiple scattering regime. Then several auxiliary algorithms, e.g., a whitecap removal algorithm, a sun glitter masking algorithm, etc., are presented. Next, the required ancillary data are itemized, the approximations used in the development of the algorithm are examined, and the remaining research issues are discussed. Finally, an implementation of the algorithm is described and the effects of MODIS radiometric calibration uncertainty is considered.

3.1.1 Physics of the Algorithm

The radiance received by a sensor at the top of the atmosphere (TOA) in a spectral band centered at a wavelength λ_i, $L_t(\lambda_i)$, can be divided into the following components: $L_{path}(\lambda_i)$ the radiance generated along the optical path by scattering in the atmosphere *and* by specular reflection of atmospherically scattered light (skylight) from the sea surface; $L_g(\lambda_i)$ the contribution arising from specular reflection of direct sunlight from the sea surface (sun glitter); $L_{wc}(\lambda_i)$ the contribution arising from sunlight and skylight reflecting from individual whitecaps on the sea surface; and $L_w(\lambda_i)$ the desired water-leaving radiance; i.e.,

$$L_t(\lambda_i) = L_{path}(\lambda_i) + T(\lambda_i)L_g(\lambda_i) + t(\lambda_i)L_{wc}(\lambda_i) + t(\lambda_i)L_w(\lambda_i). \qquad (5)$$

L_{wc} and L_w are area-weighted averages of the radiance leaving whitecap-covered and whitecap-free areas of the surface, respectively. In this equation, T and t are the direct and diffuse, transmittance of the atmosphere, respectively. The diffuse transmittance is appropriate for the water-leaving radiance and the whitecap radiance as they have near-uniform angular distribution. It is discussed in detail in Section 3.1.1.5. In contrast, to the diffuse transmittance, the direct transmittance is appropriate when the angular distribution of the radiance is approximately a Dirac delta function. As the sun glitter is highly directional (except at high wind speeds), its transmittance is approximated by the direct transmittance. The direct transmittance is given by

$$T(\theta_v, \lambda) = \exp\left[-\Big(\tau_r(\lambda) + \tau_{Oz}(\lambda) + \tau_a(\lambda)\Big)\left(\frac{1}{\mu_v}\right)\right],$$

where $\mu_v = \cos\theta_v$, θ_v is the angle the exiting radiance makes with the upward normal at the TOA, and τ_r, τ_a, and τ_{Oz} are, respectively, the Rayleigh, aerosol, and Ozone optical thicknesses. In this equation, we have ignored the possibility of weak continuum (in the atmospheric windows) absorption by water vapor [*Eldridge*, 1967; *Tomasi*, 1979a; *Tomasi*, 1979b] due to the extreme difficulty in separating the direct effect of water vapor absorption from the indirect effect that water vapor will have on the extinction of hygroscopic aerosols [*Fraser*, 1975]. Converting to reflectance, Eq. (5) becomes

$$\rho_t(\lambda_i) = \rho_{path}(\lambda_i) + T(\lambda_i)\rho_g(\lambda_i) + t(\lambda_i)\rho_{wc}(\lambda_i) + t(\lambda_i)\rho_w(\lambda_i). \tag{6}$$

Thus, from the measured $\rho_t(\lambda_i)$ we require an algorithm that provides accurate estimates of $\rho_{path}(\lambda_i)$, $T(\lambda_i)\rho_g(\lambda_i)$, $t(\lambda_i)\rho_{wc}(\lambda_i)$, and $t(\lambda_i)$. Near the sun's glitter pattern $T(\lambda_i)\rho_g(\lambda_i)$ is so large that the imagery is virtually useless and must be discarded. A sun glitter mask to remove seriously contaminated pixels is described in Section 3.1.1.7. Away from the glitter pattern, i.e., where values of $T(\lambda_i)\rho_g(\lambda_i)$ become negligibly small, the largest of the remaining terms, and most difficult to estimate, is $\rho_{path}(\lambda_i)$. This difficulty is principally due to the aerosol by virtue of its highly variable concentration and optical properties. Thus, we concentrate on this term first, then consider the rest, and the ancillary data required to operate the algorithm.

In general, ρ_{path} can be decomposed into several components:

$$\rho_{path} = \rho_r(\lambda) + \rho_a(\lambda) + \rho_{ra}(\lambda) \tag{7}$$

where ρ_r is the reflectance resulting from multiple scattering by air molecules (Rayleigh scattering) in the absence of aerosols, ρ_a is the reflectance resulting from multiple scattering by aerosols in the absence of the air, and ρ_{ra} is the interaction term between molecular and aerosol scattering [*Antoine and Morel*, 1998; *Deschamps, Herman and Tanre*, 1983]. The term ρ_{ra} accounts for the interaction between Rayleigh and aerosol scattering, e.g., photons first scattered by the air then scattered by aerosols, or photons first scattered by aerosols then air, etc. This term is zero in the single scattering case, in which photons are only scattered once, and it can be ignored as long as the amount of multiple scattering is small, i.e., at small Rayleigh and aerosol optical thicknesses. We note that given the surface atmospheric pressure (to determine the value of τ_r) and the surface wind speed (to define the roughness of the sea surface), ρ_r can be computed accurately, even accounting for polarization by scattering [*Gordon, Brown and Evans*, 1988; *Gordon and Wang*, 1992b].

In modeling the propagation of radiance in the ocean-atmosphere system, we assume that the atmosphere can be considered to be a vertically stratified, plane parallel medium. The medium is described by providing the extinction coefficient, $c(h)$, as a function of altitude h, the scattering phase function for scattering of radiance from direction $\hat{\xi}'$ to direction $\hat{\xi}$, $P(h;\hat{\xi}' \to \hat{\xi})$, and the single scattering albedo $\omega_0(h)$. Replacing h by the optical depth τ defined as

$$\tau(h) = \int_h^\infty c(h)\,dh,$$

the propagation of radiance in such a medium in the scalar approximation (the polarization state of the radiance, and the change in polarization induced by the scattering process is ignored) is governed by the radiative transfer equation (RTE):

$$\hat{\xi} \bullet \hat{n} \frac{dL(\tau,\hat{\xi})}{d\tau} = -L(\tau,\hat{\xi}) + \frac{\omega_0(\tau)}{4\pi} \int_{\text{all }\hat{\xi}'} P(\tau;\hat{\xi}' \to \hat{\xi}) L(\tau,\hat{\xi}')\, d\Omega(\hat{\xi}'),$$

where $d\Omega(\hat{\xi}')$ is the differential of solid angle around the direction $\hat{\xi}'$, and $\hat{n}$ is a unit vector in the nadir direction (normal to the sea surface pointed down). Analytical solutions to the RTE are possible only in the simplest case, e.g., $\omega_0 = 0$, so normally one must be satisfied with numerical solutions.

In principal this equation must be solved for the coupled ocean-atmosphere system; however, because of the very low albedo of the ocean (Table 1) it is not necessary to consider the coupling [*Gordon*, 1976], i.e., we can ignore processes such as photons being backscattered out of the water and then scattered back into the water and backscattered out again, etc. The water-leaving radiance simply propagates to the sensor (i.e., ρ_{path} is independent of ρ_w in Eq. (6)) and the ocean and atmosphere decouple, hence, we need only understand the solution of the atmospheric part of the problem, i.e., an atmosphere bounded by a Fresnel-reflecting ocean surface.

As the goal of atmospheric correction is to retrieve $\rho_w(443)$ with an uncertainty less than ± 0.002, i.e., $\sim \pm 0.6\%$ of $\rho_t(443)$ (Table 1), for the development and testing of the algorithm we require solutions of the RTE that yield ρ_t with an uncertainty $\ll 0.6\%$. For the bulk of the work described here, ρ_t was generated using the successive-order-of-scattering method [*van de Hulst*, 1980]. To understand the accuracy of this code, a second code was developed employing Monte Carlo methods. Typically, the values of ρ_t produced by the two codes differ by less than 0.05%. Thus, either code meets the accuracy required for this work.

We will assume, as justified earlier, that $\rho_w = 0$ in the NIR (but, see Section 3.1.1.9). The problem we are required to solve can then be stated in a simple manner: given the satellite measurement of the radiance (reflectance) of the ocean-atmosphere system in the NIR, predict the radiance (reflectance) that would be observed in the visible. The difference between the predicted and the measured radiance (reflectance) of the ocean-atmosphere system is the water-leaving radiance (reflectance) transmitted to the top of the atmosphere.

3.1.1.1 The Single Scattering Approximation

It is useful to consider $\rho_{path}(\lambda_i)$ in the the limit that the optical thickness of the atmosphere is $\ll 1$. We refer to this as the single-scattering limit. Formulas for the reflectances in this limit are referred to as the single-scattering approximation. The CZCS algorithm was based on the single-scattering approximation. In this approximation the path reflectance reduces to

$$\rho_{path}(\lambda_i) = \rho_r(\lambda_i) + \rho_{as}(\lambda_i), \tag{8}$$

with the aerosol contribution ρ_{as} provided by

$$\rho_{as}(\lambda) = \omega_a(\lambda)\tau_a(\lambda)p_a(\theta_v,\phi_v;\theta_0,\phi_0;\lambda)/4\cos\theta_v\cos\theta_0, \tag{9}$$

$$p_a(\theta_v,\phi_v;\theta_0,\phi_0;\lambda) = P_a(\Theta_-,\lambda) + \Big(r(\theta_v) + r(\theta_0)\Big)P_a(\Theta_+,\lambda),$$

$$\cos\Theta_\pm = \pm\cos\theta_0\cos\theta_v - \sin\theta_0\sin\theta_v\cos(\phi_v - \phi_0),$$

where $P_a(\Theta,\lambda)$ is the aerosol scattering phase function for a scattering angle Θ, ω_a is the aerosol single scattering albedo, and $r(\alpha)$ is the Fresnel reflectance of the interface for an incident angle α. The angles θ_0 and ϕ_0 are, respectively, the zenith and azimuth angles of a vector from the point on the sea surface under examination (pixel) to the sun, and likewise, θ_v and ϕ_v are the zenith and azimuth angles of a vector from the pixel to the sensor. These are measured with respect to the *upward* normal so θ_v and θ_0 are both less than 90° in these equations. In what follows usually (but not always) we take the orientation of the coordinate system so that $\phi_0 = 0$.

Following the approach described above, we assume we are given the the path reflectance at two bands in the NIR at λ_s and λ_l, where the subscript "s" stands for short and "l" for long, e.g., for MODIS $\lambda_s = 748$ nm and $\lambda_l = 869$ nm. [Note that since we are ignoring sun glitter

$T(\lambda_i)\rho_g(\lambda_i)$, this implies that $t(\lambda_i)\rho_{wc}(\lambda_i)$ has also been provided.] Given estimates of the surface atmospheric pressure and the wind speed (ancillary data), $\rho_r(\lambda)$ can be computed precisely and therefore $\rho_{as}(\lambda_s)$ and $\rho_{as}(\lambda_l)$ can be determined from the associated measurements of ρ_{path} at λ_s and λ_l. This allows estimation of the parameter $\varepsilon(\lambda_s, \lambda_l)$:

$$\varepsilon(\lambda_s, \lambda_l) \equiv \frac{\rho_{as}(\lambda_s)}{\rho_{as}(\lambda_l)} = \frac{\omega_a(\lambda_s)\tau_a(\lambda_s)p_a(\theta_v, \phi_v; \theta_0, \phi_0; \lambda_s)}{\omega_a(\lambda_l)\tau_a(\lambda_l)p_a(\theta_v, \phi_v; \theta_0, \phi_0; \lambda_l)}. \tag{10}$$

If we can compute the value of $\varepsilon(\lambda_i, \lambda_l)$ for the MODIS band at λ_i from the value of $\varepsilon(\lambda_s, \lambda_l)$, this will yield $\rho_{as}(\lambda_i)$, which, when combined with $\rho_r(\lambda_i)$, provides the desired $\rho_{path}(\lambda_i)$. Clearly, the key to this procedure is the estimation of $\varepsilon(\lambda_i, \lambda_l)$ from $\varepsilon(\lambda_s, \lambda_l)$.[1]

3.1.1.1.1 The CZCS Algorithm

The atmospheric correction algorithm for CZCS was described in detail in *Evans and Gordon* [1994]. Briefly, the basic CZCS algorithm [*Gordon*, 1978; *Gordon and Clark*, 1980] was based on single scattering; however, $\rho_r(\lambda_i)$ was computed accurately, including the effects of multiple scattering and polarization [*Gordon, Brown and Evans*, 1988]. As there were no NIR bands, the algorithm could not be operated as described in Section 3.1.1.1. However, Table 1 shows that $\rho_w(670)$ can generally be taken to be zero (at least if the pigment concentration is low enough). Thus, the single scattering algorithm was typically operated with $\lambda_l = 670$ nm and $\rho_w(\lambda_l) = 0$. Unfortunately, there was no shorter wavelength (λ_s) for which $\rho_w = 0$, so in the processing of the CZCS global data set [*Feldman et al.*, 1989] $\varepsilon(\lambda_i, \lambda_s)$ was set equal to unity. This is characteristic of a maritime aerosol at high relative humidity.

For sufficiently low C values, Figure 1 (right panel) suggests that $[\rho_w(550)]_N$ is approximately constant. This fact can be used to estimate $\varepsilon(550, 670)$ for such "clear water" regions [*Gordon and Clark*, 1981] in a scene, allowing a basis for extrapolation to 520 and 443 nm. If the resulting $\varepsilon(\lambda_i, \lambda_l)$ is then assumed to be valid for the entire image, retrieval of $[\rho_w(\lambda_i)]_N$ and C can be effected for the image. This is the procedure used by *Gordon et al.* [1983] in the Middle Atlantic Bight. Figure 3 provides an example of atmospheric correction in this region. Note that the intense

[1] It is important to note that p_a in the definition of $\varepsilon(\lambda_s, \lambda_l)$ is *not* $P_a(\Theta)$ as has implicitly assumed by some authors, i.e., it involves both forward $P_a(\Theta_+)$ and backward $P_a(\Theta_-)$ scattering. Since $P_a(\Theta)$ is strongly peaked in near-forward directions (e.g., see Figure 10), the surface-reflected term $P_a(\Theta_+)$ makes a significant contribution to $\rho_{as}(\lambda)$, i.e., as much as 30% in some geometries.

haze layer seen in $L_t(443)$ is absent from $L_w(443)$, revealing the rich underlying horizontal structure in water-leaving reflectance. Unfortunately, there are serious difficulties applying this procedure

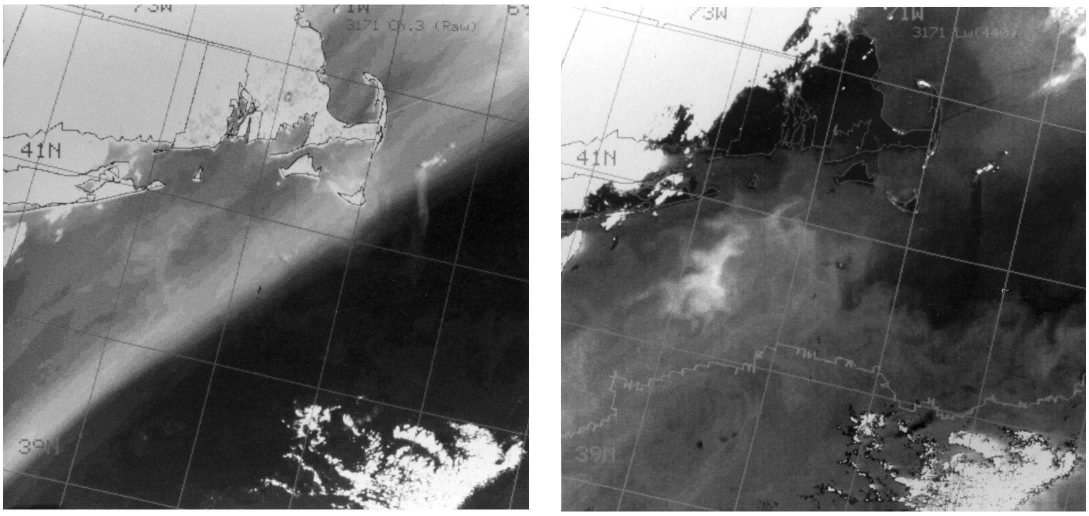

Figure 3. $L_t(443)$ (left panel) and $L_w(443)$ (right panel) for CZCS image from Orbit 3171 over the Middle Atlantic Bight. The correction was based on the method described in the text with a warm core ring located between the cloud and the lower right corner of the image used as the "clear water" area for determining $\varepsilon(550, 670)$.

routinely. For example, the image of interest may contain no "clear water," the ε's may vary over the image because of variations in aerosol type, and the pigment concentration may not be small enough to take $\rho_w = 0$ at 670 nm. Morel and his co-workers have developed a promising approach for dealing these problems in Case 1 waters [*André and Morel*, 1991; *Bricaud and Morel*, 1987] based on the ideas of *Smith and Wilson* [1981]. This involves utilizing a modeled relationship between C and $[\rho_w(\lambda_i)]_N$. Fortunately, for the sensors of concern in this document (SeaWiFS and MODIS), these problems are (usually) circumvented by virtue of the additional spectral bands with $\lambda > 700$ nm. However, the heart of the Morel approach – modeling *both* the reflectance of the water and the aerosols – forms the basis of algorithms for use in the presence of strongly absorbing aerosols or Case 2 waters [*Chomko and Gordon*, 1998; *Gordon, Du and Zhang*, 1997b].

3.1.1.1.2 Application to MODIS

As the key to application of the single scattering algorithm to the EOS era sensors is the extrapolation from $\varepsilon(\lambda_s, \lambda_l)$ to $\varepsilon(\lambda_i, \lambda_l)$, which involves more than a factor of two in wavelength, it is important to try to gain some insight into the possible spectral behavior of $\varepsilon(\lambda_i, \lambda_l)$. This has been attempted by *Gordon and Wang* [1994a] by computing $\varepsilon(\lambda_i, \lambda_l)$ for several aerosol models. Briefly, they used aerosol models that were developed by *Shettle and Fenn* [1979] for LOWTRAN-6 [*Kenizys et al.*, 1983]. These models consist of particles distributed in size according to combinations of log-normal distributions. The size frequency distribution $n(D)$ is given by

$$n(D) = \sum_{i=1}^{2} n_i(D),$$

with

$$n_i(D) = \frac{dN_i(D)}{dD} = \frac{N_i}{\log_e(10)\sqrt{2\pi}\sigma_i D} \exp\left[-\frac{1}{2}\left(\frac{\log_{10}(D/D_i)}{\sigma_i}\right)^2\right],$$

where, $dN_i(D)$ is the number of particles per unit volume between D and $D + dD$, D_i and σ_i are the median diameter and the standard deviation, respectively, and N_i is the total number density of the i^{th} component. Since hygroscopic particles swell with increasing relative humidity (RH), D_i and σ_i are functions of RH. The smaller size fraction is a mixture of 70% water soluble and 30% dust-like particles called the Tropospheric aerosol. It has been used to represent the aerosols within the free troposphere above the boundary-layer [*Shettle and Fenn*, 1979]. The refractive index m for this component at 555 nm ranges from $1.53 - 0.0066i$ at RH $= 0$, to $1.369 - 0.0012i$ at RH $= 98\%$. Thus, as the particles absorb more water, the real part of their refractive index approaches that of water and the imaginary part (proportional to the absorption coefficient) decreases. Because of the moderate imaginary part of the refractive index, these particles have weak absorption and ω_a ranges from 0.959 to 0.989 for $0 \le \text{RH} \le 98\%$ at 555 nm. The modal diameter of this component is always < 0.1 μm. The larger fraction is a sea salt-based component, the "Oceanic" aerosol. Its modal diameter varies from about 0.3 to 1.2 μm as RH varies from 0 to 98%. Its index of refraction is essentially real (imaginary part $\sim 10^{-8}$), so $\omega_a = 1$. Like the tropospheric aerosol its real part ranges from 1.5 at RH $= 0$ to 1.35 at RH $= 98\%$.

From these components, three basic models were constructed: the Tropospheric model with no Oceanic contribution; the Maritime model for which 99% of the particles have the Tropospheric characteristics and 1% the Oceanic; and the Coastal model for which 99.5% of the particles have the Tropospheric characteristics and 0.5% the Oceanic. *Gordon and Wang* [1994a] introduced the Coastal aerosol model to represent the aerosol over the oceans nearer the coast (less Oceanic contribution). The properties of all three aerosol models depend on the wavelength and relative humidity. With the values of D_i, σ_i, and $m_i(\lambda)$ taken from *Shettle and Fenn* [1979], Mie theory was used to calculate the optical properties for all three models for the SeaWiFS and MODIS spectral bands at different relative humidities.

Sample results for $\varepsilon(\lambda_i, \lambda_l)$, where λ_l is taken to be 865 nm (SeaWiFS), are presented in Figure 4 (left panel). These computations suggest that there should be a strong variation of ε with aerosol model and RH. The increase in particle size (due to swelling) with increasing RH clearly reduces the spectral variation of ε. The spectral variation of ε is due in large part to the spectral variation

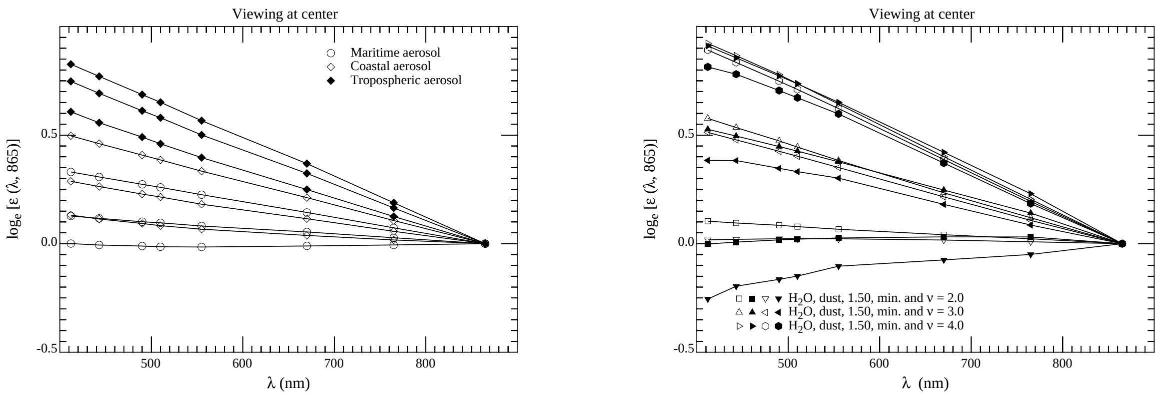

Figure 4. $\varepsilon(\lambda, 865)$ for nadir viewing with $\theta_0 = 60°$. Left panel: Maritime, Coastal, and Tropospheric aerosol models (the RH values are 50, 80, and 98% from the upper to the lower curves). Right panel: Haze C models (the open symbols are for models with little or no absorption, while the filled symbols are for absorbing models).

of the aerosol optical thickness, τ_a; however, additional variation is produced by the aerosol phase function. Note that Figure 4 is plotted in a format that would yield a straight line under the hypothesis that $\varepsilon(\lambda_i, \lambda_l) = \exp\bigl[c(\lambda_l - \lambda_i)\bigr]$, where c is a constant. This shows that over the range 412–865 nm $\varepsilon(\lambda_i, \lambda_l)$ can be considered to be an exponential function of $\lambda_l - \lambda_i$, for the *Shettle and Fenn* [1979] models. *Wang and Gordon* [1994b] have used this fact to extend the CZCS algorithm for use with SeaWiFS and MODIS.

We now examine the accuracy of this CZCS-type single-scattering algorithm based on an assumed exponential spectral variation of $\varepsilon(\lambda_i, \lambda_l)$. For this purpose, we simulated atmospheres using an array of aerosol models. First, the aerosol optical properties were taken from the Tropospheric, Coastal, and Maritime models at RH = 80%, denoted, respectively, as T80, C80, and M80. Then, we simulated the aerosol using the *Shettle and Fenn* [1979] Urban model at RH = 80% (U80). This model shows strong absorption. In addition to the water soluble and dust-like particles of the Tropospheric model, the Urban model contains soot-like particles (combustion products). Also, the Urban model has a second, larger particle, mode in addition to that of the Tropospheric model. At 865 nm the Mie theory computations yielded, $\omega_a = 0.9934$, 0.9884, and 0.9528, respectively, for the Maritime, Coastal, and Tropospheric models (RH = 80%), while in contrast, $\omega_a = 0.7481$ for the Urban model. Here, the Urban model is intended to represent aerosols that might be present over the oceans near areas with considerable urban pollution, e.g., the Middle Atlantic Bight off the U.S. East Coast in summer. Finally, we examined aerosols with a different analytical form for the size distribution [*Junge*, 1958]:

$$\begin{aligned} n(D) = \frac{dN(D)}{dD} &= K, && D_0 < D < D_1, \\ &= K\left(\frac{D_1}{D}\right)^{\nu+1}, && D_1 < D < D_2, \\ &= 0, && D > D_2, \end{aligned} \tag{11}$$

with $D_0 = 0.06$ μm, $D_1 = 0.20$ μm, and $D_2 = 20$ μm. Following *Deirmendjian* [1969] we call these Haze C models. Twelve separate Haze C models were considered: $\nu = 2$, 3, and 4, with the refractive index of the particles taken to be that of liquid water (from *Hale and Querry* [1973]), close to that of the dust component in the Tropospheric model ($1.53 - 0.008i$), nonabsorbing crystals ($1.50 - 0i$), and absorbing minerals that might be expected from desert aerosols transported over the oceans [*d'Almeida, Koepke and Shettle*, 1991]. The spectral behavior of $\varepsilon(\lambda, 865)$ for these models is presented in Figure 4 (right panel). We see that the absorption-free (open symbols) Haze C models display a behavior similar to the Shettle and Fenn models; however, for models with strong absorption (solid symbols) departures are seen, especially for the mineral models for which the imaginary part of the refractive index increases with decreasing λ. An important observation from Figure 4 (right panel) is that, in general, $\varepsilon(765, 865)$ cannot be utilized to discriminate between weakly- and strongly-absorbing aerosols with similar size distributions.

Using these aerosol models we generated hypothetical atmospheres with a two-layer structure: the aerosols occupying the lower layer, and all molecular scattering confined to the upper layer. This distribution of aerosols is similar to that typically found over the oceans when the aerosol is locally generated, i.e., most of the aerosol is confined to the marine boundary layer [*Sasano and Browell*, 1989]. The atmosphere was bounded by a flat (smooth) Fresnel-reflecting sea surface, and all photons that penetrated the interface were assumed to be absorbed in the ocean. The RTE in the scalar approximation was solved for this hypothetical atmosphere using the successive-order-of-

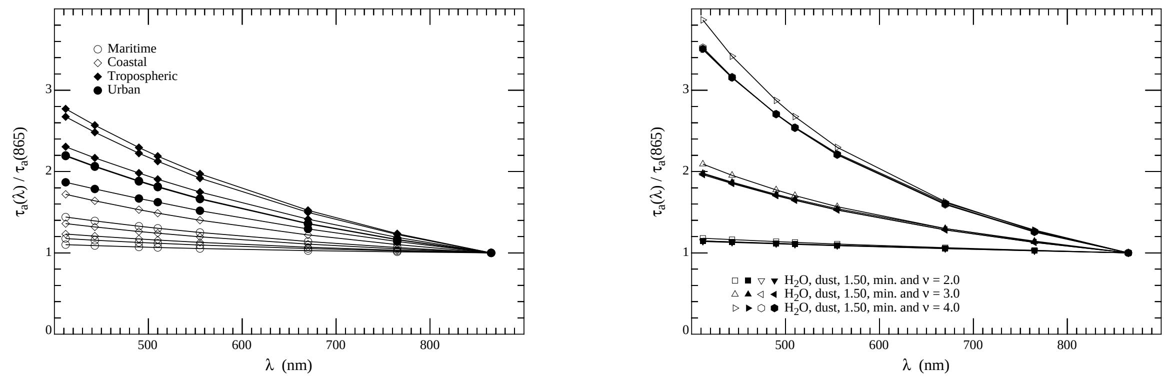

Figure 5. Spectral variation of τ_a. Left panel: Maritime, Coastal, and Tropospheric aerosol models (the RH values are 50, 80, and 98% from the upper to the lower curves). Right panel: Haze C models (the open symbols are for models with little or no absorption, while the filled symbols are for absorbing models).

scattering method [*van de Hulst*, 1980] to provide pseudo TOA reflectance (ρ_t) data. All significant orders of multiple scattering were included. As the surface was assumed to be smooth (no wind), the sun glitter and whitecap terms in Eq. (6) are absent. The simulations of ρ_t were carried out for the following geometries: $\theta_0 = 20°$, $40°$, and $60°$, with $\theta_v \approx 1°$ and $\phi_v - \phi_0 = 90°$, i.e., viewing near the MODIS scan center; and $\theta_0 = 0°$, $20°$, $40°$, and $60°$, with $\theta_v \approx 45°$ and $\phi_v - \phi_0 = 90°$, i.e., viewing near the scan edge. In this manner a wide range of sun-viewing geometries were included. Four wavelengths were considered: $\lambda_i = 443$, 555, 765, and 865 nm. The values used for the aerosol optical thickness at 865 nm, $\tau_a(865)$, were 0.1, 0.2, 0.3, and 0.4. The values of $\tau_a(\lambda_i)$

at the other wavelengths were determined from the spectral variation of the extinction coefficient for each particular model. These are provided in Figure 5. The Haze C models clearly show that the spectral variation of τ_a is principally determined by the size distribution, with the index of refraction playing only a minor role. Equation (10) suggests that there should be a relationship between $\tau_a(\lambda)/\tau_a(865)$ and $\varepsilon(\lambda, 865)$. Figure 6 provides an example of this for $\theta_0 = 60°$ and nadir viewing, i.e., the same geometry as in Figure 4, with $\varepsilon(765, 865)$ used rather than $\varepsilon(\lambda, 865)$. Thus, for a given $\tau_a(865)$, $\tau_a(443)$ will generally increase with increasing $\varepsilon(765, 865)$. This will be useful in interpreting the results described below.

As the true $\rho_w(\lambda_i)$ was taken to be zero in the pseudo data (all photons entering the water were absorbed), the error in atmospheric correction, i.e., the error in the retrieved water-leaving

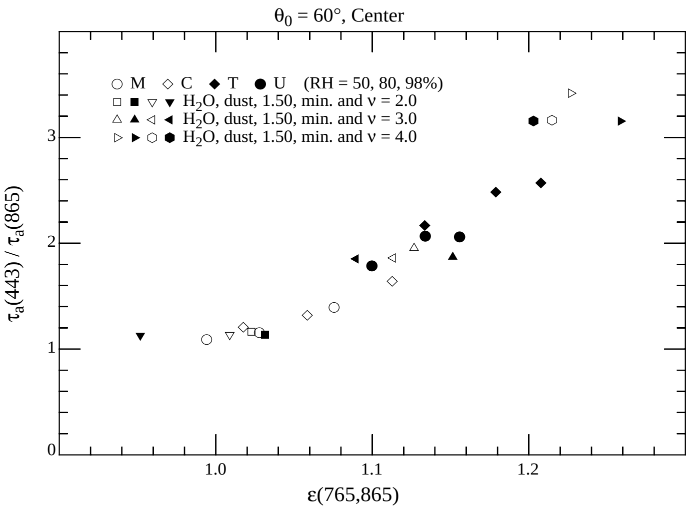

Figure 6. Relationship between $\varepsilon(765, 865)$ and $\tau_a(443)/\tau_a(865)$ for the various aerosol models with $\theta_0 = 60°$ and nadir viewing.

reflectance, $\Delta(t\rho_w)$, is just the error in the predicted path radiance. This is

$$\Delta\big(t\rho_w(\lambda_i)\big) = \rho_t(\lambda_i) - \rho_{path}(\lambda_i) = \rho_t(\lambda_i) - \rho_r(\lambda_i) - \varepsilon^{(e)}(\lambda_i, \lambda_l)\rho_{as}(\lambda_l), \tag{12}$$

where $\varepsilon^{(e)}(\lambda_i, \lambda_l)$ is the estimated value of $\varepsilon(\lambda_i, \lambda_l)$ assuming an exponential variation with λ_i:

$$\varepsilon^{(e)}(\lambda_i, \lambda_l) \equiv \exp[c(\lambda_l - \lambda_i)] = \exp\left[\left(\frac{\lambda_l - \lambda_i}{\lambda_l - \lambda_s}\right)\log_e\left(\frac{\rho_{as}(\lambda_s)}{\rho_{as}(\lambda_l)}\right)\right].$$

$\rho_r(\lambda_i)$ was computed using the same radiative transfer code, i.e., it includes all effects of multiple scattering, but not polarization. In an actual application, $\rho_r(\lambda_i)$ would be computed using a code that included polarization as well [*Gordon, Brown and Evans*, 1988]. Figure 7 provides the error in the retrieved normalized water-leaving reflectance, $\Delta[\rho_w(443)]_N$, for the seven sun-viewing geometries and for $\tau_a(865) = 0.1$ and 0.2. To derive $\Delta[\rho_w]_N$ from $\Delta t\rho_w$, the approximation for t similar to that used in processing CZCS imagery was utilized (See Section 3.1.1.5). The x-axis in Figure 7, $\varepsilon^{(e)}(765, 865)$, is the *estimated* value for the indicated model and geometry.

In the absence of aerosol absorption (open symbols), the performance of this simple algorithm is truly remarkable, as Figures 5 (right panel) and 6 show that for $\nu = 4$, $\tau_a(443) \approx 0.35$ and 0.70 for Figure 7 (top panels), respectively. The large negative errors for $\nu = 4$ occur at the scan edge with $\theta_0 = 60°$, i.e., the geometry with the most multiple scattering. For $\nu = 3$ ($\tau_a(443) \sim 0.2$ and 0.4 (Figures 5 and 6 for Figure 7 (top panels), respectively), the retrieved value of $[\rho_w(443)]_N$ is usually within the acceptable limits.

In the case of absorbing aerosols, the errors are seen to be mostly negative, and to grow rapidly with $\tau_a(443)$. Negative errors are particularly troublesome as they can lead to negative values in the retrieved $[\rho_w(443)]_N$ when the pigment concentration $\gtrsim 0.5 - 1.0$ mg/m^3. The source of the error for absorbing aerosols is twofold. For the Haze C aerosol, it can be seen from Figure 4 (right panel) that, in contrast to the nonabsorbing aerosols, an exponential extrapolation of $\varepsilon(765, 865)$ to $\varepsilon(443, 865)$ would lead to an erroneous overestimation of $\varepsilon(443, 865)$, the single exception being the mineral aerosol with $\nu = 2$. This will cause an overestimation of the aerosol contribution at 443 nm, which in turn will result in a negative error in $[\rho_w(443)]_N$. In contrast, the extrapolation does work well for T80 (Figure 4, left panel) and, as we shall see later, in this case the error is principally due to multiple scattering, which is strongly influenced by even weak aerosol absorption.

The error in $[\rho_w(550)]_N$ as related to the associated error in $[\rho_w(443)]_N$ is provided in Figure 7 (lower panels). The observed improvement in atmospheric correction at 550 compared to 443 nm can be traced to the facts that (1) the ε determination requires a smaller extrapolation at 550

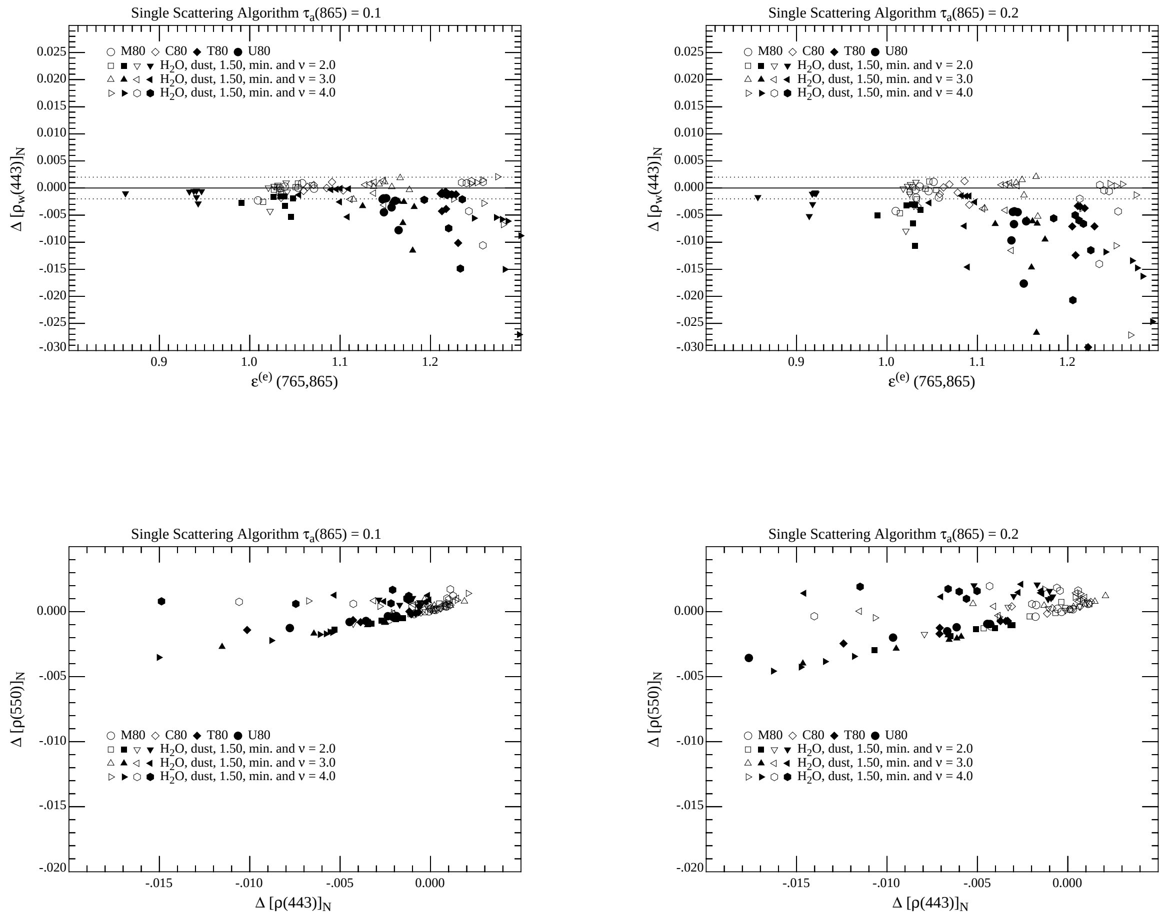

Figure 7. $\Delta[\rho_w(443)]_N$ as a function of $\varepsilon^{(e)}(765, 865)$ and $\tau_a(865)$ (top) and $\Delta[\rho_w(550)]_N$ as a function of $\Delta[\rho_w(443)]_N$ (bottom) for all of the aerosol models and viewing geometries examined in the study. Left panels: $\tau_a(865) = 0.1$. Right panels: $\tau_a(865) = 0.2$.

nm, and (2) there is less multiple scattering at 550 nm as both τ_a (Figure 5) and τ_r are smaller. Notably, the error at 550 nm is usually much less than that at 443 nm, there being a tendency for $\Delta[\rho_w(550)]_N \sim (1/4)\Delta[\rho_w(443)]_N$, although occasionally $|\Delta[\rho_w(550)]_N| \gtrsim |\Delta[\rho_w(443)]_N|$. Thus, in a pigment ratio algorithm such as Eq. (4), the error at 443 nm would usually be the more significant error in the R ratio.

It is useful at this point to review the sparse direct observations of the aerosol optical thickness over the oceans. In the open ocean, far from sources of pollution and/or sources of desert aerosols, the atmosphere is very clear. In the Pacific $\tau_a(550)$ is found in the range 0.04 to 0.24 with a mean of 0.13 and Angstrom exponent of 0.56 [*Villevalde et al.*, 1994], suggesting a mean $\tau_a(865)$ of ~ 0.1 and a maximum of ~ 0.19. Similar results are obtained for the North Atlantic [*Korotaev et al.*, 1993; *Reddy et al.*, 1990]. In such a region, *Lechner et al.* [1989] found that there were low concentrations of aerosol in the free troposphere possessing a Haze C-like distribution with an average ν of ~ 3.5, while in the marine boundary layer the concentration was much higher (and highly variable) with an average ν of ~ 1.8, and sometimes even a bimodal size distribution (the large mode presumably resulting from local generation of aerosols by breaking waves). In contrast, in the region of the Atlantic off West Africa subject to Saharan dust, *Reddy et al.* [1990] found a mean $\tau_a(550)$ of 0.4 with $\tau_a(865) \approx 0.3$, in agreement with the observations of *Korotaev et al.* [1993], $\tau_a(550) \sim 0.3$ to 0.5. In areas subject to urban pollution, even higher optical thicknesses are observed, e.g., *Reddy et al.* [1990] found a mean $\tau_a(550) \approx 0.5$ and $\tau_a(865) \approx 0.3$ in the Western North Atlantic in summer when trajectory analysis suggested the origin of the air mass was the North American continent.

Thus, direct observation suggests that over the open ocean most of the aerosol is in the marine boundary layer and, for mean conditions $\tau_a(865) \approx 0.1$. Furthermore, the size distribution is either similar to Haze C with $\nu \approx 2.5$ or bimodal like M80 or C80. Such aerosols would have $\varepsilon(765, 865) < 1.1$ (Figure 6). Figure 7 (top left panel, open symbols) with $\varepsilon(765, 865) < 1.1$ is appropriate to these mean conditions and shows that the single scattering CZCS-type algorithm should be capable of retrieving $[\rho_w(443)]_N$ with the desired accuracy. For the maximum $\tau_a(865)$ (~ 0.19), Figure 7 (top right panel, open symbols) is appropriate and under the same conditions for maximum end of the observed $\tau_a(865)$ range, and for most of the geometries good retrievals are obtained, although in some cases, the error is outside the acceptable range.

For situations with a strong continental influence, e.g., Saharan dust or urban pollution carried over the oceans by the wind, the aerosol is likely to be moderately- to strongly-absorbing. Also, $\tau_a(\lambda)$ will be sufficiently large that aerosol single scattering will no longer be an adequate approximation. Thus, we are forced to consider a full multiple scattering approach.

3.1.1.2 Multiple Scattering Effects

Multiple scattering effects have already been shown [*Deschamps, Herman and Tanre*, 1983; *Gordon, Brown and Evans*, 1988; *Gordon and Castaño*, 1987] to be significant at the level of accuracy required for SeaWiFS and MODIS, i.e., $\Delta[\rho_w(443)]_N \approx 0.001 - 0.002$. Although the single scattering approach is seen to work well only for sufficiently small optical depth (Figure 7) and nonabsorbing aerosols, typically the case over the open ocean, we desire an algorithm that can cope with even extreme situations. To begin the study of the effects of multiple scattering, we examine the properties of the solutions to the RTE used in providing the pseudo data for Figure 7. Since we are ignoring sun glitter and whitecaps for the moment, we can assess the multiple scattering effects by noting that

$$\rho_t - \rho_r - t\rho_w = \rho_a + \rho_{ra} \overset{\text{Single Scattering}}{\longrightarrow} \rho_{as}.$$

Thus, comparison of $\rho_t - \rho_r - t\rho_w$ and ρ_{as} provides a direct assessment of multiple scattering. Figure 8

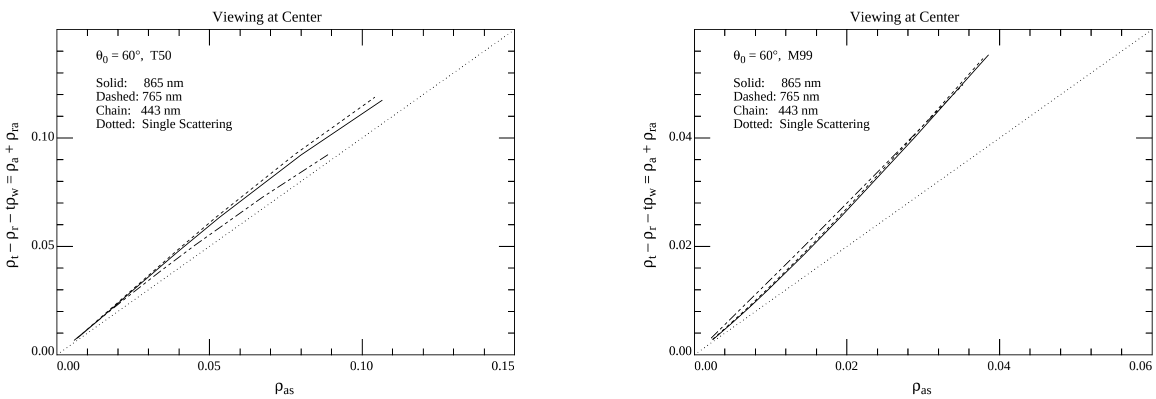

Figure 8. $\rho_a(\lambda) + \rho_{ra}(\lambda)$ as a function of $\rho_{as}(\lambda)$ at $\theta_0 = 60°$ and nadir viewing. Left panel: T80. Right panel: M99.

provides such a comparison for the Tropospheric model with RH = 50% (T50) and the Maritime model with RH = 99% (M99). Note that for the Maritime aerosol for $\rho_{as} \gtrsim 0.01$, the value of $\rho_a + \rho_{ra}$ is about 40% greater than ρ_{as}, i.e., multiple scattering significantly increases the reflectance due to the aerosol. In contrast, for the Tropospheric model at RH = 50% the aerosol reflectance is only increased by $\sim 10\%$. Thus, we see that the influence of multiple scattering depends significantly on the aerosol model. In contrast to the algorithm in Section 3.1.1.1.2, for which multiple scattering was ignored, and for which no knowledge of the aerosol properties was required to effect the atmospheric correction, the model-dependent multiple scattering will make it necessary to utilize aerosol models in the ρ_w retrieval algorithm.

3.1.1.3 The Multiple-Scattering Retrieval Algorithm

From the last section it should be clear that a way must be found to deal with multiple scattering. However, the success of the single-scattering algorithm at low values of τ_a, and the fact that the only *direct* link to the aerosol models is through $\varepsilon(\lambda, \lambda_l)$, or in particular through $\varepsilon(\lambda_s, \lambda_l)$, it seems reasonable to retain the formalism of the single scattering algorithm, but modify it to include multiple scattering. This is the approach taken here. Writing

$$\rho_a(\lambda) + \rho_{ra}(\lambda) = K[\lambda, \rho_{as}(\lambda)]\rho_{as}(\lambda), \tag{13}$$

where the dependence of K on $\rho_{as}(\lambda)$ represents the departure of the $\rho_a(\lambda) + \rho_{ra}(\lambda)$ versus $\rho_{as}(\lambda)$ relationship from linearity, we see that K is nearly the same for the two NIR bands, but can be significantly different at 443 nm (Figure 8, left panel). It is irrelevant whether the dependence of K on λ is explicit ($K = K[\lambda]$) or implicit ($K = K[\rho_{as}(\lambda)]$) or both, the effect is the same: Eq. (12) becomes

$$\Delta\big(t\rho_w(\lambda_i)\big) = \rho_t(\lambda_i) - \rho_r(\lambda_i) - \frac{K[\lambda_i, \rho_{as}(\lambda_i)]}{K[\lambda_l, \rho_{as}(\lambda_l)]}\varepsilon(\lambda_i, \lambda_l)\big[\rho_a(\lambda_l) + \rho_{ra}(\lambda_l)\big],$$

and the $\rho_a(\lambda) + \rho_{ra}(\lambda)$ versus $\rho_{as}(\lambda)$ relationship must be known at each wavelength.

Gordon and Wang [1994a] solved the RTE for a set of N candidate aerosol models to provide what is essentially a set of lookup tables for $K[\lambda, \rho_{as}(\lambda)]$. As in the single scattering algorithm, the NIR bands are used to provide the aerosol model through

$$\varepsilon(\lambda_s, \lambda_l) = \frac{K[\lambda_l, \rho_{as}(\lambda_l)]}{K[\lambda_s, \rho_{as}(\lambda_s)]}\left[\frac{\rho_a(\lambda_s) + \rho_{ra}(\lambda_s)}{\rho_a(\lambda_l) + \rho_{ra}(\lambda_l)}\right];$$

however, since the aerosol model is not known at this point, the K ratio is unknown. Figure 8 suggests that this K ratio for λ_l and λ_s should not deviate significantly from unity, so *Gordon and*

Wang [1994a] proposed computing $\varepsilon(\lambda_s, \lambda_l)$ though

$$\varepsilon(\lambda_s, \lambda_l) = \frac{1}{N} \sum_{j=1}^{N} \varepsilon_j(\lambda_s, \lambda_l),$$

where $\varepsilon_j(\lambda_s, \lambda_l)$ is the value of $\varepsilon(\lambda_s, \lambda_l)$ derived from $\rho_a(\lambda_l) + \rho_{ra}(\lambda_l)$ and $\rho_a(\lambda_s) + \rho_{ra}(\lambda_s)$ by assuming that the K ratio for the j^{th} aerosol model is correct. This procedure works reasonably well because the values of ε_j derived using the individual models are all close to the correct value. The procedure has been further modified by recomputing a new average formed by dropping the two models with the largest values of $\varepsilon(\lambda_s, \lambda_l) - \varepsilon_j(\lambda_s, \lambda_l)$ and the two models with the most negative values. This procedure is carried out several times until the final value is computed using four models: two with $\varepsilon - \varepsilon_j < 0$ and two models with $\varepsilon - \varepsilon_j > 0$.

Having derived a value for $\varepsilon(\lambda_s, \lambda_l)$, the next task is to estimate $\varepsilon(\lambda_i, \lambda_l)$. In general, the derived value of $\varepsilon(\lambda_s, \lambda_l)$ will be bracketed by two of the N candidate aerosol models. We then assume that $\varepsilon(\lambda_i, \lambda_l)$ falls between the same two aerosol models proportionately in the same manner as $\varepsilon(\lambda_s, \lambda_l)$. Finally, we also assume that $K[\lambda_i, \rho_{as}(\lambda_i)]$ falls between the two values for these models in the same proportion as $\varepsilon(\lambda_s, \lambda_l)$. These assumptions are required to proceed, and as we shall see, they are not always valid. However, to the extent that the actual aerosols are similar in their optical properties to the candidate models, the assumptions appear to be reasonably valid.

Initially, twelve candidate aerosol models were used: the Maritime, Coastal, and Tropospheric models with RH = 50, 70, 90, and 99%. Tables of the $\rho_a(\lambda)+\rho_{ra}(\lambda)$ versus $\rho_{as}(\lambda)$ relationship were constructed by solving the RTE for each model for $\theta_0 = 0$ to $80°$ in increments of $2.5°$, and at 33 values of θ_v. The azimuthal dependence of the reflectance was determined through Fourier analysis. Computations were carried out for eight values of $\tau_a(\lambda_i)$ from 0.05 to 0.8. The total number of separate solutions to the RTE used in the preparation of the tables exceeded 33,000 (including the four Urban models used later). To reduce storage, for a given set (θ_0, θ_v) the simulations were fit to

$$\log\bigl[\rho_t(\lambda) - \rho_r(\lambda) - t\rho_w(\lambda)\bigr] = \log\bigl[a(\lambda)\bigr] + b(\lambda)\log\bigl[\rho_{as}(\lambda)\bigr] + c(\lambda)\log^2\bigl[\rho_{as}(\lambda)\bigr] \qquad (14)$$

by least-squares. In the case of the azimuth angle ϕ_v, we expanded $a(\lambda)$, $b(\lambda)$ and $c(\lambda)$ in a Fourier series in ϕ_v and stored only the Fourier coefficients. As the reflectances are even functions of the relative azimuth angle ϕ_v, $a(\lambda)$, $b(\lambda)$, and $c(\lambda)$ will be even functions of ϕ_v. Thus, we can write

$$a(\theta_v,\theta_0,\phi_v,\lambda) = a^{(0)}(\theta_v,\theta_0,\lambda) + 2\sum_{m=1}^{M} a^{(m)}(\theta_v,\theta_0,\lambda)\cos m\phi_v,$$

with

$$a^{(m)}(\theta_v,\theta_0,\lambda) = \frac{1}{\pi}\int_0^{\pi} a(\theta_v,\theta_0,\lambda,\phi_v)\cos m\phi_v \, d\phi_v,$$

etc. Using Fourier analysis with $M = 14$ produced about the same accuracy in the results as interpolating with an increment in ϕ_v of 5° or 10°.[2]

3.1.1.4 Simulated Test of the Multiple-Scattering Algorithm

We have tested this multiple-scattering algorithm by applying it to pseudo data created using the *Shettle and Fenn* [1979] Tropospheric, Coastal, Maritime, and Urban models at RH = 80%, denoted by T80, C80, M80, and U80, respectively. Note that these are *not* part of the candidate aerosol set, although the size and refractive index distributions of T80, C80, and M80 are similar to members of the set. In contrast to the others, and unlike any members of the candidate set, U80 has strong aerosol absorption.

Comparison between the single-scattering and multiple-scattering algorithms for pseudo data created with these models at the seven sun-viewing geometries described earlier is provided in Figure 9 for $\tau_a(865) = 0.2$. Clearly, including multiple scattering in the algorithm significantly improves the retrieval of $[\rho_w(443)]_N$ for the T80, C80, and M80 cases, for which $\tau_a(443) \approx 0.50$, 0.32, and 0.24, respectively (Figures 5, left panel, and 6). In contrast, the U80 retrievals, although somewhat improved over single scattering, are still very poor. Thus, even though the size distribution of the U80 model is similar to the candidates (both in modal diameter and standard deviation), the fact that the particles are strongly absorbing causes as large an error in the retrieval of $[\rho_w(443)]_N$ as neglecting multiple scattering completely. Clearly, particle absorption must have a profound impact on multiple scattering.

[2] Note: when θ_v is near θ_0, $\rho_a + \rho_{ra}$ and ρ_{as} can become very large because of the specular reflection of forward-scattered light from the sea surface. As it would take a very large number of Fourier components to reproduce this "spike" in the reflectances, it is removed before the Fourier analysis. This is of no consequence in the processing, because this is the region of the maximum sun glitter; however, it does considerably reduce the value of M required for a given accuracy.

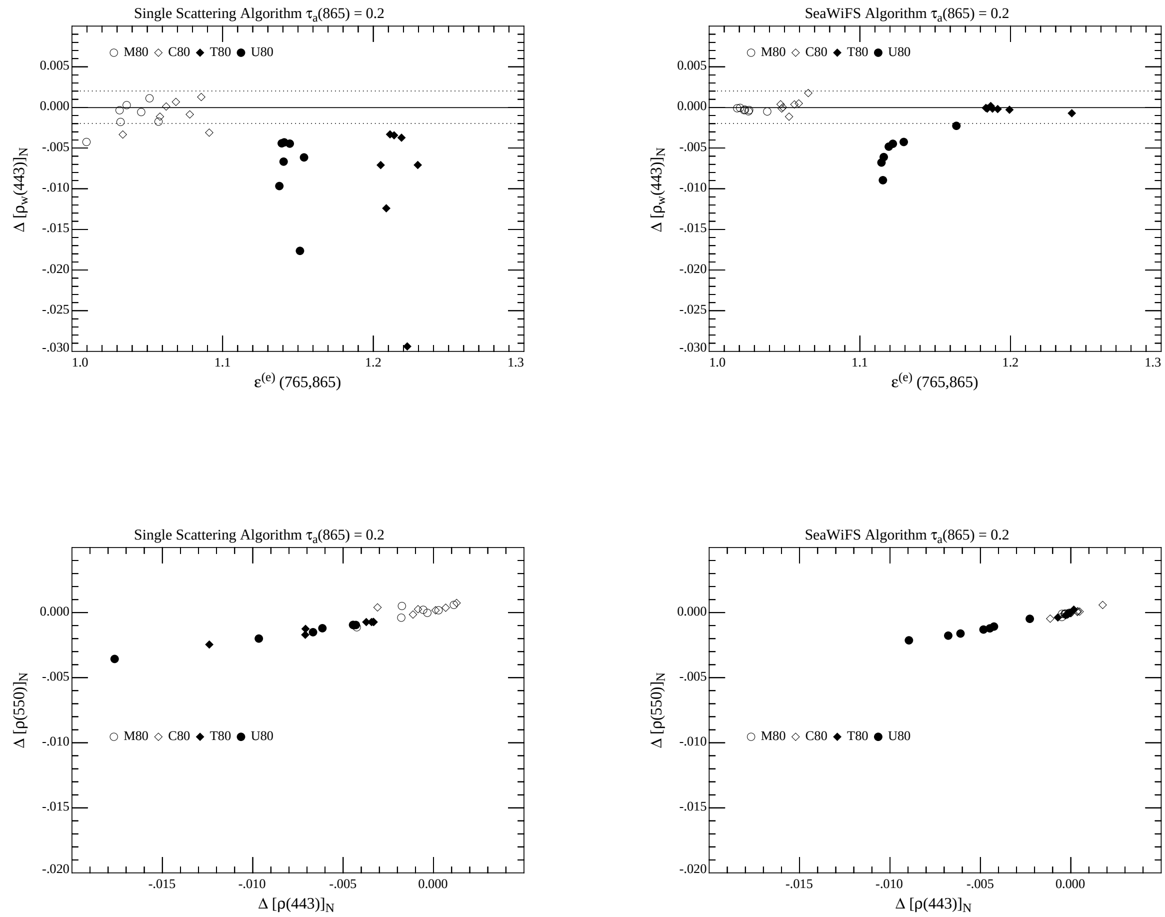

Figure 9. Similar to Figure 7, but compares single and multiple (SeaWiFS) scattering algorithms. Left panels: Single scattering algorithm. Right panels: Multiple scattering algorithm.

As in Figure 7 (bottom panels), Figure 9 (bottom panels) provides the relationship between $[\rho_w(550)]_N$ and $[\rho_w(443)]_N$ for the single-scattering and the multiple-scattering (SeaWiFS) algorithms. For the multiple-scattering algorithm, $\Delta[\rho_w(550)]_N \approx (1/4)\Delta[\rho_w(443)]_N$, and with the exception of very low pigment concentrations, the error in atmospheric correction at 443 nm will contribute more significantly to the error in R [Eq. (4)] than that at 550 nm. Fortuitously, the errors at 443 and 550 nm typically have the same sign and, therefore, tend to cancel in R.

Table 2: Mean value of C obtained for seven viewing geometries and three aerosol models (M80, C80, and T80). The number in parenthesis is the standard deviation divided by the mean (in %).

$\tau_a(865)$	$C_{\text{True}} = 0.10$ mg/m^3	$C_{\text{True}} = 0.47$ mg/m^3	$C_{\text{True}} = 0.91$ mg/m^3
0.1	0.101 (1.6)	0.466 (3.4)	0.912 (9.1)
0.2	0.100 (3.1)	0.470 (4.7)	0.940 (12.8)
0.3	0.098 (5.5)	0.493 (15.3)	0.936 (25.3)

The error in the pigment concentration induced by $\Delta[\rho_w(550)]_N$ and $\Delta[\rho_w(443)]_N$ in the multiple-scattering algorithm is provided in Table 2. To prepare this table, the errors were added to values of $[\rho_w(550)]_N$ and $[\rho_w(443)]_N$ that are characteristic of three pigment concentrations (0.10, 0.47, and 0.91 mg/m^3) in order to produce retrieved reflectances that include the atmospheric correction error. These were then inserted into Eq. (4) and the resulting pigment concentration was derived for each sun-viewing geometry for the M80, C80, and T80 aerosol models. For each true pigment concentration, the twenty-one retrieved values of C (seven geometries times three aerosol models) were averaged and the standard deviation was computed. The computations were carried out for $\tau_a(865) = 0.1$, 0.2, and 0.3.

As expected, the quality of the retrievals is best for the smallest value of $\tau_a(865)$. Excellent retrievals of C (as indicated by excellent mean values and small relative standard deviations) were obtained for $\tau_a(865) = 0.1$ and 0.2, and for the two lower concentrations for $\tau_a(865) = 0.3$. As mentioned earlier, $\tau_a(865)$ is typically $\lesssim 0.2$ in regions not subjected to urban pollution or desert dust. For $\tau_a(865) = 0.3$ and a true value of C of 0.91 mg/m^3, one retrieved value of C was ≈ 9 mg/m^3 ($\theta_0 = 60°$, $\theta_v \approx 45°$, T80, for which $\tau_a(443) \approx 0.75$ and $\tau_a(550) \approx 0.6$). This value was not included in the average or the standard deviation computation. These results suggest that the multiple-scattering algorithm will provide excellent results as long as the candidate aerosol models are similar in size and composition to the aerosol actually present, they need not be *precisely* representative of the actual aerosol.

To try to understand the effect of particle absorption on multiple scattering, a set of multiple scattering computations of $\rho_a + \rho_{ra}$ was carried out in which particle absorption *alone* was varied. Specifically, we used the phase functions for the T50 and M99 aerosol models evaluated at 865 nm (Figure 10). These models have the most weakly (T50) and the most strongly (M99) forward peaked scattering phase function among the candidate models. Simulations of $\rho_a + \rho_{ra}$ as a function of τ_a (or equivalently ρ_{as}) were made for $\theta_0 = 60°$ and $\theta_v \approx 1°$, with $\tau_r = 0.015$ (865 nm) and 0.236 (443 nm), as ω_a assumed the values of 0.6, 0.8, and 1.0. The results are presented in Figure 11. Two facts concerning the $\rho_a + \rho_{ra}$ versus ρ_{as} relationship emerge from these simulations. First, for $\omega_a = 1$, the relationship is nearly linear and, for the sharply peaked M99 phase function, the Rayleigh-aerosol interaction ($\sim$ the difference between the dashed and solid curves caused by changing τ_r) is small, while for the smoother T50 phase function the Rayleigh-aerosol interaction is significantly larger. This is to be expected, since the mid-angle scattering by T50 is much larger than M99 (Figure 10). Second, as ω_a decreases, there are greater departures from linearity and an

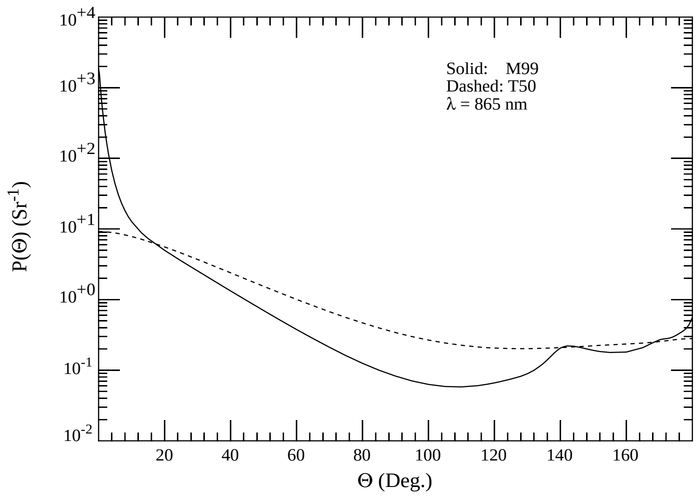

Figure 10. Scattering phase functions for the T50 and M99 aerosol models at 865 nm.

increase in the significance of the Rayleigh-aerosol interaction for *both* T50 and M99. The general shape of the curves is explained by the fact that $\rho_a + \rho_{ra}$ must approach an asymptotic value as $\tau_a \to \infty$. Also, increasing τ_r causes more diffuse light to enter the aerosol layer and traverse longer paths through it, with the concomitant greater chance of absorption. This explains the strong influence of ω_a on ρ_{ra}.

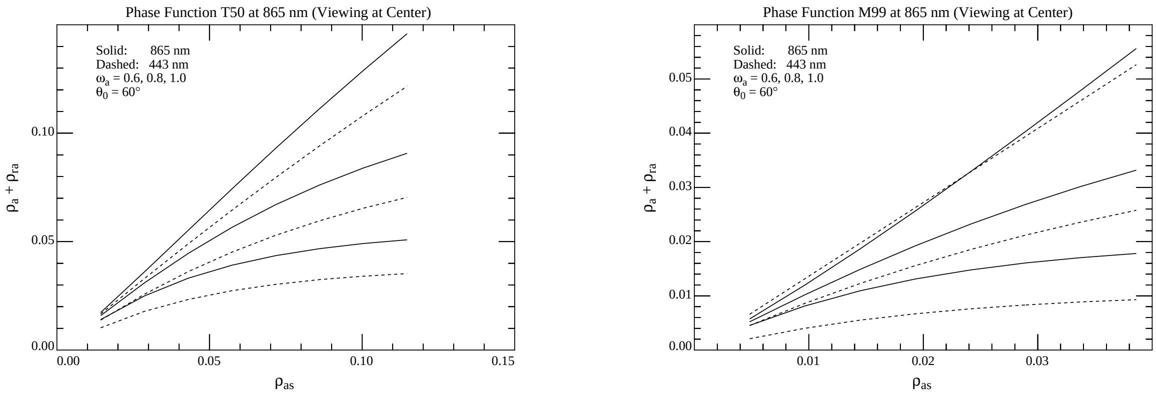

Figure 11. $\rho_a + \rho_{ra}$ as a function of ρ_{as} and ω_a for 443 nm (dashed) and 865 nm (solid) Curves from bottom to top correspond to $\omega_a = 0.6$, 0.8, and 1.0. Left panel: T80. Right panel: M99.

The impact of the absorption in Figure 11 is serious. Consider a hypothetical situation in which the M99 phase function is appropriate and $\epsilon(\lambda_i, \lambda_l) = 1$, so $\rho_{as}(\lambda_i) = \rho_{as}(\lambda_l)$. Also, assume that $\epsilon(\lambda_i, \lambda_l)$ is correctly determined by the algorithm and that $\rho_a + \rho_{ra} \approx 0.02$ at 865 nm. Then, if $\omega_a = 1$ were used for estimating $\rho_a + \rho_{ra}$ at 443 nm, but the true value of ω_a was actually 0.8, Figure 11(right panel) shows that the error in $\rho_a + \rho_{ra}$ at 443 nm would be ~ -0.004. In contrast, if the $\omega_a = 1$ assumption was correct the error would be $\sim +0.001$. Clearly, the effect of absorption is to produce large negative errors in $t\rho_w$, i.e., to overestimate the effect of the atmosphere. Figure 4 (left panel) suggests that when $\epsilon(\lambda_i, \lambda_l)$ is estimated from $\epsilon(\lambda_s, \lambda_l)$ using weakly- or nonabsorbing aerosol models, it will be overestimated, i.e., $\epsilon(\lambda_i, \lambda_l)$ will be too large, if the aerosol strongly absorbs. This effect will cause a further overestimation of the atmospheric effect.

As the twelve candidate models in Section 3.1.1.3 are combinations of two components with physical properties dependent on RH, they represent a fixed set of values of ω_a at each wavelength, i.e., there are only twelve different values of ω_a. At 865 nm, these range from 0.99857 (M99) to 0.92951 (T50). Furthermore, each model possesses a unique value of $\varepsilon(\lambda_s, \lambda_l)$ and a more or less unique value of $\varepsilon(\lambda_i, \lambda_l)$ for a given sun-viewing geometry (Figure 4, left panel). Thus, the choice of the twelve candidates forces a definite relationship between ω_a and $\varepsilon(\lambda_i, \lambda_l)$. In the case of the twelve models chosen here, there is a steady decrease in ω_a with increasing $\varepsilon(\lambda_i, \lambda_l)$. If this relationship is more or less correct, an excellent correction is effected (Figure 9 (top right panel), T80); however, with its low value of ω_a (0.74806 for U80 at 865 nm) the Urban model falls considerably outside this relationship and the resulting atmospheric correction is very poor (U80 in Figure 9, top right). This is further shown in Figure 12 in which the multiple-scattering

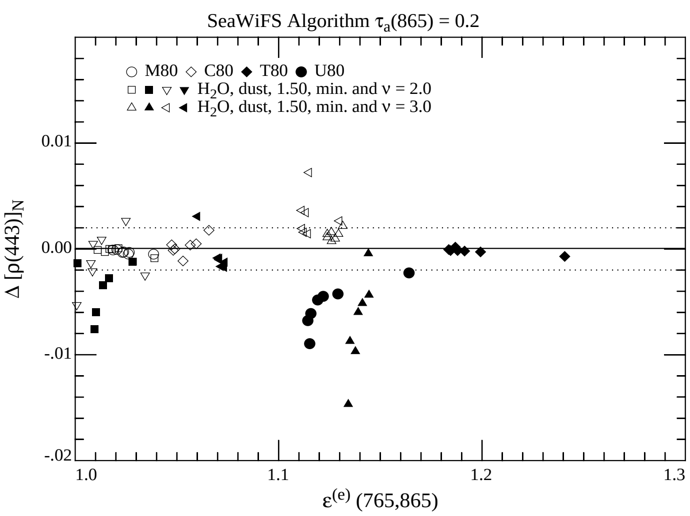

Figure 12. $\Delta[\rho_w(443)]_N$ as a function of $\varepsilon^{(e)}(765, 865)$ for the Haze C models with $\tau_a(865) = 0.2$ and all of the viewing geometries examined in the study, using the multiple-scattering algorithm.

algorithm is applied to the Haze C models. In this Figure we have limited the models to those that fall within the range of variation of the values of $\varepsilon(\lambda_s, \lambda_l)$ of the candidate models, and also models for which $\tau_a(443) \lesssim 0.8$, the upper limit of τ_a used in the preparation of the $\rho_a + \rho_{ra}$ versus ρ_{as} look up tables. Haze C models with a real index of refraction ($\omega_a = 1$) and $\nu \geq 3$ do not follow the $\omega_a - \varepsilon(\lambda_s, \lambda_l)$ relationship implied by the candidate models, and the values of $\Delta[\rho_w(443)]_N$ are positive. In contrast, the dust and mineral models both display ω_a-values less than T50, and for these the $\Delta[\rho_w(443)]_N$ are large and negative. Thus, it should be clear that it is imperative to use candidate aerosol models that possess an approximately correct relationship between ω_a and $\varepsilon(\lambda_s, \lambda_l)$, or physically, an approximately correct relationship between particle size and absorption. Such a relationship must be based on climatology, e.g., when the aerosol optical thickness over the North Atlantic Saharan dust zone is high, one should use candidate models consisting of a linear combination of a Maritime model and Saharan dust model, either uniformly mixed in the marine boundary layer or having a two-layer structure. Given such climatology-based models, preparation of the appropriate look up tables for incorporation into the algorithm is a simple process.

As an example, we modified the algorithm to utilize only four candidate models, the *Shettle and Fenn* [1979] Urban models at RH = 50%, 70%, 90%, and 99%, and tested it using pseudo data

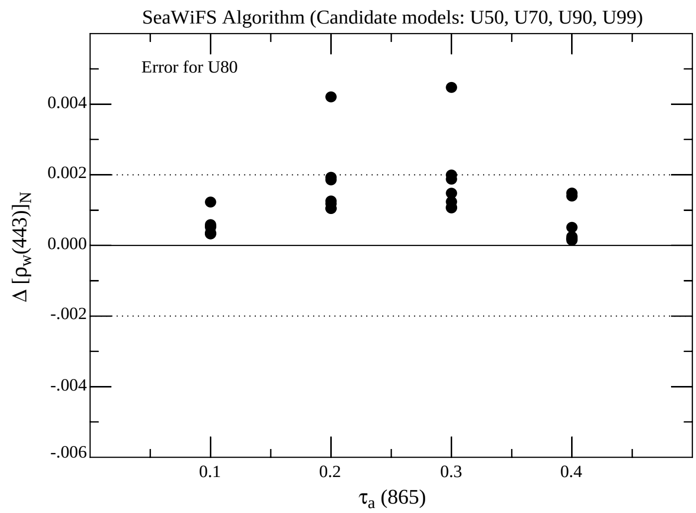

Figure 13. $\Delta[\rho_w(443)]_N$ as a function of $\tau_a(865)$ for the U80 model, when the candidate aerosol models in the multiple-scattering algorithm are restricted to U50, U70, U90, and U99.

created with the U80 model. In this manner, the ω_a and $\varepsilon(\lambda_s, \lambda_l)$ relationship was approximately correct. The results are provided in Figure 13, which shows the error in $[\rho_w(443)]_N$ as a function of the aerosol optical thickness of U80 at 865 nm. Recall, from Figure 5 (left panel), that $\tau_a(443) \approx 1.75\tau_a(865)$. Comparison with Figure 12, for which $\tau_a(865) = 0.2$, shows that the maximum error (which occurs at the scan edge with $\theta_0 = 60°$), when the Urban models are used as candidates, is only twice the minimum error when the original twelve candidate aerosol models were used. This underscores the necessity of having realistic climatologically-based aerosol models in situations in which the aerosol concentration is sufficiently large to require consideration of multiple scattering.

3.1.1.5 The diffuse transmittance

The diffuse transmittance was mentioned in Section 3.1.1. It is defined as the water-leaving radiance in a particular viewing direction (θ_v, ϕ_v) "transmitted" to the top of the atmosphere, i.e.,

$$t(\theta_v, \phi_v) = \frac{\rho_w(\theta_v, \phi_v)_{\rm Top}}{\rho_w(\theta_v, \phi_v)}. \tag{15}$$

Thus, if the atmosphere were only illuminated from below with radiance $\rho_w(\theta, \phi)$, the radiance measured at the top of the atmosphere in the direction (θ_v, ϕ_v) would be $t(\theta_v, \phi_v)\rho_w(\theta_v, \phi_v)$. The diffuse transmittance accounts for the direct loss from $\rho_w(\theta_v, \phi_v)$ due to absorption and scattering within the atmosphere, as well as for the gain in radiance in the direction (θ_v, ϕ_v) due to scattering of $\rho_w(\theta, \phi)$, i.e., from all other upward directions, into (θ_v, ϕ_v). It is interesting to note that, unlike the direct transmittance T, there is no requirement that the diffuse transmittance be less than unity. For example, if $\rho_w(\theta, \phi) = 0$ for a particular viewing direction, but not others, then $\rho_w(\theta_v, \phi_v)_{\rm Top} > 0$ because of atmospheric scattering from other directions into (θ_v, ϕ_v). Thus, in this admittedly bizarre example, $t(\theta_v, \phi_v) = \infty$! We present it only to underscore the fact that the diffuse transmittance is *not* a fundamental property of the atmosphere, but depends on the *angular distribution* of L_w as well as the optical properties of the atmosphere. In the case of the CZCS, it was assumed that $\rho_w(\theta_v, \phi_v)$ is independent of (θ_v, ϕ_v). We also employ a similar assumption in the present algorithm and, for emphasis, we designate the diffuse transmittance so computed by t^* to avoid confusion with the correct diffuse transmittance.[3] Then, extending a single scattering analysis of t^* to approximately include the effects of multiple scattering (by replacing $(1 - x)$ in single scattering formulas by $\exp(-x)$), *Gordon et al.* [1983] approximated t^* by

$$t^*(\theta_v, \phi_v, \lambda) = \exp\Big[-\left(\frac{\tau_r(\lambda)}{2} + \tau_{Oz}(\lambda)\right)\left(\frac{1}{\mu_v}\right)\Big]t_a(\theta_v, \lambda), \tag{16}$$

[3] Actually in the MODIS algorithm it is assumed that the upwelling radiance distribution just *beneath* the sea surface, $L_u(\theta'_v, \phi'_v)$, is uniform. $\rho_w(\theta_v, \phi_v)$ is related to L_u through $\rho_w(\theta_v, \phi_v) = \pi L_u(\theta'_v, \phi'_v)T_f(\theta'_v, \phi'_v)/(m^2 F_0 \cos\theta_0)$, where $T_f(\theta'_v, \phi'_v)$ is the Fresnel transmittance of the sea surface for light incident from (θ'_v, ϕ'_v), m is the refractive index of water, and (θ'_v, ϕ'_v) relates to (θ_v, ϕ_v) through Snell's law.

where

$$t_a(\theta_v, \lambda) = \exp\Big[-\frac{[1-\omega_a(\lambda)F_a(\mu_v,\lambda)]\tau_a(\lambda)}{\mu_v}\Big], \tag{17}$$

and $\mu_v = \cos\theta_v$. $F_a(\mu_v, \lambda)$ is related to the scattering phase function of the aerosol and is given by

$$F_a(\mu_v, \lambda) = \frac{1}{4\pi}\int_0^1 P_a(\alpha, \lambda)\, d\mu\, d\phi,$$

where $P_a(\alpha, \lambda)$ is the aerosol phase function at λ (normalized to 4π) for a scattering angle α, and

$$\cos\alpha = \mu\mu_v + \sqrt{(1-\mu^2)(1-\mu_v^2)}\cos\phi.$$

If θ_v is $\lesssim 60^\circ$ the factor $[1-\omega_a(\lambda)F_a(\mu_v,\lambda)]$ is usually $\ll 1$, so t_a depends only weakly on the aerosol optical thickness and was taken to be unity for CZCS.

Later, *Yang and Gordon* [1997] carried out a through study of the diffuse transmittance, including its dependence on the $\rho_w(\theta_v, \phi_v)$. For the case where the upwelling radiance just *beneath* a flat sea surface is uniform, they derived

$$t^*(-\hat{\xi}_0) = \frac{E_d(\hat{\xi}_0)}{F_0\cos\theta_0 T_f(\hat{\xi}_0)}, \tag{18}$$

where the solar beam is propagating in the direction $\hat{\xi}_0$ and E_d is the downwelling irradiance just *beneath* the sea surface. This leads to a very simple monte carlo procedure for computing t^*, i.e., to find $t^*(\theta_v)$, simply inject photons from the sun into the atmosphere with a solar zenith angle $\theta_0 = \theta_v$ and record the number that penetrate the water surface ($E_d/F_0\cos\theta_0$ equals number penetrating divided by the number injected). Thus, to compute t^* (photons propagating from the ocean to the top of the atmosphere) we actually solve a *reciprocal* problem (photons propagating from the sun to the water). Henceforth, t^* will be used to designate the diffuse transmittance computed in this manner, as opposed to that computed using the approximate single scattering formulas above. Because the correction algorithm provides models of the aerosol, it is possible to incorporate all of the multiple scattering and aerosol effects into t^* in the form of look up tables.

As retrieval of ρ_w from ρ_t requires t, and relative error in t will yield an equivalent relative error in ρ_w, it is important to compute this quantity as accurately as possible. Replacing t by t^* leads to error that is assessed in a later Section (3.1.1.9.5).

3.1.1.6 Whitecap Removal Algorithm

As mentioned earlier, the term $t(\lambda_i)\rho_{wc}(\lambda_i)$ in Eq. (6) has been ignored in the development of the algorithm. If we indicate the reflectance measured at the top of the atmosphere as $\rho_t^{(m)}$, this reflectance consists of two parts; that which would be measured in the absence of whitecaps, and the reflectance *added* by the whitecaps $t^*\rho_{wc}$,[4] i.e.,

$$\rho_t^{(m)} = \rho_t + t^*\rho_{wc}. \tag{19}$$

Since the $[\rho_w]_N$-retrieval algorithm must be operated with ρ_t rather than $\rho_t^{(m)}$, $t^*\rho_{wc}$ must be removed from the imagery *before* the algorithm can be applied.

As in the case of the normalized water-leaving radiance, we define the normalized whitecap reflectance (or the albedo) $[\rho_{wc}]_N$ to be the area-weighted reflectance (over several pixels) of oceanic whitecaps *at* the sea surface. Then the whitecap component of the radiance leaving the surface is

$$L_{wc}(\lambda) = [\rho_{wc}(\lambda)]_N \frac{F_0 \cos\theta_0}{\pi} t^*(\theta_0, \lambda),$$

where the whitecaps are assumed to be lambertian. Converting to reflectance we have

$$\rho_{wc}(\lambda) = [\rho_{wc}(\lambda)]_N \, t^*(\theta_0, \lambda).$$

At the top of the atmosphere, the whitecaps contribute

$$t^*\rho_{wc}(\lambda) = [\rho_{wc}(\lambda)]_N \, t^*(\theta_0, \lambda) t^*(\theta_v, \lambda).$$

The problem faced in removing $t^*\rho_{wc}(\lambda)$ from $\rho_t(\lambda)$ in Eq. (6) is the estimation of $[\rho_{wc}(\lambda)]_N$.

Based on previous research on the relationship between whitecaps and environmental parameters, *Koepke* [1984] estimated that the reflectance R of whitecaps can be expressed as

$$R = 6.49 \times 10^{-7} \, W^{3.52}, \tag{20}$$

[4] The use of t^* (as defined in the last section) is not rigorously correct here, as t^*, when used with ρ_w requires that the upwelling radiance just *beneath* the sea surface be uniform, while $[\rho_{wc}]_N$ is assumed to be lambertian *above* the surface. However, the error induced by using the incorrect transmittance is negligible compared to the large uncertainty in $[\rho_{wc}]_N$.

where W is the wind speed in m/s measured 10 m above the sea surface. Note that this included the background reflectance as well. Figure 14 provides Koepke's reflectance as a function of W, along with data derived from *Monahan* [1971]. It shows that Eq. (20) predicts R with a standard deviation approximately equal to the reflectance itself.

To estimate the error in the retrieved ρ_w due to whitecaps, *Gordon and Wang* [1994b] used Koepke's reflectance as an approximation to $[\rho_{wc}(\lambda)]_N$, however, the effect of the any error in the estimation of $[\rho_{wc}]_N$ on the retrieved water-leaving reflectance is strongly dependent on its spectral variation. In *Gordon and Wang* [1994b] it was assumed, based on measurements carried out by *Whitlock, Bartlett and Gurganus* [1982], that $[\rho_{wc}(\lambda)]_N$ was independent of λ; however, *Schwindling* [1995] and *Frouin, Schwindling and Deschamps* [1996] have reported measurements on breaking waves in the surf zone suggesting that whitecaps may reflect considerably less in the NIR than in the visible, presumably because a significant component of the whitecap reflectivity is due to scattering from submerged bubbles. To understand the effect of spectral variation in $[\rho_{wc}]_N$ on the accuracy

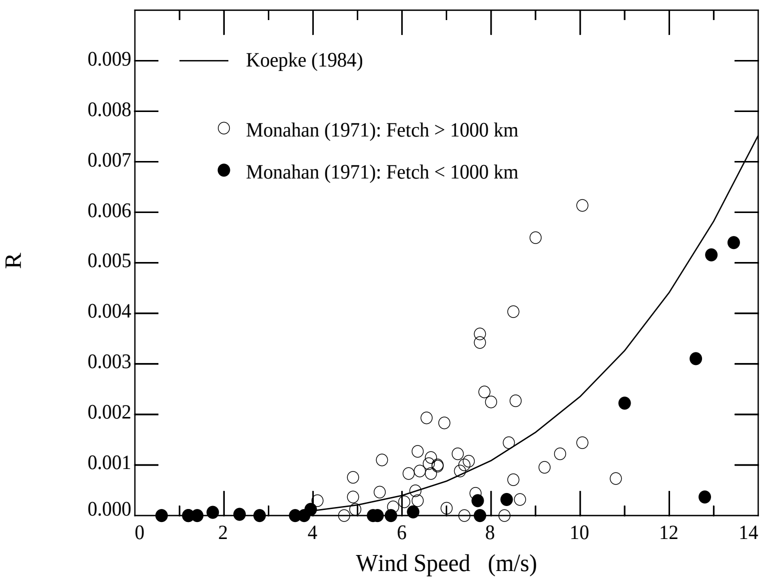

Figure 14. R from *Koepke* [1984] (solid line) as a function of wind speed. Points are computed using the data from *Monahan* [1971].

of atmospheric correction, the multiple scattering algorithm has been operated in the presence of whitecaps displaying both nonspectral reflectance and the spectral reflectance suggested by *Frouin, Schwindling and Deschamps* [1996]. Figure 15 compares the error in $[\rho_w(443)]_N$ as a function of θ_0

for viewing at the edge of the MODIS scan with the M80 aerosol model ($\tau_a(865) = 0.2$) for these two cases when the error in the *estimate* of $[\rho_{wc}]_N$ (Figure 14) at 443 nm is ± 0.002. This error in $[\rho_{wc}(443)]_N$ corresponds to a wind speed of $\sim 8-9$ m/s. Figure 15 shows that for wavelength-independent whitecap reflectivity, the resulting error in $[\rho_w(\lambda)]_N$ can be significantly less ($\sim 1/4$) than the error in the estimate of $[\rho_{wc}(443)]_N$. In contrast, if whitecaps reflect in a manner consistent with the *Frouin, Schwindling and Deschamps* [1996] observations, the error in $[\rho_w(443)]_N$ can be expected to be of the same order-of-magnitude as the error in $[\rho_{wc}(443)]_N$. Similar simulations using the T80 aerosol model, for which $\varepsilon(\lambda, 865)$ displays strong variation with λ, show similar effects for the case of whitecaps with the *Frouin, Schwindling and Deschamps* [1996] reflectance; however, the error for the *Whitlock, Bartlett and Gurganus* [1982] reflectance model can also be the same order of magnitude as $\Delta[\rho_{wc}(443)]_N$ [*Gordon and Wang*, 1994b]. Figure 15 shows that an overestimation of $[\rho_{wc}(443)]_N$ leads to a negative error in $[\rho_w(443)]_N$. The same is true at 550 nm.

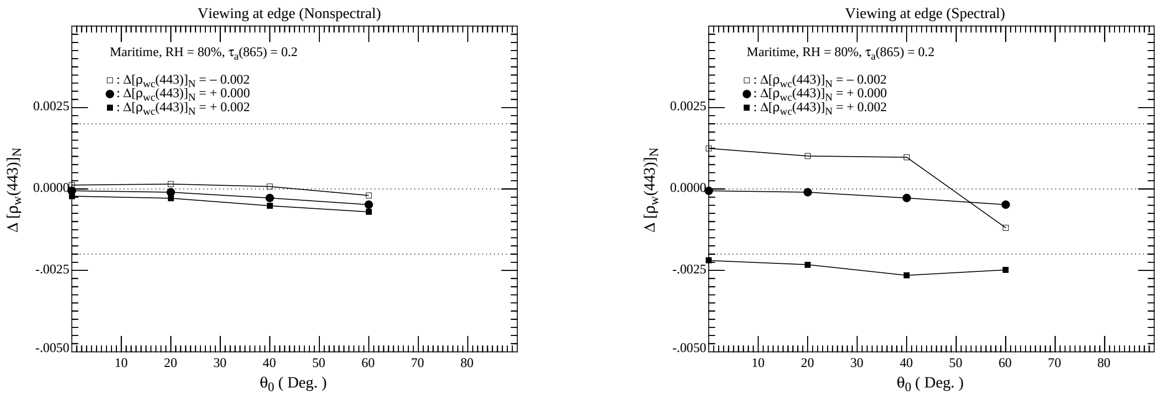

Figure 15. $\Delta[\rho_w(443)]_N$ as a function of the error in the whitecap reflectance at 443 nm and θ_0 at the edge of the scan for the M80 aerosol model with $\tau_a(865) = 0.2$. Left panel: whitecap reflectance spectrum is that proposed by *Whitlock, Bartlett and Gurganus* [1982]. Right panel: whitecap reflectance spectrum is that proposed by *Frouin, Schwindling and Deschamps* [1996].

When the errors in $[\rho_w(\lambda)]_N$ are negative, algorithms such as Eq. (4), that use radiance ratios, can lead to very large errors in the derived products. Because of this, it is better to underestimate the $[\rho_{wc}(443)]_N$ in the whitecap correction algorithm than to overestimate it.

As whitecaps have the potential of producing errors of a magnitude similar to the magnitude of the acceptable error in $[\rho_w(\lambda)]_N$, it was important to obtain radiometric data of actual oceanic whitecaps, and validate its dependence on wind speed. In particular, it is critical to understand the spectral dependence of $[\rho_{wc}]_N$ in the NIR. Our approach to this was to construct a ship-based radiometer for observing whitecaps while a ship is on station or underway [*Moore, Voss and Gordon*, 1998]. The radiometer, suspended from a boom off the bow of the ship, continuously views a spot about 12 cm in diameter on the sea surface, continuously measuring a radiance L_s. A video image, from a TV camera mounted along side of the radiometer to visually observe the water surface, is used to reject sun glitter. A second radiometer on the deck of the ship records the incident irradiance E_d. The radiance of the surface measured by the radiometer is recorded as a function of time ($\sim$ 7 samples/sec). This radiance consists of background radiance (L_b) from whitecap-free areas (the predominant situation) and a much higher radiance ($L_{wc} + L_b$) whenever a portion of a whitecap is in the field of view of the radiometer. After determining the radiance of the whitecap-free areas (L_b, essentially the "baseline" of the radiance), and subtracting it from the entire record, we are left with the time-average radiance due to the whitecaps,

$$\langle L_{wc} \rangle = \langle L_s \rangle - \langle L_b \rangle.$$

The associated reflectance (the remote-sensing augmented reflectance, $RSAR$) is

$$RSAR = \frac{\pi \langle L_{wc} \rangle}{E_d}.$$

Since, under clear skys (see footnote 4),

$$E_d \approx F_0 \cos\theta_0 t^*(\theta_0),$$

we see that

$$[\rho_{wc}(\lambda)]_N \approx RSAR(\lambda).$$

The radiometer is accompanied by a meteorological package to provide the speed of the wind relative to the ship (and other, possibly relevant, parameters) and a GPS unit to provide the absolute speed of the ship. Combining these will yield W. The whitecap radiometer records in 10 nm bands centered at 6 wavelengths: 410, 510, 550, 670, 750, and 860 nm, and the downward surface irradiance is measured in 5 bands, also 10 nm wide, centered at 410, 510, 550, 670, and 860 nm. Thus, we are able to study the validity of Eq. (20) throughout the relevant spectral region.

An example of two whitecaps passing under the radiometer (deployed from the NOAA ship *RV Malcolm Baldrige*, April 1996) is shown in Figure 16. The 96 consecutive samples shown are acquired over a period of $\sim$ 15 seconds. In this example a large whitecap suddenly breaks in view of the radiometer with thick white foam (sample point 11) reaching a peak reflectance of $\sim$ 55%. Six traces are plotted representing the six radiometer channels. The lower trace corresponds to the 860 nm reflectance. The thick foam is temporarily replaced by a region of submerged bubbles and less thick foam ($\sim$ sample points 13, 14, 15) and some thick foam comes into view again at sample point 17. At sample point 20 and 21 a thin layer of foam passes followed by the decaying thicker foam to about sample point 35. Sample points from about 35 to 55 show the reflectance

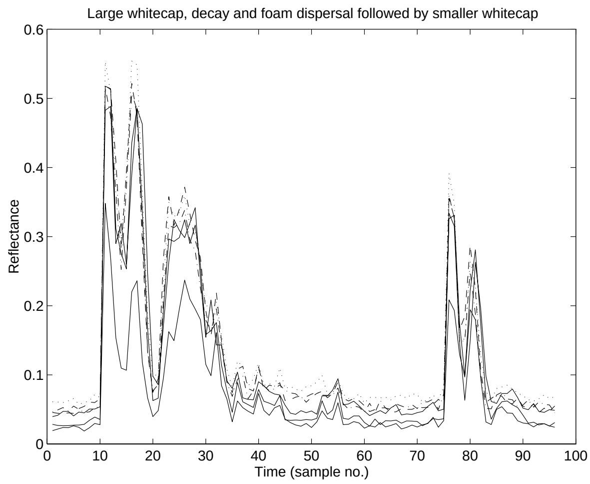

Figure 16. An approximately 15 second record of the reflectance of two whitecaps passing within the field of view of the radiometer. The lowest line corresponds to 860 nm.

of thinning residual foam. From 60 to about 75 the reflectance of the foam free water surface is shown and is suddenly followed by another whitecap of smaller magnitude (sample point 76) and continues to decay out to about sample point 96. The data clearly suggest a significant fall in the NIR reflectance of whitecaps in agreement with the measurements of *Frouin, Schwindling and Deschamps* [1996] in the surf zone.

From 1 to 13 November 1996, the whitecap radiometer was operated on a cruise from Manzanillo, Mexico to Honolulu, Hawaii. This cruise provided whitecap data under conditions of steady winds (the trades) of essentially unlimited duration and fetch. Unfortunately, analysis of the data was not as straightforward as expected. Under clear skys it proved very difficult to separate whitecaps from sun glint events. Thus, we performed the analysis only under overcast conditions. Furthermore, the determination of the "baseline" reflectance is critical to the analysis and proved to be difficult as well.

The analysis for estimating $RSAR$ is described in detail in *Moore, Voss and Gordon* [1997]. The dependence of $RSAR$ at 410 nm on wind speed is provided in Figure 17. The black triangles (joined by a vertical line) are the results of two different methods of data analysis (establishing the baseline). The larger (lower) black triangles are believed to be the better analysis of the data. For these,

$$RSAR \sim 3 \times 10^{-6} W^{2.55}.$$

The data also fit the Koepke formula (corrected to $RSAR$) reasonably well with the multiplier

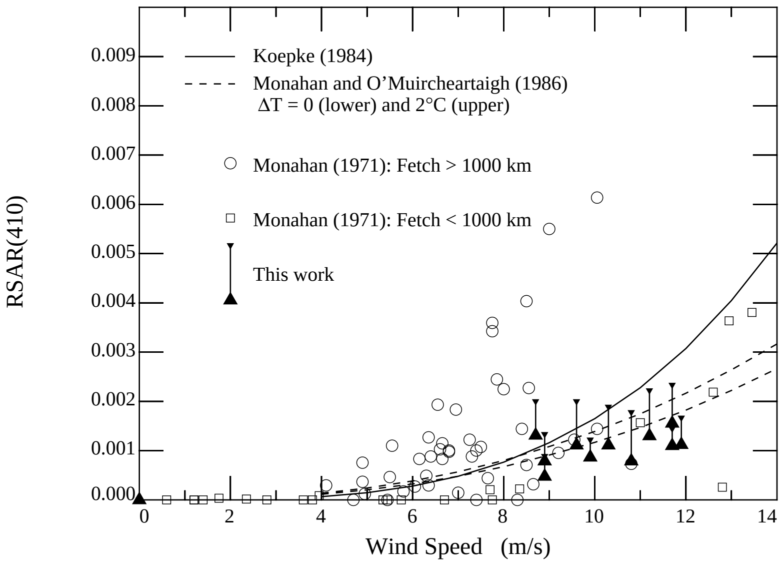

Figure 17. Remote-sensing augmented reflectance of whitecaps at 410 nm. The small and large triangles are from *Moore, Voss and Gordon* [1997] and correspond to two methods of analyzing the whitecap measurements. The open symbols are the *Monahan* [1971] fractional coverage multiplied by 0.155, the *Koepke* [1984] effective whitecap reflectance of 0.22 minus 0.065 to convert from reflectance to augmented reflectance. The dashed lines use the *Monahan and O'Muircheartaigh* [1986] model for a neutrally stable ($\Delta T = 0$) and an unstable ($\Delta T = 2C$) atmosphere to provide fractional coverage for use in computing the augmented reflectance: RSAR $= 3 \times 10^{-6}\, W^{2.55}\ \exp(0.861 \times \Delta T)$.

reduced by $\sim 1/3$, i.e.,

$$RSAR \sim 1.6 \times 10^{-7} W^{3.52}.$$

Finally, although there was no discernable spectral variation of $RSAR$ in the visible, the $RSAR$ was significantly lower at 860 nm than at 410 nm. (Figure 18). Although the data are very noisy, they suggest that

$$RSAR(860) \sim 0.85 \times RSAS(410),$$

for $RSAR(410) \lesssim 0.06$. This reduction of $RSAR$ in the NIR was less than observed in the surface zone [*Frouin, Schwindling and Deschamps*, 1996] and in ship wakes [*Moore, Voss and Gordon*, 1998].

Combining all of the observations, the algorithm for correcting the data for the effects of whitecaps is

$$[\rho_{wc}(\lambda)]_N = S(\lambda) \times 1.6 \times 10^{-7} W^{3.52}, \tag{21}$$

where $S(\lambda)$ is a spectral reflectance factor for whitecaps taken to be unity in the visible, 0.925 at 750 nm and 0.85 at 860 nm. While this correction is conservative (underestimate) in the region of our measurements, it may provide a better estimate for $W > 12$ m/s.

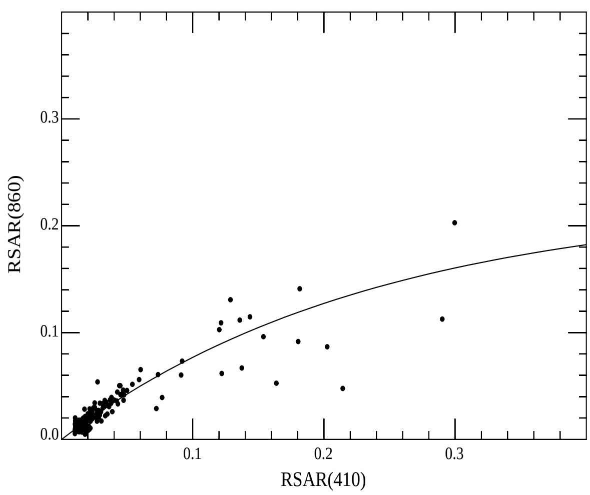

Figure 18. Relationship between RSAR at 865 nm and 410 nm (from *Moore, Voss and Gordon* [1997]).

3.1.1.7 Sun Glitter Mask and Correction

The contribution to the MODIS-measured radiance (or reflectance) at the TOA from sun glitter — the specular reflection of direct sunlight from the sea surface and subsequent propagation to the sensor — can be sufficiently large that the sensor will actually saturate. As such, severely perturbed pixels cannot be processed and need to be masked. For all other pixels, an estimate of the contribution of sun glitter is required for its removal. This estimate is based on the formulation of *Cox and Munk* [1954]. In their development the sea surface is modeled as a collection of facets with individual slope components z_x and z_y. It is a matter of simple geometry to determine the direction that the normal to a facet must have in order to reflect direct sunlight toward the sensor.

Consider a coordinate system (Figure 19) with the $+y$ axis pointing toward the sun (the projection of the sun's rays on the sea surface is along the $-y$ axis). The solar zenith angle is θ_0. Let the angles θ and ϕ specify the reflected ray, where ϕ is measured from the $-y$ axis *toward* the $-x$ axis (i.e., ϕ as shown in Figure 19 is positive). Then, the orientation (β, α) of the facet normal $\mathbf{n_f}$ (Figure 19) required for the facet to reflect sunlight in the direction of (θ, ϕ) is found from the following equations:

$$\begin{aligned}
\cos(2\omega) &= \cos\theta\cos\theta_0 - \sin\theta\sin\theta_0\cos\phi \\
\cos\beta &= (\cos\theta + \cos\theta_0)/2\cos\omega \\
\cos\alpha &= (\cos\theta_0\cos\beta - \cos\omega)/2\sin\theta_0\sin\beta \\
z_x &= \sin\alpha\tan\beta \\
z_y &= \cos\alpha\tan\beta.
\end{aligned}$$

Note that for a flat (smooth) surface, $\phi = 0$. Let ψ be the the angle between the projection of the sun's rays on the sea surface and the direction of the wind vector $\vec{W}$, i.e., if $\psi = 0$ the wind vector points in the direction of $-y$ in Figure 19. ψ is measured positive in a clockwise direction (looking toward the surface), i.e., if $0 < \psi < 90°$, the wind vector is in the quadrant formed by the $-x$ and $-y$ axes. Then, the defining the glitter reflectance ρ_g to be the radiance reflected from the sea surface, L_g, times $\pi/F_0 \cos\theta_0$, where F_0 is the extraterrestrial solar irradiance, ρ_g is given by

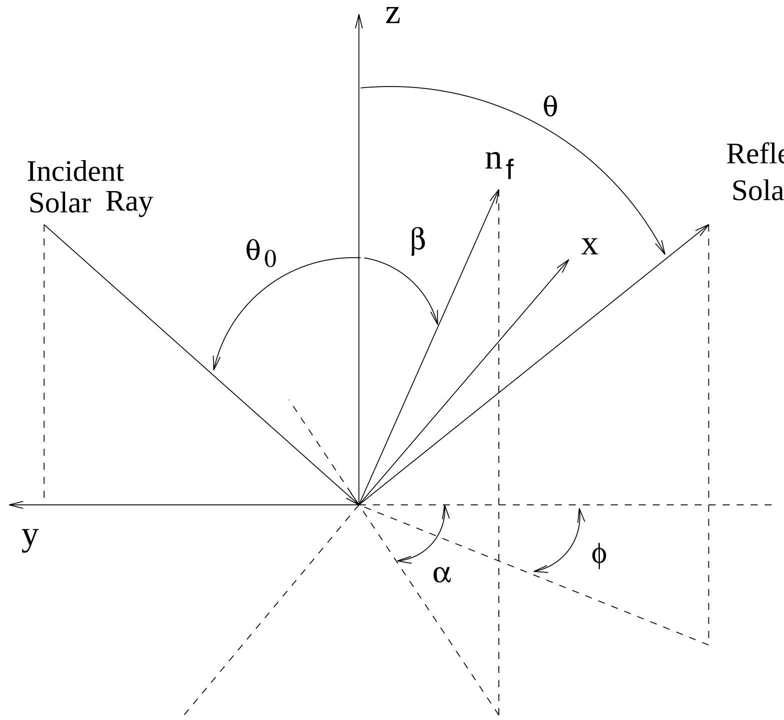

Figure 19. Geometry of reflection from a rough sea surface. n_f is the unit normal to the facet that is oriented properly to reflect the sunlight as shown.

$$\rho_g(\theta,\phi;\theta_0,\phi_0) = \frac{\pi r_+(\omega)}{4\cos\theta_0\cos\theta\cos^4\beta}\, p(z'_x, z'_y)$$

where $p(z'_x, z'_y)$ is the probability density of surface slopes given by

$$p(z'_x, z'_y) = (2\pi\sigma_u\sigma_c)^{-1}\exp[-(\xi^2+\eta^2)/2]\left[1+\sum_{i=1}^{\infty}\sum_{j=1}^{\infty} c_{ij}H_i(\xi)H_j(\eta)\right],$$

with

$$\xi = z'_x/\sigma_c = \sin\alpha'\tan\beta/\sigma_c$$

$$\eta = z'_y/\sigma_u = \cos\alpha'\tan\beta/\sigma_u$$

$$\alpha' = \alpha - \psi.$$

H_i is the Hermite polynomial of order i. $r_+(\omega)$ is the Fresnel reflectance for unpolarized light incident at an angle ω. It can be found from

$$r_{\pm}(\omega) = \frac{1}{2}\left[\frac{\tan^2(\omega-\omega')}{\tan^2(\omega+\omega')} \pm \frac{\sin^2(\omega-\omega')}{\sin^2(\omega+\omega')}\right],$$

where

$$\sin\omega' = \frac{1}{m_w}\sin\omega$$

and m_w is the refractive index of water.

The constants σ_u, σ_c, and c_{ij} were determined by Cox and Munk by fitting the radiance from glitter patterns photographed from aircraft of the coast of California to these equations. They are

$$\begin{aligned}
\sigma_c^2 &= 0.003 + 1.92 \times 10^{-3}\,W \quad \pm 0.002 \\
\sigma_u^2 &= 0.000 + 3.16 \times 10^{-3}\,W \quad \pm 0.004 \\
c_{21} &= 0.01 - 8.6 \times 10^{-3}\,W \quad \pm 0.03 \\
c_{03} &= 0.04 - 33 \times 10^{-3}\,W \quad \pm .012 \\
c_{40} &= 0.40 \quad \pm 0.23 \\
c_{22} &= 0.12 \quad \pm 0.06 \\
c_{04} &= 0.23 \quad \pm 0.41.
\end{aligned}$$

There is considerable debate as to the validity of the values assigned to these parameters. *Shaw and Churnside* [1997] have directly measured σ_u using a scanning-laser glint meter. Their results showed a strong dependence of σ_u on the atmospheric stability. The atmospheric stability is characterized by the Richardson number Ri given by

$$Ri = g\frac{(T_a - T_w)}{T_w W^2},$$

where T_a and T_w are, respectively, the air and water temperatures (°C), and g is the gravitational constant (9.8 m/s^2). The atmosphere is stable when $Ri > 0$ and unstable when $Ri < 0$. They combined their measurements with those of *Hwang and Shemdin* [1988] and developed the relationship between σ_u and Ri provided in Figure 20. The lines on the figure correspond to

$$\begin{aligned}
\frac{\sigma_a^2}{\sigma_{cm}^2} &= 1.42 - 2.8\,Ri \qquad \text{for} \qquad -0.23 < Ri < 0.27 \\
\frac{\sigma_a^2}{\sigma_{cm}^2} &= 0.65 \qquad \text{for} \qquad Ri > 0.27.
\end{aligned}$$

Cox and Munk [1954] collected most of their data for positive stability, thus for unstable atmospheres, σ_u is considerably larger than that suggested by their equations. It is expected that σ_c behaves in a manner similar to σ_u in respect to its dependence on stability. It is important to note that a larger σ implies a more diffuse glitter pattern, i.e., it extends farther from the specular

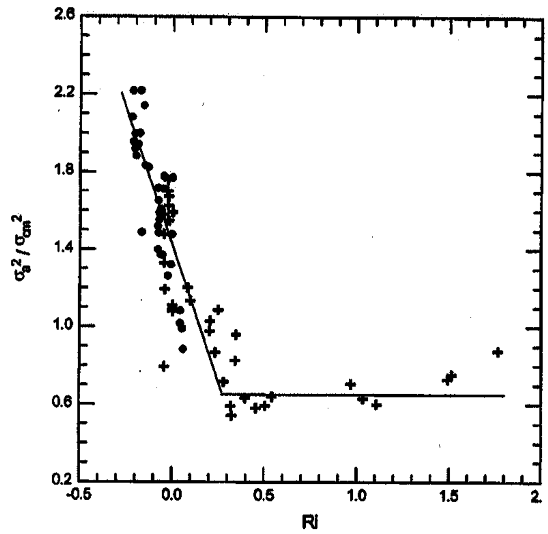

Figure 20. Relationship between direct measurements of σ_u^2 by *Shaw and Churnside* [1997] (dots) and *Hwang and Shemdin* [1988] (crosses) and the stability of the atmosphere. σ_a is the direct measurement, and σ_{cm} is the prediction by the *Cox and Munk* [1954] equations. (Reproduced from *Shaw and Churnside* [1997].)

point (the point at which sunlight would be reflected from a *flat* surface toward the sensor), but with smaller radiance near the specular point.

In contrast to direct measurements of the surface slope statistics, *Ebuchi and Kizu* [2002] combined directly observed glitter patterns (from a geostationary satellite) with satellite estimates of the wind speed and direction from spaceborne radar scatterometers. They assumed that the apparent radiance of the surface in the visible is proportional to $p(z_x', z_y')$, and on this basis, derived the surface slope parameters. Their resulting σ_c agreed well with that measured by *Cox and Munk* [1954]; however, their σ_u showed a considerably *weaker* dependence on W. Considering that most of their measurements were in the tropics, where the atmosphere is expected to be unstable, their conclusions are *opposite* to *Shaw and Churnside* [1997] and *Hwang and Shemdin* [1988]. *Ebuchi* *and Kizu* [2002] attribute this to the likelihood that the direct measurements were made under conditions in which the waves were *growing* with the wind, whereas in their measurements the waves were in *equilibrium* with the wind, and therefore, represent *average* conditions. In our opinion the question of the most realistic values for σ_c and σ_u remains open.

In the MODIS algorithm, the following values are used

$$\sigma_c^2 = 2.73 \times 10^{-3}\, W$$
$$\sigma_u^2 = 2.46 \times 10^{-3}\, W.$$

They were chosen to minimize the variation of ρ_t before MODIS enters saturation due to sun glitter and after it leaves saturation on the other side of the scan. In addition, ρ_g was multiplied by a scaling factor of 0.90 for $\lambda \leq 551$ nm and 0.98 for $\lambda > 551$ nm to improve the performance.

The contribution of ρ_g to the reflectance measured at the top of the atmosphere, $T\rho_g$, where T is the direct transmittance of the atmosphere, is just

$$\rho_g \exp\left[-\tau\left(\frac{1}{\cos\theta} + \frac{1}{\cos\theta_0}\right)\right],$$

where τ is the total optical thickness of the atmosphere. However, there is a question the appropriateness of using the direct transmittance T. Near the center of the glitter pattern (the specular point) the sun glitter overwhelms all other components of the radiance and the radiance distribution is more in the form of a beam, for which the direct transmittance is appropriate. In contrast, away from the specular point, where direct sun glitter is a significantly smaller component of the radiance, e.g., comparable to the aerosol, the glitter radiance distribution is more diffuse, implying that the diffuse transmittance should be more appropriate. As such, it is not possible that a single transmittance factor, appropriate to all pixels, exists.

The sun glitter mask uses the wind vector $\vec{W}$ to estimate ρ_g for each pixel, and if the estimate is larger than a threshold value the pixel is flagged and the normalized water-leaving radiance algorithm is not applied. As the aerosol optical thickness at a given pixel is unknown at the time of the application of the mask, the value determined at the previous pixel along the scan line is used. For pixels that are not masked (or saturated) a sun glitter *correction* is carried out. This consists of subtracting the computed reflectance $T\rho_g(\lambda)$ from each pixel along the scan line.

In order to correct the total radiance for the polarization sensitivity of MODIS (Section 3.1.1.8), it is important to note that the sun glitter displays partial linear polarization. The polarization properties are relatively easy to establish using the results from electromagnetic theory for refection of electromagnetic waves from a flat dielectric interface. The only complication is referencing them to the standard reference system used in atmospheric optics — the plane formed by the direction of propagation of the light and the vertical. Here, we present the final results. The degree of polarization of the glitter, P_g and the direction χ_g are given by

$$P_g = \left| \frac{r_-(\omega)}{r_+(\omega)} \right| \qquad \text{and} \qquad \chi_g = \frac{\pi}{2} - \alpha_r,$$

where

$$\sin \alpha_r = \frac{\sin \theta_0 \sin \phi}{\sin 2\omega}.$$

3.1.1.8 MODIS Polarization Sensitivity Effects

All scanning radiometers display some sensitivity to the polarization of the radiance they are intended to measure. For MODIS, it was specified that this polarization sensitivity should be less than 2% for all ocean bands (except the 412 nm band for which the agreed-upon limit of 2.3% was inadvertently left out of the final specifications). It was also specified that the polarization sensitivity (amplitude and phase) be mapped as part of the sensor characterization procedure.

The polarization sensitivity of MODIS can be specified in the following manner. Introduce completely (linearly) polarized monochromatic light into MODIS. Let the direction of polarization (the plane of oscillation of the electric field vector) of the incident light be specified by an angle χ measured with respect to a direction fixed relative to the sensor, e.g., the scan plane. Then, as the angle χ is varied through 360°, the output of the sensor will be

$$L^{\text{Measured}} = m_1 \, L^{\text{Source}} \left[1 + a \cos 2(\chi - \delta)\right],$$

where L^{Source} is the (constant) radiance of the source, m_1 is a calibration constant, L^{Measured} is the radiance "measured" by the sensor, a the amplitude of the polarization sensitivity, and δ the phase angle of the polarization sensitivity. Both a and δ are required to characterize the polarization sensitivity of the instrument. Figure 21 provides the measured values of a for two of the MODIS bands. Clearly, MODIS exceeds the polarization sensitivity specification at 869 nm and the polarization sensitivity is significantly larger at 412 nm.

Because MODIS does not meet the specifications in all bands, a correction is required to remove the residual polarization effects from ρ_t. (The influence of uncorrected polarization sensitivity on the retrieved water-leaving reflectance ρ_w is similar to that of calibration errors, which are discussed in Section 3.1.3. Roughly, a 1% error in ρ_t at 412 nm leads to a 10% error in the retrieved ρ_w

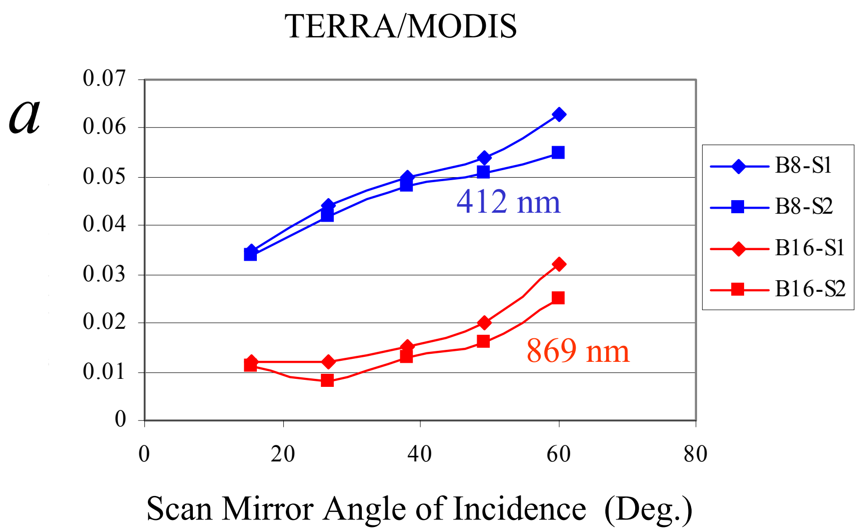

Figure 21. Polarization-sensitivity amplitude a for the Terra version of MODIS for Bands 8 (412 nm) and 16 (869 nm). S1 and S2 refer to the two sides of the MODIS scan mirror.

when the chlorophyll a concentration is low.) *Gordon* [1988] developed a formalism that provides the framework for removal of instrument polarization-sensitivity effects. Briefly, a beam of partially polarized light can be described as the incoherent superposition of a beam of unpolarized light of radiance L_u, and a beam of completely polarized light of radiance L_p. The total radiance of the beam is then $L_u + L_p$, and the *degree of polarization*, P, is given by

$$P = \frac{L_p}{L_u + L_p}.$$

The polarized component, as above, is described by specifying the plane of oscillation of the electric field vector through the angle, χ, it makes with some reference direction. The partially polarized beam is then characterized by its radiance $L_u + L_p$, its degree of polarization P, and its direction of polarization specified by the angle χ. In atmospheric optics, the direction χ is usually the angle of inclination of the plane of the electric field oscillations of L_p measured with respect to the plane containing the vertical and the direction of propagation. Specifying the polarization of the reflectance ρ_t in this manner, the measured reflectance (by the polarization-sensitive radiometer) is related to the true reflectance by

$$\rho_t^{\text{Measured}} = \rho_t^{\text{True}} \left[1 + aP \cos 2(\chi - \delta)\right].$$

We note that the maximum error in ρ_t is $\pm aP$.

The difficulty with removing the polarization sensitivity error, i.e., recovering ρ_t^{True} from ρ_t^{Measured} given a and δ is that the polarization properties of the radiance backscattered by the aerosol and the water are unknown. *Gordon, Du and Zhang* [1997a] developed an approximate method for reducing the instrument polarization effects. This method assumes the polarization of the light field at the sensor is that of a pure Rayleigh-scattering atmosphere. In this case,

$$\rho_t^{\text{True}} = \frac{\rho_t^{\text{Measured}}}{\left[1 + aP_r \cos 2(\chi_r - \delta)\right]},$$

where P_r and χ_r are, respectively, the degree and direction of polarization in an aerosol-free atmosphere with $\rho_w = 0$. As the look up tables for the Rayleigh-scattering component ρ_r contain the complete Stokes vector, the polarization properties of this component of the light field are available within the processing code.

The *Gordon, Du and Zhang* [1997a] method was implemented in the first version of the algorithm. It uses an analysis of the polarization sensitivity for the instrument based on pre-launch characterization measurements. The polarization sensitivity measured for detector 5, the detector at the center of the linear array for each spectral bands, was used for each spectral band, as it was assumed to be the most accurate.

Prior to the first partial reprocessing, the polarization correction was revised. In the new correction procedure it is assumed that ρ_r is the only component of the light field that is polarized. That is, it is assumed that ρ_{ra}, ρ_a, ρ_{wc}, ρ_g, and ρ_w are totally unpolarized, i.e., the degree of polarization associated with these individual components is zero. Then,

$$\rho_t^{\rm True} = \frac{\rho_t^{\rm Measured}}{[1 + aP\cos 2(\chi_r - \delta)]},$$

where

$$P = P_r \frac{\rho_r}{\rho_t^{\rm True}}.$$

Note that the unknown $\rho_t^{\rm True}$ in the above equation for P can be replaced by $\rho_t^{\rm Measured}$ with little loss in accuracy. Figure 22 shows the efficacy of this revised correction method using simulated

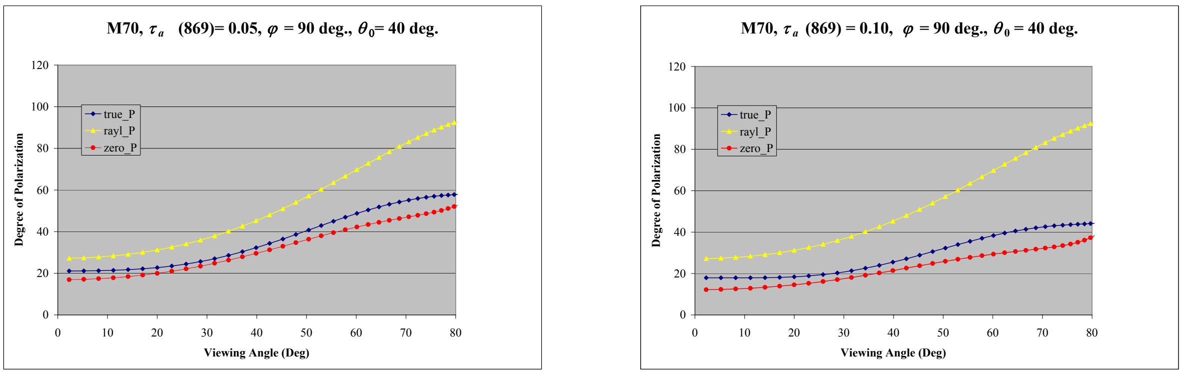

Figure 22. Efficacy of the revised polarization-sensitivity correction method. The true degree of polarization is compared to that in a pure Rayleigh scattering atmosphere and that in which all other contributors to the radiance are unpolarized. The computations are for a wavelength of 869 nm and the geometry is the perpendicular plane (similar to the MODIS scan at moderate sun angles) for a solar zenith angle of 40°. The aerosol model M70, characteristic of the MOBY calibration site, is used in the simulation. Left panel is for $\tau_a(869) = 0.05$ (a clear maritime atmosphere) and the right panel is for $\tau_a(869) = 0.10$ (a more typical maritime atmosphere).

data. Figures 21 and 22 also underscore the importance of this correction. In an aerosol-free atmosphere, P is similar at all wavelengths and $P \approx 0.5$ near the scan edge. At one edge of the scan, where $a \approx 0.06$ and 0.03 at 412 and 869, the error in the uncorrected ρ_t could be as much as $\pm 2.5\%$ and 1.5%, respectively.

Finally, as the polarization of the sun glitter contribution $T\rho_g$ is relatively straightforward to determine, it has been included in the correction. The full polarization-sensitivity correction in use at the completion of this document is

$$\rho_t^{\text{True}} = \frac{\rho_t^{\text{Measured}}}{[1 + aP\cos 2(\chi - \delta)]},$$

where P and χ are found from

$$P\cos 2\chi = \frac{\rho_r P_r \cos 2\chi_r + T\rho_g P_g \cos 2\chi_g}{\rho_t^{\text{True}}},$$
$$P\sin 2\chi = \frac{\rho_r P_r \sin 2\chi_r + T\rho_g P_g \sin 2\chi_g}{\rho_t^{\text{True}}},$$

and the sun glitter reflectance, ρ_g, degree of polarization, P_g, and direction of polarization χ_g are provided in Section 3.1.1.7. As before, the unknown ρ_t^{True} in the above equations for P and χ is replaced by ρ_t^{Measured}.

3.1.1.9 Non-zero $[\rho_w]_N$ in the NIR

A fundamental assumption in the atmospheric correction algorithm is that $[\rho_w]_N = 0$ in the NIR (748 and 869 nm for MODIS). However, it is well known that at high chlorophyll a concentrations there is a small, but non-zero, water-leaving reflectance in the NIR, even in Case 1 waters. Therefore, it is necessary to estimate $[\rho_w]_N$ in the NIR. A scheme for effecting this was provided by *Siegel et al.* [2000] for SeaWiFS, and has been adapted to operate with the MODIS spectral bands.

The water-leaving reflectance can be written [*Gordon et al.*, 1988]

$$[\rho_w]_N \approx 1.7 \sum_{i=1}^{2} g_i \left[\frac{b_b}{a + b_b}\right]^i, \tag{22}$$

where a is the absorption coefficient of the water plus constituents, b_b the backscattering coefficient, $g_1 = 0.0949$, $g_2 = 0.0794$, and the factor 1.7 accounts to the transmission and refraction effects across the air-sea interface. In the NIR, the absorption by sea water is large, so a can be replaced by a_w, the absorption coefficient of pure sea water. The backscattering coefficient can be decomposed into that due to particles and that due to water:

$$b_b = b_{bp} + b_{bw}.$$

Morel [1988] has related b_{bp} to the concentration of chlorophyll a (C) and the wavelength through

$$b_{bp}(\lambda) = 0.416\, C^{0.766} \left[0.002 + 0.02(0.5 - 0.25 \log_{10} C) \left(\frac{550}{\lambda} \right) \right].$$

Table 3 provides the values of a_w and b_{bw} used in the estimation of $[\rho_w]_N$.

Table 3: Parameters needed for Eq. (22).

Parameter	Wavelength (nm) 748	869
a_w (m^{-1})	2.586	4.436
b_{bw} (m^{-1})	0.00024	0.00014

The estimate of $[\rho_w]_N$ is incorporated in the atmospheric correction algorithm in the following manner. First, an atmospheric correction is carried out assuming that $[\rho_w]_N = 0$ in the NIR. The retrieved reflectances are then used in a ratio algorithm, e.g., similar to Figure 2, to estimate the concentration of chlorophyll a. The estimate of C (if greater than 0.3 mg/m^3) is then used to estimate $[\rho_w]_N$ in the NIR using the above relationships. The estimate of $[\rho_w]_N$ in the NIR is used to estimate $t^*\rho_w$ in the NIR, which is then subtracted from ρ_t and the atmospheric correction algorithm operated again. This procedure is carried out until the retrieved C changes by less than 20% from the previous iteration, up to a maximum of four iterations.

3.1.1.10 Estimation of Aerosol Optical Depth τ_a

There is considerable interest now in the global distribution of aerosols because of their role in climate forcing and biogeochemical cycling [*Charlson et al.*, 1992]. The hypothesis [*Charlson et al.*, 1987] that dimethylsulfide (DMS) from phytoplankton activity leads to an increase in cloud condensation nuclei in the marine atmosphere argues for simultaneous study of aerosols and productivity where possible [*Falkowski et al.*, 1992]. There has been effort in recent years directed toward estimating the aerosol concentration ($\propto \tau_a$) and other properties using Earth-orbiting satellites [*Durkee et al.*, 1986; *Fraser*, 1976; *Griggs*, 1975; *Griggs*, 1981; *Griggs*, 1984; *Griggs*, 1981; *Koepke and Quenzel*, 1979; *Koepke and Quenzel*, 1981; *Mekler et al.*, 1977; *Rao et al.*, 1988]. In this section we show that τ_a can be retrieved with a simple extension of the atmospheric correction algorithm.

Even in the single scattering approximation, one notes from Eq. (9) that it is not possible to estimate τ_a without assuming a model for the aerosol to provide ω_a and P_a. For example, *Rao et al.* [1988] assume that the aerosol consists of spherical particles with a size frequency distribution $\propto$ (radius)$^{-4.5}$ and a refractive index of 1.5. The assumption of an incorrect model can produce significant errors (up to a factor of 2–3) in the recovered τ_a. As in atmospheric correction, we will try to avoid using an incorrect model in the retrieval of τ_a by utilizing the only other aerosol information available on a pixel-by-pixel basis — the spectral variation of ρ_{as}.

Our retrieval algorithm is a simple extension of the atmospheric correction algorithm, i.e., the correction algorithm yields the two models which most closely bracket $\varepsilon(765, 865)$, and we use these two models to invert Eq. (9) to obtain two estimates of τ_a. As with the atmospheric correction, it is necessary to know the absorption properties of the aerosol. Assuming the aerosols are weakly absorbing, i.e., that the aerosol consists of particles that are accurately described by the Maritime, Coastal, or Tropospheric aerosol models with RH = 80%, ρ_t is simulated for this aerosol and inserted into the multiple-scattering atmospheric correction algorithm. The correction algorithm provides two candidate models based on $\varepsilon(765, 865)$ and these specify two sets of P_a and ω_a values for two estimates of τ_a. The estimated value of τ_a is then determined from the weighted average of the two estimates as in the correction algorithm. Tables 4 and 5 provide the % error in the retrieved $\tau_a(865)$ for three aerosol models at the center and the edge of the MODIS scan as a function of θ_0. The true value of $\tau_a(865)$ was 0.2 or 0.4. All the calculations were carried out for

Table 4: Error in retrieved $\tau_a(865)$ for viewing at the center and edge of the scan. The true value of $\tau_a(865)$ is 0.20.

Position	θ_0	Error (%) in $\tau_a(865)$		
		Maritime	Coastal	Tropospheric
Center	20°	+17.4	+0.09	+0.63
	40°	−1.53	−2.88	−0.41
	60°	+2.96	−10.5	−2.41
Edge	0°	+0.55	−3.64	−0.88
	20°	+1.31	−4.74	−1.28
	40°	+2.41	−9.27	−2.54
	60°	+3.71	−14.0	−4.18

$\phi_v = 90°$. From the tables, we can see that the error in the retrieved aerosol optical thickness is typically within ±10% (and usually considerably less) for most of the cases examined.

Finally, it is of interest to estimate the upper limit to the value of $\tau_a(865)$ that can be estimated with SeaWiFS or MODIS given its design saturation reflectance ($\rho_{\max}$). This is dependent on the particular aerosol model because for a given τ_a the backscattering (scattering at angles > 90°)

Table 5: Error in retrieved $\tau_a(865)$ for viewing at the center and edge of the scan. The true value of $\tau_a(865)$ is 0.40.

Position	θ_0	Error (%) in $\tau_a(865)$		
		Maritime	Coastal	Tropospheric
Center	20°	+16.9	+0.32	+0.19
	40°	−1.03	−4.57	+0.72
	60°	+3.78	−8.18	+2.05
Edge	0°	+1.12	−4.13	+1.04
	20°	+1.87	−4.94	+1.18
	40°	+3.41	−7.58	+1.69
	60°	+6.49	−7.80	+2.77

Table 6: Approximate value of $\tau_a(865)$ required to saturate SeaWIFS/MODIS at 865 nm.

Position	θ_0	Maximum value of $\tau_a(865)$	
		Maritime (RH = 98%)	Tropospheric (RH = 70%)
Center	20°	0.72	0.54
	40°	1.04	0.72
	60°	1.69	0.80
Edge	0°	0.88	0.51
	20°	0.98	0.51
	40°	1.04	0.50
	60°	1.02	0.50

is strongly dependent on the aerosol size distribution and the refractive index. We estimate the upper limit of $\tau_a(865)$ that can be estimated by using the Tropospheric model with RH = 70% (largest backscattering of the models used here) and the Maritime model with RH = 98% (small backscattering). The results are presented in Table 6.

3.1.1.11 Ancillary Data

Several sets of ancillary data are required to operate the $[\rho_w]_N$ retrieval algorithm. These are listed in Table 7. They may be needed on at most a $1^\circ \times 1^\circ$ latitude-longitude grid, but probably a coarser grid, e.g., $3^\circ \times 3^\circ$ will be sufficient considering the expected quality of some of the data. We will discuss each ancillary data set required below.

Table 7: Quantities and required ancillary data.

Quantity	Ancillary Data
$\rho_t(\lambda_i)$	$F_0(\lambda_i)$
$\rho_r(\lambda_i)$	$\tau_{Oz}(\lambda_i)$, W, P_0
$\rho_{wc}(\lambda_i)$	W, ΔT, T_W
$\rho_g(\lambda_i)$	$\vec{W}$
$t(\lambda_i)$	$\tau_{Oz}(\lambda_i)$, P_0
$T(\lambda_i)$	$\tau_{Oz}(\lambda_i)$, P_0, $\tau_a(\lambda_i)$
$\epsilon(\lambda_i, \lambda_j)$	RH

3.1.1.11.1 Extraterrestrial Solar Irradiance F_0

Unless MODIS is calibrated directly in reflectance units, the extraterrestrial solar irradiance is required to convert from L_t to ρ_t. It is planned that this be taken from *Neckel and Labs* [1984] unless newer, more accurate, determinations become available in the future. In the event that MODIS is calibrated directly in reflectance units, this quantity is only needed to turn $[\rho_w]_N$ into the desired $[L_w]_N$ and to effect the appropriate out-of-band corrections (see Section 3.1.1.8.5).

3.1.1.11.2 Ozone Optical Thickness

In the radiative transfer model the atmosphere is assumed to be composed of three layers.

The top is the Ozone layer and is nonscattering, the second is a molecular scattering layer and the third is the aerosol layer. The Ozone optical thickness $\tau_{Oz}(\lambda)$ is needed to compute the two way transmittance of ρ_r, ρ_w, ρ_{wc} and ρ_g through the Ozone layer. Since the Ozone absorption is small ($\tau_{Oz} \lesssim 0.035$) high accuracy is not needed. It is estimated that an error in the Ozone concentration of $\sim 20 - 40$ mAtm–cm (Dobson Units) could be tolerated. These data are acquired from the Goddard DAAC.

3.1.1.11.3 Surface Atmospheric Pressure P_0

The atmospheric pressure is needed to compute the Rayleigh optical thickness (τ_r) required for the computation of ρ_r. It is also used in the transmittances t and T. The value of τ_{r_0}, the Rayleigh optical thickness at the standard atmospheric pressure P_0 of 1013.25 mb is given by [*Hansen and Travis*, 1974]

$$\tau_{r_0} = 0.008569\lambda^{-4}\left(1 + 0.0113\lambda^{-2} + 0.00013\lambda^{-4}\right),$$

where λ is in μm. At any surface pressure P, the Rayleigh optical depth is

$$\tau_r = \frac{P}{P_0}\tau_{r_0}.$$

An error $< \pm 5$ mB should be sufficient for the computation of τ_r. The source of this data set will be the output of numerical weather models.

3.1.1.11.4 Wind Speed W and Wind Vector $\vec{W}$

The wind speed, if known, is used in the computation of ρ_r, otherwise ρ_r is computed with $W = 0$. It is also required for the estimation of $[\rho_{wc}]_N$. The wind vector is required for the construction of a glint mask, i.e., a mask to remove areas contaminated by sun glint from the imagery before processing. The importance of creating a realistic mask is that good data may be masked if the mask is made in too conservative a manner. An error of $< 1 - 2$ m/s in the speed and $< 30°$ on the direction should be sufficient. The source of this data set will be the output of numerical weather models.

3.1.1.11.5 Sea Surface Temperature and Atmospheric Stability

It was originally thought that these may be needed to estimate $[\rho_{wc}]_N$, if another estimate replaces Koepke's (Eq. (20)), e.g., *Monahan and O'Muircheartaigh* [1986]. However, use of Eq. (21) obviates the need for these quantities.

3.1.1.11.6 Relative Humidity RH

The surface relative humidity (RH) is not really needed by the algorithm; however, it could be useful as a constraint on the candidate aerosol models chosen by the algorithm as described in Section 3.1.1.3. The error in the value of RH should be $< \pm 5 - 10\%$ to be useful. The source of this data set will be the output of numerical weather models.

3.1.1.11.7 Total Column Water Vapor

Total column water vapor is needed to effect out-of-band corrections for MODIS spectral bands near strong atmospheric water vapor absorption features. The accuracy needed is expected to be $\sim \pm 0.5$ - 1 gm/cm^2. The source of this data set will be the output of numerical weather models.

All of the meteorological data (P, $\vec{W}$, T_W, ΔT, RH, and water vapor) will be acquired from NOAA by the GSFC Data Assimilation Office (DAO) and then supplied to the GSFC DAAC. MODIS will acquire the data fields directly from the GSFC DAAC.

3.1.1.12 Second-Order Effects

In this section we examine the adequacy of the various approximations that were made in the development of the algorithm.

3.1.1.12.1 Aerosol Vertical Structure

The reflectance of the atmosphere in the single-scattering approximation is independent of the manner in which the aerosol is distributed with altitude. However, this independence does not extend to a multiple-scattering atmosphere. As the multiple-scattering algorithm assumes that the aerosol is all located in the bottom layer of a two-layer atmosphere, it is important to understand the effect of aerosol vertical structure on the correction algorithm. This has been studied by comparing the error in the algorithm when the pseudo data are simulated using the "correct" two-layer model, i.e., all of the aerosol at the bottom of the atmosphere as assumed in the algorithm, with the error when the pseudo data are simulated using a model in which the aerosol and Rayleigh scattering have an altitude-independent mixing ratio, i.e., a uniformly mixed model. Figure 23 (left panel) provides such a comparison for the M80 and T80 aerosol models with $\tau_a(865) = 0.2$. It is seen that the effect of an incorrect assumption regarding the vertical structure will not lead to serious errors in this case. However, in the case of strongly absorbing aerosols, e.g., the Urban models, the assumed vertical structure is very important. Figure 23 (right panel) provides the two-layer versus uniformly mixed cases for the Urban models with $\tau_a(865) = 0.2$. In this case the candidate aerosol models were restricted to U50, U70, U90, and U99, as in the results for Figure 13. For the U80 case, the error becomes excessive, increasing by over an order of magnitude compared to the two-layer case. More disturbing is the performance of the U70 aerosol model. U70 is actually one of the candidate aerosol models in this case. When the vertical structure is the same as assumed by the algorithm, the error is negligible. In contrast, when the incorrect structure is assumed, the error becomes very large.

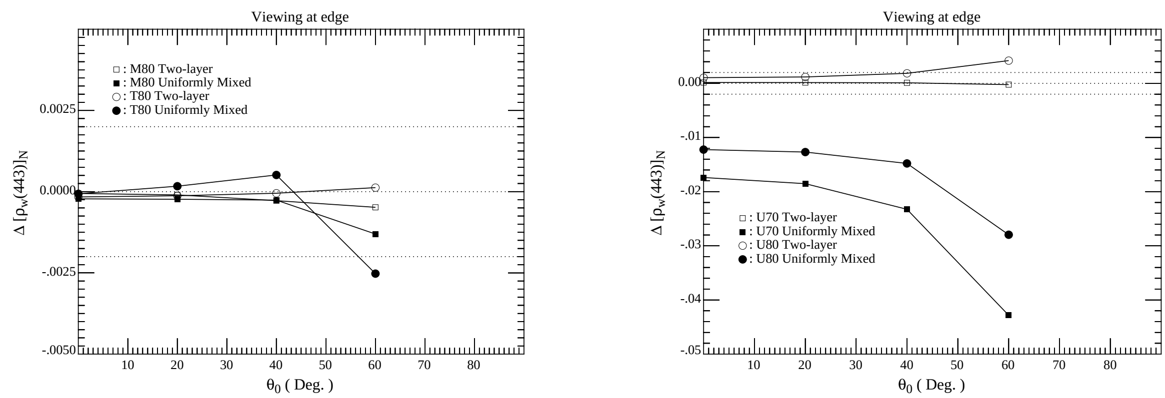

Figure 23. Effect of the vertical distribution of aerosol on $\Delta[\rho_w(443)]_N$ as a function of θ_0 at the edge of the scan $\tau_a(865) = 0.2$. Note that the correction algorithm assumes that the "Two-layer" stratification is correct. Left panel: T80 and M80. Right panel: U70 and U80.

As we have examined only an extreme deviation from that assumed by the correction algorithm, it is of interest to quantify how the correction algorithm performs as the aerosol layer thickens from being confined just near the surface to being mixed higher in the atmosphere. Thus, the top-of-atmosphere reflectance was simulated using a two layer model with aerosol *plus* Rayleigh scattering in the lower layer and *only* Rayleigh scattering in the upper layer. The fraction of the Rayleigh scattering optical thickness assigned to the lower layer was consistent with aerosol-layer thickness of 0, 1 km, 2 km, 4 km, 6 km, and ∞. The aerosol model used in the simulations was U80, and $\tau_a(865)$ was kept constant at 0.2. The multiple-scattering algorithm was then operated with this pseudo data using U50, U70, U90, and U99 as candidate models. The results of this exercise are provided in Figure 24. Clearly, progressive thickening of the layer in which the aerosol resides leads to a progressive increase in the error in the retrieved water-leaving reflectance.

This influence of vertical structure on the algorithm when the aerosol is strongly absorbing is easy to understand. The algorithm assumes all of the aerosol resides in a thin layer beneath the molecular scattering layer. As the aerosol layer thickens and encompasses more and more of the molecular scattering layer, the amount of Rayleigh scattering within the aerosol layer will increase causing an increase in the average path length of photons through the layer, and a concomitant

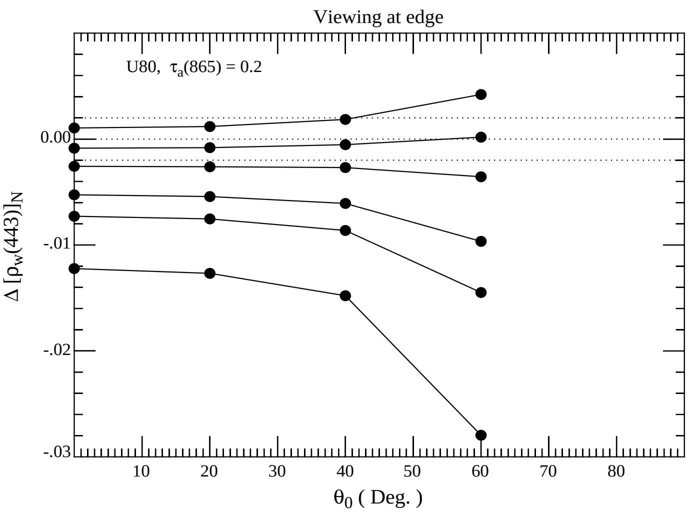

Figure 24. Effect of the vertical distribution of aerosol on $\Delta[\rho_w(443)]_N$ as a function of θ_0 at the edge of the scan for the U80 aerosol models with $\tau_a(865) = 0.2$. Curves from top to bottom refer to situations in which the aerosol is confined to a layer just above the surface, between the surface and 1, 2, 4, and 6 km, and uniformly mixed throughout the atmosphere.

increase in absorption. In addition, as the aerosol moves higher into the atmosphere, less Rayleigh scattering from the lower atmosphere will reach the TOA than would were the aerosol layer at the surface. The influence of the vertical extent of a strongly-absorbing aerosol layer is shown graphically in Figure 25 which relates the spectral variation of $\rho_a + \rho_{ra} = \rho_t - \rho_r - t\rho_w$ to the thickness of the aerosol layer for a *fixed* $\tau_a(865)$ of 0.2. Clearly, for a given τ_a, ρ_t will decrease as

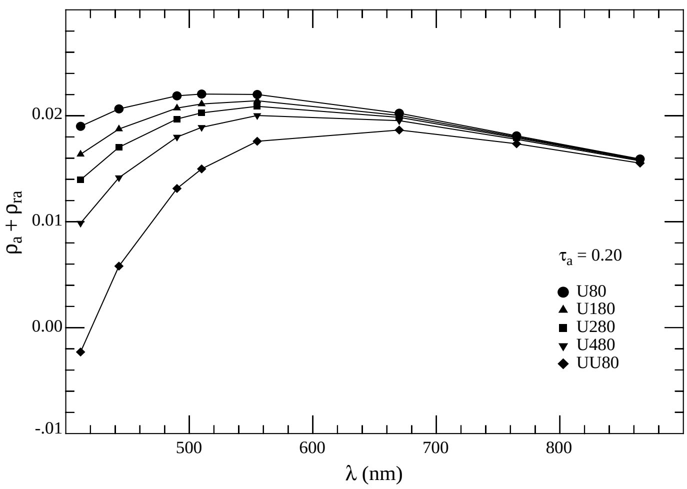

Figure 25. Influence of the physical thickness of the aerosol layer on the spectrum of $\rho_a + \rho_{ra}$. For U80 the aerosol is confined to a thin layer near the surface, while for U180, U280, U480, and UU80, the aerosol is uniformly mixed with air to a height of 1 km, 2 km, 4 km, and the whole atmosphere, respectively. Viewing is near nadir and $\theta_0 = 60°$.

the thickness of the aerosol layer increases. This decrease is relatively more in the visible than in the NIR, so as the layer thickens, the algorithm will predict values of $\rho_a + \rho_{ra}$ in the visible that are too large, yielding an over correction, $\Delta[\rho_w(443)]_N < 0$. Note that the behavior of $\rho_a + \rho_{ra}$ in the NIR provides little or no information regarding the vertical distribution of the aerosol.

Ding and Gordon [1995] (Figures 9 and 10) have provided some examples of the error in the multiple-scattering algorithm for vertical structures in which the aerosol model as well as concentration varies with altitude. For the weakly-absorbing aerosol of the models that they investigated ($\omega_a \gtrsim 0.93$), the conclusions are similar to those here: as long as the aerosol is weakly absorbing, the error is negligible, but as ω_a decreases, the error becomes progressively larger. Clearly, more study is required for a quantitative assessment of the impact of vertical structure in a strongly absorbing atmosphere; however, the computations provided here demonstrate that a large error in the vertical structure of the aerosol layer assumed for the lookup tables will result in a very poor atmospheric correction, even if the candidate aerosol models are appropriate. Figures 24 and 25 suggest that at a minimum, the lookup tables for the Urban candidates need to be recalculated under the assumption of an aerosol layer of finite physical thickness, i.e., some Rayleigh scattering in the aerosol layer. It also suggests that, for the case studied, if the lookup tables were computed for an aerosol layer of physical thickness 2 km, they would provide reasonable retrievals for layers with thicknessess from 1 to 3 km, i.e., the algorithm could tolerate a ± 1 km error in the layer thickness for this case. The influence of absorbing aerosols and methods for atmospheric correction in their presence is discussed further in Chapter 5.

3.1.1.12.2 Earth-Atmosphere Curvature Effects

All atmospheric corrections algorithms developed thus far ignore the curvature of the earth, i.e., the plane-parallel atmosphere approximation has been used in the radiative transfer simulations. However, at the level of accuracy required to utilize the full sensitivity of MODIS, it may be necessary to take the curvature of the earth into account, especially at high latitudes with their associated large θ_0 values. *Ding and Gordon* [1994] have examined this problem in detail using a model based on a spherical shell atmosphere solved with Monte Carlo techniques. It was found that as long as ρ_r was computed using a spherical shell atmosphere model, the multiple-scattering algorithm performed as well at high latitudes as at low latitudes. They provided a method for the computation of ρ_r for the spherical shell atmosphere; however, it has yet to be implemented for image processing.

3.1.1.12.3 Aerosol Polarization

All of the radiative transfer simulations described in Section 3.1.1 were carried out using scalar radiative transfer theory, i.e., polarization was ignored. In the case of single scattering, except for the terms involving the Fresnel reflectance, scalar (ignores polarization) and vector (includes polarization) radiative transfer theory lead to the same radiances. Thus, the single scattering algorithm is little influenced by polarization. It is well known, however, that, when multiple scattering is present, the use of scalar theory leads to small errors ($\sim$ few %) in the radiance compared to that computed using exact vector theory [*Gordon, Brown and Evans*, 1988; *Kattawar, Plass and Hitzfelder*, 1976]. As with CZCS, in the actual application of the algorithm, ρ_r is computed using vector theory; however, the lookup tables relating $\rho_a + \rho_{ra}$ to ρ_{as} have been computed using scalar theory. To understand the influence of neglecting polarization in the computation of the lookup tables, simulations of the top-of-the-atmosphere reflectance ρ_t were carried out using both scalar and vector radiative transfer theory. In the case of the scalar simulations, $[\rho_w(443)]_N$ was retrieved as described in Section 3.1.1.3. An identical retrieval procedure was used for the vector simulations with a single exception: as in the case of CZCS, ρ_r was computed using vector theory. The results are presented in Figure 26 for the M80 and T80 aerosol models. These figures provide

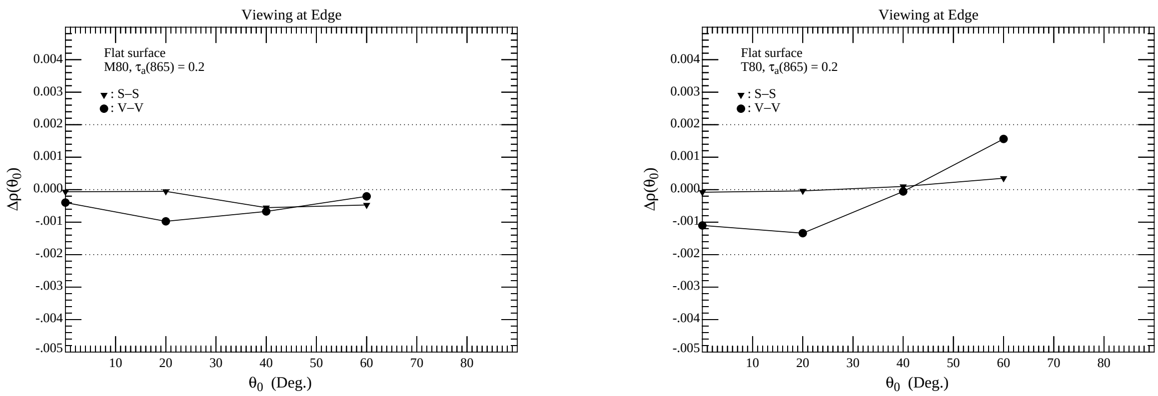

Figure 26. Effect of neglecting polarization in the multiple-scattering lookup tables. S–S and V–V are for ρ_t and ρ_r computed using scalar and vector radiative transfer theory, respectively. $\Delta\rho \equiv t\Delta\rho_w$ and $\tau_a(865) = 0.2$. Left panel: M80. Right panel: T80.

$\Delta\rho \equiv t\Delta\rho_w(443)$ (rather than $\Delta[\rho_w(443)]_N$ in the previous figures) produced by the multiple-scattering correction algorithm as a function of θ_0 for $\tau_a(865) = 0.2$. The notation "S–S" and "V–V" means that *both* ρ_t and ρ_r were computed using scalar (S–S) and vector (V–V) radiative transfer theory, respectively. Note that the difference between computations is the error induced by ignoring polarization in the preparation of the $\rho_a + \rho_{ra}$ versus ρ_{as} lookup tables. At present, only a small number of simulations of the type shown in Figure 26 have been carried out; however, for these the difference between S–S and V–V was typically $\lesssim$ 0.001 but reached as much as 0.002 in isolated cases. Thus, compared to the errors possible when strongly absorbing aerosols are present, this error appears negligible. It could be removed by recomputing the look up tables using vector radiative transfer theory, but at considerable computational cost.

3.1.1.12.4 Sea surface roughness

The roughness of the sea surface caused by the wind can play a large role on the reflectance measured at the top of the atmosphere. The principal effect of the rough surface is to redirect the direct solar beam reflected from the sea surface into a range of angles. This leads to a very large reflectance close to the specular image of the sun, know as sun glitter or the sun's glitter pattern.

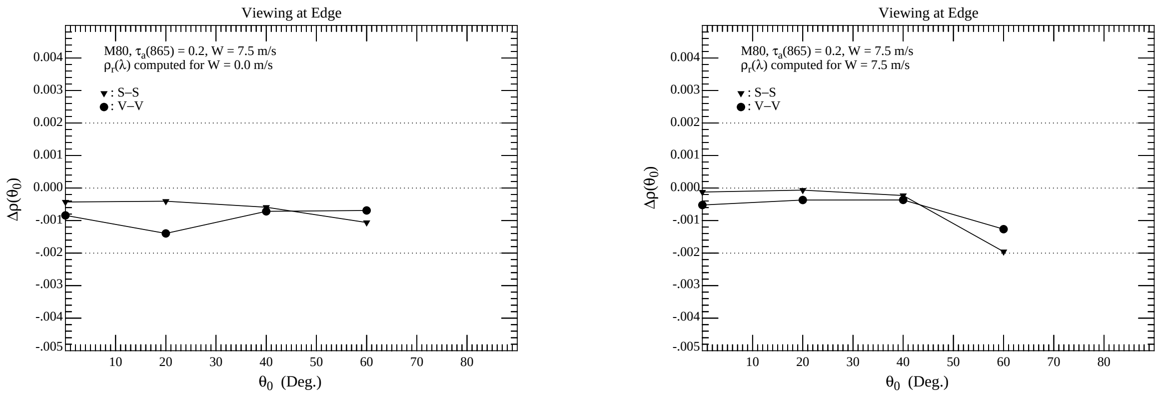

Figure 27. Effect of neglecting sea surface roughness in the multiple-scattering lookup tables. S–S and V–V are for ρ_t and ρ_r computed using scalar and vector radiative transfer theory, respectively. $\Delta\rho \equiv t\Delta\rho_w$, the aerosol model is M80, and $\tau_a(865) = 0.2$. Left panel: ρ_r has been computed assuming that $W = 0.0$ m/s. Right panel: ρ_r has been computed assuming that $W = 7.5$ m/s.

As this can be many times the radiance exiting the atmosphere in the smooth-surface case, the data in the region of the sun glitter must be discarded. This is accomplished by a mask as described in Section 3.1.1.7. The remainder of the rough-surface effect is due to a redistribution of light scattered from the reflected solar beam (because it is redirected) and a redistribution of sky light reflected from the surface (the Fresnel reflection terms in Eq. (9)). This redistribution of radiance contaminates the imagery over all viewing angles. As the lookup tables relating $\rho_a + \rho_{ra}$ to ρ_{as} were computed under the assumption that the surface was flat, it is necessary to examine the error in the water-leaving reflectance induced when viewing a rough ocean. This was effected by computing ρ_t for an ocean roughened by the wind and inserting the result into the multiple-scattering correction algorithm. In this simulation, the sea surface roughness was based on the *Cox and Munk* [1954] surface slope distribution function. For computational simplicity, an omnidirectional wind was assumed [*Cox and Munk*, 1954]. The wind speed was taken to be $\sim$ 7.5 m/s. Since *Gordon and Wang* [1992b] and *Gordon and Wang* [1992a] showed that at the radiometric sensitivity of SeaWIFS and MODIS, correct computation of the influence of surface roughness on ρ_r required use of vector radiative transfer theory, the computations were carried out using *both* scalar and vector theory. Sample results from one set of the small number of simulations that have been carried out to assess the effect of surface roughness are provided in Figure 27. These are in the same format as Figure 26. The differences between the two panels is that, in Figure 27 (left panel) ρ_r has been computed assuming a smooth sea surface (a wind speed of zero), while in Figure 27 (right panel) it has been computed using the correct (7.5 m/s) wind speed. For reference, Figure 26 (left panel) provides similar results for a smooth sea surface. Comparing Figures 26 and 27 (left panels) shows that the residual effect of the rough surface external to the sun's glitter pattern is small ($\Delta\rho \sim 0.0005$), and comparing Figures 26 (left panel) and 27 (right panel) shows that the residual effect can be removed by using the correct wind speed in the computation of ρ_r, i.e., ignoring the surface roughness in computation of the lookup tables relating $\rho_a + \rho_{ra}$ to ρ_{as} does not appear to lead to significant error.

In the present version of the algorithm, *both* polarization *and* wind speed (but not direction) are included in the computation of ρ_r.

3.1.1.12.5 Out-of-band Response

In the development of the algorithm, it has been assumed that the MODIS spectral bands were monochromatic, i.e., the reflectance ρ_t is measured at discrete wavelengths. However, the MODIS bands actually average the reflectance over spectral regions that are nominally 10–15 nm wide. Also, the possibility exists that there could be significant out-of-band response, i.e., contributions to the reflectance from spectral regions far from the band center. This problem was particularly severe in the case of the SeaWiFS band at 865 nm [*Barnes et al.*, 1994], for which $\sim$ 9% of the power measured in this band when observing Rayleigh-scattered sun light originates at wavelengths shorter than 600 nm. *Gordon* [1995] has developed a methodology for delineating the influence of finite spectral band widths and significant out-of-band response of sensors for remote sensing of ocean color. The basis of the method is the application of the sensor's spectral response functions to the individual components of the TOA radiance rather than the TOA radiance itself.

Let $S_i(\lambda)$ be the spectral response of the i^{th} spectral band. $S_i(\lambda)$ provides the output current (or voltage) from the detector for a unit radiance of wavelength λ, e.g., $\int S_i(\lambda)\,d\lambda$ would be the output current for a *spectrally flat* source of radiance of magnitude 1 mW/cm$^2\mu$m Sr. We define the "band" radiance for the i^{th} spectral band when viewing a source of radiance $L(\lambda)$ to be

$$\langle L(\lambda)\rangle_{S_i} \equiv \frac{\int L(\lambda)S_i(\lambda)\,d\lambda}{\int S_i(\lambda)\,d\lambda} \tag{23}$$

The output current (or voltage) will then be $\propto \langle L(\lambda)\rangle_{S_i}$.

Given $S_i(\lambda)$, we can compute the band-averaged quantities needed to operate the algorithm following *Gordon* [1995]. These are $\langle F_0(\lambda)\rangle_{S_i}$, $\langle k_{Oz}(\lambda)\rangle_{F_0S_i}$, and $\langle \tau_r(\lambda)\rangle_{F_0S_i}$, where $k_{Oz}(\lambda)$ is the Ozone absorption coefficient defined so that the Ozone spectral optical depth for a concentration of DU (Dobson units or milliatmosphere centimeters) is

$$\tau_{Oz}(\lambda) = k_{Oz}(\lambda)\frac{DU}{1000},$$

$$\langle k_{Oz}(\lambda)\rangle_{F_0S_i} \equiv \frac{\int k_{Oz}(\lambda)F_0(\lambda)S_i(\lambda)\,d\lambda}{\int F_0(\lambda)S_i(\lambda)\,d\lambda}, \tag{24}$$

and

$$\langle \tau_r(\lambda)\rangle_{F_0S_i} \equiv \frac{\int \tau_r(\lambda)F_0(\lambda)S_i(\lambda)\,d\lambda}{\int F_0(\lambda)S_i(\lambda)\,d\lambda}. \tag{25}$$

We have computed these band-averaged quantities using the MODIS relative spectral response functions (Table 8). In addition, we examined the influence of the water vapor absorption bands on the computation of the Rayleigh reflectance. For MODIS, the error in ignoring water vapor (up to a concentration of 3.3 g/cm^2) is a maximum of 0.25% (for Band 15). For the other spectral bands, the error is $< 0.1\%$. In contrast, for SeaWiFS the maximum error is 0.55%.

Table 8: Band-averaged quantities needed to compute the Rayleigh reflectance and the Ozone transmittance for the MODIS bands.

λ (nm)	Band (i)	$\langle \tau_r(\lambda) \rangle_{F_0 S_i}$	$\langle F_0(\lambda) \rangle_{S_i}$ mW/cm$^2\mu$m sr	$\langle k_{Oz}(\lambda) \rangle_{F_0 S_i}$ ($\times$1000)
412	8	0.3167	170.37	1.47
443	9	0.2377	186.50	3.78
488	10	0.1610	191.82	22.21
531	11	0.1135	188.57	65.66
551	12	0.0999	187.16	83.22
667	13	0.0446	154.15	48.69
678	14	0.0417	149.88	39.95
748	15	0.0286	128.07	12.02
869	16	0.0156	97.30	3.75

Finally, the presence of other absorbing gases, over and above Ozone, e.g., water vapor, and the out-of-band response will also influence the aerosol part of the atmospheric correction algorithm. *Gordon* [1995] showed that this can be taken into account by introducing a factor f_i (for band i) defined by

$$f_i \equiv \frac{\langle \varepsilon(\lambda, 865) \rangle_{F_0 S_i}}{\varepsilon(\lambda_i, 865)},$$

where λ_i is the nominal center wavelength for band i, i.e., the wavelength at which the radiative transfer simulations are carried out to produce the lookup tables required by the algorithm. The algorithm is then operated in the normal manner, but with Eq. (13) replaced by

$$\langle \rho_a(\lambda) + \rho_{ra}(\lambda) \rangle_{F_0 S_i} = f_i \, K[\lambda, \rho_{as}(\lambda_i)] \, \rho_{as}(\lambda_i).$$

Approximating $\varepsilon(\lambda_i, \lambda_l)$ by

$$\varepsilon(\lambda_i, \lambda_l) = \exp[c(\lambda_l - \lambda_i)],$$

where c is a constant, and using LOWTRAN to compute the atmospheric transmittance, *Gordon* [1995] found that

$$f_i = f_i(c, M, w),$$

where M is the two-way air mass $(1/\cos\theta_v + 1/\cos\theta_0)$ and w is the column water vapor concentration. This function can be approximated by an equation of the form

$$\begin{aligned} f_i(c, M, w) = {} & (a_{01} + a_{02}M) + (a_{03} + a_{04}M)c \\ & + \big[(a_{11} + a_{12}M) + (a_{13} + a_{14}M)c\big]w \\ & + \big[(a_{21} + a_{22}M) + (a_{23} + a_{24}M)c\big]w^2. \end{aligned} \tag{26}$$

Only in the case of Bands 13 (667 nm) and 15 (749 nm) does f_i differ from unity by more than 1%.

Table 9: Coefficients a_{nm} in Eq. (26) for MODIS Bands 12–16, for c in nm^{-1} and w in gm/cm^2. Notation ± 2 stands for $10^{\pm 2}$, etc.

Coefficient	a_{nm}				
	Band 12	Band 13	Band 14	Band 15	Band 16
a_{01}	+1.000 −0	+9.993 −1	+9.989 −1	+9.983 −1	+9.995 −1
a_{02}	−4.530 −6	−4.413 −4	−3.736 −4	−9.267 −4	−2.086 −4
a_{03}	+4.389 +0	−1.662 −1	−4.619 −1	+3.304 +0	+3.197 +0
a_{04}	−1.887 −4	+1.661 −2	+2.127 −2	−9.455 −3	−1.267 −3
a_{11}	−2.210 −5	−1.815 −3	−8.808 −4	−3.692 −3	−8.618 −4
a_{12}	−9.093 −6	−1.107 −3	−3.267 −4	−2.222 −3	−4.033 −4
a_{13}	+1.498 −3	+7.502 −2	+8.673 −2	−2.516 −2	+5.332 −3
a_{14}	+1.225 −3	+1.323 −2	+1.670 −2	−1.816 −2	−2.000 −3
a_{21}	+2.646 −6	+1.808 −4	+9.649 −5	+3.295 −4	+9.147 −5
a_{22}	+1.002 −6	+1.003 −4	+3.504 −5	+2.263 −4	+4.084 −5
a_{23}	+1.395 −4	−8.489 −3	−9.963 −3	+2.104 −3	−8.560 −4
a_{24}	−2.259 −4	−2.504 −3	−2.678 −3	+1.814 −3	+1.008 −4

However, except for Bands 8–11, f_i differs from unity by more than 0.5%, so correction is required. The coefficients a_{nm} have been computed for the individual MODIS spectral bands (12–16). The values of a_{nm} for these bands are provided in Table 9.

3.1.1.13 Remaining Issues

Although the algorithm described above has been implemented and used for Terra MODIS processing, there are other questions and issues that are also being studied but are *not* included in the present processing code. These are outlined in the present section. Plans for enhancing the processing code to address some of these issues are provided in Chapter 5.

3.1.1.13.1 Stratospheric Aerosols and Thin Cirrus Clouds

In some situations, e.g., following volcanic eruptions or when there are thin cirrus clouds present, there can be significant quantities of aerosol in the stratosphere. *Gordon and Castaño* [1988] showed that the presence of the El Chichón aerosol [*King, Harshvardhan and Arking*, 1984] had little effect on CZCS atmospheric correction; however, at the higher correction accuracy required for MODIS the *Gordon and Wang* [1994a] algorithm may be degraded by the presence of stratospheric aerosol. Although not listed in Table 1, MODIS is equipped with a spectral band at 1380 nm that can be used to assess the contamination of the imagery by stratospheric aerosol. This spectral band is centered on a strong water vapor absorption band and photons penetrating through the stratosphere will usually be absorbed by water vapor in the free troposphere [*Gao, Goetz and Wiscombe*, 1993]. Thus, any radiance measured at 1.38 μm can, in the first approximation, be assumed to be scattered by the stratospheric aerosol alone, providing a mechanism for estimating the stratospheric contribution.

The author and coworkers [*Gordon et al.*, 1996] have assessed the effect of stratospheric aerosols on atmospheric correction and studied ways in which to correct the contamination, assuming that all radiance detected at 1380 nm results from scattering by the stratospheric aerosol *alone*. Briefly, the stratospheric aerosol contributes to the reflectance at all wavelengths. Thus, in its presence the total reflectance will be changed by an amount $\delta\rho_t^{(s)}$, i.e.,

$$\rho_t^{(s)}(\lambda) = \rho_t(\lambda) + \delta\rho_t^{(s)}(\lambda),$$

where $\rho_t^{(s)}$ is the reflectance of the entire ocean-atmosphere system in the presence of stratospheric aerosol, and ρ_t the reflectance in its absence. To assess the impact of the stratospheric aerosol, the multiple-scattering algorithm was operated using simulated values of $\rho_t^{(s)}(\lambda)$ in the place of $\rho_t(\lambda)$, for four stratospheric aerosol types. The results suggest that stratospheric aerosol/cirrus cloud contamination does not seriously degrade the *Gordon and Wang* [1994a] algorithm except for large ($\sim 60°$) solar zenith angles and large ($\sim 45°$) viewing angles, for which multiple scattering effects can be expected to be particularly severe.

The performance of a hierarchy of algorithms for using the 1380 nm MODIS band to correct for stratospheric aerosol/cirrus clouds, was also examined. The approach was to use $\rho_t^{(s)}(1380)$

to estimate $\delta\rho_t^{(s)}(\lambda)$ in the visible and NIR. The procedures investigated ranged from from simply subtracting the reflectance at 1380 nm from that in the visible bands, i.e., $\delta\rho_t^{(s)}(\lambda) = \rho_t^{(s)}(1380)$, to assuming all of the optical properties of the stratospheric aerosol are known (the reflectance measurement at 1380 nm providing the concentration) and carrying out multiple scattering computations to estimate $\delta\rho_t^{(s)}(\lambda)$. It is not surprising that the most complex procedures yield the best results; however, it was surprising that the complex procedures appear to only reduce the error in the retrieved water-leaving radiance by $\lesssim$ a factor of two compared to the simplest procedures.

In the case of thin cirrus clouds, *Gordon et al.* [1996] investigated an empirical correction approach in which a detailed model of the cloud optical properties was not required. This correction proved to be satisfactory for cloud optical thicknesses as large as 0.5 with only a coarse estimate of the cloud scattering phase function; however, the correction requires some knowledge regarding the aerosol in the marine boundary layer and, therefore, *requires two passes* through the aerosol correction algorithm.

The 1.38 μm band has not yet been used to screen or correct for thin cirrus, due to its initial poor performance on the Terra platform. Performance on Aqua appears to be much better and these ideas could be implemented in Aqua processing.

3.1.1.13.2 Appropriateness of aerosol models

Operation of the multiple-scattering algorithm requires a set of candidate aerosol models. Thus far, models from, or derived from, the work of *Shettle and Fenn* [1979] have been used as candidates. These models were basically developed from the analysis of aerosol physical-chemical properties and are believed to provide realistic approximations to the extinction and absorption cross section of real aerosols. However, they have never been validated for the role they are being used for here, i.e., for their ability to provide realistic aerosol phase functions and their spectral variation. It is important to utilize as candidates, aerosol models that closely approximate the optical properties of actual aerosols over the ocean, and studies of the optical properties of aerosols over the ocean have been carried out and are on going.

Measurements over and above aerosol optical thickness and its spectral variation are required to understand the adequacy of candidate aerosol models. *Schwindling* [1995] compared estimates of the aerosol scattering phase function obtained from a pier at Scripps Institution of Oceanography, La Jolla, CA, with the properties of the *Shettle and Fenn* [1979] models and concluded that within the accuracy of their measurements the models fit both the phase function and the spectral variation of the aerosol optical thickness. It was also confirmed that $\tau_a(\lambda)$ becomes very low off the coast of California. However, as there was a need to carry out such measurements in different regions and at different times, the AERONET aerosol monitoring network [*Holben et al.*, 1998] based on CIMEL sun/sky radiometers was expanded to include stations at the coast and on small islands.

Smirnov et al. [2003] have analyzed the CIMEL data acquired on the islands of Bermuda (Atlantic Ocean), Lanai, Hawaii (Pacific Ocean), and Kaashidhoo, Maldives (Indian Ocean). The results of their analysis are the size distributions from which aerosol scattering phase functions and other optical properties are derived. Since the basic measurement is optical (sky radiance and sun photometry), the retrieved columnar optical properties should be reasonably accurate. The size distribution components representing average conditions, when the optical depth is low ($\tau_a(500) < 0.15$), are compared with those of *Shettle and Fenn* [1979] (for dry particles) in Figure 28. In the figure, the individual components have been normalized to their maximum values. In

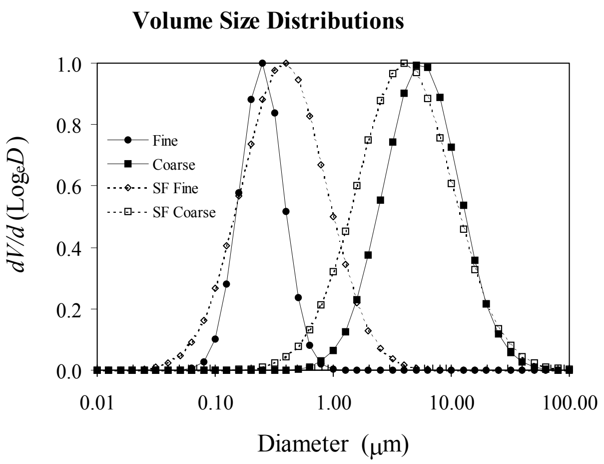

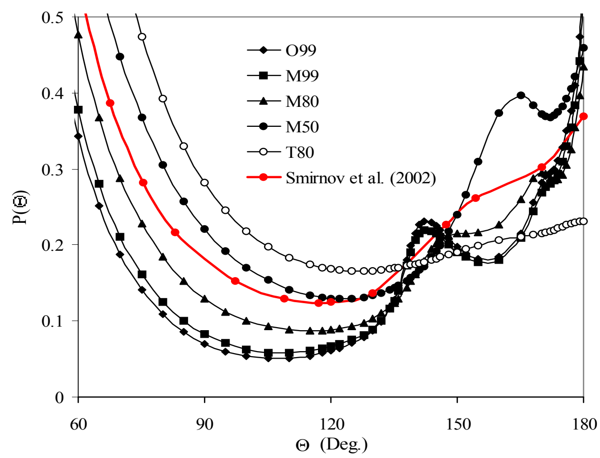

Figure 28. Comparison of size distribution modes (fine and course) and scattering phase functions (865 nm) derived from CIMEL measurements at remote island stations, with a selection from *Shettle and Fenn* [1979] ("SF") used in MODIS processing.

reality, the total volume of the fine mode (smaller size) is approximately 20% of the total; however, in a maritime atmosphere influenced by anthropogenic activities, the relative contribution of the fine component increases. It is seen that the individual mode distributions are similar; however, as the relative humidity increases, the median size of the *Shettle and Fenn* [1979] coarse mode (the Oceanic) shifts to larger particle sizes. (Note, the *Smirnov et al.* [2003] are for the *ambient* relative humidity.) Figure 28 also compares the scattering phase functions (at 865 nm) used in MODIS processing with the mean for a maritime atmosphere from *Smirnov et al.* [2003]. The mean *Smirnov et al.* [2003] falling approximately midway between the *Shettle and Fenn* [1979] M50 and M80. This suggests that the optical properties predicted by the *Shettle and Fenn* [1979] maritime models should be reasonably representative of an unpolluted marine aerosol.

The agreement between the size distributions and scattering phase functions of *Smirnov et al.* [2003] and *Shettle and Fenn* [1979] for a marine atmosphere does not suggest that the *Shettle and Fenn* [1979] models are appropriate for all situations. Rather, it suggests that the models that are employed in the SeaWiFS and MODIS processing are appropriate for *most* of the open ocean. Indeed, there are special situations, e.g., marine environments influenced by anthropogenic pollution or mineral dust transported by the winds. *Remer and Kaufman* [1998] analyzed CIMEL measurements made in the mid-Atlantic region of the U.S. in the summer of 1993, and found that there was a strong correlation between the size distribution and the optical thickness. For low optical depth, their retrieved size distribution is similar to *Smirnov et al.* [2003]; however as the optical depth increases beyond 0.2 (at 670 nm) they found that an additional fine mode was required with modal diameter about twice that of the original fine mode. The contribution of this second fine mode increased as the optical thickness increased, as did the course mode. Thus, the size distribution is dynamically related to τ_a.

In the case of windblown dust, the absorption properties are of special interest because the dust is colored (saharan dust is a pale shade of red). Thus, the refractive index is a strong function of wavelength. Appropriate models for atmospheric correction in the presence of Saharan dust are provided in Section 5.1.1.

Pragmatically, the appropriateness of the aerosol models is determined by the success of atmospheric correction. This can be assessed using SeaWiFS imagery because it is more mature than MODIS, i.e., there are more comparison data available. It has been clearly demonstrated that the Gordon and Wang algorithm, using the Shettle and Fenn aerosol models, works well with SeaWiFS data [*Hooker and McClain*, 2000]. In addition, although unnecessary for atmospheric correction, *Wang, Bailey and McClain* [2000] and *Wang et al.* [2000] have shown that the SeaWiFS algorithm also provides reasonably good estimates of the aerosol optical depth at 865 nm. To first order, the error in optical depth estimates in the NIR is directly proportional to the error in the product of the aerosol phase function and the single scattering albedo [*Wang and Gordon*, 1994a] Thus, application of the present scheme, including the Shettle and Fenn models, has been shown to provide an acceptable atmospheric correction and even reasonably good optical depth retrievals in *most* situations. This implies that the presently used models are realistic enough for the task of atmospheric correction of most ocean color imagery produced by the present-generation sensors. However, it was noticed that with SeaWiFS, the measured $\varepsilon(765, 865)$ was often below the lowest

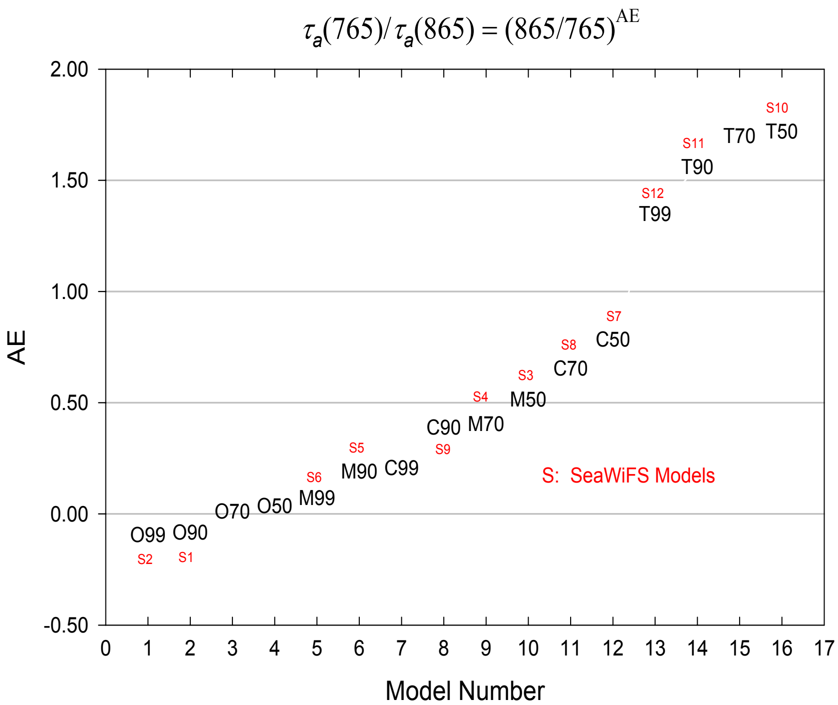

Figure 29. Candidate aerosol models used in the MODIS and SeaWiFS atmospheric correction as a function of their Angstrom exponent (AE). The SeaWiFS model numbers are preceded by "S," i.e., the MODIS model number 1, O99, is the SeaWiFS model number 2, etc.

value for the M, C, and T models. This suggested models with fewer small particles was required. Thus, we (and the SeaWiFS Project) added the "Oceanic" ("O") models of *Shettle and Fenn* [1979] to the candidate list, expanding the number of candidates from 12 to 16 (for MODIS). Figure 29 provides the MODIS and SeaWiFS aerosol models (by number) that are being used for routine processing at the present time.

3.1.1.13.3 Strongly Absorbing Aerosols

In Section 3.1.1.4 it was shown that in the presence of strongly absorbing aerosols, the candidate aerosol models must be restricted to those with values of ω_a similar to the true aerosol. This was effected there by limiting the candidate models to U50, U70, U90, and U99 when the test aerosol was U80 (Figure 13), since when the initial twelve candidate models were used, the error was excessive (Figure 12). Without a method of determining the absorption characteristics of the aerosols from satellite measurements, an aerosol climatology is required to be able to provide realistic candidate models. Furthermore, in Section 3.1.1.12.1 it was shown that, for strongly absorbing aerosols, even given the appropriate set of candidate models, knowledge of the vertical distribution of the aerosol was required for an adequate correction (Figure 24). Thus, the aerosol climatology needs to contain information concerning the aerosol-layer thickness for regions with strongly absorbing aerosols.

The effort toward building a climatology for absorbing aerosols involves measurements of the type discussed in Section 3.1.1.13.2, i.e., measurements of sky radiance and aerosol optical thickness from ships or small islands in the appropriate regions as are being carried out by AERONET [*Holben et al.*, 1998]. A climatology for the aerosol vertical distribution can be built most effectively using LIDAR measurements [*Sasano and Browell*, 1989]. An excellent start toward a vertical distribution climatology can be made utilizing data from the Lidar In-Space Technology Experiment (LITE) [*McCormick*, 1995]. On the basis of LITE-based and aircraft-based measurements *Grant et al.* [1995] observed that the Saharan dust layer over the Eastern Caribbean extended in altitude from 1-4 km. This is in contrast to the dust-free atmosphere in which the thickness of the aerosol layer is typically 1-2 km. Examining a LITE pass from Wallops Island, Virginia to Bermuda, *Ismail et al.* [1995] found that the plume of pollution from the U.S. East Coast was in a 1-2 km thick layer above the 0.5-1.0 km thick maritime boundary layer. These observations suggest that the principal absorbing aerosols expected in the Atlantic are mixed higher in the atmosphere than assumed in the existing candidate aerosol model lookup tables. We have been using a micro pulse lidar [*Spinhirne*, 1993] to study the vertical distribution of aerosol in conjunction with large-scale aerosol experiments, e.g., ACE-2, INDOEX, ACE-Asia, etc. [*Voss et al.*, 2001; *Welton et al.*, 2000; *Welton et al.*, 2002].

It must be pointed out that, with the exception of TOMS [*Herman et al.*, 1997], there is no space-borne way of discriminating between weakly- and strongly-absorbing aerosols (however, see Chapter 5). Clearly, it would be extremely useful to be able to detect the presence of absorbing aerosols from measurements made by the ocean color sensor alone, e.g., to be able to distinguish between absorbing and nonabsorbing aerosols. *Gordon* [1997] proposed a method for using $\rho_t(\lambda)$ for $\lambda > 865$ nm for detecting mineral dust based on the variation of its optical properties in the short-wave infrared (SWIR). Because the performance of the MODIS SWIR bands may not be as good as expected, this approach has not been pursued.

Finally, the fact that TOMS is capable of detecting the presence of strongly-absorbing aerosols [*Herman et al.*, 1997] provides an exciting possibility of using such data to aid in atmospheric correction. We note, however, that using this data on an operational basis would introduce a delay in the processing of MODIS data. Two alternatives to using TOMS data are provided in Chapter 5.

3.1.1.13.4 In-Water Radiance Distribution

Algorithms for retrieving total pigments, chlorophyll, etc., from ocean color imagery are developed by relating the nadir-viewing water-leaving radiance to the quantity in question. In the analysis of ocean color imagery it has always been assumed that $[\rho_w]_N$ is independent of the viewing angle. This assumption was based on a small number of observations, e.g., see *Smith* [1974] and references therein, which suggests that $L_u(z, \theta, \phi)$, the upwelling radiance at depth z beneath the surface and traveling in a direction specified by the angles (θ, ϕ), is only weakly dependent on θ and ϕ. However, in a series of papers Morel and Gentili [*Morel and Gentili*, 1991; *Morel and Gentili*, 1993; *Morel and Gentili*, 1996] studied theoretically the bidirectional effects as a function of the sun-viewing geometry and the pigment concentration. Their simulations suggest that, although the bidirectional effects nearly cancel in the estimation of the pigment concentration using radiance ratios (Eq. (4)), $L_u(z, \theta, \phi)$ can depend significantly on θ, ϕ and θ_0. This means that the value of $[\rho_w]_N$ retrieved in atmospheric correction is actually appropriate only to the viewing direction in which the measurement of ρ_t is made. Since most in-water algorithms have been developed based on nadir-viewing measurements, the derived $[\rho_w]_N$ values should be corrected to nadir-viewing geometry. This requires understanding the bidirectional effects, i.e., validating the *Morel and Gentili* [1996] model or developing a new model. This is being effected by direct determination of the upwelling radiance distribution for a variety of waters and solar zenith angles using an electro-optics radiance camera system developed by *Voss* [1989], e.g., see *Morel, Voss and Gentili* [1995]. These measurements provide direct determination of the effect, and will yield an algorithm for extrapolation to the nadir viewing direction as required for derived product algorithms.

It is useful to review the bidirectional nature of the water-leaving radiance in some detail. Although we have used reflectance rather than radiance to develop and explain the algorithm, here we revert to radiance, noting that the normalized water-leaving reflectances and radiances are related through

$$[\rho_w]_N = \frac{\pi}{F_0}[L_w]_N.$$

Following *Morel, Antoine and Gentili* [2002], the normalized water-leaving radiance seen by MODIS based on the retrieval of $L_w(\theta_v, \phi_v)$ is given by

$$[L_w(\theta_v, \phi_v; \theta_0)]_N = \left[\frac{\overline{T}_f(\theta_0)T_f(\theta_v')}{m^2\big(1 - rR(\theta_0)\big)}\right]\frac{R(\theta_0)}{Q(\theta_v', \phi_v; \theta_0)}, \tag{27}$$

where θ_0 is the solar zenith angle, θ_v and ϕ_v are the viewing angles (ϕ_v measured relative to the sun), $R(\theta_0)$ is the subsurface irradiance reflectance for a solar zenith angle θ_0, and $Q(\theta_v', \phi_v; \theta_0)$ is the so-called "Q-factor" defined as the upwelling irradiance just beneath the water surface E_u divided by the upwelling radiance just beneath the surface in the viewing direction $L_u(\theta_v', \phi_v; \theta_0)$. The angles θ_v' and θ_v are related by Snell's law : $m \sin\theta_v' = \sin\theta_v$, where m is the refractive index of sea water. $\overline{T}_f(\theta_0)$ is the transmittance (above the sea surface $\rightarrow$ below the sea surface) for downwelling irradiance from the sun and sky, and $T_f(\theta_v')$ is the transmittance of $L_u(\theta_v', \phi_v; \theta_0)$ across the air-sea interface, i.e.,

$$L_w(\theta_v, \phi_v; \theta_0) = \frac{T_f(\theta_v')}{m^2}L_u(\theta_v', \phi_v; \theta_0).$$

Note that in this section we depart from our usual notation for the water-leaving radiance, i.e., $L_w(\theta_v, \phi_v)$, and specifically introduce the solar zenith angle θ_0 in the argument list. This is to provide the reader with a reminder of the position of the sun in each definition below.

The term in the brackets in Eq. (27) is denoted $\Re(\theta_v, \theta_0)$ by Morel and Gentili, i.e.,

$$\Re(\theta_v', \theta_0) = F_0 \frac{\overline{T}_f(\theta_0) T_f(\theta_v')}{m^2\big(1 - rR(\theta_0)\big)}.$$

With the exception of $R(\theta_0)$ in the denominator, this term depends solely on the air-sea interface, i.e., the actual roughness of the wind roughened sea surface (and therefore the wind speed and direction), the sun angle, and the viewing direction. The term r accounts for the contribution of internal reflections reflections within the medium. When the upward radiance is totally diffuse, $r \approx 0.48$ and almost independent of surface roughness [*Austin*, 1974], so since R is usually < 0.1, the contribution of this term is small; however it does depend on the angular distribution of the upwelling radiance distribution.

There are three important normalized water-leaving radiances that can be defined. The first is that of *Gordon and Clark* [1981], the radiance that exits the water traveling toward the zenith when the sun is at the zenith and there is no atmosphere:

$$[L_w]_N^{\text{Exact}} \equiv [L_w(0, \bullet; 0)]_N = F_0 \Re(0, 0) \, \frac{R(0)}{Q(0, \bullet; 0)}. \tag{28}$$

The second is the normalized water-leaving radiance that is usually measured at sea, i.e., the radiance propagating toward the zenith, but with the sun not necessarily at the zenith:

$$[L_w]_N^{\text{Field}} \equiv [L_w(0, \bullet; \theta_0)]_N = F_0 \Re(0, \theta_0) \, \frac{R(\theta_0)}{Q(0, \bullet; \theta_0)}. \tag{29}$$

Finally, the third is the normalized water-leaving radiance deduced from the measurement of $L_w(\theta_v, \phi_v)$ by a space-borne sensor:

$$[L_w]_N^{\text{Space}} \equiv [L_w(\theta_v, \phi_v; \theta_0)]_N = F_0 \Re(\theta_v', \theta_0) \, \frac{R(\theta_0)}{Q(\theta_v', \phi_v; \theta_0)}. \tag{30}$$

It is reasonable to refer all $[L_w]_N$ measurements, either from the surface or from space, to the same geometry. This is conventionally taken to be $[L_w]_N^{\text{Exact}}$. Thus,

$$[L_w]_N^{\text{Exact}} = \frac{\Re(0, \theta_0)}{\Re(0, 0)} \frac{Q(0, \bullet, 0)}{Q(0, \bullet, \theta_0)} \frac{R(\theta_0)}{R(0)} [L_w]_N^{\text{Field}} \tag{31}$$

and

$$[L_w]_N^{\text{Exact}} = \frac{\Re(\theta'_v, \theta_0)}{\Re(0,0)} \frac{Q(0, \bullet, 0)}{Q(\theta'_v, \phi_v, \theta_0)} \frac{R(\theta_0)}{R(0)} [L_w]_N^{\text{Space}}. \tag{32}$$

We note that deriving $[L_w]_N^{\text{Exact}}$ requires detailed modeling of Q as a function of sun-viewing geometry, R as a function of the solar zenith angle, and $\Re$ as a function of surface roughness (wind speed). $[L_w]_N^{\text{Exact}}$ is the radiance that is planned for the TERRA/MODIS Level 2 product after validation; however, for vicarious calibration and/or validation purposes, one wants to compare simultaneous measurements of $[L_w]_N^{\text{Field}}$ and $[L_w]_N^{\text{Space}}$. These quantities are related through

$$\frac{[L_w]_N^{\text{Field}}}{[L_w]_N^{\text{Space}}} = \frac{\Re(0, \theta_0)}{\Re(\theta'_v, \theta_0)} \frac{Q(\theta'_v, \phi_v, \theta_0)}{Q(0, \bullet, \theta_0)} = \frac{T_f(0)}{T_f(\theta'_v)} \frac{Q(\theta'_v, \phi_v, \theta_0)}{Q(0, \bullet, \theta_0)}, \tag{33}$$

with no dependence[5] on R. This is the normalization that has been reported in the TERRA/MODIS Level 2 product, i.e., $[L_w]_N^{\text{Space}}$ has been converted to $[L_w]_N^{\text{Field}}$ using (33). This conversion is effected using a revised Morel-Gentili model [*Morel, Antoine and Gentili*, 2002].

3.1.1.13.5 Diffuse transmittance

As described in Section 3.1.1.5, the present MODIS algorithm replaces the actual diffuse transmittance $t(\theta_v, \phi_v)$, computed using the actual upwelling radiance distribution just beneath the sea surface, $L_u(\theta'_v, \phi'_v)$, with the diffuse transmittance $t^*(\theta_v, \phi_v)$, computed for a uniform L_u, i.e., an L_u independent of viewing direction. This introduces error into the retrieval of ρ_w. To find the effect of $L_u(\theta'_v, \phi'_v)$ on the true diffuse transmittance consider the following problem. Let F_0 be the extraterrestrial solar irradiance, $\hat{\xi}_0$ a unit vector in the direction of propagation of the solar beam, and $L_R(\hat{\xi})$ the resulting radiance propagating downward just beneath the sea surface in the direction $\hat{\xi}$. Then, *Yang and Gordon* [1997] show that

$$t(-\hat{\xi}_0) = \frac{1}{F_0 |\hat{\xi}_0 \bullet \hat{n}_0| T_f(\hat{\xi}_0)} \int_{\Omega_d} |\hat{\xi} \bullet \hat{n}| L_R(\hat{\xi}) \frac{L_u(-\hat{\xi})}{L_u(-\hat{\xi}'_0)} d\Omega(\hat{\xi}), \tag{34}$$

where $L_u(-\hat{\xi})$ is the upward radiance distribution incident just beneath the sea surface for which we want t, $\hat{\xi}'_0$ and $\hat{\xi}_0$ are related by Snell's law, and Ω_d indicates the integral is to be evaluated over all downward $\hat{\xi}$. Note that when L_u is taken to be totally diffuse (independent of $\hat{\xi}$), the result reduces to the formula for t^* in Section 3.1.1.5.

[5] This ignores the weak dependence of r on Q.

The error in the retrieved ρ_w induced by using t^* in place of t is just

$$\frac{\Delta\rho_w(-\hat{\xi}_0)}{\rho_w(-\hat{\xi}_0)} = \frac{t(-\hat{\xi}_0) - t^*(-\hat{\xi}_0)}{t^*(-\hat{\xi}_0)}. \tag{35}$$

Yang and Gordon [1997] have examined the magnitude of the error for measured radiance distributions $L_u(-\hat{\xi})$ [*Voss*, 1989] and various aerosol concentrations. They conclude that the error induced in using t^* in place of t can be as large as $\pm 4\%$, and is largest in the blue. Thus, derivation of $\rho_w(443)$ within $\pm 5\%$ will require knowing, or estimating, the shape of the subsurface radiance distribution. It is important to understand that this error represents the natural limit in the accuracy of atmospheric correction when t^* is employed rather than t. *Morel and Gentili* [1996] have devised an iterative scheme for estimating the shape of the subsurface radiance distribution from an estimate of the pigment concentration. Such a scheme (or some alternative that requires multiple passes through the atmospheric correction algorithm) will be required to provide a more realistic value for t; however, this cannot be effected until the Morel and Gentili model is completely validated using the measurement program described in Section 3.1.1.13.4.

3.1.2 Mathematical Description of the Algorithm

The multiple-scattering algorithm was initially implemented as described in Section 3.1.1.3, i.e., lookup tables (LUTs) providing $K[\lambda, \rho_{as}(\lambda)]$, in the form of $a(\lambda)$, $b(\lambda)$, and $c(\lambda)$ in Eq. (14), for all required viewing geometries, solar zenith angles, wavelengths, aerosol models, and aerosol concentrations, were used to provide the $\rho_t - \rho_r - t\rho_w$ versus ρ_{as} relationship. These tables were derived by solving the RTE for each aerosol model and geometry using a two-layer representation of the vertical structure of the atmosphere — aerosols in the lower layer and Rayleigh scattering in the upper layer. Late in the implementation it was found that for strongly absorbing aerosols, e.g., the Urban models, and large θ_0, it was possible that $\rho_t - \rho_r - t\rho_w < 0$, making it impossible to use Eq. (14) because of the logarithms. To avoid this, we reformulated the LUTs by replacing Eq. (14) with

$$\rho_t(\lambda) - \rho_r(\lambda) - t\rho_w(\lambda) = a(\lambda)\rho_{as} + b(\lambda)\rho_{as}^2 + c(\lambda)\rho_{as}^3 + d(\lambda)\rho_{as}^4,$$

where, as before, for each θ_v, ϕ_v, θ_0, and ϕ_0, the coefficients a, b, c, and d were obtained from the simulations by least-squares. As in the case of Eq. (14), for the azimuth difference $\phi_v - \phi_0$, we expanded $a(\lambda)$, $b(\lambda)$, $c(\lambda)$ and $d(\lambda)$ in a Fourier series and stored only the Fourier coefficients. As the reflectances are even functions of the azimuth difference $\phi_v - \phi_0$, $a(\lambda)$, $b(\lambda)$, $c(\lambda)$ and $d(\lambda)$ will be even functions of $\phi_v - \phi_0$. Thus, we can write

$$a(\theta_v, \phi_v \theta_0, \phi_0, \lambda) = a^{(0)}(\theta_v, \theta_0, \lambda) + 2\sum_{m=1}^{M} a^{(m)}(\theta_v, \theta_0, \lambda) \cos m(\phi_v - \phi_0),$$

with

$$a^{(m)}(\theta_v, \theta_0, \lambda) = \frac{1}{\pi}\int_0^{\pi} a(\theta_v, \theta_0, \lambda, \phi_v) \cos m(\phi_v - \phi_0)\, d\phi_v,$$

etc. The LUTs contain these coefficients for $m = 0$ to M with $M = 14$. This modification produces virtually no change in the retrieved $[\rho_w]_N$ for the cases tested earlier.[6]

We now describe the algorithm steps in detail with the aid of the annotated flow diagram in Figure 30. All quantities in this diagram are assumed to have been weighted with respect to the MODIS spectral response functions (where required) as described in Section 3.1.1.12.5 and *Gordon* [1995], e.g., F_0 stands for $\langle F_0(\lambda)\rangle_{S_i}$, L_m for $\langle L_m(\lambda)\rangle_{S_i}$, ρ_r for $\langle \rho_r(\lambda)\rangle_{F_0 S_i}$, etc., where S_i is the spectral response of the i^{th} MODIS spectral band.

We assume that modis measures the radiance L_m, and that this is converted to reflectance ρ_m using F_0. Alternatively, MODIS may be calibrated to measure ρ_m directly, in which case this step is omitted. The Ozone concentration is used to compute $\langle \tau_{Oz}(\lambda)\rangle_{F_0 S_i}$ in order to remove the effect of Ozone absorption by multiplying ρ_m by

$$\exp[\langle \tau_{Oz}(\lambda)\rangle_{F_0 S_i} M],$$

where M is the two-way air mass

$$M = \frac{1}{\cos\theta_v} + \frac{1}{\cos\theta_0}.$$

The wind speed W is then used to estimate the whitecap reflectance, $[\rho_{wc}]_N$ using Eq. (20), and the whitecap contribution

$$t^*(\theta_0)t^*(\theta_v)[\rho_{wc}]_N,$$

where $t^*(\theta_0)$ is provided in Eq. (3), is subtracted from the Ozone-corrected ρ_m. The parameters T_w and ΔT are not used in the present implementation, but are available should a more sophisticated

[6] The procedure described in footnote 2 was also employed here.

whitecap removal algorithm require them. The wind speed also provides the sun glitter mask as described in Section 3.1.1.7. These procedures return the quantity

$$\rho_t = \rho_r + \rho_a + \rho_{ra} + t\rho_w$$

at unmasked pixels.

The next step in the algorithm is the computation of ρ_r. This requires the atmospheric pressure to provide the Rayleigh optical depth, the wind speed to provide an estimate of the surface roughness, and the viewing-sun geometry. For a given solar zenith angle θ_0 and azimuth angle ϕ_0, the Stokes vector $\mathbf{I}_r$ for the Rayleigh scattering contribution to the radiance leaving the TOA can be written

$$\mathbf{I_r} = \begin{pmatrix} I_r(\theta_v,\phi_v,\theta_0,\phi_0) \\ Q_r(\theta_v,\phi_v,\theta_0,\phi_0) \\ U_r(\theta_v,\phi_v,\theta_0,\phi_0) \\ V_r(\theta_v,\phi_v,\theta_0,\phi_0) \end{pmatrix} = \begin{pmatrix} I_r^{(0)}(\theta_v,\theta_0) + 2\sum_{m=1}^{2} I_r^{(m)}(\theta_v,\theta_0)\cos m(\phi_v-\phi_0) \\ Q_r^{(0)}(\theta_v,\theta_0) + 2\sum_{m=1}^{2} Q_r^{(m)}(\theta_v,\theta_0)\cos m(\phi_v-\phi_0) \\ 2\sum_{m=1}^{2} U^{(m)}(\theta_v,\theta_0)\sin m(\phi_v-\phi_0) \\ 2\sum_{m=1}^{2} V^{(m)}(\theta_v,\theta_0)\sin m(\phi_v-\phi_0) \end{pmatrix}. \quad (36)$$

The Rayleigh contribution to the reflectance is $\rho_r = \pi I_r(\theta_v,\phi_v,\theta_0,\phi_0)/F_0\cos\theta_0$. The quantities $Q_r(\theta_v,\phi_v,\theta_0,\phi_0)$ and $U_r(\theta_v,\phi_v,\theta_0,\phi_0)$ are used to correct the total radiance for the polarization sensitivity of the sensor following *Gordon, Du and Zhang* [1997a] in Section 3.1.1.8. The degree, P_r, and the direction, χ_r, of polarization of ρ_r used in Section 3.1.1.8 are

$$P_r = \frac{\sqrt{Q_r^2 + U_r^2}}{I_r} \qquad \text{and} \qquad \tan 2\chi_r = \frac{U_r}{Q_r}.$$

LUTs consisting of I_r^m, Q_r^m, and U_r^m are provided for $\theta_0 = 0(2°)88°$ for 100 values of θ_v. $V_r^{(m)}$ is identically zero. Bilinear interpolation is used to determine the values specific to the particular viewing geometry.

The ρ_r-LUTs have been prepared for standard atmospheric pressure, the value of ρ_r is corrected to the actual pressure by multiplying the interpolated value by [*Gordon, Brown and Evans*, 1988]

$$\frac{1-\exp[-(P/P_0)\langle\tau_{r_0}(\lambda)\rangle_{F_0S_i}/\cos\theta_v]}{1-\exp[-\langle\tau_{r_0}(\lambda)\rangle_{F_0S_i}/\cos\theta_v]},$$

where $\langle\tau_{r_0}(\lambda)\rangle_{F_0S_i}$ is the band-averaged Rayleigh optical depth for band i at a pressure P_0 and P is

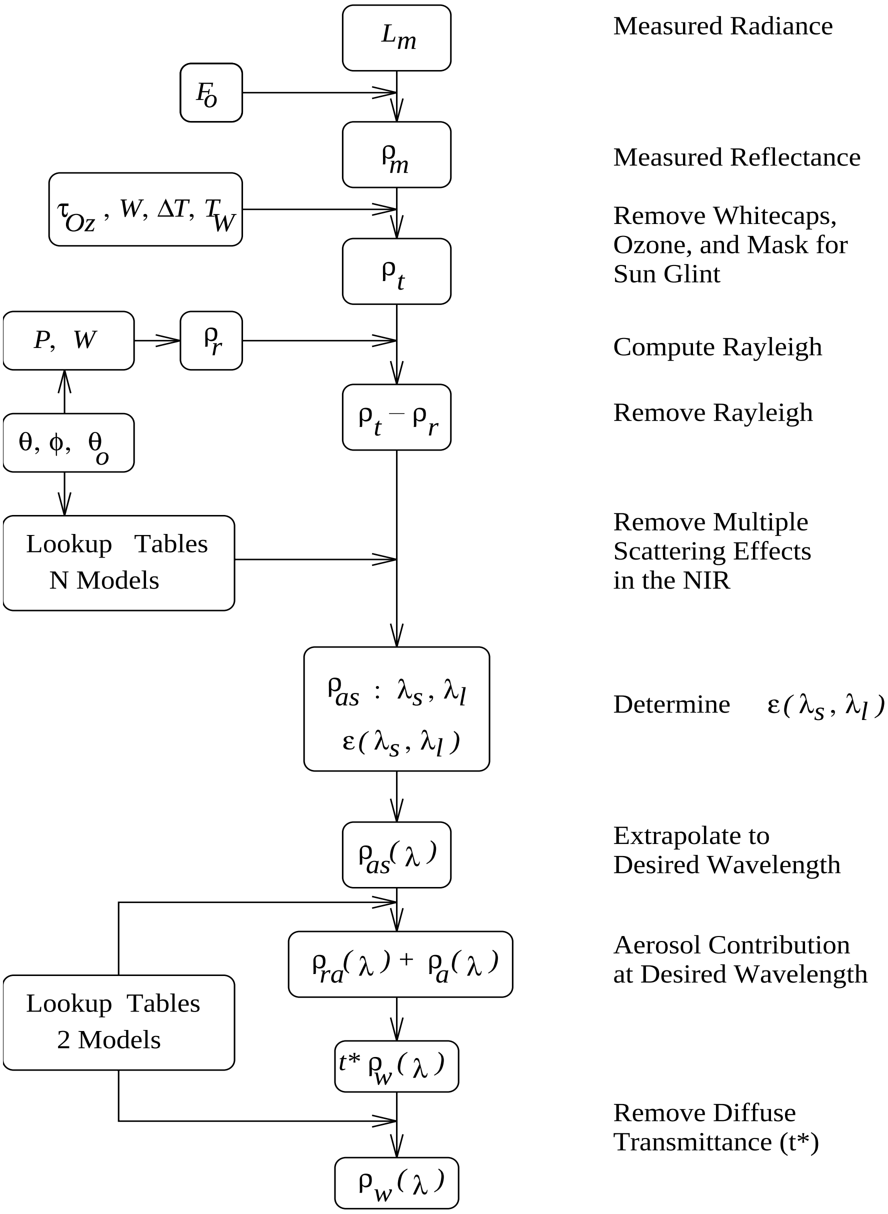

Figure 30. Annotated flow diagram of the algorithm.

the actual atmospheric pressure. In the present implementation LUTs are constructed for five wind speeds, and ρ_r is interpolated to the wind provided in the ancillary data.

After ρ_r has been determined, it is subtracted from ρ_t to form

$$\rho_t - \rho_r = \rho_a + \rho_{ra} + t\rho_w.$$

The fact that ρ_w is essentially zero in the NIR, i.e., at λ_s and λ_l, then enables the determination of

$$\rho_a(\lambda_s) + \rho_{ra}(\lambda_s) \qquad \text{and} \qquad \rho_a(\lambda_l) + \rho_{ra}(\lambda_l).$$

These quantities are used in a manner described in Section 3.1.1.3 to estimate $\varepsilon(\lambda_s, \lambda_l)$, and then to find the two aerosol models from among the N candidates that bracket the observed $\varepsilon(\lambda_s, \lambda_l)$. In the process, the $\rho_a + \rho_{ra}$ LUTs are used to convert multiple scattering quantities $(\rho_a + \rho_{ra})$ to single scattering quantities (ρ_{as}). Interpolating between these two models enables estimation of $\rho_{as}(\lambda)$ for $\lambda < \lambda_s$, and a second application of the $\rho_a + \rho_{ra}$ LUTs provides $\rho_a + \rho_{ra}$ in the visible. This procedure yields $t(\lambda)\rho_w(\lambda)$ in the visible.

To derive the water-leaving reflectance ρ_w, the diffuse transmittance t is required. A third set of LUTs provide $t^*(\theta_0, \lambda)$ for each λ and each aerosol model as a function of the aerosol optical thickness $\tau_a(\lambda)$. Once $\rho_{as}(\lambda_l)$ is determined for each aerosol model it is a simple matter to determine $\tau_a(\lambda)$ for that model using Eq. (9). The t^*-LUTs provide the diffuse transmittance for a given aerosol model in the form

$$t^*(\theta_0, \lambda) = A(\theta_0, \lambda)\exp[-B(\theta_0, \lambda)\tau_a(\lambda)],$$

where A and B are determined from radiative transfer simulations. (It should be noted that in this implementation of the algorithm the bi-directional reflectance distribution function of the upwelling radiance just beneath the surface is assumed to be lambertian, i.e., we are using t^* instead of t.) t^* is then interpolated between the two models in a manner similar to $\rho_a + \rho_{ra}$. Finally, estimation of $t^*(\theta_v, \lambda)$ provides $\rho_w(\lambda) = t\rho_w/t^*(\theta_v, \lambda)$.

This completes the retrieval of ρ_w in the visible. The final products are either the normalized water-leaving reflectances or radiances:

$$[\rho_w(\lambda)]_N = \rho_w(\lambda)/t^*(\theta_0, \lambda) \quad \text{or} \quad [L_w(\lambda)]_N = \frac{\overline{F}_0(\lambda)[\rho_w(\lambda)]_N}{\pi}.$$

The latter was referred to as $[L_w]_N^{\rm Space}$ in Section 3.1.1.13.4. Note that when the spectral response of the sensor is explicitly displayed, the final products are $\langle[\rho_w(\lambda)]_N\rangle_{F_0 S_i}$ and $\langle[L_w(\lambda)]_N\rangle_{S_i}$. These are related by [*Gordon*, 1995]

$$\langle[L_w(\lambda)]_N\rangle_{S_i} = \frac{\langle[\rho_w(\lambda)]_N\rangle_{F_0 S_i}\langle\overline{F}_0(\lambda)\rangle_{S_i}}{\pi}.$$

The ρ_w retrieval procedure described above requires the use of three different LUTs: (1) tables of the Stokes' vector of the Rayleigh component of the TOA reflectance (Rayleigh-LUTs); (2) tables to provide the relationship between $\rho_a+\rho_{ra}$ and ρ_{as} for the individual aerosol models, and (3) tables of A and B relating the diffuse transmittance of the atmosphere to the aerosol optical thickness for each aerosol model. The Rayleigh-LUTs (item 1) are separate from those in items 2 and 3. The LUTs for items 2 and 3 are combined (Aerosol-LUTs), with a single LUT for each aerosol model used. The Aerosol-LUTs also contain the aerosol phase functions specific to the given aerosol model (these are used to compute the value of $\varepsilon(\lambda, \lambda_l)$ in the algorithm). The Rayleigh-LUTs are small. In contrast, the Aerosol-LUTS are large: approximately 10 MB per aerosol model for a maximum viewing angle of $\sim 60°$ and a maximum solar zenith angle of 80°. As the algorithm is presently implemented, there is no limit to the number (N) of aerosol models that can be used although it *is* assumed that N is an *even* number.

Finally, LUTs are required to provide the quantities to convert $[L_w]_N^{\rm Space}$ to $[L_w]_N^{\rm Field}$ (and later to $[L_w]_N^{\rm Exact}$). These have been provided by André Morel based on *Morel, Antoine and Gentili* [2002].

There are two approximations to these procedures that are used to make the processing faster. First, the a, b, c, and d coefficients are evaluated only once for each 5×5-pixel box in the image. This was based on tests in which $\rho_a + \rho_{ra}$ for a given ρ_{as} was computed using the a, b, c, and d coefficients for the true values of θ_v, θ_0 and $\phi_v - \phi_0$ and compared with those offset by a given number of pixels. Second, the procedure described for the computation of $\varepsilon(\lambda_s, \lambda_l)$ is applied at only every fifth pixel. After evaluation at a pixel as described in this section, the indices of the final two bounding models are retained and used at the next pixel to compute

$$\varepsilon(\lambda_s, \lambda_l) = \frac{\varepsilon_{\text{low model}}(\lambda_s, \lambda_l) + \varepsilon_{\text{high model}}(\lambda_s, \lambda_l)}{2},$$

where $\varepsilon_{\text{low model}}(\lambda_s, \lambda_l)$ is the value of $\varepsilon(\lambda_s, \lambda_l)$ computed using the aerosol model that gave the lower bounding value of ε at a previous pixel, etc. If $\varepsilon(\lambda_s, \lambda_l)$ still falls between the ε for the original bounding models, these models are used for the present pixel. Thus, the full ε-determination procedure is only used at every fifth pixel. The basis for this modification is that the physical-chemical properties of the aerosol are not expected to change significantly over the spatial scales of a few pixels.

3.1.3 Uncertainty Estimates

There are four major sources of error in the algorithm as described thus far. The first is the fact that the N candidate aerosol models chosen to describe the aerosol may be unrepresentative of the natural aerosol. The magnitude of this effect has been estimated in Section 3.1.1.4. (In particular see Figure 12.) The second is the error in the estimate of the whitecap reflectance ρ_{wc}. In Section 3.1.1.6 we showed that when the whitecap reflectance depends on wavelength as suggested by *Frouin, Schwindling and Deschamps* [1996], the error in $[\rho_w]_N$ is similar to the error in the estimate of $[\rho_{wc}]_N$, which exceeds ± 0.002 at 443 nm for a wind speed of $\sim$ 9–10 m/s; however, the modeled $[\rho_{wc}]_N$ may be too large in the visible for a given wind speed. The third is the error associated with either the missidentification of strongly-absorbing aerosols as being weakly-absorbing, or in the case of strongly-absorbing aerosols, an inaccurate estimate of their vertical extent. The magnitude of these errors was discussed in Sections 3.1.1.4 and 3.1.1.12.1. The forth is the error in the sensor's radiometric calibration, i.e., the error in $\rho_t(\lambda)$. In this section we will describe some simulations to estimate the magnitude of the effect of the radiometric calibration error.

Since the desired water-leaving reflectance is only a small part of ρ_t, at most $\sim 10 - 15\%$ (Table 1), accurate calibration of the sensor is critical [*Gordon*, 1987]. In this section we describe simulations to estimate the magnitude of the effect of the radiometric calibration error, and discuss how accurate on-orbit calibration can be effected.

To assess the effect of calibration errors, we add a small error to each of the measured reflectances, i.e.,

$$\rho_t'(\lambda) = \rho_t(\lambda)[1 + \alpha(\lambda)], \tag{37}$$

where $\alpha(\lambda)$ is the fractional error in $\rho_t(\lambda)$ and $\rho_t'(\lambda)$ is the value of $\rho_t(\lambda)$ that the incorrect sensor calibration would indicate. The atmospheric correction algorithm is then operated by inserting $\rho_t'(\lambda)$ as the measured value rather than the true value $\rho_t(\lambda)$ and $t\Delta\rho_w \equiv \Delta\rho$ is computed as before.

Assuming the single-scattering algorithm, Eq. (12), is exact, and $\varepsilon(\lambda_i,\lambda_l) = \exp[c(\lambda_l - \lambda_i)]$, it is easy to show that to first order in $\alpha(\lambda)$, the error in the retrieved ρ_w is

$$\begin{aligned} t(\lambda_i)\Delta\rho_w(\lambda_i) &= \alpha(\lambda_i)\rho_t(\lambda_i) - \varepsilon(\lambda_i,\lambda_l)\alpha(\lambda_l)\rho_t(\lambda_l) \\ &- \left(\frac{\lambda_l - \lambda_i}{\lambda_l - \lambda_s}\right)\left[\frac{\varepsilon(\lambda_i,\lambda_l)}{\varepsilon(\lambda_s,\lambda_l)}\alpha(\lambda_s)\rho_t(\lambda_s) - \varepsilon(\lambda_i,\lambda_l)\alpha(\lambda_l)\rho_t(\lambda_l)\right] \end{aligned} \tag{38}$$

The first term represents the direct effect of calibration error at λ_i on $\rho_w(\lambda_i)$, while the remaining terms represent the indirect effect from calibration error in the atmospheric correction bands at λ_s and λ_l. The second term obviously increases in importance as λ_i decreases. Note that if all of the spectral bands have calibration error with the same sign, i.e., all $\alpha(\lambda)$ have the same sign, significant cancelation of the atmospheric correction contribution can occur; however, if $\alpha(\lambda_s)$ and $\alpha(\lambda_l)$ have different signs, the error is magnified as the last two terms in Eq. (38) will add.

To see if this holds for the multiple-scattering algorithm as well, it was also operated by inserting $\rho_t'(\lambda)$ as the measured value rather than the true value $\rho_t(\lambda)$. The results of this exercise are presented in Figure 31 for the M80 aerosol model at the center of the scan. In the top panels, $\alpha(765) = \alpha(865)$ with $\alpha(443) = 0$ or with $\alpha(443) = \alpha(765) = \alpha(865)$. They show the effect of a calibration bias that is the same at 765 and 865 nm. The lower panels show the effect of having calibration errors that are of opposite sign at 765 and 865 nm. Note that in this case even a small calibration error (1%) can make as significant an error in $\rho_w(443)$ as a large calibration error (5%) when the signs are all the same. As discussed above, the reason the error is so much larger when it is of opposite sign at 765 and 865 nm is that it will cause a large error in the estimated value of $\varepsilon(765, 865)$, and this will propagate through the algorithm causing a large error in the retrieved water-leaving reflectance at 443 nm. In the cases examined in Figure 31, the magnitude of the errors is in quantitative agreement with that predicted by Eq. (38).

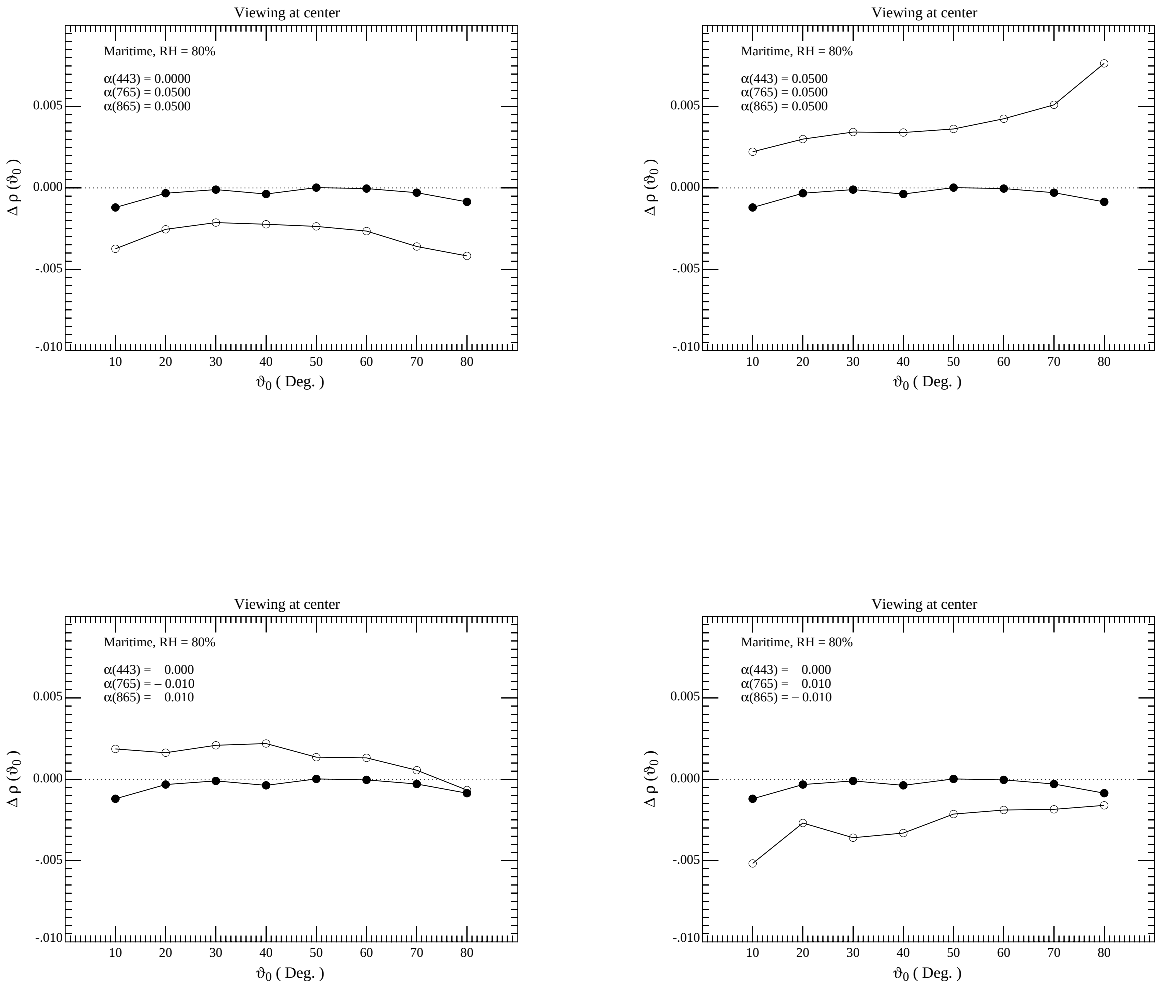

Figure 31. Error in the retrieved $t(443)\rho_w(443)$ for viewing at the center of the scan with a Maritime aerosol at RH = 80% as a function of the solar zenith angle with $\tau_a(865) = 0.2$ and calibration errors $\alpha(443)$, $\alpha(765)$, and $\alpha(865)$ in Eq. (37) (open circles). Solid circles are for $\alpha(\lambda_i) = 0$ for all λ_i.

As the goal for the calibration of the relevant ocean color bands on MODIS is that L_t have an uncertainty of $< \pm 5\%$, and Figure 31 (lower panels) show that such an error (even if it were the same in each band) would cause the error in the retrieved $\rho_w(443)$ to be outside the acceptable range. A method for overcoming these calibration difficulties is discussed in Section 3.2.2.

3.2 Practical Considerations

The present algorithm is not capable of adequately dealing with strongly-absorbing aerosols, e.g., the Urban model. Failure of the correction algorithm for aerosols of this type needs to be addressed. This will require that a system be developed to indicate the presence of such aerosols — by unacceptable $[\rho_w]_N$'s, unacceptable pigments, etc. — and initiate a second pass through the algorithm using a special set of candidate aerosol models with the appropriate absorption properties. This problem is the focus of Chapter 5.

3.2.1 Programming and Procedural Considerations

These considerations are described in the ATBD "Processing Framework and Matchup Data Base: MODIS Algorithm" by R. Evans. The report also includes data volume, networking, and CPU requirements.

3.2.2 Calibration, Initialization, and Validation

In Section 3.1.3 examples were provided to show the sensitivity of the algorithm to sensor calibration errors (Figure 31). It was demonstrated that calibration errors of the order of $\pm 5\%$, the absolute radiometric calibration uncertainty specified for the MODIS visible bands, would lead to excessive error in $[\rho_w]_N$, even if the calibration error the errors in bands 15 and 16 were of the same sign. When errors in these bands are small ($\sim \pm 1\%$) but have opposite signs (Figure 31, lower panels), the error in the water-leaving reflectance becomes large because of the extrapolation of ε into the visible. Thus, it is clear the the calibration uncertainty of MODIS must be reduced in order to provide acceptable $[\rho_w]_N$, retrievals.

3.2.2.1 Calibration Initialization

Although the calibration requirement is difficult if not impossible to meet using standard laboratory methods, it should be possible to perform an adequate calibration in orbit using surface measurements to deduce the true water-leaving radiance and the optical properties of the aerosol. This is normally referred to as *vicarious* calibration [*Evans and Gordon*, 1994; *Fraser and Kaufman*, 1986; *Gordon*, 1987; *Koepke*, 1982; *Slater et al.*, 1987]. *Gordon* [1998] has outlined a plan for effecting such calibration, the process of which we refer to as *initialization.* This calibration is *not* radiometric, rather, it is a calibration of the entire system — the sensor *plus* the algorithms. The sensor calibration is adjusted to force the algorithm to conform to surface measurements of water-leaving radiance and atmospheric (aerosol) properties. A similar procedure was carried out for CZCS [*Evans and Gordon*, 1994], but without any surface-based atmospheric measurements. It was only moderately successful because the calibration of that instrument varied in time, and there was no independent way of determining the temporal variation. Here, we make the assumption that any change in the sensitivity of the instrument with time can be determined by other methods, e.g., using the SRCA, the solar diffuser, or imagery of the moon.

Gordon [1998] provides the complete details of the initialization procedure along with estimates of the expected accuracy. Briefly, it is assumed that the spectral band at λ_l has no calibration error. The effect of calibration error at λ_l has been described by *Wang and Gordon* [2002]. Measurements of the aerosol properties (spectral variation in optical depth) and L_w are then used to predict L_t at the other wavelengths from $L_t(\lambda_l)$, and the calibration of these wavelengths is adjusted to provide the predicted L_t. Analysis shows that the residual calibration error at a given λ is reduced by a factor of approximately $(\lambda/\lambda_l)^4$, i.e., approximately the ratio of the contributions of L_r to L_t, below the radiometric calibration error at λ_l. *Gordon* [1998] shows that procedure alone is sufficient to reduce the error in the retrieval of ρ_w from ρ_t, using the algorithm described in Section 3.1.1.3, to desirable limits. Reduction of the error in $L_t(\lambda_l)$, using methods described by *Gordon and Zhang* [1996], will further reduce the error in ρ_w, but only slightly [*Gordon*, 1998].

This procedure was applied to SeaWiFS [*Gordon et al.*, 1998] using data acquired in January and February 1998 near Hawaii. Prior to that time, the SeaWiFS project had used MOBY [*Clark et al.*, 1997] measurements of $[L_w(\lambda)]_N$ near Hawaii, along with the atmospheric correction algorithm described in this ATBD, to adjust the sensor calibration, for $\lambda < \lambda_l$ and λ_s, by forcing the retrieved and measured $[L_w(\lambda)]_N$ to agree [*McClain et al.*, 1998]. The *Gordon et al.* [1998] calibration results were in excellent agreement with the SeaWiFS project's, suggesting that a MOBY time series of $[L_w(\lambda)]_N$ alone can be used to effect an adequate vicarious calibration. This underscores the importance of *continuing the MOBY measurements through the lifetime* of MODIS.

A significant difficulty with MODIS (Terra) is that the calibration does not appear to be stable, i.e., it under goes random variations that must be removed in order to provide a consistent data set. This being the case, the data of highest quality are always produced by *retrospective* processing. Providing high-quality products has not been possible to date.

3.2.2.2 Validation

By validation of atmospheric correction, we mean quantification of the uncertainty expected to be associated with the retrieval of the water-leaving radiance from the measurement of the total radiance exiting the ocean-atmosphere system. This uncertainty includes that associated with the measurement or estimation of auxiliary data required for the retrieval process, e.g., surface wind speed, surface atmospheric pressure, and total Ozone concentration. For a definitive validation, this quantification should be carried out over the full range of atmospheric types expected to be encountered. However, funding constraints require that the individual validation campaigns must be planned to address the individual components of the atmospheric correction algorithm believed to represent the greatest potential sources of error.

The validation of the $[\rho_w]_N$ product is being effected by comparing simultaneous surface-based measurements and MODIS-derived values at locations not used in the initialization measurements. Station locations will be chosen to provide a wide range of values of $[\rho_w]_N$ and aerosol types. For ship-based validation experiments, aerosol properties (τ_a, ω_a, P_a) will be derived from measurements with sun photometers and sky radiance cameras. The specific details of the validation plan are provided in *Clark et al.* [1997].

3.2.3 Quality Assurance and Diagnostics

By "quality assurance" (QA) we mean providing the $[\rho_w]_N$-user with information concerning when the product may not conform to expectations and should be used with caution. QA procedures have been developed in conjunction with R. Evans. A detailed discussion is included in the ATBD "Processing Framework and Matchup Data Base: MODIS Algorithm" by R. Evans. Basically, if our assumptions are valid (Section 4.1), and the wind speed is $\lesssim$ 10 m/s, the algorithm can be expected to perform properly except in situations where strongly absorbing aerosols are present (Sections 3.1.1.2 – 3.1.1.4). For these, no reliable algorithm enhancement is available in the processing code at present. Generally absorbing aerosols will result in an over correction and $[\rho_w]_N$ will be too small; however, as $[\rho_w]_N$ may be small for other reasons, e.g., high pigment concentration, there is generally no simple rule that can be applied to determine whether the derived values are reasonable; however, the authors along with R. Evans and V. Banzon are presently developing a simple method for detection of dust-contaminated pixels.

3.2.4 Exception Handling

Exceptions occasionally occur in a manner that prevents operation of the algorithm, e.g., missing data in bands 15 or 16, or in a manner that would cause exceptions in algorithms using $[\rho_w]_N$, e.g., negative values of $[\rho_w]_N$ caused by atmospheric correction errors (particularly in the blue at high pigment concentrations where $[\rho_w]_N$ is small). A series of flags have been developed to indicate when atmospheric correction should not be attempted, or to indicate that algorithm failed to operate of failed to provide realistic values for $[\rho_w(\lambda)]_N$.

3.2.5 Data Dependencies

The required ancillary data is described in detail in Section 3.1.1.11. All will come to MODIS via the GSFC/DAAC. If a particular data set is not available either a nominal value, e.g., the oceanic average, or a climatology will be substituted.

3.2.6 Output Products

The output products are the normalized water-leaving radiances in MODIS Bands 8–14, the aerosol optical thickness $\tau_a(\lambda_l)$, $\varepsilon(\lambda_s, \lambda_l)$, and an index describing the two candidate models selected by the algorithm to perform the $[\rho_w]_N$ retrievals. At present $[L_w]_N^{\mathrm{Field}}$ rather than $[L_w]_N^{\mathrm{Exact}}$ is provided to facilitate comparison with measurements made at MOBY. Based on our observations that the combination of $\varepsilon(\lambda_s, \lambda_l) \sim 1$ and small $\tau_a(\lambda_l)$ yields a very good retrieval of $[\rho_w]_N$, while $\varepsilon(\lambda_s, \lambda_l) \sim 1.2$ and large $\tau_a(\lambda_l)$ may yield a poor retrieval, it may be possible to develop a quality index based on a combination of the values of $\varepsilon(\lambda_s, \lambda_l)$ and $\tau_a(\lambda_l)$.

4.0 Assumptions and Constraints

In this section we describe the assumptions that have been made and how they may influence the resulting $[\rho_w]_N$. We also provide a list of situations in which the algorithm cannot be operated.

4.1 Assumptions

The principal assumption is the validity of the aerosol models used for the implementation of the algorithm, i.e., in developing the lookup tables described in Section 3.1.1.3. We have seen in Section 3.1.1.4 that the algorithm will work well if the models are a reasonable approximation to nature, but if they are unrealistic, i.e., mineral dust without absorption, the error in $[\rho_w]_N$ can be excessive (Figure 12). In fact, Figure 12 shows that it is of vital importance to have the correct absorptive properties of the aerosol. The adequacy of the aerosol models is difficult to judge. For the most part they were developed to model beam propagation, i.e., the total scattering and extinction coefficients, not the scattering phase function and the single scatter albedo. They have not been validated for these quantities; however, *Schwindling* [1995] showed that the aerosol off the coast of Southern California appeared to fall within the boundaries of the *Shettle and Fenn* [1979] aerosol models used here. Similar conclusions can be stated for the clean maritime aerosol based on the analysis of *Smirnov et al.* [2003]. Also, the success of SeaWiFS [*Hooker and McClain*, 2000] suggests that the models used here are adequate most of the time.

A second, probably less important, assumption is that the radiative transfer in the atmosphere can be adequately described by a two-layer model (aerosols in the lower layer only). Based on tests with absorbing aerosols, we know that this model will have to be changed, e.g., Saharan dust will have to be mixed higher into the atmosphere. This will require generation of new lookup tables. Such tables have been developed for Saharan dust (see Section 5.1.1).

Finally, it is assumed that at low chlorophyll *a* concentrations the water-leaving radiance in the NIR is near zero. This is usually an excellent assumption in the open ocean; however, in very concentrated coccolithophore blooms [*Balch et al.*, 1991; *Gordon et al.*, 1988] it is possible that the ocean will contribute NIR radiance. The magnitude of this NIR radiance as a function of the coccolith concentration is being studied experimentally as part of a study to derive the concentration from MODIS imagery. For routine processing, we assume that the *Siegel et al.* [2000] correction is sufficiently accurate to address this issue (Section 3.1.1.9).

4.2 Constraints

Although algorithm will employ the cloud mask being developed by the MODIS Atmosphere Group to indicate the presence of thin cirrus clouds; an atmospheric correction will be attempted for all imagery that is not saturated in any of Bands 8-16. Of these cloud-free pixels, the algorithm requires that they contain no land and that the estimated sun glitter contamination be below a pre-determined threshold. Also, the algorithm should not be applied closer than a distance x from land (the value of x is a few km) due to the adjacency effect from land pixels [*Otterman and Fraser*, 1979] and the possibility of sufficiently high sediment loads in the water that $[\rho_w]_N$ can not be considered negligible in the NIR.

5.0 Future Algorithm Enhancements

Section 3 describes the algorithm and its present implementation. There are, however, several planned enhancements proposed for the future. These deal mainly with the issues discussed in Section 3.1.1.13: strongly absorbing aerosols, nonuniform in-water radiance distribution effects, etc. Of the issues discussed there, development of an atmospheric correction algorithm that can deal with strongly absorbing aerosols, e.g., wind-blown desert dust and/or urban pollution, is considered to be the most important.

5.1 Strongly Absorbing Aerosols

As discussed earlier (Sections 3.1.1.4, 3.1.1.12.1, and 3.1.1.13.3) the ρ_w-retrieval algorithm as presently implemented (Section 3.1.2) cannot produce acceptable results in the presence of strongly absorbing aerosols. Briefly, two observations indicate how the algorithm is confounded: (1) although aerosol absorption can seriously reduce $\rho_a + \rho_{ra}$ in the visible, it is not possible on the basis of the observed TOA radiance in the NIR to infer the presence of aerosol absorption, because the spectral variation of $\rho_a + \rho_{ra}$ in the NIR depends mostly on the aerosol's size distribution, e.g., Figure 4 (right panel); and (2) the vertical distribution of strongly absorbing aerosols profoundly influences their TOA reflectance in the visible (especially in the blue) but not in the NIR (Figure 25). In the case of mineral aerosol such as Saharan dust transported over large distances over the ocean by the winds, there is an additional complication: the dust is colored, i.e., the absorption properties of the material itself varies strongly with wavelength. Saharan dust is more absorbing in the blue and green than the red, explaining its reddish color. When such desert aerosol is in the atmosphere over the oceans, the present algorithm will seriously overestimate $\rho_a + \rho_{ra}$ in the blue and therefore underestimate ρ_w there. This underestimation will appear as an elevated pigment concentration C. Interestingly, there are observations suggesting that mineral aerosols, by virtue of the trace nutrients they supply when they settle out of the atmosphere into the water, can actually induce an increase in primary productivity and elevate the pigment concentration [*Young et al.*, 1991]. Thus, observation of an elevated pigment concentration could be the result of a poor atmospheric correction and/or "fertilization" of the water by the aerosol itself. Clearly, a robust ρ_w-retrieval algorithm for areas subjected to desert dust is of paramount importance.

The fact that the absorption properties cannot be determined on the basis of the observations of $\rho_a + \rho_{ra}$ in the NIR means that observations in the visible are required as well. However, in the visible (especially in the blue) ρ_w can be significant, and cannot be estimated *a priori*. This suggests that the retrieval of ρ_w (or the pigment concentration) and the atmospheric correction (retrieval of $\rho_a + \rho_{ra}$) must be carried out simultaneously. As retrieval of $\rho_a + \rho_{ra}$ in the existing algorithm requires aerosol models, retrieval of ρ_w will require an optical model of the ocean. Two algorithms, based on simultaneous determination of oceanic and atmospheric properties, that show promise in dealing with absorbing aerosols have been developed [*Chomko and Gordon*, 1998; *Gordon, Du and Zhang*, 1997b]. In the following, these two approaches are described and some results of their application to ocean color imagery is provided.

5.1.1 The Spectral Matching Algorithm

The "spectral matching algorithm" is described in detail in *Gordon, Du and Zhang* [1997b]. In this algorithm, the properties of the ocean and the atmosphere are retrieved simultaneously. Briefly, assuming that $[\rho_w(\lambda_l)]_N = 0$ (an assumption that can be relaxed as we will see later), $\rho_t(\lambda_l) - \rho_r(\lambda_l)$ provides $\rho_a(\lambda_l) + \rho_{ra}(\lambda_l)$. Now, given an aerosol model (the i^{th}) one can find the value of the aerosol optical depth, $\tau_a^{(i)}(\lambda_l)$, that reproduces $\rho_a(\lambda_l) + \rho_{ra}(\lambda_l)$. Then from $\tau_a^{(i)}(\lambda_l)$ and the model, $\rho_a^{(i)}(\lambda_j) + \rho_{ra}^{(i)}(\lambda_j)$ and $t^{*(i)}(\theta, \lambda_j)$ can be determined for all spectral bands j. This provides the quantity

$$t(\theta_v, \lambda_j)\rho_w^{(i)}(\lambda_j) = \rho_t(\lambda_j) - \rho_r(\lambda_j) - \rho_a^{(i)}(\lambda_j) - \rho_{ra}^{(i)}(\lambda_j)$$

retrieved assuming that the i^{th} aerosol model is correct. At this point the *Gordon et al.* [1988] two-parameter model of the water-leaving reflectance that uses the pigment concentration, C, and a pigment-related scattering parameter at 550 nm, b_0, is employed to compute $[\rho_w(\lambda)]_N$ for a discrete set of values of C and b_0 that fall within the typical range of variation. The residual

$$\delta(i, C, b_0) \equiv 100\% \sqrt{\frac{1}{n-1}\sum_{j=1}^{n}\left[\frac{t^{*(i)}(\theta_v, \lambda_j)t^{*(i)}(\theta_0, \lambda_j)[\rho_w(\lambda_j)]_N - t(\theta_v, \lambda_j)\rho_w^{(i)}(\lambda_j)}{t^{*(i)}(\theta_v, \lambda_j)t^{*(i)}(\theta_0, \lambda_j)[\rho_w(\lambda_j)]_N}\right]^2},$$

where n is the number of visible wavelengths, is computed for each model and set of ocean parameters. One might suggest that the set of parameters i, C, and b_0, that yield the smallest $\delta(i, C, b_0)$ should be chosen as the best, i.e., the solution the problem; however, as it is unlikely that the "correct" model is one of the set of candidates, *Gordon, Du and Zhang* [1997b] suggest averaging for the ten best retrievals (ten retrievals with the lowest values of $\delta(i, C, b_0)$) to obtain the retrieved ocean and aerosol parameters. Extensive tests using simulated pseudo data with Urban models as representative of strongly-absorbing aerosols suggest that this approach is capable of excellent retrievals in the presence of either weakly- and strongly-absorbing aerosols [*Gordon, Du and Zhang*, 1997b]. Of particular importance is that the algorithm has no difficulty indicating the presence of strongly absorbing aerosols. The algorithm can also incorporate vertical structure by having candidate models with any prescribed vertical structure.

An important feature of this algorithm is that it can be configured to use the *same* LUTs as the standard algorithm, and therefore could be run concurrently with it. Thus, at a minimum, it could be operated at reduced resolution (say every tenth line and every tenth pixel) to provide a flag for indicating the presence of absorbing aerosols. An unattractive feature of the algorithm is that it requires realistic aerosol models to effect the correction, i.e., the better the models approximate the real aerosol, the better the parameter retrievals. Obviously the results depend on the quality of the ocean model.

In the Atlantic and Indian Oceans, a predominant absorbing aerosol in the marine atmosphere is the mineral dust coming from Africa [*Herman et al.*, 1997]. This dust is strongly absorbing in the blue because it contains ferrous minerals [*Patterson*, 1981]. In addition, the impact of this absorption is very dependent on the vertical distribution of the aerosol (Section 3.1.1.12.1). This is of primary importance for Saharan dust [*Moulin et al.*, 2001a]. Because of these difficulties, the present MODIS and SeaWiFS algorithms do not process pixels if high ρ_t is detected in the NIR. The quasi-permanent presence of dust degrades satellite ocean color products in the Tropical Atlantic and Arabian Sea where large areas are not sampled, sometimes for as long as an entire month. An example from the Arabian Sea (SeaWiFS) is provided in Figure 32. It shows that almost the entire Arabian Sea is unsampled during the Southwest Monsoon because of dust from Africa. This failure of the atmospheric correction also prevents observation of the potential fertilization effect due to the supply of nutrients contained in dust to the surface water [*Young et al.*, 1991]. *Moulin et al.* [2001b] have reported a technique for atmospheric correction through African dust, based in the spectral matching algorithm (SMA), that allows retrieval of $[\rho_w]_N$ and the chlorophyll concentration at dust optical depths as high as 0.8. *Banzon et al.* [2004] have used this algorithm to process the SeaWiFS imagery from the Arabian Sea during 2000 shown in Figure 33 in a novel manner. SMA was used to select the best aerosol model from a set of 18 developed for use in this region [*Moulin et al.*, 2001a]. The selected model was then used to subtract the aerosol component from the imagery yielding the normalized water-leaving reflectance. These values of $[\rho_w]_N$ were used as input to the now-standard SeaWiFS OC4v4 bio-optical algorithm to estimate the concentration of chlorophyll a (Chl). The comparison with the standard SeaWiFS algorithm is striking – there is a dramatic increase in coverage during the monsoon period that clearly reveals the enhanced productivity unseen in the standard processing.

The aerosol models for use in Saharan dust [*Moulin et al.*, 2001a] were developed using SeaWiFS because of its significantly higher saturation radiance than MODIS in the ocean bands. They provide an example of tailoring aerosol models to reproduce actual satellite imagery. The derived optical properties were later found to be consistent with surface-based sky radiance retrievals of the single scattering albedo of Saharan dust [*Cattrall, Carder and Gordon*, 2003].

Application of the SMA to MODIS is straightforward only at low dust concentrations because of the low saturation radiances of the ocean bands; however, the possibility exists of using the NIR MODIS land bands in conjunction with the SMA to derive $[\rho_w]_N$ for pixels that do not saturate in the blue and green. This is the subject of a future study.

5.1.2 The Spectral Optimization Algorithm

The "spectral optimization algorithm" (SOA) is described in detail in *Chomko and Gordon* [1998]. As in the spectral matching algorithm, the properties of the ocean and the atmosphere are retrieved simultaneously. In contrast to the spectral matching algorithm, no attempt is made to use realistic aerosol models, i.e., aerosol models described by the overly-simple power-law size distributions [Eq. (11)] are employed to derive the ocean properties. Briefly, for a given value of the parameter ν of the power-law distribution, assuming the particles are spherical, and ignoring the aerosol vertical distribution for the moment, the aerosol reflectance $\rho_a(\lambda) + \rho_{ra}(\lambda)$ depends only on the real (m_r) and imaginary (m_i) parts of the aerosol refractive index and the aerosol optical

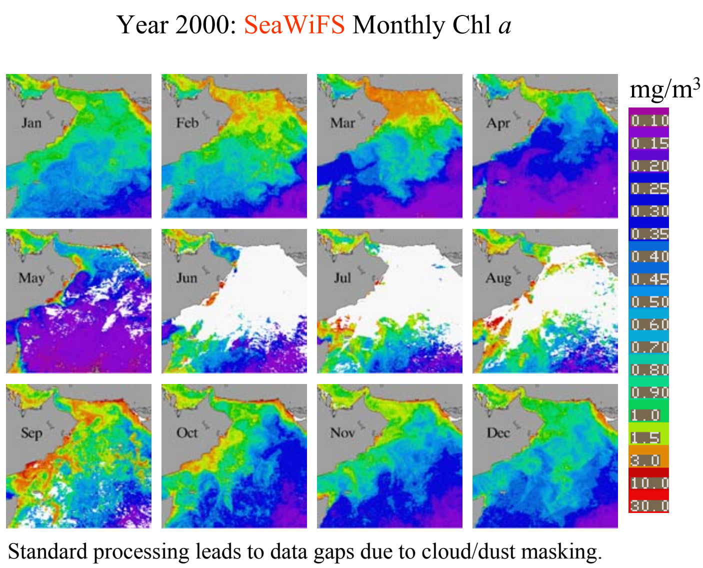

Figure 32. Monthly concentration of chlorophyll *a* derived from SeaWiFS imagery using the standard atmospheric correction algorithm [*Gordon and Wang*, 1994a].

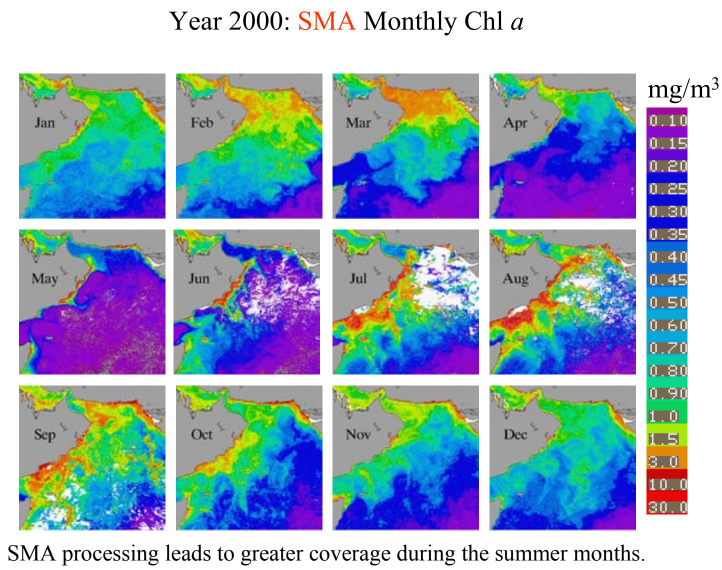

Figure 33. Monthly concentration of chlorophyll *a* derived from SeaWiFS imagery using the spectral matching algorithm [*Moulin et al.*, 2001b].

depth ($\tau_a(\lambda_l)$). The values of m_r and m_i are assumed to be independent of λ, so such a model will apply only to wavelength-independent absorbing aerosols, e.g., carbonaceous. As in the spectral matching algorithm, the water contribution to the TOA reflectance depends on the parameters C and b_0 through the *Gordon et al.* [1988] reflectance model. Nonlinear optimization is then used to determine the values of these parameters.

Application to SeaWiFS imagery off the U.S. East Coast has been presented by *Chomko and Gordon* [2001]. It showed consistent retrieved water properties between days with turbid and clear atmospheres. Unfortunately, because the bio-optical model differed considerably from that for the standard SeaWiFS processing, an unbiased comparison of the SOA and SeaWiFS ocean products was not possible. Rather than discussing these results in detail, we will present a version of the SOA that is improved through the addition of a more complete bio-optical model.

In the *Chomko et al.* [2003] version of the SOA, the *Gordon et al.* [1988] bio-optical model is replaced by the *Garver and Siegel* [1997] model as modified by *Maritorena, Siegel and Peterson* [2002]. In this model (which henceforth we refer to as "GSM01") of Case 1 waters there are three constituent parameters (as opposed to two in *Gordon et al.* [1988]): $a_{ph}(443)$, the absorption coefficient of phytoplankton at 443 nm; $a_{cdm}(443)$, the sum of the absorption coefficients of dissolved and suspended detrital material at 443 nm; and $b_{bp}(443)$, the backscattering coefficient of suspended particles at 443 nm. The spectral variation of these components is given by

$$\begin{aligned} a_{ph}(\lambda) &= a^*_{ph}(\lambda)\, C, \\ a_{cdm}(\lambda) &= a_{cdm}(443)\exp[-S(\lambda-443)], \\ b_{bp}(\lambda) &= b_{bp}(443)\,\left[\frac{443}{\lambda}\right]^n, \end{aligned}$$

where $a^*_{ph}(\lambda)$ is the specific (to C) absorption spectrum of phytoplankton. The parameters $a^*_{ph}(\lambda)$, S and n have been determined by *Maritorena, Siegel and Peterson* [2002] through an optimized fit to surface data for Case 1 waters. Thus, ρ_w is a function of C, $a_{cdm}(443)$, and $b_{bp}(443)$. We follow *Chomko et al.* [2003] and write the model-estimated value of $[\rho_w(\lambda)]_N$ functionally as

$$\left[\hat{\rho}_w(\lambda)\right]_N = \left[\hat{\rho}_w\big(\lambda, C, a_{cdm}(443), b_{bp}(443)\big)\right]_N.$$

The size distribution for the aerosol model is Junge power-law distribution. The same limits, D_0, D_1, and D_2, are used as in Eq. (11), so the modeled aerosol contribution to the reflectance

$\hat{\rho}_A \equiv \hat{\rho}_a + \hat{\rho}_{ra}$ will be a function of the solar-viewing geometry, m_r, m_i, ν, and τ_a. Functionally,

$$\hat{\rho}_A = \hat{\rho}_A\big(G, \lambda, m_r, m_i, \nu, \tau_a(\lambda)\big),$$

where G represents the parameters associated with the sun-viewing geometry, e.g., θ_0, θ_v, etc. In the SOA, m_r is either 1.50 or 1.333, and m_i = 0, 0.001, 0.003, 0.010, 0.030, and 0.040. The parameter ν ranges from 2.0 to 4.5 in steps of 0.5. Thus there are 72 separate aerosol models (2 values of m_r $\times$ 6 values of m_i $\times$ 6 values of ν). For each of these models, $\hat{\rho}_A$ is computed as a function of the aerosol optical thickness $\tau_a(\lambda)$ for a wide range of viewing and solar geometries and fit to a quartic expression

$$\begin{aligned}\hat{\rho}_A\big(G, \lambda, m_r, m_i, \nu, \tau_a(\lambda)\big) &= a(G, \lambda, m_r, m_i, \nu)\tau_a(\lambda)\\ &= b(G, \lambda, m_r, m_i, \nu)\tau_a^2(\lambda)\\ &= c(G, \lambda, m_r, m_i, \nu)\tau_a^3(\lambda)\\ &= d(G, \lambda, m_r, m_i, \nu)\tau_a^4(\lambda),\end{aligned}$$

and the quantities a, b, c, and d, are stored in the form of lookup tables. Similarly, the diffuse transmittances $t^*(\theta_v) \equiv t_v^*$ and $t^*(\theta_0) \equiv t_0^*$ are computed and stored in lookup tables.

After correcting ρ_t for sun glitter and whitecaps, the aerosol and water contribution to the reflectance in a particular geometry is given by

$$\rho_{Aw}(G, \lambda) = \rho_t(G, \lambda) - \rho_r(G, \lambda),$$

where

$$\rho_{Aw}(G, \lambda) = \rho_A(G, \lambda) + t_v(G, \lambda)\rho_w(G, \lambda).$$

The modeled counterpart of ρ_{Aw} is then

$$\begin{aligned}\hat{\rho}_{Aw}\big(G, \lambda, m_r, m_i, \nu, \tau_a(\lambda), C, a_{cdm}(443), b_{bp}(443)\big) \equiv\ & \hat{\rho}_A\big(G, \lambda, m_r, m_i, \nu, \tau_a(\lambda)\big)\\ & + \hat{t}_v^*\big(G, \lambda, m_r, m_i, \nu, \tau_a(\lambda)\big)\\ & \times \hat{t}_0^*\big(G, \lambda, m_r, m_i, \nu, \tau_a(\lambda)\big)\\ & \times \left[\hat{\rho}_w\big(\lambda, C, a_{cdm}(443), b_{bp}(443)\big)\right]_N.\end{aligned}$$

As in the SMA, it is assumed that the water-leaving reflectance in the NIR (i.e., at λ_s and λ_l) is negligible (this is relaxed later). This allows the direct estimation of ν and $\tau_a(\lambda_l)$ from determinations of $\rho_{Aw}(\lambda_s)$ and $\rho_{Aw}(\lambda_l)$. Thus for each index set (m_r, m_i) the values of ν and $\tau_a(\lambda_l)$ that *exactly* reproduce $\rho_{Aw}(\lambda_s)$ and $\rho_{Aw}(\lambda_l)$ are determined. This results in 12 combinations (ν, τ_a) from which the functions $\nu = \nu(m_r, m_i)$ and $\tau_a = \tau_a(m_r, m_i)$ are found through interpolation. Then the quantity

$$\sum_{\lambda_i} \{\hat{\rho}_{Aw}(G, \lambda_i, m_r, m_i, \nu, \tau_a, C, a_{cdm}(443), b_{bp}(443)) - \rho_{Aw}(G, \lambda_i)\}^2 ,$$

where the sum is over the remaining spectral bands, is minimized subject to the constraints $\nu = \nu(m_r, m_i)$ and $\tau_a = \tau_a(m_r, m_i)$, using standard optimization techniques, to find the other 5 parameters. In effect, we have optimized for 7 parameters:

$$C,\ a_{cdm}(443),\ b_{bp}(443),\ m_r,\ m_i,\ \nu, \text{ and } \tau_a(\lambda_l).$$

The SOA algorithm has been applied to a full resolution SeaWiFS image from the Middle Atlantic Bight (MAB) acquired on Day 279 of 1997 [*Chomko et al.*, 2003]. SeaWiFS was used rather than MODIS because the calibration difficulties associated with MODIS made testing new algorithms difficult. As described in *Chomko and Gordon* [2001], the atmosphere over the MAB on this day was quite turbid with $\tau_a(865)$ exceeding 0.2 over large portions of the image. Retrieved images of C and $a_{cdm}(443)$ are shown in Figure 34. A partial validation of this algorithm was

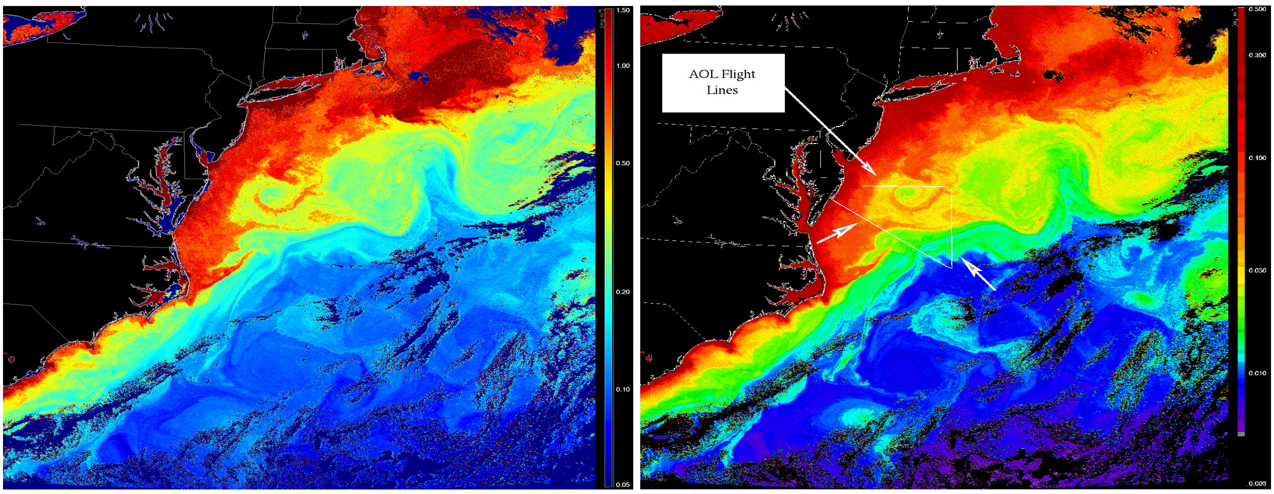

Figure 34. C (left panel) and $a_{acdm}(443)$ (right panel) retrieved from SeaWiFS imagery obtained on day 279, 1997. (C-scale is logarithmic and labels are 0.05, 0.10, 0.30, 0.50, 1.00, and 1.50 mg/m^3.) (a_{cdm}-scale is logarithmic and labels are 0.003, 0.010, 0.030, 0.100, and 0.300 m^{-1}.)

effected by comparing the retrieved C with that from the standard SeaWiFS 8-day mean C that included Day 279. The results were in excellent agreement. The retrieved a_{cdm} was compared with measurements of the absorption coefficient of the *dissolved* portion of the detritial material made using the Airborne Oceanographic Lidar (AOL) [*Hoge et al.*, 1995] along the flight line on the right panel of the figure. The agreement was also excellent in the open ocean, with areas of disagreement near the coast explained by the variability of the parameter S (not considered in the algorithm) from the coastal to the open ocean regime.

An important aspect of the SOA is the ease with which it can be extended to Case 2 waters. A major difficulty for atmospheric correction in Case 2 waters is that the assumption that $\rho_w = 0$ in the NIR is rarely valid. In fact, ρ_w is often large in the NIR because of the presence of high quantities of suspended sediment. Extension of the algorithm to the cases where $\rho_w \neq 0$ in the NIR is immediate: operate the algorithm in an iterative manner, where at each stage in the iteration, water-leaving reflectance in the NIR is computed from the derived bio-optical parameters from the previous iteration. We have tested this idea in the sediment-dominated Case 2 waters of Pamlico Sound, NC. Figure 35 shows the two retrieved parameters of the aerosol model ν (upper panel), the free parameter in the power-law size distribution, and ω_0 (lower panel), the aerosol single scattering albedo. Neither of these atmospheric parameters would be expected to be very different over the Sound and over the near-by ocean, i.e., we would expect continuity in both going from the Sound into the open ocean. Figure 35 shows that when the algorithm is operated in the Case 1 mode ω_0 is lower and ν is higher over the Sound than the off-shore waters. In contrast, almost complete continuity is observed when the algorithm is operated in the Case 2 mode. This suggests that atmospheric correction was achieved in these turbid Case 2 waters. In this case, the quality of the retrieved bio-optical properties will be completely determined by the quality of the bio-optical model.

We believe that it should be possible to tune the *Garver and Siegel* [1997] model parameters to the particular Case 2 waters under examination to retrieve bio-optical parameters; however, such tuning will have to be site specific and season specific. We are in the process of attempting validation of this algorithm for the Case 2 waters of the Chesapeake Bay, and have begun implementation in the MODIS processing environment.

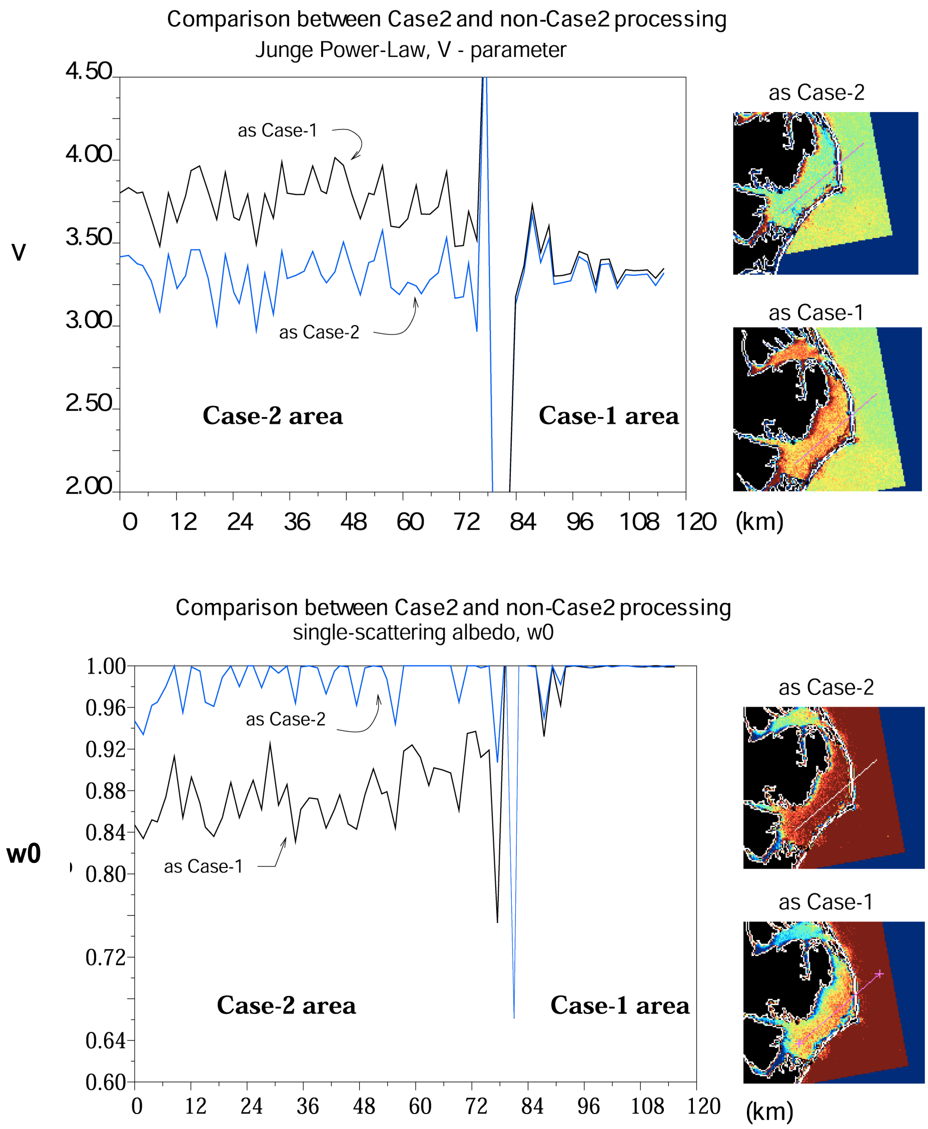

Figure 35. Comparison of the retrieved values of ν (upper panel) and ω_0 (lower panel) between Case 1 and Case 2 processing with the SOA. Note that the atmospheric parameters are virtually unchanged in going from the open ocean to the coastal waters with the Case 2 processing.

5.2 Other Enhancements

There are several other enhancements that require further study, but that should be implemented when the studies are complete.

5.2.1 Use actual $L_u(\theta_v, \phi_v)$ in the computation of t.

Presently, the diffuse transmittance t is computed by assuming the distribution $L_u(\theta_v, \phi_v)$ is uniform, i.e., independent of θ_v and ϕ_v. When a valid distribution model is available, t^* should be replaced by the correct t. The *Morel, Antoine and Gentili* [2002] model of the angular distribution of L_u is being used to correct ρ_w for bidirectional effects. As described in Section 3.1.1.13.4, we are in the process of attempting to validate this model using our own measurements of the upwelling subsurface radiance distribution. An example of this validation attempt is presented in Figure 36. This shows that the *Morel, Antoine and Gentili* [2002] model is excellent in the principal plane in

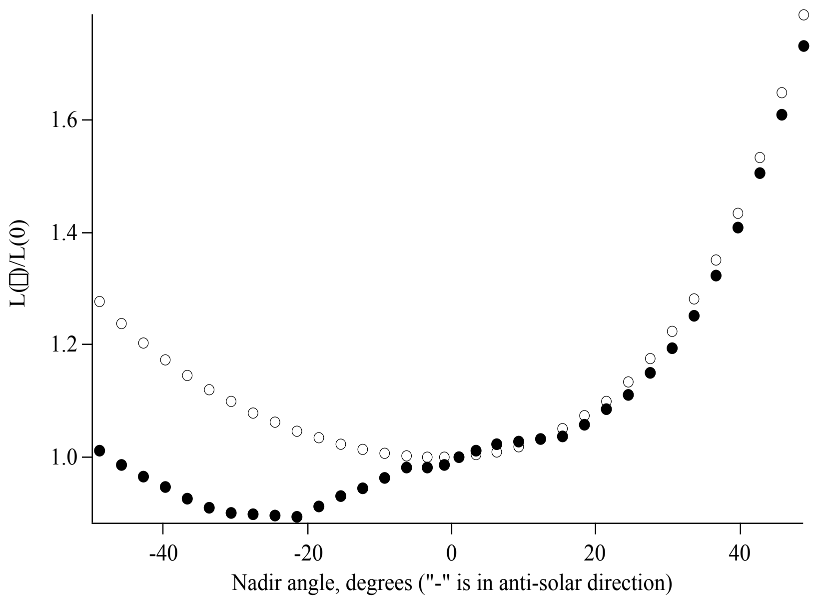

Figure 36. Comparison of the L_u model of *Morel, Antoine and Gentili* [2002] (open symbols) with experimental measurements (filled symbols) in the principal plane (plane containing the sun and the zenith). Measurement conditions: 440 nm, $\theta_0 = 38°$, $C = 10.1$ mg/m^3.

the direction of the sun, but fails in the direction opposite to the sun. It also provides an example of the magnitude of the dependence of L_u on viewing direction.

5.2.2 Introduce the earth curvature effect at high latitude.

As described in Section 3.1.1.12.2 at large θ_0 the influence of the curvature of the earth can be significant, especially in the computation of ρ_r. *Ding and Gordon* [1994] described a method for incorporating the earth-curvature effects, but it was not implemented. Implementation of the *Ding and Gordon* [1994] method, or something similar to include earth curvature, is necessary for processing high-latitude imagery in winter.

5.2.3 Cirrus Clouds.

If the 1.38 μm band (Band 26) on Aqua MODIS performs properly (as it appears to), it is important to incorporate at least a simple procedure to partially correct imagery corrupted by thin cirrus. The methods studied by *Gordon et al.* [1996] may not be applicable if spectral matching or spectral optimization is used to address absorbing aerosols.

References

d'Almeida, G. A., P. Koepke and E. P. Shettle, *Atmospheric Aerosols — Global Climatology and Radiative Characteristics*, A. Deepak Publishing, Hampton, VA, 1991.

André, J. -M. and A. Morel, Atmospheric Corrections and Interpretation of Marine Radiances in CZCS Imagery, Revisited, *Oceanologica Acta*, *14*, 3–22, 1991.

Antoine, D. and A. Morel, Relative importance of multiple scattering by air molecules and aerosols in forming the atmospheric path radiance in the visible and near-infrared parts of the spectrum, *Applied Optics*, *37*, 2245–2259, 1998.

Austin, R. W., The Remote Sensing of Spectral Radiance from below the Ocean Surface, in *Optical Aspects of Oceanography*, edited by N. G. Jerlov and E. S. Nielsen, pp. 317–344, Academic Press, London, 1974.

Balch, W. M., P. M. Holligan, S. G. Ackleson and K. J. Voss, Biological and optical properties of mesoscale coccolithophore blooms in the Gulf of Maine, *Limnology and Oceanography*, *34*, 629–643, 1991.

Banzon, V. F., R. E. Evans, H. R. Gordon and R. M. Chomko, SeaWiFS observations of the Arabian Sea Southwest Monsoon bloom for the year 2000, 2004, *Deep Sea Research II* (Submitted).

Barnes, R. A., A. W. Holmes, W. L. Barnes, W. E. Esaias, C. R. McClain and T. Svitek, *SeaWiFS Technical Report Series: Volume 23, SeaWiFS Prelaunch Radiometric Calibration and Spectral Characterization*, NASA, Greenbelt, MD, Technical Memorandum 104566, October 1994.

Bricaud, A. and A. Morel, Atmospheric Corrections and Interpretation of Marine Radiances in CZCS Imagery: Use of a Reflectance Model, *Oceanologica Acta*, *7*, 33–50, 1987.

Cattrall, C., K. L. Carder and H. R. Gordon, Columnar aerosol single-scattering albedo and phase function retrieved from sky radiance over the oceans: Measurements of African dust, *Jour. Geophys. Res.*, *108(D9)*, 4287, 2003, (doi:10.1029/2002JD002497).

Charlson, R. J., J. E. Lovelock, M. O. Andreae and S. G. Warren, Oceanic phytoplankton, atmospheric sulphur, cloud albedo and climate, *Nature*, *326*, 655–661, 1987.

Charlson, R. J., S. E. Schwartz, J. M. Hales, R. D. Cess, J. A. Coakley, J. E. Hansen and D. J. Hofmann, Climate Forcing by Anthropogenic Aerosols, *Science*, *255*, 423–430, 1992.

Chomko, R. and H. R. Gordon, Atmospheric correction of ocean color imagery: Use of the Junge power-law aerosol size distribution with variable refractive index to handle aerosol absorption, *Applied Optics*, *37*, 5560–5572, 1998.

Chomko, R. M. and H. R. Gordon, Atmospheric correction of ocean color imagery: Test of the spectral optimization algorithm with SeaWiFS, *Applied Optics*, *40*, 2973–2984, 2001.

Chomko, R. M., H. R. Gordon, S. Maritorena and D. A. Siegel, Simultaneous determination of oceanic and atmospheric parametters for ocean color imagery by spectral optimization: A validation, *Rem. Sens. Environ.*, *84*, 208–220, 2003.

Clark, D. K., H. R. Gordon, K. J. Voss, Y. Ge, W. Broenkow and C. Trees, Validation of Atmospheric Correction over the Oceans, *Jour. Geophys. Res.*, *102D*, 17209–17217, 1997.

Clarke, G. L., G. C. Ewing and C. J. Lorenzen, Spectra of Backscattered Light from the Sea Obtained From Aircraft as a Measurement of Chlorophyll Concentration, *Science*, *167*, 1119–1121, 1970.

Cox, C. and W. Munk, Measurements of the Roughness of the Sea Surface from Photographs of the Sun's Glitter, *Jour. Opt. Soc. of Am.*, *44*, 838–850, 1954.

Deirmendjian, D., *Electromagnetic Scattering on Spherical Polydispersions*, Elsevier, New York, NY, 1969, 290 pp.

Deschamps, P. Y., M. Herman and D. Tanre, Modeling of the atmospheric effects and its application to the remote sensing of ocean color, *Applied Optics*, *22*, 3751–3758, 1983.

Ding, K. and H. R. Gordon, Atmospheric correction of ocean color sensors: Effects of earth curvature, *Applied Optics*, *33*, 7096–7016, 1994.

Ding, K. and H. R. Gordon, Analysis of the influence of O_2 A-band absorption on atmospheric correction of ocean color imagery, *Applied Optics*, *34*, 2068–2080, 1995.

Durkee, P. A., D. R. Jensen, E. E. Hindman and T. H. V. Haar, The Relationship Between Marine Aerosol Particles and Satellite-Detected Radiance, *Jour. Geophys. Res.*, *91D*, 4063–4072, 1986.

Ebuchi, N. and S. Kizu, Probability Distribution of Surface Wave Slope Derived Using Sun Glitter Images from Geostationary Meteorological Satellite and Surface Vector Winds from Scatterometers, *Jour. of Oceanogr.*, *58*, 477–486, 2002.

Eldridge, R. G., Water Vapor Absorption of Visible and Near Infrared Radiation, *Applied Optics*, *4*, 709–713, 1967.

Evans, R. H. and H. R. Gordon, CZCS 'System Calibration:' A retrospective examination, *Jour. Geophys. Res.*, *99C*, 7293–7307, 1994.

Falkowski, P. G., Y. Kim, Z. Kolber, C. Wilson, C. Wirick and R. Cess, Natural Versus Anthropogenic Factors Affecting Low-Level Cloud Albedo over the North Atlantic, *Science*, *256*, 1311–1313, 1992.

Feldman, G. C., N. Kuring, C. Ng, W. Esaias, C. R. McClain, J. Elrod, N. Maynard, D. Endres, R. Evans, J. Brown, S. Walsh, M. Carle and G. Podesta, Ocean Color: Availability of the Global Data Set, *EOS Trans. Amer. Geophys. Union*, *70*, 634–641, 1989.

Fraser, R. S., Degree of Interdependence among Atmospheric Optical Thickness in Spectral Bands between 0.36 and 2.4 μm, *Applied Optics*, *14*, 1187–1196, 1975.

Fraser, R. S., Satellite measurement of mass of Sahara dust in the atmosphere, *Applied Optics*, *15*, 2471–2479, 1976.

Fraser, R. S. and Y. J. Kaufman, Calibration of satellite sensors after launch, *Applied Optics*, *25*, 1177–1185, 1986.

Frouin, R., M. Schwindling and P. Y. Deschamps, Spectral reflectance of sea foam in the visible and near-infrared: In-situ measurements and implications for remote sensing of ocean color and aerosols, *Jour. Geophys. Res.*, *101C*, 14,361–14,371, 1996.

Gao, B. -C., A. F. H. Goetz and W. J. Wiscombe, Cirrus cloud detection from airborne imaging spectrometer data using the 1.38 micron water vapor band, *Geophysical Research Letters*, *20*, 301–304, 1993.

Garver, S. A. and D. A. Siegel, Inherent optical property inversion of ocean color spectra and its biogeochemical interpretation: 1 time series from the Sargasso Sea, *Jour. Geophys. Res.*, *102C*, 18607–18625, 1997.

Gordon, H. R., Radiative Transfer: A Technique for Simulating the Ocean in Satellite Remote Sensing Calculations, *Applied Optics*, *15*, 1974–1979, 1976.

Gordon, H. R., Removal of Atmospheric Effects from Satellite Imagery of the Oceans, *Applied Optics*, *17*, 1631–1636, 1978.

Gordon, H. R., Calibration Requirements and Methodology for Remote Sensors Viewing the Oceans in the Visible, *Remote Sensing of Environment*, *22*, 103–126, 1987.

Gordon, H. R., Ocean Color Remote Sensing Systems: Radiometric Requirements, *Society of Photo-Optical Instrumentation Engineers, Recent Advances in Sensors, Radiometry, and Data Processing for Remote Sensing*, *924*, 151–167, 1988.

Gordon, H. R., Radiometric Considerations for Ocean Color Remote Sensors, *Applied Optics*, *29*, 3228–3236, 1990.

Gordon, H. R., Remote sensing of ocean color: a methodology for dealing with broad spectral bands and significant out-of-band response , *Applied Optics*, *34*, 8363–8374, 1995.

Gordon, H. R., Atmospheric Correction of Ocean Color Imagery in the Earth Observing System Era, *Jour. Geophys. Res.*, *102D*, 17081–17106, 1997.

Gordon, H. R., In-orbit calibration strategy for ocean color sensors, *Remote Sensing of Environment*, *63*, 265–278, 1998.

Gordon, H. R., J. W. Brown and R. H. Evans, Exact Rayleigh Scattering Calculations for use with the Nimbus-7 Coastal Zone Color Scanner, *Applied Optics*, *27*, 862–871, 1988.

Gordon, H. R., O. B. Brown, R. H. Evans, J. W. Brown, R. C. Smith, K. S. Baker and D. K. Clark, A Semi-Analytic Radiance Model of Ocean Color, *Jour. Geophys. Res.*, *93D*, 10909–10924, 1988.

Gordon, H. R. and D. J. Castaño, The Coastal Zone Color Scanner Atmospheric Correction Algorithm: Multiple Scattering Effects, *Applied Optics*, *26*, 2111–2122, 1987.

Gordon, H. R. and D. J. Castaño, The Coastal Zone Color Scanner Atmospheric Correction Algorithm: Influence of El Chichón, *Applied Optics*, *27*, 3319–3321, 1988.

Gordon, H. R. and D. K. Clark, Atmospheric effects in the remote sensing of phytoplankton pigments, *Boundary-Layer Meteorology*, *18*, 299–313, 1980.

Gordon, H. R. and D. K. Clark, Clear water radiances for atmospheric correction of coastal zone color scanner imagery, *Applied Optics*, *20*, 4175–4180, 1981.

Gordon, H. R., D. K. Clark, J. W. Brown, O. B. Brown, R. H. Evans and W. W. Broenkow, Phytoplankton pigment concentrations in the Middle Atlantic Bight: comparison between ship determinations and Coastal Zone Color Scanner estimates, *Applied Optics*, *22*, 20–36, 1983.

Gordon, H. R., D. K. Clark, J. L. Mueller and W. A. Hovis, Phytoplankton pigments derived from the Nimbus–7 CZCS: initial comparisons with surface measurements, *Science*, *210*, 63–66, 1980.

Gordon, H. R., T. Du and T. Zhang, Atmospheric correction of ocean color sensors: analysis of the effects of residual instrument polarization sensitivity, *Applied Optics*, *36*, 6938–6948, 1997a.

Gordon, H. R., T. Du and T. Zhang, Remote sensing of ocean color and aerosol properties: resolving the issue of aerosol absorption, *Applied Optics*, *36*, 8670–8684, 1997b.

Gordon, H. R., K. J. Voss, P. V. F. Banzon, R. E. Evans, D. K. Clark, L. Koval, M. Yuen, M. Yarbrough and M. Feinholz, SeaWiFS Calibration Initialization: Preliminary Results, 1998, Ocean Optics XIV, Hawaii, HI, November 1998.

Gordon, H. R. and M. Wang, Surface Roughness Considerations for Atmospheric Correction of Ocean Color Sensors. 2: Error in the Retrieved Water-leaving Radiance, *Applied Optics*, *31*, 4261–4267, 1992a.

Gordon, H. R. and M. Wang, Surface Roughness Considerations for Atmospheric Correction of Ocean Color Sensors. 1: The Rayleigh Scattering Component, *Applied Optics*, *31*, 4247–4260, 1992b.

Gordon, H. R. and M. Wang, Retrieval of water-leaving radiance and aerosol optical thickness over the oceans with SeaWiFS: A preliminary algorithm, *Applied Optics*, *33*, 443–452, 1994a.

Gordon, H. R. and M. Wang, Influence of Oceanic Whitecaps on Atmospheric Correction of SeaWiFS, *Applied Optics*, *33*, 7754–7763, 1994b.

Gordon, H. R. and T. Zhang, How well can radiance reflected from the ocean-atmosphere system be predicted from measurements at the sea surface?, *Applied Optics*, *35*, 6527–6543, 1996.

Gordon, H. R., T. Zhang, F. He and K. Ding, Effects of stratospheric aerosols and thin cirrus clouds on atmospheric correction of ocean color imagery: Simulations, *Applied Optics*, *36*, 682–697, 1997.

Grant, W. B., E. V. Browell, C. F. Butler, M. A. Fenn and G. D. Nowicki, Comparisons of Electra-Lidar and LITE Atmospheric Measurements Near the East Coast of the U.S. and the Caribbean, *EOS, Transactions, American Geophysical Union*, *76*, S70, 1995.

Griggs, M., Measurements of the Aerosol Optical Thickness Over Water Using ERTS-1 Data, *Jour. Air Poll. Contr. Assoc.*, *25*, 622–626, 1975.

Griggs, M., Satellite Measurements of Tropospheric Aerosols, NASA, Contractor Report 3459, August 1981.

Griggs, M., AVHRR Aerosol Ground Truth Experiment, NOAA National Environmental Satellite Service, Final Report Contract No. NA–83–SAC–00106, January 1984.

Griggs, M., AVHRR Measurements of Atmospheric Aerosols Over Oceans, NOAA National Environmental Satellite Service, Final Report Contract No. M0–A01–78–00–4092, November 1981.

Hale, G. M. and M. R. Querry, Optical Constants of Water in the 200-nm to 200-μm Wavelength Region, *Applied Optics*, *12*, 555–563, 1973.

Hansen, J. E. and L. D. Travis, Light Scattering in Planetary Atmospheres, *Space Science Reviews*, *16*, 527–610, 1974.

Herman, J. R., P. K. Bhartia, O. Torres, C. Hsu, C. Seftor and E. Celarier, Global Distribution of Absorbing Aerosols from Nimbus-7/TOMS Data, *Jour. Geophys. Res.*, *102D*, 16911–16922, 1997.

Hoge, F. E., A. Vodacek, R. N. Swift, J. K. Yungel and N. V. Blough, Inherent optical properties of the ocean: retrieval of the absorption coefficient of chromophoric dissolved organic matter from airborne laser spectral fluorescence measurements, *Applied Optics*, *34*, 7032—7038, 1995.

Holben, B. N., T. F. Eck, I. Slutsker, D. Tanre, J. P. Buis, A. Setzer, E. Vermote, J. Reagan, Y. Kaufman, T. Nakajima, F. Lavenu, I. Jankowiak and A. Smirnov, AERONET–A federated instrument network and data archive for aerosol characterization, *Remote Sensing of Environment*, *66*, 1–16, 1998.

Hooker, S. B. and C. R. McClain, The calibration and validation of SeaWiFS data., *Progress in Oceanography*, *45*, 427–465, 2000.

Hovis, W. A., D. K. Clark, F. Anderson, R. W. Austin, W. H. Wilson, E. T. Baker, D. Ball, H. R. Gordon, J. L. Mueller, S. Y. E. Sayed, B. Strum, R. C. Wrigley and C. S. Yentsch, Nimbus 7 coastal zone color scanner: system description and initial imagery, *Science*, *210*, 60–63, 1980.

van de Hulst, H. C., *Multiple Light Scattering*, Academic Press, New York, 1980, 739 pp.

Hwang, P. A. and O. H. Shemdin, The dependence of sea surface slope on atmospheric stability and swell conditions, *Jour. Geophys. Res.*, *93C*, 13903–13912, 1988.

Ismail, S., E. V. Browell, S. A. Kooi and G. D. Nowicki, Simultaneous LASE and LITE Aerosol Profile Measurements over the Atlantic, *EOS, Transactions, American Geophysical Union*, *76*, S71, 1995.

Junge, C., Atmospheric Chemistry, *Advances in Geophysics*, *4*, 1–108, 1958.

Kattawar, G. W., G. N. Plass and S. J. Hitzfelder, Multiple scattered radiation emerging from Rayleigh and continental haze layers. 1: Radiance, polarization, and neutral points, *Applied Optics*, *15*, 632–647, 1976.

Kenizys, F. X., E. P. Shettle, W. O. Gallery, J.H.Chetwynd, L. W. Abreu, J. E. A. Selby, S. A. Clough and R. W. Fenn, Atmospheric Transmittance/Radiance: The LOWTRAN 6 Model, Air Force Geophysics Laboratory, Hanscomb AFB, MA 01731, AFGL–TR–83–0187, 1983, NTIS AD A137796.

King, M. D., Harshvardhan and A. Arking, A Model of the Radiative Properties of the El Chichón Stratospheric Aerosol Layer, *Journal of Climate and Applied Meteorology*, *23*, 1121–1137, 1984.

Koepke, P., Vicarious Satellite Calibration in the Solar Spectral Range by Means of Calculated Radiances and its Application to Meteosat, *Applied Optics*, *21*, 2845–2854, 1982.

Koepke, P., Effective Reflectance of Oceanic Whitecaps, *Applied Optics*, *23*, 1816–1824, 1984.

Koepke, P. and H. Quenzel, Turbidity of the Atmosphere Determined From Satellite: Calculation of Optimum Viewing Geometry, *Jour. Geophys. Res.*, *84*(C12), 7847–7856, 1979.

Koepke, P. and H. Quenzel, Turbidity of the Atmosphere Determined From Satellite: Calculation of Optimum Wavelength, *Jour. Geophys. Res.*, *86*(C10), 9801–9805, 1981.

Korotaev, G. K., S. M. Sakerin, A. M. Ignatov, L. L. Stowe and E. P. McClain, Sun-Photometer Observations of Aerosol Optical Thickness over the North Atlantic from a Soviet Research Vessel for Validation of Satellite Measurements, *Jour. Atmos. Oceanic Technol.*, *10*, 725–735, 1993.

Lechner, I. S., G. W. Fisher, H. R. Larsen, M. J. Harvey and R. A. Knobben, Aerosol Size Distributions in the Southwest Pacific, *Jour. Geophys. Res.*, *94D*, 14893–14903, 1989.

Lee, Z. P., K. L. Carder, S. K. Hawes, R. G. Steward, T. G. Peacock and C. O. Davis, Model for the interpretation of hyperspectral remote-sensing reflectance, *Applied Optics*, *33*, 5721–5732, 1994.

Lee, Z. P., K. L. Carder, S. K. Hawes, R. G. Steward, T. G. Peacock and C. O. Davis, Method to derive ocean absorption coefficients from remote sensing reflectance, *Applied Optics*, *35*, 453–462, 1996.

Maritorena, S., D. A. Siegel and A. R. Peterson, Optimization of semi-analytical ocean color model for global scale applications, *Applied Optics*, *41*, 2705–2714, 2002.

McClain, C. R., M. L. Cleave, G. C. Feldman, W. W. Gregg, S. B. Hooker and N. Kuring, Science quality SeaWiFS data for global biosphere research, paper presented at Sea Technology, 1998, September, 10–16.

McCormick, M. P., LITE – An Overview, *EOS, Transactions, American Geophysical Union*, *76*, S66, 1995.

Mekler, Y., H. Quenzel, G. Ohring and I. Marcus, Relative Atmospheric Aerosol Content from Erts Observations, *Jour. Geophys. Res.*, *82*, 967–970, 1977.

Monahan, E. C., Oceanic Whitecaps, *J. Phys. Oceanogr.*, *1*, 139–144, 1971.

Monahan, E. C. and I. G. O'Muircheartaigh, Whitecaps and the passive remote sensing of the ocean surface, *Int. J. Remote Sensing*, *7*, 627–642, 1986.

Moore, K. D., K. J. Voss and H. R. Gordon, Spectral reflectance of whitecaps: Their contribution to water-leaving radiance, *Jour. Geophys. Res.*, *105C*, 6493–6499, 2000.

Moore, K. D., K. J. Voss and H. R. Gordon, Spectral reflectance of whitecaps: Instrumentation, calibration, and performance in coastal waters, *Jour. Atmos. Ocean. Tech.*, *15*, 496–509, 1998.

Morel, A., Optical Modeling of the Upper Ocean in Relation to Its Biogenous Matter Content (Case I Waters), *Jour. Geophys. Res.*, *93C*, 10,749–10,768, 1988.

Morel, A. and J. -M. André, Pigment Distribution and Primary Production in the Western Mediterranean as Derived and Modeled From Coastal Zone Color Scanner Observations, *Jour. Geophys. Res.*, *96C*, 12,685–12,698, 1991.

Morel, A., D. Antoine and B. Gentili, Bidirectional reflectance of oceanic waters: accounting for Raman emission and varying particle scattering phase function, *Applied Optics*, *41*, 6289 – 6306, 2002.

Morel, A. and B. Gentili, Diffuse reflectance of oceanic waters: its dependence on Sun angle as influenced by the molecular scattering contribution, *Applied Optics*, *30*, 4427–4438, 1991.

Morel, A. and B. Gentili, Diffuse reflectance of oceanic waters. II. Bidirectional aspects, *Applied Optics*, *32*, 6864–6879, 1993.

Morel, A. and B. Gentili, Diffuse reflectance of oceanic waters. III. Implication of bidirectionality for the remote sensing problem, *Applied Optics*, *35*, 4850–4862, 1996.

Morel, A., K. J. Voss and B. Gentili, Bidirectional reflectance of oceanic waters: A comparison of modeled and measured upward radiance fields, *Jour. Geophys. Res.*, *100C*, 13,143–13,150, 1995.

Moulin, C., H. R. Gordon, V. F. Banzon and R. H. Evans, Assessment of Saharan dust absorption in the visible from SeaWiFS imagery, *Jour. Geophys. Res.*, *106D*, 18,239–18,250, 2001a.

Moulin, C., H. R. Gordon, R. M. Chomko, V. F. Banzon and R. H. Evans, Atmospheric correction of ocean color imagery through thick layers of Saharan dust, *Geophys. Res. Lett.*, *28*, 5–8, 2001b.

Neckel, H. and D. Labs, The Solar Radiation Between 3300 and 12500 Å, *Solar Physics* , *90*, 205–258, 1984.

Neville, R. A. and J. F. R. Gower, Passive Remote Sensing of Phytoplankton via Chlorophyll α Fluorescence, *Jour. Geophys. Res.*, *82C*, 3487–3493, 1977.

Otterman, J. and R. S. Fraser, Adjacency effects on imaging by surface reflection and atmospheric scattering: cross radiance to zenith, *Applied Optics*, *18*, 2852–2860, 1979.

Patterson, E. M., Optical properties of crustal aerosol: relation to chemical and physical characteristics, *Jour. Geophys. Res.*, *86C*, 3236–3246, 1981.

Platt, T. and S. Sathyendranath, Oceanic Primary Production: Estimation by Remote Sensing at Local and Regional Scales, *Science*, *241*, 1613–1620, 1988.

Rao, C. R. N., L. L. Stowe, E. P. McClain and J. Sapper, Developemnt and Application of Aerosol Remote Sensing with AVHRR Data from the NOAA Satellites, in *Aerosols and Climate*, edited by P. Hobbs and M. P. McCormick, pp. 69–80, Deepak, Hampton, VA, 1988.

Reddy, P. J., F. W. Kreiner, J. J. Deluisi and Y. Kim, Aerosol Optical Depths Over the Atlantic Derived From Shipboard Sunphotometer Observations During the 1988 Global Change Expedition, *Global Biogeochemical Cycles*, *4*, 225–240, 1990.

Remer, L. A. and Y. A. Kaufman, Dynamical aerosol model: Urban/industrial aerosol, *Jour. Geophys. Res.*, *103D*, 13859–13871, 1998.

Sasano, Y. and E. V. Browell, Light scattering characteristics of various aerosol types derived from multiple wavelength lidar observations, *Applied Optics*, *28*, 1670–1679, 1989.

Schwindling, M., Modeles et measures pour l'observation spatiale de la couleur de l'ocean: Diffusion atmospherique par les aerosols et reflexion de surface par l'ecume, 1995, Docteur de L'Universite these, Univ. des Sci. et Tech. de Lille. 245 pp.

Shaw, J. A. and J. H. Churnside, Scanning-laser glint measurements of sea-surface slope statistics, *Applied Optics*, *36*, 4202–4213, 1997.

Shettle, E. P. and R. W. Fenn, Models for the Aerosols of the Lower Atmosphere and the Effects of Humidity Variations on Their Optical Properties, Air Force Geophysics Laboratory, Hanscomb AFB, MA 01731, AFGL–TR–79-0214, 1979.

Siegel, D. A., M. Wang, S. Maritorena and W. Robinson, Atmospheric correction of satellite ocean color imagery: the black pixel assumption, *Applied Optics*, *39*, 3582–3591, 2000.

Slater, P. N., S. F. Biggar, R. G. Holm, R. D. Jackson, Y. Mao, M. S. Moran, J. M. Palmer and B. Yuan, Reflectance- and Radiance-Based Methods for the In-Flight Absolute Calibration of Multispectral Sensors, *Remote Sensing of Environment*, *22*, 11–37, 1987.

Smirnov, A., B. N. Holben, O. Dubovik, R. Frouin, T. F. Eck and I. Slutsker, Maritime component in aerosol optical models derived from Aerosol Robotic Network data, *Jour. Geophys. Res.*, *108D*, AAC 14–1–14-11, 2003, doi:10.1029/2002JD002701.

Smith, R. C., Structure of Solar Radiation in the Upper Layers of the Sea, in *Optical Aspects of Oceanography*, edited by N. G. Jerlov and E. S. Nielsen, pp. 95–119, Academic Press, New York, NY, 1974.

Smith, R. C. and W. H. Wilson, Ship and satellite bio-optical research in the California Bight, in *Oceanography from Space*, edited by J. F. R. Gower, pp. 281–294, Plenum, New York, NY, 1981.

Spinhirne, J. D., Micro Pulse Lidar, *IEEE Transactionson Geoscience and Remote Sensing*, *31*, 48–55, 1993.

Tomasi, C., Weak Absorption by Atmospheric Water Vapour in the Visible and Near-Infrared Spectral Region, *Nuovo Cimento*, *2C*, 511–526, 1979a.

Tomasi, C., Non-selective absorption by atmospheric water vapour at visible and near infrared wavelengths, *Quart. J. R. Met. Soc.*, *105*, 1027–1040, 1979b.

Villevalde, Y. V., A. V. Smirnov, N. T. O'Neill, S. P. Smyshlyaev and V. V. Yakovlev, Measurement of Aerosol Optical Depth in the Pacific Ocean and North Atlantic, *Jour. Geophys. Res.*, *99D*, 20983–20988, 1994.

Voss, K. J., Electro-optic Camera System for Measurement of the Underwater Radiance Distribution, *Optical Engineering*, *28*, 241–247, 1989.

Voss, K. J., E. J. Welton, J. Johnson, A. Thompson, P. K. Quinn and H. R. Gordon, Lidar Measurements During Aerosols99, *Jour. Geophys. Res.*, *106D*, 20821–20832, 2001.

Wang, M., S. Bailey and C. R. McClain, SeaWiFS provides unique global aerosol optical property data, *EOS, Trans. Am. Geophys. Union*, *81*, 197 & 202, 2000.

Wang, M., S. W. Bailey, C. M. Pietras and C. R. McClain, *Sea WIFS Postlaunch Technical Report Series: Volume 10, Validation analysis, Part 2: Chapter 6, SeaWiFS Aerosol Optical Thickness Match-up Analysis*, NASA, Greenbelt, MD, Technical Memorandum 2000-206892, 2000.

Wang, M. and H. R. Gordon, Estimating aerosol optical properties over the oceans with the multiangle imaging spectroradiometer: Some preliminary studies, *Applied Optics*, *33*, 4042–4057, 1994a.

Wang, M. and H. R. Gordon, A Simple, Moderately Accurate, Atmospheric Correction Algorithm for SeaWiFS, *Remote Sensing of Environment*, *50*, 231–239, 1994b.

Wang, M. and H. R. Gordon, Calibration of ocean color scanners: How much error is acceptable in the near infrared?, *Remote Sensing of Environment*, *82*, 497–504, 2002.

Welton, E. J., K. J. Voss, H. R. Gordon, H. Maring, A. Smirnov, B. Holben, B. Schmid, J. M. Livingston, P. B. Russell,, P. A. Durkee, P. Formenti and M. O. Andreae, Ground-based lidar measurements of aerosols during ACE-2: Instrument description, results, and comparisons with other ground-based and airborne measurements, *Tellus*, *52B*, 568–593, 2000.

Welton, E. J., K. J. Voss, P. K. Quinn, P. J. Flatau, K. Markowicz, J. R. Campbell, J. D. Spinhirne, H. R. Gordon and J. Johnson, Measurements of aerosol vertical profiles and optical properties during INDOEX 1999 using micro-pulse lidars, *Jour. Geophys. Res.*, *107D*, 18–1–18-20, 2002, doi:10.1029/2000JD000038.

Whitlock, C. H., D. S. Bartlett and E. A. Gurganus, Sea Foam Reflectance and Influence on Optimum Wavelength for Remote Sensing of Ocean Aerosols, *Geophys. Res. Lett.*, *7*, 719–722, 1982.

Yang, H. and H. R. Gordon, Remote sensing of ocean color: Assessment of the water-leaving radiance bidirectional effects on the atmospheric diffuse transmittance, *Applied Optics*, *36*, 7887–7897, 1997.

Young, R. W., K. L. Carder, P. R. Betzer, D. K. Costello, R. A. Duce, G. R. Ditullio, N. W. Tindale, E. A. Laws, M. Uematsu, J. T. Merrill and R. A. Feeley, Atmospheric Iron Inputs and Primary Productivity: Phytoplankton Responses in the North Pacific, *Global Biogeochemical Cycles*, *5*, 119–134, 1991.

Glossary

AERONET	Aerosol Robotic Network
ATBD	Algorithm Theoretical Basis Document
CZCS	Coastal Zone Color Scanner
DAAC	Distributed Active Archive Center
GAC	Global Area Coverage
GSFC	Goddard Space Flight Senter
IOP	Inherent Optical Property
MOBY	Marine Optical Buoy
MODIS	Moderate-Resolution Spectroradiometer
NE$\Delta\rho$	Noise Equivalent Reflectance
NIR	Near infrared (700–1000 nm)
RTE	Radiative Transfer Equation
SeaWiFS	Sea-viewing Wide-Field-of-view Sensor
SNR	Signal-to-noise Ratio
SRCA	Spectroradiometric Calibration Assembly
TBD	To be determined
TOMS	Total Ozone Mapping Spectrometer (Nimbus-7)